The Use of Simple Physical Models in Seismology and Glaciology

A dissertation presented
by

Victor Chen Tsai

to

The Department of Earth and Planetary Sciences

in partial fulfillment of the requirements
for the degree of
Doctor of Philosophy
in the subject of
Earth and Planetary Sciences

Harvard University
Cambridge, Massachusetts
May 2009

Dissertation Advisor:

Professor James R. Rice

Author:

Victor Chen Tsai

The Use of Simple Physical Models in Seismology and Glaciology

Abstract

In this thesis, I present results that span a number of largely independent topics within the broader disciplines of seismology and glaciology. The problems addressed in each section are quite different, but the approach taken throughout is to use simplified models to attempt to understand more complex physical systems. In these models, use of solid and fluid mechanics are important elements, though in some cases the mechanics are greatly simplified so that progress can be more easily made. The five primary results of this thesis can be summarized as follows: (1) Glacial earthquakes, which were known as enigmatic $M_S \sim 5$ seismic sources prior to the work presented here, are now characterized and understood as being due to coupling of gravitational energy from large calving icebergs into the solid Earth. (2) Rapid drainage events from meltwater lakes on Greenland can be understood in terms of models of turbulent hydraulic fracture at the base of the Greenland Ice Sheet. (3) The form of 'lake star' melt patterns on lake ice can be quantitatively modeled as arising from flow of warm water through slushy ice. (4) The 2004 Sumatra earthquake can be approximated using a 5-point rupture model, and this model helps resolve some uncertainties of previous models. (5) The accuracy of seismic noise tomography results can be better

understood and calculated through use of a new theoretical approach. While there is no overarching theme to the results obtained in this thesis, all results represent an increase in our understanding of some area of geophysics.

Contents

Citations to Previously Published Work

Chapters 2, 3 (with Appendix A), 5, and 6 have been published in their entirety in the following 4 papers [*Tsai and Ekström*, 2007; *Tsai et al.*, 2008; *Tsai and Wettlaufer*, 2007; *Tsai et al.*, 2005]:

> Victor C. Tsai and Göran Ekström (2007), "Analysis of glacial earthquakes", *J. Geophys. Res.*, **112**, F03S22, doi:10.1029/2006JF000596.
>
> Victor C. Tsai, James R. Rice and Mark Fahnestock (2008), "Possible mechanisms for glacial earthquakes", *J. Geophys. Res.*, **113**, F03014, doi:10.1029/2007JF000944.
>
> Victor C. Tsai and J. S. Wettlaufer (2007), "The formation of lake stars", *Phys. Rev. E*, **75**, doi:10.1103/PhysRevE.75.066105.
>
> Victor C. Tsai, Meredith Nettles, Göran Ekström, and Adam M. Dziewonski (2005), "Multiple CMT source analysis of the 2004 Sumatra earthquake", *Geophys. Res. Lett.*, **32**, L17304, doi:10.1029/2005GL023398.

Chapter 7 (with Appendix C) has been accepted for publication as the following:

> Victor C. Tsai (2009), "On establishing the accuracy of noise tomography travel-time measurements in a realistic medium", *Geophys. J. Int.*, accepted.

Chapter 4 (with Appendix B) will soon be submitted for publication as the following:

> Victor C. Tsai and James R. Rice (2009), "A model for turbulent hydraulic fracture and application to crack propagation at glacier beds", *J. Geophys. Res.*

Acknowledgments

There are many more people who deserve my thanks than those listed here, but I hope I have not been overly forgetful in my omissions. Firstly, I owe a great deal to the many great advisors I have been lucky enough to have had in my career so far. I thank Jim Rice for the countless insightful pieces of advice, for encouraging my varied pursuits, and being understanding of these interests. Thanks to Göran Ekström for similar encouragement and advice, and for initiating a significant portion of this thesis. To Adam Dziewonski and John Wettlaufer for getting me intrigued about interesting questions. To Dave Stevenson, who broadened my mind early in my career. To Hiroo Kanamori, who introduced me to the exciting world of geophysics and has been an irreplaceable mentor through the years. To Alan Weinstein, my first research advisor, who bravely took on an uninformed freshman and allowed him to explore.

Thanks to all of the Harvard people for helping make the past 5 years of my life interesting and enjoyable. To my groupmates Colleen Dalton, Bogdan Kustowski, Meredith Nettles, Elizabeth Templeton, Rob Viesca, Nora DeDontney, Harsha Bhat, Yajing Liu, Eric Dunham, Renata Dmowska for much help, numerous conversations and interesting discussion. To Glenn Sterenborg, John Crowley, Jon Mound, Laurel Senft, Veronika Soukhovitskaya, Hilary Close, Rick Kraus, Ian Eisenman, Rita Parai, Jenny Fisher, Kate Dennis, Brendan Meade, Rick O'Connell, Shreyas Mandre, Jon Fan, Teresa Tang, Cindy Jao, Stefano Giglio for untold chats, adventures and randomness. To the great EPS and SEAS staff who made everything possible. To the entire EPS department for providing a great place to work.

I owe a lot to the many special programs I have been lucky enough to be a part of, and I would not be the person I am today without them. To the SF Bay Area

for being an eye-opening place to grow up; to the Summer Science Program where I found myself; to the COSMOS, SURF, GFD and CIDER programs for wonderful summers. To Caltech and Harvard for being truly amazing institutions. To Dover, Davis and Albany for remarkably great public school teachers and peers.

To the teachers who all contributed to my education, including: Mr. Childers, who encouraged a fifth grader's imagination; Ms. Sorg for making science fun; Mr. Bruner, Mr. DePasquale, Mr. Elby, Mr. Lohman, Ms. Klein for showing me how to explore; and to Ms. Divenyi, Ms. Gibson, Ms. Imes who were no less an important part of my education, in the form of music, language and hard work. To the many Albany friends who contributed to my broader education. To A. E. H., Y. W. and C. W. L. who helped me develop as a person.

To my family, who I have not thanked enough throughout my life. Thank you, mom, for making my life possible and giving me the endless opportunities that one can only dream of. I do not think I will ever fully understand the hardships you have endured or the sacrifices you have made for us, but thank you. Thank you, dad, similarly for the opportunities and sacrifices, and for allowing us to develop in our own way. To Elbert, for being a big brother whenever I needed one and a great brother in general.

Finally, to a few other people who have contributed to my sanity. To Tyson M., Mike B. and other Techers for being an important part of my life. And lastly, to my dear Pulin L., for constantly bearing with my strange habits and keeping me happy.

Dedicated to everyone
who has improved the lives
of those around them.

Chapter 1

Introduction and Summary

A note about this thesis

Science in general, and geophysics in particular, is traditionally subdivided into disciplines that have minimal amounts of overlap with other disciplines. However, interdisciplinary research is becoming more and more popular, and my own interests naturally gravitate towards the boundaries of well-defined research areas. Furthermore, I have had the privilege to work with a number of people with very different interests and approaches to doing science. This good fortune of mine is reflected in the varied nature of the many parts of this thesis as well as the somewhat tenuous connections between these parts. However, there is a common element that ties this thesis together: the use of simple models to understand observed dynamic phenomena in the physical world. While the topics of this thesis range substantially, the approach taken in all of them is to simplify the physics of the problems to a few key components and to attempt to understand the relevant systems in terms of these simplified models. In some cases these models are constructed analytically, in some

cases numerically, and in some cases they are used to analyze extensive amounts of data. But they all share a fundamental conviction regarding the usefulness of simple physical models.

Structure of this thesis

The 6 main chapters of this thesis fall naturally into 5 relatively independent parts:

- Characterizing, modeling and understanding glacial earthquakes (Chapters 2 and 3),
- Modeling the turbulent flow of water within cracks in glaciers (Chapter 4),
- Modeling the growth of meltwater features on lake ice (Chapter 5),
- Creating a simple 5-point rupture model of the 2004 Sumatra earthquake (Chapter 6), and
- Establishing the accuracy of noise tomography measurements (Chapter 7).

Since the parts of this thesis have very different goals, here I separately summarize the motivation behind each section and the results obtained. At the end of each individual chapter is also a short discussion of connections between the given chapter and other chapters.

Chapters 2 and 3: Characterizing, modeling and understanding glacial earthquakes

In 2003, *Ekström et al.* [2003] discovered a new class of earthquakes that they coined 'glacial earthquakes', which occurred primarily in Greenland. It was proposed that the events correspond to large and sudden sliding motion of glaciers, but little was known about these strange events other than their approximate magnitudes ($M_S \approx 4.5 - 5.0$) and approximate mechanisms (equivalent to near-horizontal faulting). In order to obtain a more complete characterization of these events, we decided to perform waveform inversions of all (184) known Greenland events using a simple single-force model of the source (equivalent to an acceleration and deceleration over a certain timescale). This modeling of seismic data yielded improved locations, times, force amplitudes and force directions. This improvement allowed direct association between glacial earthquakes and the calving fronts of very large, fast-flowing outlet glaciers; clearly showed that different outlets behaved differently (both seasonally and in their long-term trends) in manners consistent with other observed differences in outlet features (such as extent of local sea ice and presence of melt); and suggested characteristic event sizes dependent on physical properties of the local outlet glaciers (such as outlet glacier speed and calving front width).

With this new characterization done, we then proceeded to try to model the events in a self-consistent physical framework that accounted for as much near-terminus outlet glacier dynamics as possible. This modeling effort resulted in only 2 types of models that could plausibly explain the salient observations. One model relied on meter-scale sliding of the glacier itself and predicted similarly large surface displace-

ments of the near-terminus part of the glacier, whereas the other model relied on 100-meter-scale motion of large calved icebergs with minimal glacier displacement. While this work was ongoing, observations by *Joughin et al.* [2008b] and *Nettles et al.* [2007] clarified that large icebergs were detaching from the calving fronts at the same time as glacial earthquakes [*Joughin et al.*, 2008b] but that no glacier surface displacements occurred simultaneously [*Nettles et al.*, 2007]. Thus, the first model type was clearly invalidated and the second model type was corroborated. The confluence of our modeling efforts and the recent observations therefore strongly implicated the physical calving process involved in creating glacial earthquakes, although there are still complications regarding the detailed calving process that remain unsolved. Recent papers by *Amundson et al.* [2008] and *Nettles et al.* [2008] confirm that calving of large icebergs is associated with glacial earthquakes.

Chapter 4: Modeling the turbulent flow of water within cracks in glaciers

For a long time, it has been known that meltwater lakes periodically form on the surface of the lower elevation portions of the Greenland Ice Sheet during the warm ($> 0°$C) summer months. It is also known that these lakes sometimes drain rapidly, but a drainage event had not been well characterized until last year, when *Das et al.* [2008] captured the drainage of one of the meltwater lakes with GPS, seismic and water-level instruments. These observations of maximum drainage rates exceeding that over Niagara Falls, and complete lake drainage within a few hours, were well explained by turbulent flow of water into a crack down to the base of the ice sheet, but a quantitative model of this process was lacking. Having such a quantitative

model would be important both to test our understanding of the physical processes involved in the drainage as well as to be able to predict how these drainage events affect the long-term stability of the ice sheet. Thus, we constructed a quantitative model of turbulent hydraulic fracture, with turbulent flow of water through a vertical crack to the base and then through a basal crack that opens as water is pumped into the crack. Using an elastic rheology to approximate the ice deformation and making a few other model simplifications, we were able to solve the turbulent flow problem and make model predictions that agreed reasonably well with observations. Although so far no long-term stability predictions have been made, our model predicts relatively large areas of complete loss in basal resistance, thus implying that if these drainage events are (or become) prevalent then they will cause significant increases in the average ice discharge rate of the Greenland Ice Sheet.

Chapter 5: Modeling the growth of meltwater features on lake ice

When a thick snowfall on thin lake ice becomes infiltrated with warm lake water, a melting front expands through slushy ice in a beautiful star-like pattern that has been observed in many locations, including by Thoreau at Walden Pond. While there is no doubt that the physical process behind this phenomenon has to do with the flow of water through the slushy ice [*Knight*, 1987], the process had not ever been quantitatively modeled and it was not known what set the characteristic spacing of the arms of the star patterns. We therefore undertook this problem, and found that the shape of the melting front results from a competition between high flow causing increased melting (leading to instability) and diffusion of heat (resulting in

stability). To test our (linear stability) theory, we compared our predictions against both laboratory experiments of flow through slushy ice and field observations of 'lake stars'. These predictions agreed relatively well.

Chapter 6: Creating a simple 5-point rupture model of the 2004 Sumatra earthquake

The 2004 Sumatra earthquake was one of the largest earthquakes of the past century, and one of the deadliest natural disasters ever. Due to its large size, standard simple point-source models did not accurately characterize the rupture. Rupture models were made by a number of groups using different methods [*Ammon et al.*, 2005; *Banerjee et al.*, 2005; *Ishii et al.*, 2005; *Vigny et al.*, 2005], but all of these models needed to make assumptions regarding the geometry of the fault and were primarily constrained by data that were convolved with other signals, making it somewhat difficult to determine the actual rupture history. In order to address this problem, we constructed a simple 5-point-source model of the earthquake that used only high-quality long-period seismic data as input, and as such was sensitive to only the large-scale features of the rupture. Although our model was much less detailed than others, it was well-constrained and it therefore accurately approximated the rupture. Comparison with other models showed widespread agreement between the broadest features but some disagreement in quantities such as the fault dip that were not well resolved by other studies.

Chapter 7: Establishing the accuracy of noise tomography measurements

Ever since *Lobkis and Weaver* [2001] showed that a time series resembling a Green's function can sometimes be obtained from cross-correlating noise observed at 2 receivers, seismologists have been interested in applying the technique to the Earth. If successful, average Earth structure could be easily determined between any pair of seismic stations, without needing to wait for earthquakes to obtain a signal. While these 'noise tomography' applications have generally been quite successful [*Shapiro et al.*, 2005; *Sabra et al.*, 2005; *Yao et al.*, 2006; *Yang et al.*, 2007], it has been unclear why the method works even though the Earth does not satisfy the assumptions necessary for previous theoretical results (e.g. *Lobkis and Weaver* [2001]; *Wapenaar* [2004]; *Snieder* [2004]) to hold. To address this issue, we formulated a new approach to understanding noise correlation results in which noise sources were assumed to be inherently non-uniformly distributed. Making other assumptions more realistic of the Earth, we were able to show that a cross-correlation property still holds and can be used to determine velocity structure. However, differences often arise between the expectation of previous theoretical results and the actual measured cross-correlations, especially when the noise source distribution or velocity structure is very non-uniform.

Chapter 2

Analysis of Glacial Earthquakes

2.1 Abstract

In 2003, *Ekström et al.* [2003] reported on the detection of a new class of earthquakes that occur in glaciated regions, with the vast majority being in Greenland. The events have a characteristic radiation pattern and lack the high frequency content typical of tectonic earthquakes. It was proposed that the events correspond to large and sudden sliding motion of glaciers. Here, we present an analysis of all 184 such events detected in Greenland between 1993 and 2005. Fitting the teleseismic long-period surface waves to a landslide model of the source, we obtain improved locations, timing, force amplitudes and force directions. After relocation, the events cluster into seven regions, all of which correspond to regions of very high ice flow, and most of which are named outlet glaciers. These regions are: Daugaard Jensen Glacier, Kangerdlugssuaq Glacier, Helheim Glacier, the southeast Greenland glaciers, the northwest Greenland glaciers, Rinks Isbrae, and Jakobshavn Isbrae. Event am-

plitudes range from $0.1 - 2.0 \cdot 10^{14}$ kg m. Force directions are consistent with sliding in the direction of glacial flow over a period of about 50 s. Each region has a different temporal distribution of events. All glaciers are more productive in the summer but have their peak activity in different months. Over the study period, Kangerdlugssuaq has had a constant number of events each year whereas Jakobshavn had most events in 1998-1999, and the number of events in Helheim and the northwest Greenland glaciers has increased substantially between 1993 and 2005. The size distribution of events in Kangerdlugssuaq is peaked above the detection threshold, suggesting that glacial earthquakes have a characteristic size.

2.2 Introduction

Since the 1980's, glaciologists have known that both the Greenland and Antarctic Ice Sheets are drained by narrow but fast moving features known as ice streams and outlet glaciers [*Bauer*, 1961; *Morgan et al.*, 1982]. More recently, it has been observed that these features display a wide range of time-varying behavior with timescales ranging from thousands of years down to a few minutes (e.g., *Alley and Whillans* [1991], *Bindschadler et al.* [2003] and *Howat et al.* [2005]). Although a great deal of work has been done to understand what controls these variations in ice velocity, many aspects of glacial dynamics are still poorly understood (e.g. *Paterson* [2002] and *Hooke* [2005]).

In 2003, *Ekström et al.* [2003] presented evidence for the detection of a new class of earthquakes associated with ice motion. Although seismic studies of glacial regions have described a wide range of phenomena (e.g., *VanWormer and Berg* [1973],

Weaver and Malone [1979], *Wolf and Davies* [1986], *Qamar* [1988], *Deichmann et al.* [2000], and *Stuart et al.* [2005]), all seismic studies prior to *Ekström et al.* [2003] describe earthquakes with magnitudes smaller than 2.8 and with dominant periods less than one second. In contrast, *Ekström et al.* [2003] describe earthquakes with dominant periods between 35 and 150 seconds and surface-wave magnitudes between 4.6 and 5.1, thus describing a new glacial phenomenon. The majority of these "glacial earthquakes" occur in Greenland and are characterized by their lack of high-frequency radiation compared to that of standard earthquakes of similar magnitudes. *Ekström et al.* [2003] further observe that the radiation patterns of the events are inconsistent with the standard earthquake faulting mechanism but are much better described by a "landslide" model thus leading them to interpret the events as sudden, rapid movement of ice. *Ekström et al.* [2003] and *Ekström et al.* [2006] also observe a seasonal variation in the event distribution, with fewer events in the winter months, leading them to speculate that melt water may play an important role in the occurrence of glacial earthquakes.

The earthquake detection algorithm as described by *Ekström* [2006] has now been used on all the available global seismic data from 1993 to 2005. This analysis has resulted in the detection of 184 glacial earthquakes in Greenland. Here, we present a detailed seismic analysis of these 184 events. We obtain improved estimates of the locations of the events compared with those of *Ekström et al.* [2006]. We also obtain estimates of the amplitude and direction of the force associated with each event, something that has not previously been done systematically for glacial earthquakes. These new source parameters allow us to draw a close association between glacial

earthquakes and fast flowing features (ice streams and large outlet glaciers) of the Greenland Ice Sheet. We are further able to suggest some relationships between some glacial earthquake parameters and certain glaciological parameters. However, given the lack of constraints on many key glaciological parameters, it would be premature to make conclusive statements about the glacial physics involved. Further observation and research are required to make such statements.

2.3 Analysis

We analyze 184 Greenland events that result from the application of the earthquake detection algorithm of *Ekström* [2006]. From the initial detections, we have estimates of the origin time, epicenter, and a long-period surface-wave magnitude (M_{SW}) of the events. The detection origin times are accurate to within approximately 10 seconds, locations accurate to within a few hundred km, and M_{SW} accurate to within 0.1-0.2 magnitude units. As will be shown, the analysis presented here significantly decreases all of these uncertainties. The range of M_{SW} for the glacial events is 4.6 to 5.1, where $M_{SW} = 4.6$ corresponds to the lowest-magnitude earthquake that can be detected with the current detection algorithm.

We use seismic data recorded by the IRIS Global Seismographic Network (GSN), filtered in the 35-75 second, 40-100 second, or 50-150 second period band, depending on which period band has a better signal-to-noise ratio for each event. Since the signal-to-noise ratio is often small, we only use between 10 and 40 of well-distributed, high signal-to-noise stations in the analysis of each event. Vertical, transverse, and longitudinal component seismograms are all used when appropriate. Fewer stations

are typically used for smaller events.

As in *Ekström et al.* [2003], we find that the standard Centroid Moment Tensor (CMT) description [*Dziewonski et al.*, 1981] of earthquakes provides poor fits to the glacial earthquake surface-wave waveforms. Since the CMT description utilizes a 6-component moment tensor, it can represent the double-couple faulting on a plane that characterizes standard earthquakes as well as a more general source, including an isotropic explosion or a dipole-like source. For these inversions, the modeled waveforms fit the data waveforms with residual variance (normalized misfit) typically between 0.6 and 0.7.

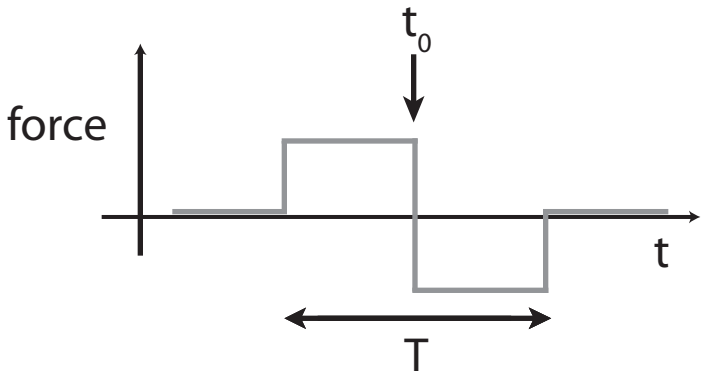

Figure 2.1: Schematic of the symmetric boxcar forcing function used for waveform inversion. T is the full duration of the event and is taken to be 50 seconds in all inversions. t_0 is the centroid time of the event.

Ekström et al. [2003] show that modeling the glacial earthquakes with the centroid single force (CSF) model of *Kawakatsu* [1989], which has been used to model landslide events successfully [*Kanamori and Given*, 1982; *Brodsky et al.*, 2003], yields more satisfactory fits to the data. The CSF model can be used to represent a mass that slides down a slope with an acceleration and then deceleration phase. As the

mass accelerates, a force is exerted on the Earth in the direction opposite to the mass acceleration, thus creating seismic waves. In the simplest formulation, there is constant acceleration followed by constant deceleration of equal and opposite amplitudes, yielding a symmetric boxcar forcing function as depicted in Figure 2.1. We use the symmetric CSF as a first approximation to the actual forcing function to perform waveform inversions. As in the standard CMT inversions [*Dziewonski et al.*, 1981], the problem is nonlinear and the best-fit solution is obtained by iterative inversion.

Under the symmetric boxcar CSF formulation, each inversion has 4 free parameters in addition to the centroid time and location of the event: the amplitudes for the 3 components of the force and the duration. All events are well fit with source duration set equal to 50 seconds, consistent with the fact that waves excited by such a source have their dominant period close to 50 seconds and the events were detected using data in the 35-150 second period band. The modeled seismograms are not very sensitive to changes in duration on the order of 10 seconds, with such changes causing residual variance to vary by between 0.01 and 0.05. Such changes of duration also cause substantial differences in retrieved force amplitude, with longer durations resulting in increased amplitudes of up to 50% and shorter durations resulting in decreased amplitudes of up to 30%. In this analysis, we set the duration of all CSFs to 50 seconds and all reported amplitudes are with this assumption for the duration. Since it is likely that larger events have longer durations than smaller events, the actual range of amplitudes is possibly a factor of two larger than the range we present.

The amplitude of the CSF (which is a twice-time-integrated force), A, has one

possible simple interpretation in terms of the simple symmetric boxcar force model [*Kawakatsu*, 1989]:

$$A = D \cdot M, \tag{2.1}$$

where M is the mass of the slider block (SB) and D is the distance traveled by the SB. The CSF amplitudes we report will be in this 'mass times distance' form. Other physical parameters can also be expressed in terms of A. The maximum velocity change of the SB is given by

$$\Delta V = 2A/(M \cdot T), \tag{2.2}$$

where T is the duration of the event. Describing the resistive force, F, in terms of an average coefficient of friction, f, then

$$F = f \cos\theta \cdot Mg, \tag{2.3}$$

where g is the gravitational acceleration and θ is the slope angle. The difference between F during an event and steady state is

$$\Delta F = 4A/T^2, \tag{2.4}$$

and the change in f is ($\theta \ll 1$ so $\cos\theta \approx 1$)

$$\Delta f = 4A/(Mg \cdot T^2). \tag{2.5}$$

Waveform inversions using the symmetric CSF model result in modeled seismograms that fit the data well, with residual variance of the best-fit inversion typically between 0.3 and 0.5. This observed improvement in residual variance compared with CMT modeling (residual variance of 0.6-0.7) is the reason we use the CSF formulation.

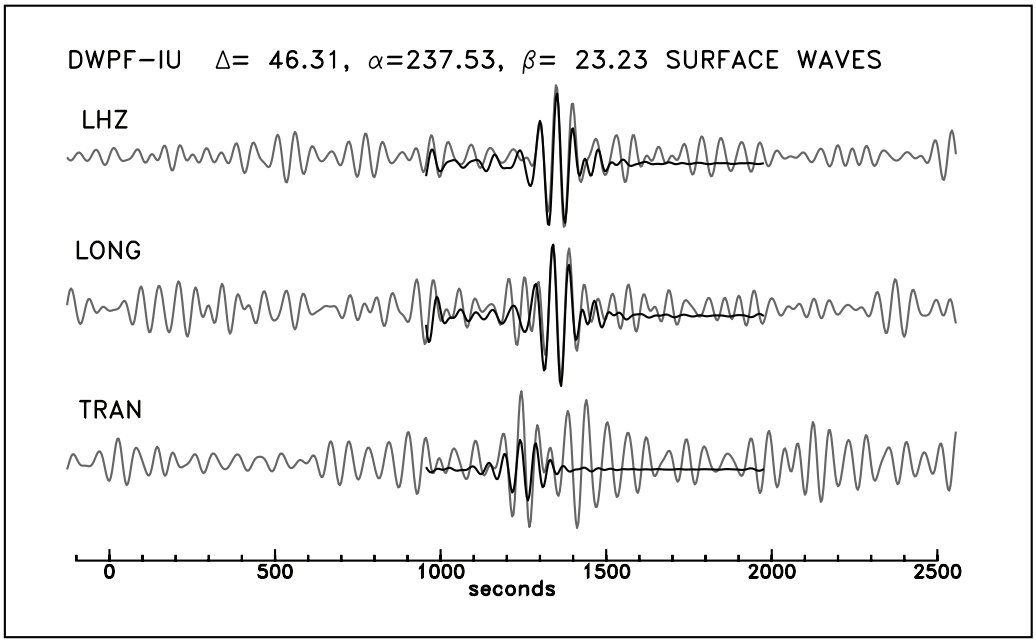

Figure 2.2: Sample seismograms for the 7 February 2001 event recorded at station DWPF (28.11° N, −81.43° E). Gray lines show data seismograms; black lines show synthetic seismograms, offset slightly vertically for clarity. Δ is the distance (in °) of the station from the earthquake. α is the azimuth of the station relative to the earthquake. β is the azimuth of the earthquake relative to the station. LHZ = vertical; LONG = longitudinal; TRAN = transverse. The zero time is as in Table 2.1. The period range is 35-75 s.

The events generally have a two-lobed radiation pattern, with maxima perpendicular to sliding for Love waves and maxima along the sliding axis for Rayleigh waves. This pattern is well captured by the CSF model. Examples of typical waveforms and the modeled fits are shown in Figure 2.2. In all cases, the filtered seismograms have a harmonic character (see Figure 2.2) and have signals not far above the noise. This makes it difficult to distinguish between two sources that are offset in time by half the dominant period and reversed in polarity with respect to each other. As the dominant period is typically around 50 seconds, the best-fit solution usually only has a small improvement in misfit over a solution with around 25 seconds delay or 25 seconds advance. These delayed or advanced solutions then have nearly opposite polarity. As an example of such ambiguity, the 15 September 2000 event has a best-fit residual variance of r = 0.364, a delay of 25.3 seconds gives r = 0.439, and an advance of 25.2 seconds gives r = 0.550. The sliding directions in all three cases are nearly horizontal and the delayed and advanced solutions point 173° and 176° (respectively) from that of the best-fit solution. Except for this possible 180° ambiguity, the direction of sliding is well constrained by the characteristic two-lobed radiation pattern. Similarly, except for the possible delay or advance by half the dominant period (20-30 seconds), the centroid time of the event is well constrained (to within 2-3 seconds) by the phase of the seismic signals.

Due to the many sources of noise and our lack of a priori knowledge of these sources of uncertainty, it is difficult to assess quantitatively the uncertainty in retrieved parameters resulting from our analysis. However, *Smith and Ekström* [1997] show that CMT inversions have a one-sigma absolute uncertainty in horizontal loca-

tion of approximately 25 km. Our CSF inversions rely on the same algorithm with slight modification to the source model so we expect our uncertainties to be roughly the same. The excitation of seismic waves is modeled within PREM [*Dziewonski and Anderson*, 1981], a 1D seismic velocity model with a water layer at 0-3 km depth and an upper crust at 3-15 km depth. Since excitation functions do not change substantially in the PREM upper crust, we choose to model all events at 12 km depth, following the practice in standard CMT analysis of very shallow earthquakes [*Dziewonski et al.*, 1981; *Ekström et al.*, 2005]. All events are well fit with model depths anywhere between 3 and 15 km, and retrieved source parameters are identical to within uncertainties. This is not meant to imply source depths are greater than 3 km (we interpret all glacial earthquakes to be shallower than 3 km), but is a limitation of the sensitivity of long-period seismic waves to source depth. All modeled vertical forces are small, with dip angles mostly shallower than 10° and all shallower than 20°. We do not trust the precise values of these shallow dips so we shall not discuss them further. Since uncertainties due to imperfect knowledge of 3D Earth structure are similar for events in the same locality, we expect our relative location uncertainties to be smaller than the absolute uncertainty. Based on numerical experiments done to test the sensitivity of including different data and using different model parameters, we estimate our relative location uncertainty to be 4-15 km, relative sliding direction uncertainty to be $5° - 20°$, and relative amplitude uncertainty to be 10-80%. For comparison, *Ekström et al.* [2003] and *Ekström et al.* [2006] report relative location uncertainties of approximately 100 km and 20 km, respectively. Lower signal-to-noise results in fewer data used and substantial noise contributing to inversions so that

small events have uncertainties on the high end of all estimated uncertainties except for amplitude uncertainties. As discussed earlier, the amplitude uncertainties may be systematic, with small events being smaller than estimated and large events being larger than estimated.

Finally, a few events are not well modeled with the symmetric boxcar CSF. Many of these complex events are much better modeled as two CSFs. The need for two CSFs may imply a large delay between the acceleration and deceleration phase of the events. Since we filter our data at 35-75 s, 40-100 s, or 50-150 s period, accelerations lasting longer than 75, 100, or 150 seconds (respectively) will not be observed well. Therefore, we may be observing two shorter period phases within a longer event. These shorter phases may not be equal in magnitude or opposite in direction since only the sum of all accelerations is constrained to be zero. Alternatively, it may imply two separate events, the second of which was likely triggered by the first. A final alternative is that the landslide source model simply is not a good description of these events. Although we list CSF model parameters for these complex events, given the above discussion, these parameters may not be particularly meaningful. Further study is needed to fully understand these complex events. They are identified by asterisks in Table 2.1.

2.4 Source Analysis Results

Our source analysis results in CSF amplitudes, force directions, and a more precise determination of centroid times and locations. A summary of these parameters for all 184 Greenland glacial earthquakes are listed in Table 2.1. Figure 2.3 displays

Table 2.1: Glacial earthquake parameters. The columns are: latitude, longitude, amplitude ($\times 10^{14}$ kg m), direction (° E of N), time lag from detection time, detection parameters (year, month, day, hour, minute, second, latitude, longitude, surface wave magnitude), region number, and complexity flag. The first five columns result from CSF waveform inversion. Region 0 = DJ, 1 = K, 2 = H, 3 = SEG, 4 = northern NWG, 5 = southern NWG, 6 = RI, 7 = JI. The dip angles for all events are less than 20°. The depths of all events are constrained at 12 km as discussed in the text. Asterisks denote complex events that are not well fit with the simple model.

Lat	Lon	A	Dir	Δt	Detection Parameters										
°N	°E		N°E	s	Yr	Mo	Dy	Hr	Mi	Sc	Lat	Lon	M	R	*
68.63	-32.94	1.97	-23.9	3.95	1993	1	24	10	21	4	68.5	-33.5	5.1	1	
65.23	-40.87	0.63	-38.5	-10.52	1993	7	26	12	26	40	65.75	-41.25	4.9	3	
68.58	-32.9	0.75	-48.8	9.84	1993	8	5	2	0	40	68.75	-32.75	4.9	1	
68.66	-33.12	0.6	-49.6	-10.65	1993	8	24	2	56	0	67	-35	4.8	1	
66.38	-37.72	0.35	100	14.83	1993	10	19	21	10	0	66.5	-37.5	4.8	2	
68.66	-32.93	1.03	147.8	2.6	1993	11	30	7	33	52	67.5	-33.5	5	1	
68.68	-32.93	1.18	-22.6	21.4	1993	12	10	15	24	56	67.25	-34.25	5	1	
68.62	-32.96	0.6	-52.2	13.09	1994	3	31	0	7	4	68.5	-33.5	4.8	1	
65.35	-41.03	0.58	131.2	13.07	1994	4	6	18	1	28	65.75	-41.25	4.8	3	
65.23	-41.12	0.15	-59.9	-3.96	1994	8	16	8	58	48	65.25	-40.75	4.7	3	
68.63	-32.88	1.09	104.6	-9.15	1994	8	21	8	36	48	68.5	-33.5	5	1	
71.92	-28.45	0.39	81	4.25	1994	8	21	9	46	56	72.5	-28.5	4.8	0	
71.77	-51.9	0.3	-121.6	17.71	1994	8	26	6	11	28	72.25	-51.25	4.9	6	
68.65	-32.99	0.77	150.7	-12.19	1994	11	26	4	11	4	69.25	-31.25	4.9	1	
68.59	-32.78	0.17	123.2	-0.4	1995	7	18	5	30	56	69	-31	4.9	1	
68.62	-32.78	0.48	-33.2	10.72	1995	7	24	23	3	52	67.25	-33.25	4.8	1	
71.92	-29.58	0.65	-72.3	5.45	1995	8	3	4	21	52	72.75	-28.75	4.9	0	
68.63	-33.22	0.83	105.1	-3.64	1995	9	4	0	25	12	69	-33	5	1	
68.56	-32.9	0.71	149	-4.71	1995	10	6	3	7	36	68	-38	4.9	1	
68.64	-32.92	1.7	145.6	0.7	1995	11	8	22	20	32	70.5	-27.5	5	1	
73.53	-54.76	0.4	60.7	-17.12	1995	11	12	2	27	20	73.75	-56.25	4.7	5	
68.54	-32.97	1.34	144.6	0.01	1995	12	11	9	35	44	68.5	-31.5	5	1	
68.55	-33.06	0.68	133.8	-6.15	1996	1	28	16	14	8	68.25	-32.75	4.9	1	
66.53	-38.44	0.4	74.8	-17.24	1996	5	14	13	50	16	66.25	-38.25	4.8	2	
68.76	-33.69	0.6	129.2	-1.34	1996	6	26	18	29	28	68.25	-33.25	4.9	1	
68.67	-33.05	1.02	-27.1	22.97	1996	7	19	18	37	28	67.5	-33.5	4.9	1	
66.25	-38.18	0.31	102.9	-8.62	1996	7	25	23	26	8	66.25	-37.75	4.8	2	
66.47	-38.1	0.28	-73.5	3.51	1996	8	8	2	47	4	68	-38	4.7	2	
68.6	-33.22	1.52	-41	13.7	1996	10	4	22	4	48	69.25	-32.25	4.9	1	
66.43	-38.18	0.52	-90	10.24	1996	11	6	3	46	0	67.5	-38.5	4.8	2	
66.47	-38.08	0.58	-94.3	16.47	1996	11	30	13	35	44	65.75	-38.25	4.9	2	
68.74	-32.93	1.09	-79.1	-18.16	1996	12	7	1	42	32	66.75	-34.25	5.1	1	*
68.63	-32.87	0.46	149.5	-0.77	1997	3	16	14	52	40	68.25	-33.25	4.9	1	
71.77	-51.6	0.47	-104.4	15.25	1997	3	28	2	28	16	71.75	-51.25	4.9	6	
68.72	-32.94	0.33	-39.9	9.84	1997	4	7	7	0	32	68.25	-33.25	4.8	1	
65.31	-41.16	0.32	-51.2	5.89	1997	5	4	16	28	48	65.75	-40.25	4.8	3	
68.56	-32.67	0.32	146.3	-10.21	1997	7	15	6	54	48	69	-33	4.8	1	
71.81	-29.17	0.45	-109.4	12.09	1997	8	15	12	1	28	72.25	-30.25	4.9	0	
68.65	-32.91	0.68	-27.6	7.15	1997	8	20	13	28	40	68.75	-32.75	4.9	1	
71.78	-51.63	0.63	-113.9	1.85	1997	9	6	3	45	52	71.75	-52.25	5	6	
68.64	-33.1	0.94	129.4	-0.68	1997	9	12	3	59	20	69.25	-32.75	5	1	*
68.74	-33.36	0.73	128	0.21	1997	9	24	22	9	12	68.25	-33.25	4.9	1	*
66.37	-38.3	0.38	115.3	-10.36	1997	10	1	17	41	28	67	-39	4.7	2	
65.36	-41.2	0.21	-51.9	9.81	1998	5	1	22	19	36	65.75	-40.75	4.7	3	
66.4	-38.02	0.22	92.3	2.85	1998	6	3	15	9	28	66.5	-38.5	4.8	2	
69.32	-50.08	0.46	-105.4	19.51	1998	6	6	16	39	44	69.75	-49.75	4.9	7	
69.34	-50.27	0.46	-113.5	9.72	1998	6	11	0	18	56	69.75	-50.75	4.9	7	
66.43	-38.08	0.34	86.1	-11.56	1998	6	13	18	11	52	66.25	-38.25	4.8	2	
69.14	-49.3	0.4	-90.1	11.88	1998	6	29	15	16	56	69.5	-49.5	4.7	7	
66.37	-38.02	0.31	77.8	-7.03	1998	7	8	9	31	12	66.75	-38.25	4.8	2	
69.32	-50.05	0.29	-100.5	21.05	1998	7	21	6	30	16	69	-49	4.8	7	
69.28	-49.3	0.27	75.9	31.8	1998	7	25	0	49	4	69	-49	4.7	7	

Table 2.2: Table 2.1 Continued

Lat	Lon	A	Dir	Δt	Detection Parameters										
°N	°E		N°E	s	Yr	Mo	Dy	Hr	Mi	Sc	Lat	Lon	M	R	*
69.29	-49.77	0.3	94.4	-10.61	1998	7	28	0	37	28	69.5	-49.5	4.8	7	
68.63	-32.75	0.24	-76.1	9.72	1998	9	20	3	36	0	68.25	-33.75	4.7	1	
68.92	-32.98	0.97	-21.2	15.93	1998	10	13	22	12	48	68.75	-32.25	5	1	
68.8	-33.06	0.72	154.1	-15.16	1998	10	27	3	30	24	68.75	-32.75	5	1	
68.74	-32.95	0.52	-32	12.18	1999	1	22	14	0	48	68.25	-34.25	4.8	1	
71.83	-51.54	0.64	-112.6	0.49	1999	4	19	23	0	24	71.75	-51.25	4.9	6	
71.81	-51.73	0.57	57.3	21.74	1999	4	21	3	49	36	69.25	-51.75	4.8	6	
69.3	-49.63	0.59	-64.7	2.73	1999	4	24	12	17	28	69.5	-50.5	4.9	7	*
69.2	-49.88	0.26	31.3	8.59	1999	5	2	23	16	24	69.75	-49.75	4.7	7	
69.27	-49.63	0.28	-110.3	13.06	1999	5	20	11	34	56	68.75	-49.75	4.8	7	
69.32	-50.06	0.45	-144.1	-13.94	1999	6	9	14	49	4	70.5	-49.5	4.8	7	
66.58	-38.23	0.34	86.6	-4.74	1999	7	18	6	30	32	66.5	-38.5	4.8	2	
69.28	-49.84	0.34	-54.1	11.68	1999	8	14	14	4	56	68.75	-50.25	4.9	7	
66.44	-38.03	0.39	83.9	-5.69	1999	9	2	9	16	56	66.75	-38.25	4.8	2	
68.66	-32.83	0.82	-24.9	21.32	1999	10	8	9	34	56	68.25	-32.75	4.9	1	
68.78	-33.7	0.45	-46.3	17.42	1999	11	15	22	56	8	68.25	-32.75	4.8	1	
68.61	-32.67	0.61	150.1	-5.7	1999	11	15	23	6	16	68.25	-32.75	4.9	1	
66.29	-38.8	0.34	-104.2	10.27	1999	12	21	4	40	16	65.5	-37.5	4.7	2	
68.62	-32.9	0.68	-30.9	-7.54	2000	3	3	14	41	12	69.25	-30.75	4.8	1	
68.75	-33.49	0.6	-40.3	-4.68	2000	3	3	14	57	12	68.5	-35.5	4.9	1	
68.7	-32.78	0.62	-42.6	0.98	2000	6	12	9	37	4	69.5	-31.5	4.8	1	
71.98	-28.32	0.45	73.5	6.2	2000	7	2	10	36	48	71.75	-28.75	4.8	0	
68.61	-32.81	1.22	-34.8	-5.08	2000	7	21	19	2	40	67.75	-34.25	5	1	*
75.4	-58.14	0.45	-145.8	0.04	2000	8	16	21	24	48	75.5	-59.5	4.9	4	
65.3	-41.32	0.41	-41.5	-5.5	2000	9	4	11	57	28	66.5	-41.5	4.8	3	
66.28	-38.05	0.32	93	-4.43	2000	9	15	7	4	32	66.25	-37.75	4.8	2	
73.53	-55.33	0.56	82.6	3.29	2000	9	17	2	18	8	73.5	-56.5	4.8	5	
68.69	-32.94	0.63	-32.9	0.52	2000	10	20	2	1	4	69	-33	4.9	1	
66.42	-37.95	0.33	-107.1	16.44	2001	2	7	5	36	8	65.75	-37.75	4.8	2	
73.07	-54.65	0.33	-121.3	15.45	2001	7	2	1	14	24	72.75	-54.25	4.7	5	
66.48	-37.96	0.35	-106.1	8.19	2001	7	6	3	25	44	66.5	-38.5	4.8	2	
75.84	-58.22	0.32	-10.9	10.96	2001	8	11	6	27	28	75.75	-59.25	4.8	4	
68.67	-32.93	0.78	148.5	9.26	2001	9	3	13	1	12	68.5	-34.5	4.9	1	
68.67	-33.05	0.55	131	-5.05	2001	10	1	16	37	36	68.75	-33.75	4.9	1	
73.15	-54.21	0.21	-115.6	0.63	2001	10	24	17	24	56	72.5	-54.5	4.6	5	
68.59	-33.03	1.15	-20.5	2.55	2001	11	29	2	46	40	67.75	-32.25	5	1	*
68.69	-32.98	0.48	-35.1	-43.96	2001	12	20	7	27	4	69	-27	4.8	1	
71.81	-51.77	0.32	-93.7	47.89	2001	12	21	3	13	36	72.75	-53.75	4.8	6	*
66.45	-38.36	0.27	108	4.13	2001	12	26	19	39	52	66.25	-38.75	4.7	2	
68.61	-32.78	0.87	-18.1	9.79	2001	12	28	17	19	36	68.75	-33.25	5	1	
68.62	-33.04	0.78	-46.5	-2.41	2002	2	27	15	43	4	69.5	-30.5	4.9	1	
68.65	-33	0.76	-37.8	1.97	2002	4	4	22	49	4	68.75	-33.25	4.9	1	
66.44	-38.22	0.29	-92.6	-11.36	2002	4	19	21	50	8	67.25	-38.25	4.7	2	
66.44	-38.3	0.35	89.2	-7.92	2002	5	1	10	13	44	66.25	-38.25	4.8	2	
66.4	-38.2	0.25	-72.2	3.51	2002	5	12	18	6	24	66.75	-38.75	4.7	2	
66.44	-38.21	0.27	110.6	2.12	2002	6	8	4	31	44	66.25	-38.25	4.7	2	
66.5	-38.05	0.22	76.3	5.75	2002	6	8	18	2	16	66.25	-38.25	4.7	2	
73.13	-54.25	0.47	-103.8	-8.62	2002	6	18	22	2	8	73.25	-57.25	4.8	5	
73.12	-54.52	0.45	-120.4	-1.6	2002	7	14	5	18	32	73	-55	4.8	5	
75.54	-58.26	0.29	-149.9	1.02	2002	7	19	0	42	16	75	-57	4.7	4	
66.38	-38.34	0.3	99.8	-2.93	2002	8	3	10	13	4	66.75	-38.25	4.8	2	
68.8	-33.53	0.36	101.8	-6.84	2002	9	20	2	0	16	68.5	-33.5	4.9	1	
68.68	-33.15	0.38	-81.1	11.56	2002	9	26	3	46	16	69	-33	4.8	1	
76.03	-59.44	0.29	45	-1.86	2002	10	2	22	25	44	76.5	-63.5	4.8	4	
75.53	-57.83	0.35	-140.1	6.99	2002	11	14	12	50	56	75.75	-59.25	4.8	4	
68.68	-33.32	0.69	132.8	1.65	2003	2	3	21	44	0	68.5	-32.5	5	1	
71.89	-51.21	0.39	-116.2	12.27	2003	2	17	19	30	40	71.5	-52.5	4.8	6	
75.92	-59.71	0.42	47.6	-13.44	2003	3	10	21	17	36	75.5	-57.5	4.9	4	
75.64	-58.08	0.31	-141.5	7.07	2003	3	26	9	21	4	75.75	-57.75	4.7	4	

Table 2.3: Table 2.1 Continued

Lat	Lon	A	Dir	Δt	Detection Parameters										
°N	°E		N°E	s	Yr	Mo	Dy	Hr	Mi	Sc	Lat	Lon	M	R	*
71.81	-51.92	0.41	63.6	9.41	2003	4	1	8	29	44	71	-53	4.8	6	
72.16	-28.65	0.55	53.4	-0.07	2003	7	26	4	41	44	72.25	-28.75	4.8	0	
66.3	-38.43	0.46	85.9	-1.63	2003	8	3	23	40	40	66.25	-37.75	4.9	2	
68.68	-33	0.41	-31.7	8.93	2003	8	5	14	0	24	68.5	-33.5	4.8	1	
68.47	-32.88	0.64	-44	3.65	2003	8	13	8	51	12	68.25	-34.75	5	1	
74.9	-56.18	0.28	-123.1	-0.2	2003	8	14	23	30	24	75	-57	4.7	4	
75.45	-58.1	0.32	-152.2	-4.63	2003	8	30	5	49	28	75.75	-58.75	4.7	4	
76.04	-59.81	0.43	63.2	15.78	2003	9	20	20	31	20	75.75	-60.25	4.8	4	
68.6	-32.97	0.36	159.5	8.08	2003	9	24	1	1	12	69.25	-32.25	4.8	1	
68.69	-33.09	0.81	-32.6	16.45	2003	9	24	1	32	0	69.25	-32.75	5	1	
66.49	-38.52	0.42	95.4	12.36	2003	10	2	9	7	4	67.25	-37.25	4.8	2	
68.56	-32.85	1.11	-40.1	23.86	2003	10	5	3	7	52	68.5	-33.5	5	1	
66.37	-38.38	0.56	101.6	3.07	2003	10	12	21	12	40	66.5	-38.5	4.9	2	
68.75	-32.87	0.52	148.2	-1.78	2003	10	18	16	10	56	68.5	-33.5	5	1	
75.99	-59.24	0.35	-136.6	-3.17	2003	10	19	9	23	44	76.25	-60.75	4.8	4	
66.4	-38.24	0.43	108.1	-8.15	2003	11	9	4	17	52	66.25	-38.25	4.8	2	
75.87	-60	0.23	27.8	11.24	2004	1	7	14	37	4	75.75	-58.75	4.7	4	
67.87	-33.51	0.2	-82.9	18.32	2004	1	27	6	15	52	68.25	-33.75	4.7	1	
66.37	-38.54	0.21	91.7	10.73	2004	3	16	14	1	36	66.5	-38.5	4.6	2	
73.56	-54.35	0.12	-175.6	-16.3	2004	4	11	4	7	36	73	-55	4.6	5	
66.43	-38.06	0.5	-93.6	20.56	2004	5	26	12	0	16	66.25	-38.75	4.8	2	
75.55	-58.34	0.32	-146.6	-15.72	2004	6	3	4	38	48	75.75	-59.25	4.8	4	
66.44	-38.42	0.7	96.5	-2.72	2004	6	25	5	58	56	66.5	-38.5	4.9	2	
66.51	-38.84	0.32	84.2	-7.79	2004	6	25	6	5	28	66.25	-38.75	4.9	2	
71.83	-51.58	0.33	40.7	-2.78	2004	7	2	6	15	20	71.25	-51.75	4.8	6	
66.38	-38.18	0.28	82.4	1.89	2004	7	6	10	15	12	66.25	-38.25	4.8	2	
66.31	-38.3	0.27	97.3	3.14	2004	7	6	10	22	48	65.75	-37.75	4.7	2	
66.45	-38.98	0.44	-88.4	19.21	2004	7	21	12	33	36	66.75	-38.25	4.8	2	
68.61	-32.84	0.29	-42.7	-1.11	2004	8	1	9	27	4	69	-33	4.8	1	
66.41	-38.26	0.36	112.3	3.81	2004	8	11	7	22	40	66.75	-39.25	4.8	2	
72.01	-28.6	0.6	-116.9	3.67	2004	8	12	13	8	8	72.75	-29.75	4.9	0	
66.4	-38.15	0.37	101	2.96	2004	8	13	19	34	0	66.25	-38.25	4.9	2	
75.71	-58.16	0.39	45.8	12.12	2004	8	22	14	9	44	75.75	-57.25	4.7	4	
76.07	-59.39	0.33	-113.3	1.63	2004	8	26	17	0	8	75.75	-58.25	4.8	4	
68.67	-33.2	0.33	-48.9	-18.84	2004	9	20	5	11	4	68.5	-33.5	4.8	1	
73.06	-54.46	0.35	-142.2	-3.93	2004	9	26	7	46	16	72.75	-54.25	4.8	5	
68.67	-33.27	0.74	-96.7	6.1	2004	11	1	16	39	12	69.25	-32.25	5	1	
66.45	-38.16	0.29	112.9	-3.35	2004	11	2	22	6	40	67	-37	4.8	2	
75.92	-59.74	0.43	38.6	22.69	2004	11	20	7	29	28	75.75	-60.75	4.9	4	
75.98	-59.84	0.37	44.8	7.69	2004	11	24	3	44	24	76.25	-60.75	4.8	4	
68.74	-33.53	0.3	92.3	-9.62	2004	11	24	20	55	12	69.5	-33.5	4.7	1	
76.09	-59.51	0.43	164.2	6.13	2004	12	16	14	53	12	76.25	-61.75	4.8	4	
75.99	-59.6	0.37	-130.1	3.91	2004	12	30	17	6	0	76.25	-60.75	4.8	4	
75.63	-57.88	0.49	-50.9	-5.7	2005	1	2	7	26	8	75.5	-59.5	4.8	4	
68.69	-33.22	1	-81.9	8.74	2005	1	12	20	39	12	68.75	-33.25	5.1	1	
66.53	-38.49	0.84	124	-0.16	2005	2	11	6	55	20	66.75	-38.75	5	2	
66.5	-38.42	0.59	116.6	-1.41	2005	2	19	13	29	28	66.5	-38.5	4.8	2	
68.65	-32.6	0.35	146.9	-5.57	2005	3	20	8	5	4	68.5	-32.5	4.8	1	
66.42	-38.01	0.39	99.8	-7.86	2005	4	5	13	3	28	66.5	-38.5	4.9	2	
68.81	-32.92	0.45	164.5	2.67	2005	4	6	16	41	20	68.75	-32.75	4.9	1	
66.48	-38.72	0.51	-63.3	26.92	2005	4	23	2	10	8	66.75	-37.75	5	2	*
68.68	-33.07	0.49	-12.7	-9.87	2005	4	26	6	13	28	68.25	-33.75	4.8	1	
66.44	-38.04	0.52	120.7	-1.63	2005	5	12	17	23	20	67.25	-37.25	5	2	
66.47	-38.22	0.68	-66.7	12.01	2005	5	12	19	16	56	66.25	-38.25	4.9	2	
75.91	-59.95	0.4	-131.3	1.13	2005	6	11	16	10	48	76.25	-61.75	4.8	4	
66.52	-38.54	0.43	110	-8.14	2005	6	16	10	23	28	76.5	-66.5	4.7	2	
66.39	-38.3	0.51	140.9	11.22	2005	6	16	13	57	44	66.5	-39.5	4.9	2	
71.81	-51.77	0.5	67.8	-15.98	2005	7	17	2	30	56	71.5	-51.5	4.8	6	
65.24	-41.48	0.37	-65.6	16.83	2005	7	28	0	45	4	65.25	-41.25	4.8	3	

Table 2.4: Table 2.1 Continued

Lat	Lon	A	Dir	Δt	Detection Parameters										
°N	°E		N°E	s	Yr	Mo	Dy	Hr	Mi	Sc	Lat	Lon	M	R	*
72.01	-28.45	0.43	-121	12.81	2005	7	28	12	22	40	72.25	-27.75	4.8	0	
69.32	-49.59	0.41	-99.6	-2.59	2005	7	30	20	28	56	69.25	-49.25	4.8	7	
71.9	-28.38	0.37	-146.7	16.51	2005	8	2	13	28	40	72.25	-29.75	4.8	0	
72.89	-54.23	0.26	52.5	-1.71	2005	8	3	0	58	0	73.5	-53.5	4.7	5	
66.42	-38.29	0.5	92.3	-6.27	2005	8	11	6	1	36	66.75	-38.75	4.9	2	
66.42	-38.21	0.23	69.5	-3.34	2005	8	11	6	40	0	65.25	-38.25	4.7	2	
77.62	-66.78	0.39	82.7	-5.98	2005	8	12	19	30	56	77.5	-66.5	4.8	4	
66.46	-38.27	0.48	-60.2	17.74	2005	8	14	3	33	12	65.75	-38.25	4.9	2	
69.22	-49.68	0.39	-108.7	-5.74	2005	8	16	0	56	40	69.75	-49.75	4.8	7	*
76.03	-59.46	0.46	53.3	-21.81	2005	8	18	1	39	4	76.25	-60.75	4.8	4	
66.39	-38.27	0.25	54.3	8.8	2005	8	20	7	54	40	67.5	-38.5	4.7	2	
67.74	-33.14	0.16	-113.1	7.64	2005	9	18	15	1	52	69.5	-34.5	4.7	1	
68.61	-33.16	0.8	-62.6	-0.68	2005	9	20	10	7	44	69.5	-32.5	5	1	
74.64	-56.46	0.35	-124.8	-10.69	2005	10	10	20	15	12	75.25	-56.75	4.8	4	

the locations of all Greenland earthquakes superimposed on a map of Greenland ice sheet balance velocities [Bamber et al., 2001]. In comparison to the original location estimates from the earthquake detection algorithm (see Table 1), we observe strong clustering of events (see Figure 2.4). Comparison with Greenland ice sheet balance velocities (see Figure 2.3) shows that we observe glacial earthquakes only in regions where the ice flow speeds are above 800 m/yr. The converse is not true since there are regions of high ice flow, such as Petermann Glacier (denoted P in Figure 2.3), where no glacial earthquakes have been detected yet.

The locations in which we observe glacial earthquakes can be grouped into roughly seven distinct regions, all of which are coincident with ice streams or outlet glaciers. In this paper, we denote these seven regions as Daugaard Jensen (DJ), Kangerdlugssuaq (K), Helheim (H), southeast Greenland (SEG), Jakobshavn Isbrae (JI), Rinks Isbrae (RI), and northwest Greenland (NWG) (see Figure 2.3). The NWG region includes the Steenstrup Glacier, Dietrichson Glacier, Sverdrup Glacier, Kong Oscar Glacier, and a number of other smaller outlet glaciers. Of the 184 events, 8 occur in DJ, 64 in K, 49 in H, 7 in SEG, 24 in northern NWG, 9 in southern NWG, 10 in RI, and 13

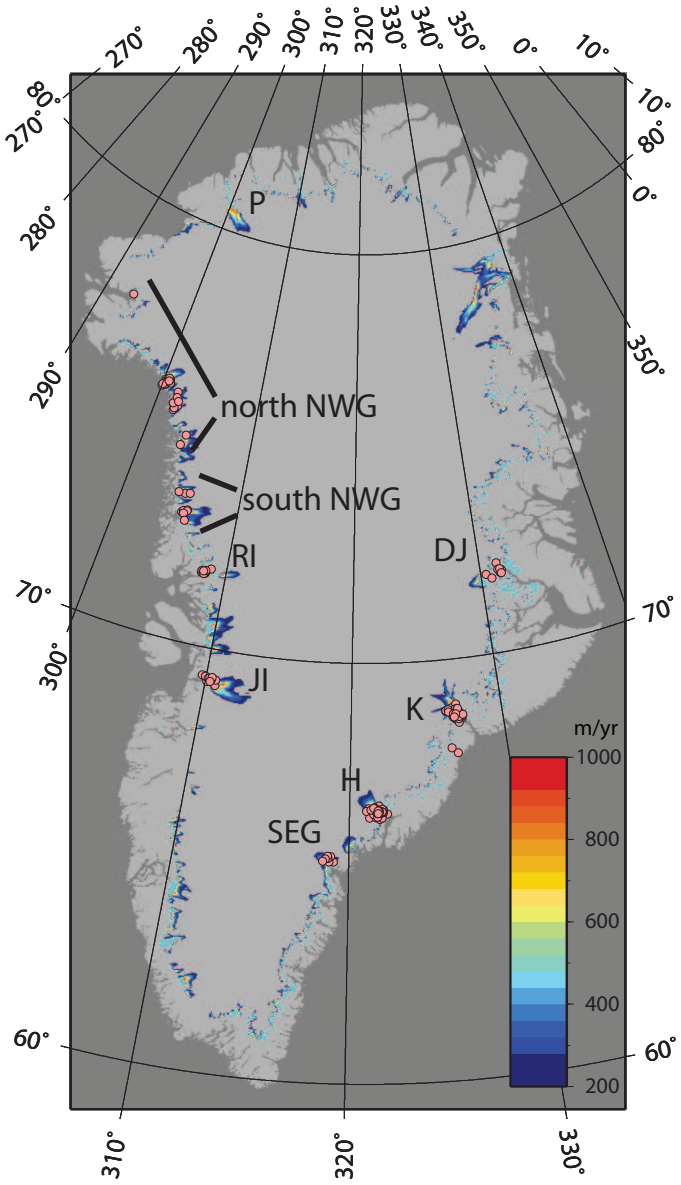

Figure 2.3: Locations of the 184 glacial earthquakes resulting from source analysis are plotted as pink circles. The background colors represent Greenland ice sheet balance velocities from *Bamber et al.* [2001] in units of m/yr. To emphasize regions of high ice flow velocity, velocities less than 200 m/yr are not plotted. Region names are Daugaard Jensen (DJ), Kangerdlugssuaq (K), Helheim (H), southeast Greenland (SEG), Jakobshavn Isbrae (JI), Rinks Isbrae (RI), and northwest Greenland (NWG).

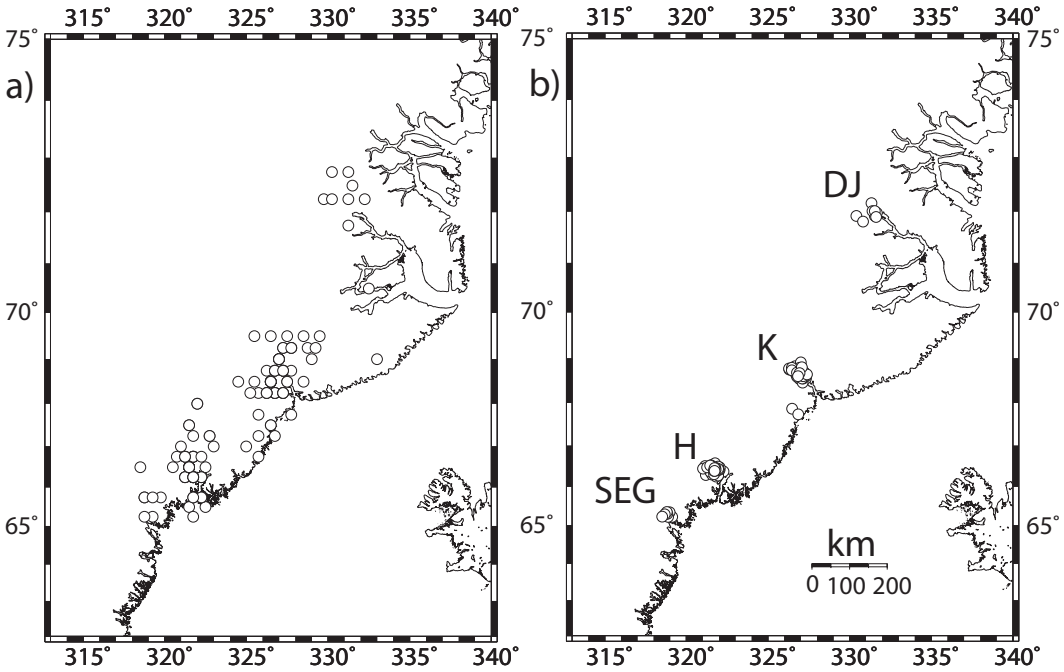

Figure 2.4: (a) The original locations of all of the East Greenland events based on the surface wave detection algorithm. (b) The revised locations of the same events from the surface-wave waveform analysis. Region names are as in Figure 2.3.

in JI. Of the 64 events that occur in the K region, all but two occur in the K Glacier with the two outliers occurring in a nearby outlet glacier (these two events are not used in the statistical descriptions of the K region). All of the events in the DJ, H, JI and RI regions occur within the glacier with the same name (to within location errors). All of the events in region H and all 62 events in the K Glacier occur within a 60 by 40 km area.

Figures 2.5 and 2.6 show detailed views of the regions, with force amplitudes and directions denoted. In all cases, the directions of the modeled sliding axes are consistent with the direction of glacial ice flow (see Figure 2.7). This is the sliding direction expected, thus validating the use of the landslide model. Many of the arrowheads point in the direction opposite the expected one. As discussed in Section 2.3, this is possibly an artifact of the simple symmetric boxcar model used, and not reflective of "upslope" sliding events. This is our preferred interpretation. The rest of the scatter in the direction of the modeled forces we attribute either to real variations in average force directions or to errors resulting from the modeling. As discussed earlier, the errors for many of the smaller events are substantial (estimated to be up to 20°) so it is difficult to distinguish between the two contributions to the scatter in direction.

2.5 Analysis and Interpretation

The dataset resulting from our source analysis contains a wealth of information that can be used to further characterize glacial earthquakes. Here, we analyze the temporal, spatial, and size distribution of the events.

As discussed in *Ekström et al.* [2006], there is a seasonal variation in when glacial

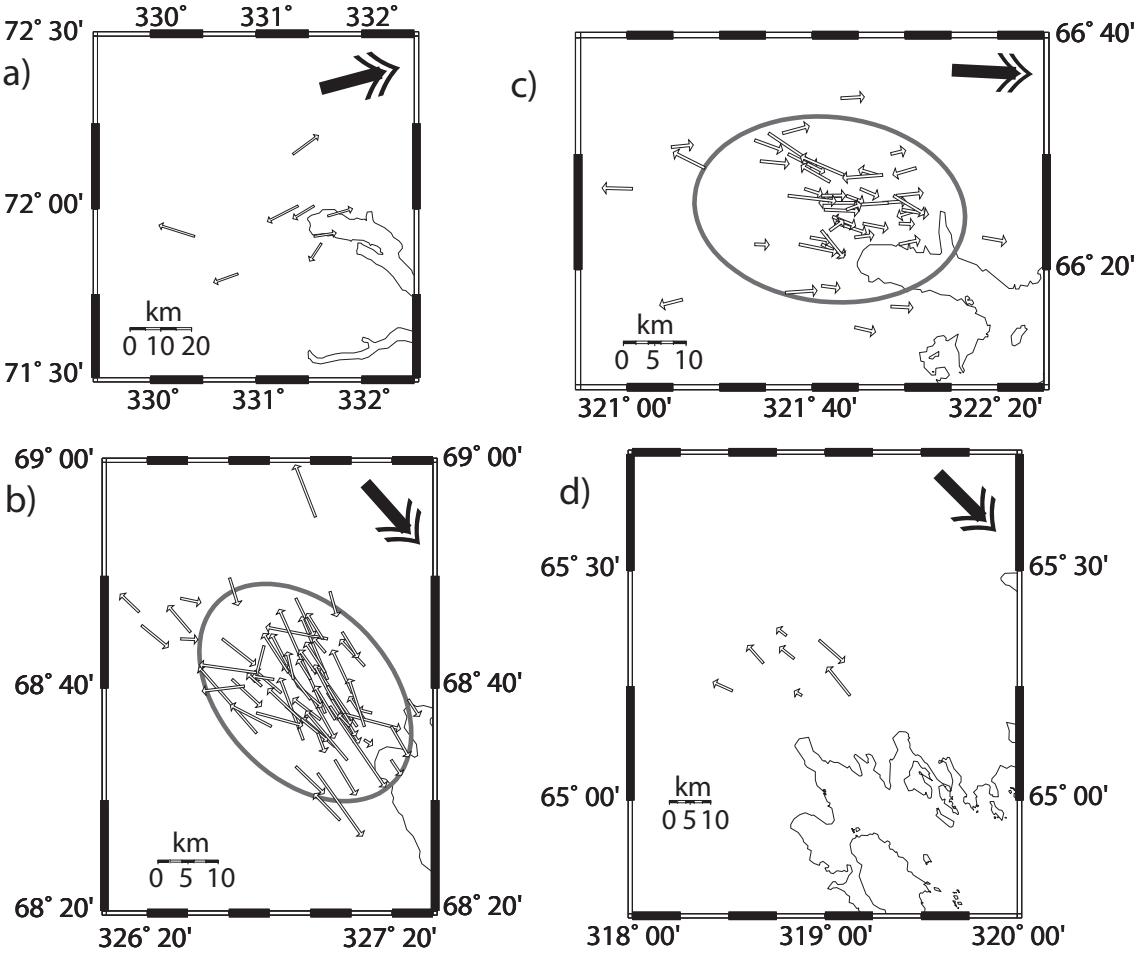

Figure 2.5: Modeled force directions for the (a) Daugaard Jensen (DJ) region, (b) Kangerdlugssuaq (K) region, (c) Helheim (H) region, and (d) South East Greenland (SEG) region. Arrows point in the direction of initial ground acceleration, centroid locations are defined by the location of the arrow tails, and arrow length is proportional to the amplitude of the event. The wide double-headed arrows represent the approximate direction of local glacial flow. The ellipses denote a 2 sigma location ellipse as discussed in Section 2.5.

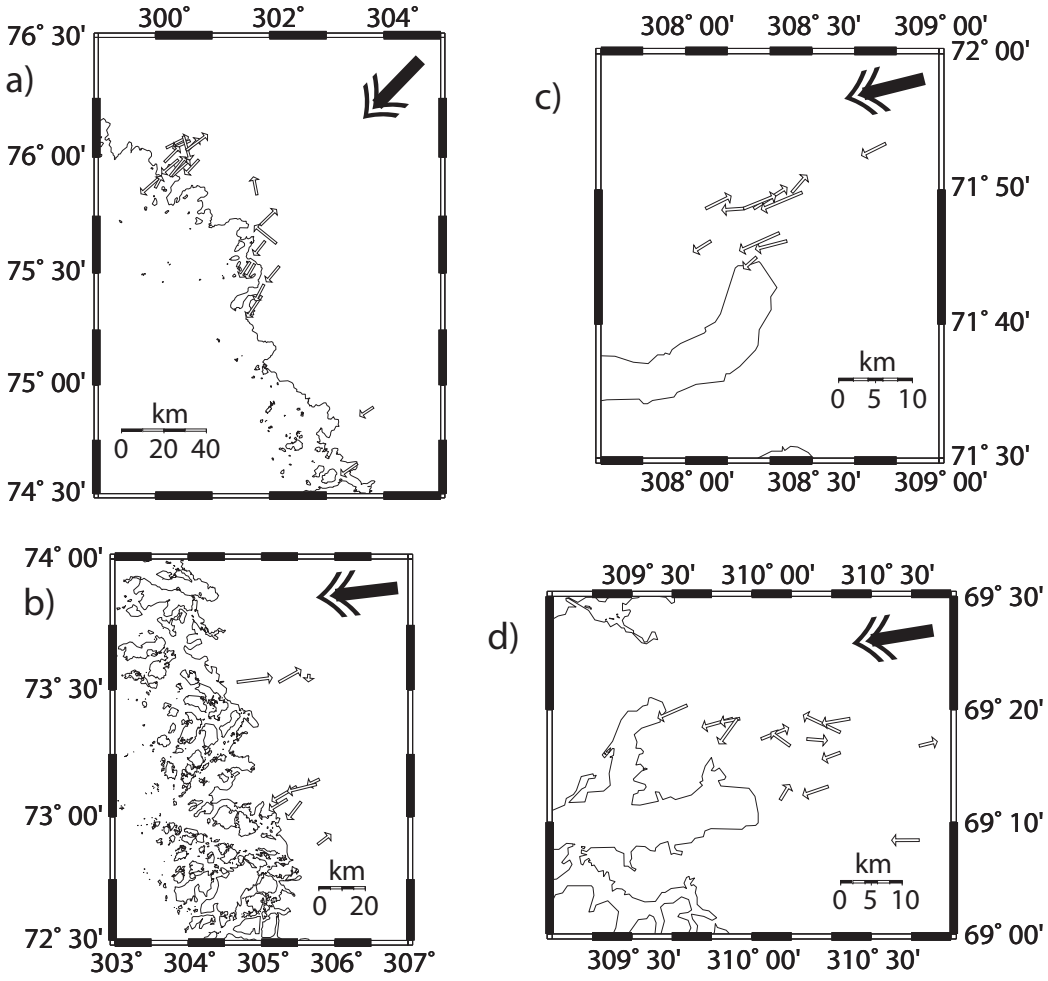

Figure 2.6: Modeled force directions for the (a) northern North West Greenland (NWG) region, (b) southern NWG region, (c) Rinks (RI) region, and (d) Jakobshavn (JI) region. Figure 2.6(a) does not include the one event occurring north of 77° N. Symbols are as in Figure 2.5.

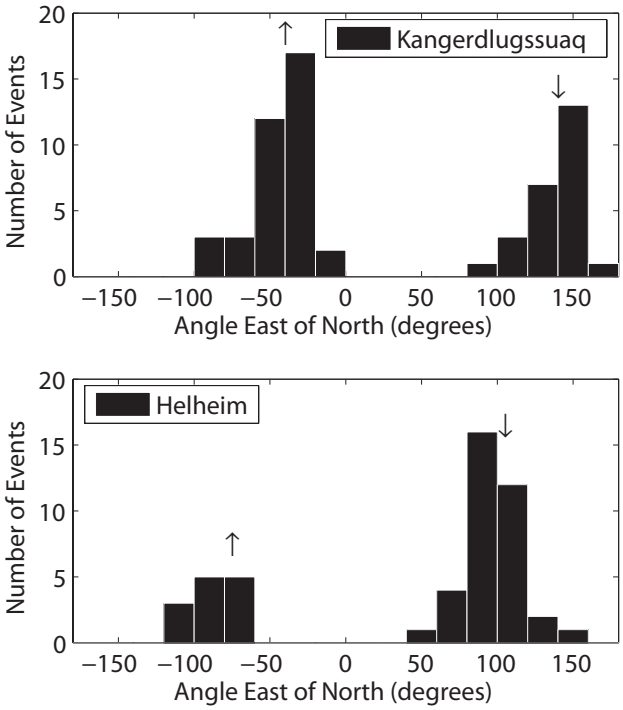

Figure 2.7: Force directions for Regions K and H, compared to glacier orientation. Up arrows correspond to the upstream direction and down arrows correspond to the downstream direction of glacial flow, estimated from *Rignot et al.* [2004].

earthquakes occur, with a peak of activity in northern summer (July, August and September) and a dearth of events in northern winter (January and February having a factor of six fewer events than August). This seasonality suggests that temperature is (indirectly) a factor in determining when glacial earthquakes occur. Examining each region separately, we find distinct differences between them (see Figure 2.8). Region DJ has a single (sharp) peak in activity in August; K has a peak in September, may have a second peak (March-April), but has activity year round that decreases to zero in May and increases afterwards; H has a broad peak in June-August, may have a second peak (October-November), but also has activity year round that deceases to zero in January; RI has two peaks of activity, with activity February-April and July-September; SEG also seems to have two peaks in activity; JI has a single peak in June-July; NWG has a sharp peak in August although other features may be obscured due to averaging over multiple outlet glaciers. Some of this variability may be due to statistics of small numbers, but some features are statistically significant. For example, using a 2-sample t test, we reject at the 95% confidence level the hypothesis that the peak in activity in region K and region H occur at the same time. In contrast to the clear progression to warmer temperatures with decreasing latitude observed in regional weather data [*Cappelen et al.*, 2000], seasonal glacial earthquake activity does not show a clear latitudinal dependence.

All of the events in the JI region prior to 2005 occurred in the summer months of 1998 and 1999, temporally coincident with very large accelerations in the average JI velocity [*Luckman and Murray*, 2005; *Joughin et al.*, 2004]. The correspondence is even more striking when compared with GPS motion upstream of JI from *Zwally*

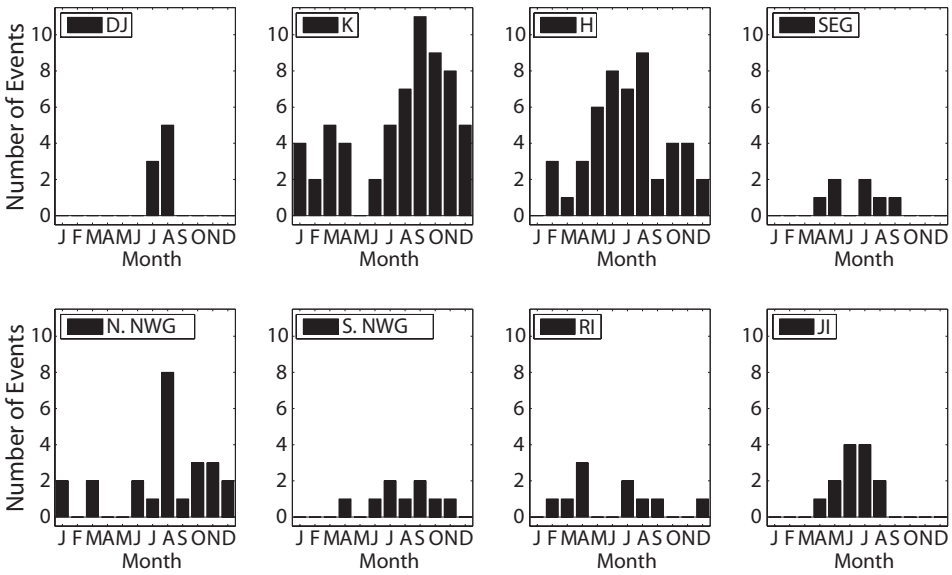

Figure 2.8: Regional monthly histograms for East Greenland (top row) and West Greenland (bottom row) over the time period 1993-2005. Region names are as in Figure 2.3.

et al. [2002], as the JI glacial earthquakes precede the observed episodes of accelerated motion by one or two months. The coincidence of surface melting with the spikes in velocity [*Zwally et al.*, 2002] gives a natural interpretation of glacial earthquakes as being influenced by meltwater reaching the glacier bed; the fact that the glacial earthquakes occur earlier could be interpreted as a consequence of melting occurring earlier downstream. However, observations of increased calving and retreat of JI during the same years [*Luckman and Murray*, 2005; *Joughin et al.*, 2004] complicate this interpretation.

A second temporal trend in the data is the dramatic increase in the total number of events since 2002, with more events detected in each successive year since 2002 and resulting in more than twice as many events in 2005 as compared with any year prior to 2003 [*Ekström et al.*, 2006]. This dramatic increase, however, has not occurred in all regions (see Figure 2.9). The K region has no distinguishable increase in events over time and is consistent with 4.8 +/- 1.2 events per year for the entire detection period. Most of the dramatic increase is due to changes in region H and NWG. In region H, there was a small peak in activity from 1996 to 1999, and from 2000 to the present there has been substantial increase to 10 or more events per year. Region NWG has a more striking change in that the northern part of region NWG did not have a single event before 2000 but has had a steadily increasing number of events until 2005. 2005 had fewer events than 2004, suggesting that the peak in activity may have passed. The southern part of region NWG displays similar behavior to the northern part but without as large of a contrast between the pre-2000 and post-2000 years.

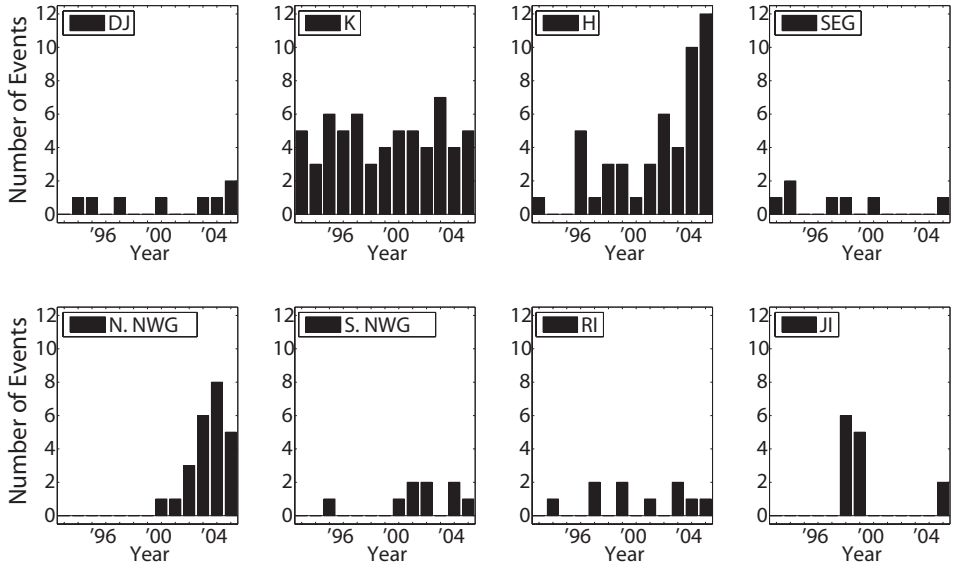

Figure 2.9: Regional yearly histograms for East Greenland (top row) and West Greenland (bottom row). Region abbreviations are as in Figure 2.3.

Other temporal trends exist but are not as compelling due to the small number of events. One such trend is the decrease in size of events in region K, especially of the largest events, with the four largest events occurring in the first four years of the study period (1993-1996). Another such trend is the increase in latitude of the highest-latitude event through the study period, going from 68.7° N in 1993 to 73.5° N in 1995 to 75.4° N in 2000 to 77.6° N in 2005. This increase in northerly extent correlates well with the decrease in southerly extent of arctic sea ice [*Walsh and Chapman*, 2001; *Stroeve et al.*, 2004] and is suggestive of a common cause.

Although we have noted the strong clustering of events, locally there is still scatter in event locations. Establishing whether events occur throughout the glacier (real scatter) or whether events occur at one location (scatter due to measurement) would

give an important constraint on the physical mechanism of glacial earthquakes. Only regions K and H have enough events to make statistical statements about the local spatial distribution of events. In both regions, we find a distribution elongated in the direction of motion (see Figure 2.5bc). In 'sliding direction' coordinates, with x in the sliding direction and y perpendicular to the sliding direction, both regions have Gaussian distributions in x and y but with different standard deviations (σ_x and σ_y). For region K, $\sigma_x = 10.4$ km and $\sigma_y = 7.0$ km. For region H, $\sigma_x = 10.9$ km and $\sigma_y = 7.4$ km. For comparison, the region of H with surface velocities greater than 7 km/yr is approximately 10 km by 5 km (in x and y, respectively) [*Howat et al.*, 2005]. All other regions also have a larger scatter in the sliding direction, although we cannot make a statistical comparison due to insufficient data. We do not observe any pervasive preferential scatter in location that could be attributed to station coverage. Because of radiation patterns, locations should be slightly better constrained in the sliding direction. Since we observe the opposite trend, the scatter in the sliding direction is likely real and not due to location errors. This has two possible implications. One possibility is that only a fraction of the whole glacier participates in individual glacial earthquakes. The scatter in locations should then be interpreted as due to sliding of different segments of the glacier. The other possibility is that the resistive force drops in a very heterogeneous fashion. Under this scenario, the scatter in locations should be interpreted as due to the drop in resistive force occurring primarily in different segments of the glacier in different events. With the data set considered here, the two scenarios are indistinguishable.

Figure 2.10a shows the size distribution for all of the events. All events have

amplitudes between $0.1 - 2.0 \cdot 10^{14}$ kg m. This corresponds to 100 km^3 of ice that travels a distance of 0.1-2.0 m (in roughly 50 seconds), although only the product of mass and distance is constrained. Using (2.1), (2.2) and (2.5), we can determine upper and lower bounds on the distance, velocity change, and change in average friction coefficient associated with each event. Taking 200 km^3 as an estimate of the size of the fast-moving portion of the largest glacier, then $M = 2 \cdot 10^{14}$ kg and the lower bounds are $D = 0.2$ meters, $V = 0.008$ m/s, and $\Delta f = 3 \cdot 10^{-5}$ for a typical event ($0.4 \cdot 10^{14}$ kg m). Taking $D = 100$ meters as an estimate for extreme values of slip, then $V = 4$ m/s, and $\Delta f = 0.016$. Although it is unlikely that the average friction coefficient describes a physical coefficient of friction (i.e. the ratio of shear stress to normal stress), $\Delta f \cdot Mg$ can be thought of as the effective driving force so Δf still gives a useful constraint on the relative size of the effective driving force. It is difficult to compare such estimates of mass and velocity changes with those measured by more standard glaciological methods since temporal and spatial resolutions are typically quite different. However, the lower bound on velocity variations is higher than all other observed velocity variations (e.g. *Zwally et al.* [2002] and *Bindschadler et al.* [2003]) by at least a factor of 20. On the other hand, masses on the order of 100 km^3 have been observed to move coherently (e.g. *Joughin et al.* [2004] and *Luckman and Murray* [2005]) but have not previously been observed to do so on such short timescales.

The scarcity of events with amplitudes below $0.3 \cdot 10^{14}$ kg m may be a result of many events being just below the detection threshold and therefore not being counted. Fitting the remainder of the data to a line in log-log space yields a slope of -2.5. The

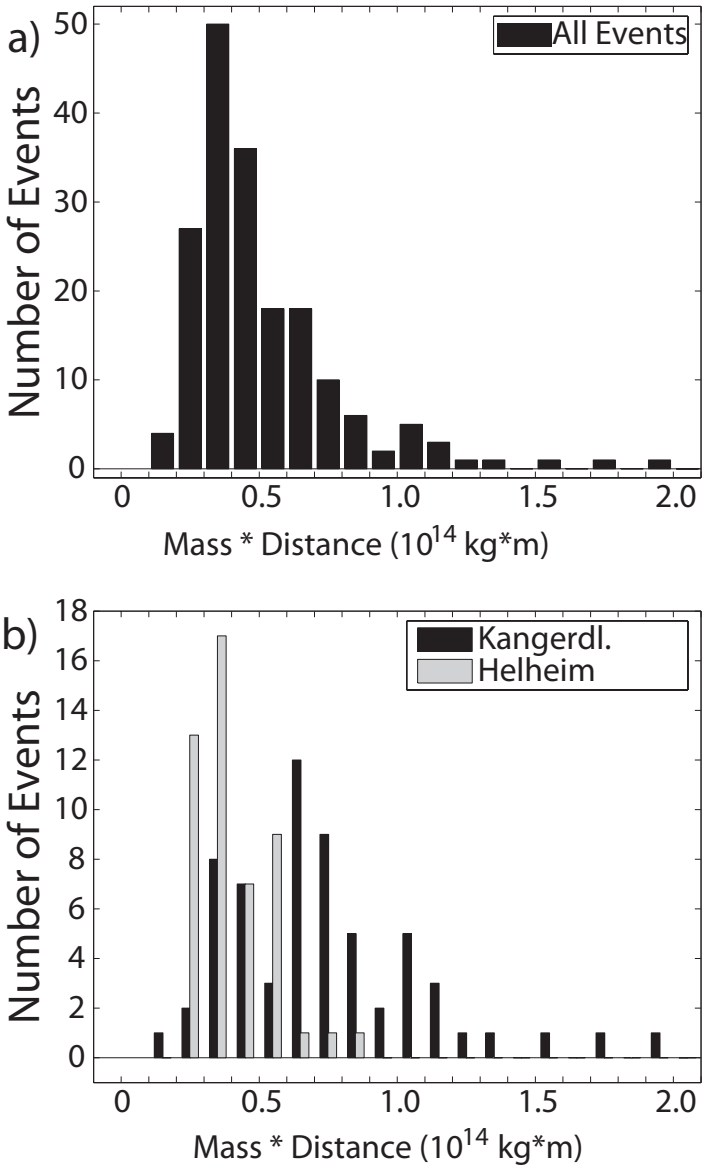

Figure 2.10: (a) Size distribution for all events. (b) Size distribution for regions K and H.

slope deviates significantly from the classic Gutenberg-Richter relation (slope of -0.67). Furthermore, the data are not well fit by the best-fit line. The reason for this poor fit becomes clear when one compares the size distributions of different regions. As shown in Figure 2.10b, the events in region K are larger on average and span a wider range of amplitudes as compared to events in region H which are smaller and have a narrower distribution of amplitudes. Only regions K and H have enough events to make a clear comparison, but the size distributions in all other regions are more similar to region H than region K. In fact, comparing Figure 2.10a with Figure 2.10b we see that every event with amplitude greater than $0.9 \cdot 10^{14}$ kg m occurs in region K.

The distribution of events in region K provides additional constraints on the nature of glacial earthquakes. As stated above, the detection threshold is approximately $0.3 \cdot 10^{14}$ kg m. We expect the threshold to be similar in all regions, yet region K has its peak number of events at $0.6 \cdot 10^{14}$ kg m and contains fewer events with amplitudes between $0.3 - 0.5 \cdot 10^{14}$ kg m. This implies that the distribution in region K is close to the true distribution of glacial earthquakes there, and not a result of the detection threshold. The lack of small events suggests the possibility that glacial earthquakes of a characteristic size are preferentially generated at each outlet glacier. If glacial earthquakes have such a characteristic size, then it would likely depends on a number of factors such as glacier size, hydrologic conditions and calving rate, some of which may change over time, and a power-law distribution should not be expected, at least not locally.

2.6 Conclusions and Implications

All 184 observed Greenland glacial earthquakes occur south of 78° N and in regions with ice flow velocities greater than 800 m/yr (ice streams and large outlet glaciers). All events have amplitudes between $0.1 - 2.0 \cdot 10^{14}$ kg m. Events of smaller amplitude may exist but are not detected. All mechanisms are consistent with sliding of large masses of ice in the direction of glacial flow over a period of about 50 s, although additional observations are required to determine the degree to which this model is just an approximation of the actual source mechanism. The seasonality and increase in total number of events in the past few years suggests that glacial earthquakes are sensitive to temperature or variables affected by temperature. Although events are tightly clustered, locations have a wider spread in the sliding direction implying that events are not all co-located.

Different glaciers display different glacial-earthquake behavior. Each glacier has slightly different seasonal behavior, with peaks in activity in different months. Some glaciers but not all show the dramatic increase in number of events in the past few years. Some regions (e.g., region K) are consistent with a constant number of events per year whereas other regions (e.g., region NWG) have had an unmistakable dramatic increase during the same time period. Glacial earthquakes in region K are larger on average than in any other region, with these events comprising all of the events larger than $0.9 \cdot 10^{14}$ kg m. The distribution of these (region K) events does not resemble a Gutenberg-Richter distribution, but instead has a peak at $0.6 \cdot 10^{14}$ kg m, suggesting that glacial earthquakes may have a characteristic size that depends on attributes of the glacier where they occur.

Any physical mechanism invoked to explain glacial earthquakes must satisfy the observational constraints presented here. Such a physical mechanism will necessarily change the understanding of glacial dynamics since glacial earthquakes are not predicted by any existing theory of glacial behavior. An improved understanding of glacial dynamics is needed to understand fully the stability of the Greenland ice sheet.

2.7 Acknowledgments

We thank R. Anderson, T. Murray, S. Anandakrishnan and an anonymous reviewer for helpful comments. This research was supported by a National Science Foundation Graduate Fellowship (VCT) and National Science Foundation grants EAR-0207608 and OPP-0352276. The seismic data were collected and distributed by the Incorporated Research Institutions for Seismology and the U.S. Geological Survey.

2.8 Connection to Other Chapters

This chapter documents many fundamental seismological constraints on glacial earthquakes and therefore is strongly connected to Chapter 3, in which these constraints are used in producing physical models for glacial earthquakes. This chapter is also connected to Chapter 6 in that similar seismic waveform modeling was done to model the 2004 Sumatra Earthquake. Finally, as will be discussed more at the end of Chapter 3, this work served as my personal tie between the fields of seismology and glaciology.

Chapter 3

Possible Mechanisms for Glacial Earthquakes

3.1 Abstract

The large glacial earthquakes reported on by *Ekström et al.* [2003], *Ekström et al.* [2006] and *Tsai and Ekström* [2007] have previously been evaluated in terms of their seismic characteristics [*Tsai and Ekström*, 2007]. In this paper we attempt to take constraints such as known glacial ice properties, outlet glacier size, calving style, and meltwater variability to construct a self consistent physical model of the glacial earthquake process. Since many glaciological parameters are poorly constrained, we parameterize a number of important processes and estimate a wide range of possible values for some properties. The range of model outputs is thus fairly large, but it is still difficult to match observational constraints under most conditions. We find that only a small class of models is able to satisfy the major observational constraints.

These models are characterized by (1) lost basal resistance coupled to viscoelastic deformation with extensive internal crevassing or with low effective elastic modulus and possibly low effective viscosity; or (2) non-equilibrium calving such as having large icebergs capsize into the glacier front. Although observational constraints cannot definitively rule out any of the proposed classes of mechanisms, the calving model has much stronger support. Fortunately, the various models make different predictions regarding observables that can potentially be measured in the near future.

3.2 Introduction

In 2003, *Ekström et al.* [2003] discovered a new class of earthquakes which they named glacial earthquakes due to their spatial association with glaciated regions. Since this initial discovery, *Ekström et al.* [2006] have reported on the strong seasonality and recent drastic increase in the number of Greenland glacial earthquakes, and *Tsai and Ekström* [2007] have performed a detailed seismic analysis of all 184 Greenland events detected between 1993 and 2005 (which comprised roughly 95% of all known glacial earthquakes). Since events had radiation patterns inconsistent with standard double-couple faulting, seismic waveforms were modeled with the centroid single force (CSF) model of *Kawakatsu* [1989]. The CSF model accurately describes a mass sliding event (mass $\times$ distance) with an acceleration and then deceleration phase (beginning and ending at rest), and yielded satisfactory fits to the data [*Tsai and Ekström*, 2007]. (The model can alternatively be thought of as a pair of forces exerted on the Earth at the same location but offset in time and in opposite directions, e.g. as in *Dahlen* [1993].) This work resulted in a characterization of many

seismic traits of Greenland events. Among the most important and robust conclusions of *Ekström et al.* [2003], *Ekström et al.* [2006] and *Tsai and Ekström* [2007] are the following: (1) Glacial earthquakes primarily occur near the calving fronts of fast-flowing (> 1 km per year) outlet glaciers. (2) They have mechanisms consistent with a near-surface horizontal temporally-symmetric CSF approximately in the direction of local glacial flow. (3) All events detected have surface-wave magnitude in the range $4.6 < M_{SW} < 5.1$ (M_{SW} is similar to the conventional M_S but is measured at 35-150 s [*Ekström*, 2006]). That corresponds to a CSF amplitude of $0.1 \cdot 10^{14}$ kg m $< A < 2.0 \cdot 10^{14}$ kg m, with lower bounds corresponding with the detection limit. (4) They have significant energy in periods between 20 and 100 seconds (much longer durations than standard earthquakes of similar magnitude). The longer durations possibly correspond with larger amplitude events. (5) The presence of events is strongly seasonal and correlates with local conditions such as high surface temperature and the absence of thick sea ice melange at the calving front. (6) Events occurring within the same outlet glacier do not all occur at the same location. The spread in locations is a factor of 2 larger than uncertainties, and correlates with ice front variations. (7) Glacial earthquakes seem to have a characteristic amplitude dependent on which outlet glacier they are associated with. To (1) to (7) we add the following: (8) *Joughin et al.* [2008b] strongly suggests that glacial earthquakes are closely associated with calving events, with glacial earthquakes occurring at times of large retreats of the calving front.

Before the discovery of glacial earthquakes, a wide range of glacial seismic phenomena were known to exist (e.g. *Neave and Savage* [1970], *VanWormer and Berg* [1973],

Weaver and Malone [1979], *Wolf and Davies* [1986], *Qamar* [1988], *Anandakrishnan and Bentley* [1993], *Anandakrishnan and Alley* [1997], *Deichmann et al.* [2000], *Stuart et al.* [2005], *Smith* [2006], and *O'Neel et al.* [2007]), some of which have well-accepted mechanisms responsible for causing the seismicity (e.g. calving of icebergs, opening of crevasses, and basal slip are discussed in *Qamar* [1988], *Deichmann et al.* [2000], *Stuart et al.* [2005], and *O'Neel et al.* [2007]). It is tempting to try to explain glacial earthquakes with a model known to describe one of these phenomena. But a number of difficulties arise in trying to quantitatively match glacial earthquake observations with the results of these models. For example, models that involve brittle crack propagation in ice (e.g. *Neave and Savage* [1970]) fail to correctly match the observed focal mechanism orientations, predict excitation at a shorter timescale than observed, and yield seismic energies much smaller than observed. Models involving basal slip of a segment of glacier (e.g. *Anandakrishnan and Alley* [1997] and *Bindschadler et al.* [2003]) fare better but still cannot achieve the large enough amplitudes or the 20-to-100 s timescales (with elastic models predicting much shorter timescales and viscous models predicting much longer timescales) without substantial modification of the model. Nevertheless some aspects of these models, such as the general block-sliding nature of the basal slip model, will be adopted and will factor heavily in our model. Current models involving calving (e.g. *O'Neel et al.* [2007]) similarly do not predict the correct timescales, mechanism orientations or energies, but further suggest that large calving events may be important to the generation of glacial earthquakes.

The goal here is to construct a glaciologically consistent physical model of glacial earthquakes that satisfies the eight observational constraints listed above. We begin

by incorporating, in general terms, the physics that we judge to be potentially relevant to the generation of glacial earthquakes. We formulate a general model framework in which ground motion (seismic signals) of various types can occur. We then utilize parameters constrained by observations such as (1), (5) and (8) and determine what range of values other, not-as-well-constrained parameters of the model must have in order to satisfy or attempt to satisfy the other seismic observations (2), (3), (4), (6) and (7). Since constraints (6), (7) and parts of (5) do not have an obvious way in which to choose model parameters to satisfy them, we focus our efforts in this paper in satisfying (2), (3) and (4), and only afterwards examine the ways in which the various classes of models are consistent with or would predict behavior described by (5), (6), and (7).

3.3 Model Inputs/Model Characterization

There are a number of hypotheses regarding the specific physics governing glacial earthquakes [*Tsai and Rice*, 2006] including processes as diverse as shear failure of marginal ice, subglacial water pressures increasing to lift-off, transition of till to a rate-weakening regime, and stress changes induced by calving. Since, a priori, it is not possible to constrain which of these many possibilities can realistically produce the seismic observations, we take the conservative route of at first attempting to include, in general terms, all possibly relevant physics in our model of short-timescale terminus dynamics. Thus, we include ice deformation modulated by crevassing and fracturing, iceberg calving processes, and basal processes modulated by hydraulic inputs (schematically shown in Figure 3.1).

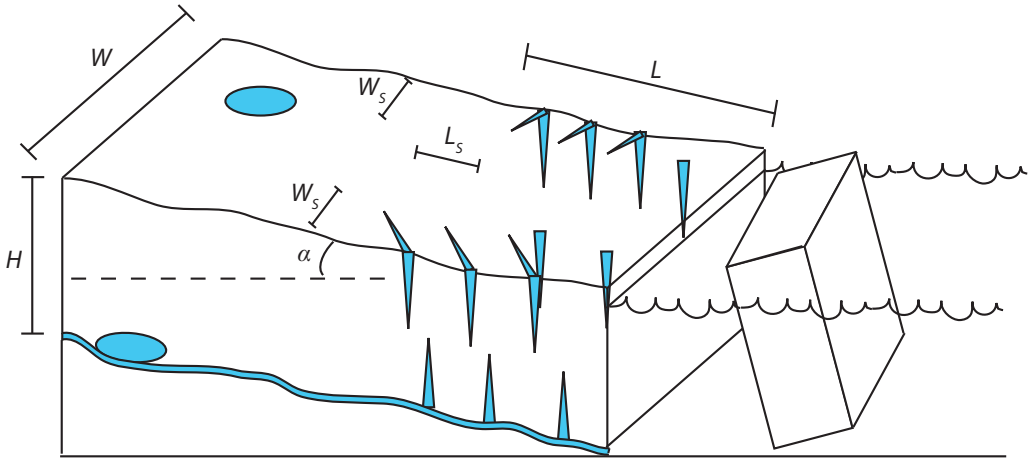

Figure 3.1: Schematic of processes modeled. We model ice deformation modulated by crevassing and fracture, basal processes modulated by hydraulic inputs, and calving of large icebergs. The mass affected has length L, width W, and height H, with ice deformation mostly confined to marginal shear zones and longitudinal deformation zone of size W_S and L_S respectively.

The cost of including such a diverse set of physical processes is that in order to make progress we must, out of ignorance, neglect many of the details of the individual processes and focus instead on how the main effects of each contribute and interact to create a seismic signal consistent with those of glacial earthquakes. Moreover, a number of the processes listed are very poorly constrained and therefore must be parameterized instead of being modeled from first principles. A full description of the components of our model is in Sections 3.3.1-3.3.5. We allow for viscoelastic deformation of ice (Section 3.3.1) that may be weakened by fracturing or other processes (Section 3.3.2), basal shear parameterized by a friction-like parameter that is a priori unconstrained (Section 3.3.3), a variety of calving styles (Section 3.3.4), and combine these into a self-consistent model framework applicable to the generation of a long-period seismic signal (Section 3.3.5).

3.3.1 Ice Deformation

We recognize that deformation of ice within the outlet glacier is likely to be important to understanding glacial earthquakes. In glaciology it is common to treat ice deformation with a non-linear viscous rheology described by Glen's law [*Glen*, 1955; *Paterson*, 2002]. However, for stress changes on the short timescale of interest to us, elastic deformation is also important [*Jellinek and Brill*, 1956; *Budd and Jacka*, 1989]. For clean, undamaged laboratory ice at timescales less than 100 seconds, only the instantaneous elastic modulus is important, at least at stresses that do not cause rapid fracture. However, since outlet glacier ice may have bulk viscoelastic-plastic and mechanical properties that differ substantially from those of laboratory specimens, we assume the more general Burgers body rheology that includes steady-state and transient creep, as in *Budd and Jacka* [1989] and *Kalifa et al.* [1992], i.e. a Kelvin element in series with a nonlinear Maxwell element as shown schematically in Figure 3.2. (The Kelvin response could, for example, represent effects of grain boundary sliding, the Maxwell response that of dislocation-dominated shear.)

The stress-strain relations are such that the volumetric part of the total strain tensor response ϵ_{ij} is purely elastic (to the neglect of internal cavitation), whereas all time-dependent responses show up as contributions to the deviatoric part $e_{ij} = \epsilon_{ij} - \delta_{ij}(\epsilon_{xx}+\epsilon_{yy}+\epsilon_{zz})/3$ of the strain tensor. For the Burgers solid, we use $e_{ij} = e_{ij}^{(I)} + e_{ij}^{(II)}$ to represent the respective Kelvin (I) and Maxwell (II) contributions. Thus, neglecting material anisotropy,

$$\epsilon_{ij} = \delta_{ij}(\sigma_{xx} + \sigma_{yy} + \sigma_{zz})/(9K) + e_{ij}^{(I)} + e_{ij}^{(II)} \tag{3.1}$$

where $i, j = x, y, z$, σ_{ij} is the stress tensor, and bulk modulus $K = 2(1+\nu)\mu_2/[3(1-$

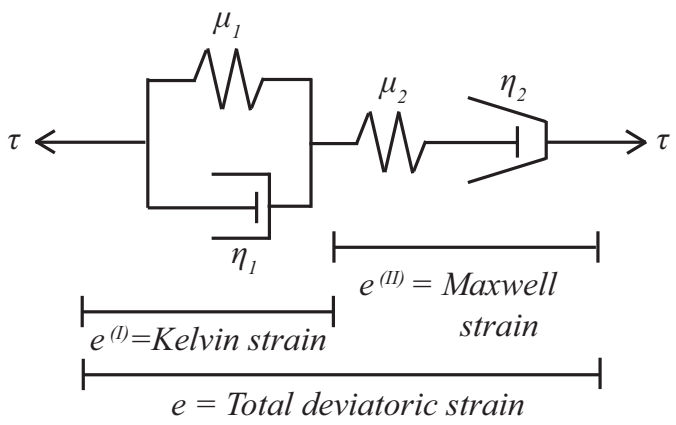

Figure 3.2: Schematic of the nonlinear Burgers body viscoelastic model used for deviatoric stress. The Maxwell viscosity η_2 is taken as nonlinear in accordance with Glen's law, $e^{(I)}$ is the strain on the Kelvin element.

$2\nu)]$ where μ_2 is the shear modulus and ν the corresponding Poisson ratio for the instantaneous elastic response. Introducing the deviatoric stress tensor $\tau_{ij} = \sigma_{ij} - \delta_{ij}(\sigma_{xx} + \sigma_{yy} + \sigma_{zz})/3$, the deviatoric strain contributions satisfy

$$\tau_{ij} = 2\mu_1 e_{ij}^{(I)} + 2\eta_1 \dot{e}_{ij}^{(I)}, \tag{3.2}$$

$$2\dot{e}_{ij}^{(II)} = \frac{\dot{\tau}_{ij}}{\mu_2} + \frac{\tau_{ij}}{\eta_2}. \tag{3.3}$$

Here μ_1 is the shear modulus for the Kelvin response, such that the overall elastic shear modulus when the Kelvin response is fully relaxed is $(\mu_1^{-1}+\mu_2^{-1})^{-1}$ (the corresponding fully relaxed Poisson ratio differs from ν above; it is the value which keeps the bulk modulus K the same in the instantaneous and relaxed states). Also, η_1 and η_2 are the respective Kelvin linear viscosity and Maxwell nonlinear viscosity; we represent that nonlinearity as $\eta_2 = \eta_2(\tau)$ where $\tau = \sqrt{(1/2)\tau_{ij}\tau_{ij}}$ is the Huber-Mises equivalent shear stress, also known in the glaciological literature as the effective shear stress.

Thus in uniaxial tensile or compressive stressing σ_{xx}, like for typical lab experi-

ments, $\tau_{xx} = 2\sigma_{xx}/3$ and $\tau_{yy} = \tau_{zz} = -\sigma_{xx}/3$, so that $\tau = |\sigma_{xx}|/\sqrt{3}$ and the longitudinal and transverse strain rates are

$$\dot{\epsilon}_{xx} = \dot{\sigma}_{xx}/[2(1+\nu)\mu_2] + \sigma_{xx}/[3\eta_2(|\sigma_{xx}|/\sqrt{3})] + \dot{e}^{(I)}_{xx} \tag{3.4}$$

with

$$\sigma_{xx} = 3\mu_1 e^{(I)}_{xx} + 3\eta_1 \dot{e}^{(I)}_{xx} \tag{3.5}$$

and

$$\dot{\epsilon}_{yy} = \dot{\epsilon}_{zz} = -\nu\dot{\sigma}_{xx}/[2(1+\nu)\mu_2] - \sigma_{xx}/[6\eta_2(|\sigma_{xx}|/\sqrt{3})] - \dot{e}^{(I)}_{xx}/2 \tag{3.6}$$

where $2(1+\nu)\mu_2$ is recognized as the instantaneous Young's modulus. In pure shear stressing $\sigma_{xy} = \sigma_{yx}$, the shear strain rate is thus

$$\dot{\epsilon}_{xy} = \dot{\sigma}_{xy}/(2\mu_2) + \sigma_{xy}/[2\eta_2(|\sigma_{xy}|)] + \dot{e}^{(I)}_{xy} \tag{3.7}$$

with

$$\sigma_{xy} = 2\mu_1 e^{(I)}_{xy} + 2\eta_1 \dot{e}^{(I)}_{xy}. \tag{3.8}$$

We choose nominal values for the viscoelastic parameters to resemble laboratory measurements at temperate ice ($> -10°$C) conditions. We choose nominal values for μ_1, μ_2 and η_1 from experiments of *Jellinek and Brill* [1956] done in tension at $-5°$C (the instantaneous elastic response has little temperature dependence [*Budd and Jacka*, 1989]). Modifying their values for use in shear instead of tensile deformation by assuming an instantaneous elastic Poisson's ratio $\nu = 0.3$ [*Vaughan*, 1995], we use $\mu_1 = \mu_2 = 2 \cdot 10^9$ Pa and $\eta_1 = 1 \cdot 10^{12}$ Pa s. In accordance with Glen's law, we take $\eta_2(\tau) = 2^{-1} A_{Gl}^{-1} \tau^{1-n}$ where $n \approx 3$ [*Glen*, 1955]. Glen's rate parameter A_{Gl} is highly temperature dependent, but for nominal conditions and $n = 3$ we choose a constant,

high value of $A_{Gl} = 68 \cdot 10^{-25}$ $s^{-1}(Pa)^{-3}$ suggested as appropriate for temperate ice [*Paterson*, 2002] although this value is perhaps too high [*Truffer et al.*, 2001].

The general form of the rheology (e.g. linear elasticity and power-law viscous) dictates that the highest stresses, deformations and deformation rates are concentrated at the side margins and near the base (and at the edges of finite slipping patches of glacier) (e.g. *Nye* [1965]). This fact is also confirmed by observations of large strain-rate gradients across prominent outlet glaciers [*Joughin et al.*, 2004; *Howat et al.*, 2005]. In order to simplify the analysis greatly, we take the approximation of no deformation in the heart of the outlet glacier (block model) of width, height and length given by W, H and L respectively, and with deformation concentrated into marginal shear zones, a basal shear zone and longitudinal deformation zones, of extent W_S, H_S and L_S respectively (see Figure 3.1; note, later we shall choose $L_S = L/2$ to conservatively approximate a roughly constant longitudinal gradient in strain rate). Under a gravity-driven linear rheology, it is straightforward to calculate that over 50% of both viscous and elastic deformation is within 30% of the margins. Nonlinear effects such as Glen-like viscosity or deformation-induced fracture or shear heating enhance the degree to which the block model is a good approximation by further enhancing deformation near the edges. Using this approach, we necessarily average material properties over the appropriate length scale and only expect to predict observations quantitatively to within the degree to which the system is block-like.

3.3.2 Crevassing, Fracture and Mechanical Weakening of Ice

Fracturing and water content of ice both strongly affect the bulk viscoelastic properties and thus strongly modulate glacier flow. Some fracturing properties of ice are relatively well understood (e.g. *van der Veen* [1998], *Rist et al.* [1999], and *Schulson* [2001]). It is, for example, well known that surface crevasses in the outlet glaciers of interest can only extend to a depth of about 30 m unless the crevasses are filled with water, in which case crevasses can extend to the glacier base (e.g. *van der Veen* [1998], *Das et al.* [2008]). In contrast, the degree to which outlet glacier termini and margins are fractured englacially and water-pervaded is only qualitatively known (e.g. *Kamb et al.* [1994], *Venteris* [1999], *Fountain et al.* [2005], *Harper et al.* [2005]). However, the terminus regions of these glaciers exhibit the highest tensile strain rates known to exist outside surges, and observations indicate that the ice is mechanically affected by internal damage.

Fortunately, "steady state" velocity profiles, i.e. profiles estimated over timescales much longer than glacial earthquakes (e.g. *Howat et al.* [2005]), can give an estimate of the degree of weakening, whether this weakening is due to fracturing or other mechanisms (e.g. shear heating, fabric reorientation or increased water content). We find that performing a fit to transverse velocity profiles, $u(r)$, near the calving front with the approximation of *Nye* [1965] for a Glen's law rheology, $u(r) = u_0[1-(r/a)^{n+1}]$ for $-a < r < a$ where $2a$ = glacier width, yields a poor fit regardless of choice of u_0 (rms misfit of $\sigma = 1380$ m/yr); but allowing for slip along the margins (constant velocity offset) in addition to the Glen's law rheology yields a better fit ($\sigma = 910$ m/yr), with as much as 50% of the surface velocity being accommodated through slip

at the margins. Farther from the front, however, a simple Glen's law rheology yields better fits (σ = 460 m/yr), and adding marginal slip does not improve the fit. This simple calculation is in agreement with observations of near-marginal slip at other outlet glaciers (e.g. *Kamb et al.* [1985]).

For the above reasons, we choose to spatially parameterize mechanical weakening by introducing a parameter $0 \leq s \leq 1$ that represents the fraction of the deforming regions over which the un-weakened rheology is applied. Low s represents highly fractured, mechanically weakened ice. The average height over which shear stressing occurs, H_{eff}, can then be defined as $H_{eff} = sH$. Similarly, $H_{crev} = (1 - s)H$ could be interpreted as the average height of crevasses or otherwise weakened ice (over which no shear stress is accommodated). Equivalently, s can be thought of simply as a scaling factor for viscoelastic parameters with e.g. $\mu_{2eff} = s\mu_2$ where μ_2 is the laboratory value and μ_{2eff} is the value appropriate for the region of the glacial system of interest, whether or not the physical reason for this scaling is due to crevassing. This scaling may, for example, be due to enhanced localized shear heating, high water content, or a softer fabric inherited from extensive straining [*Harrison et al.*, 1998]. As in other studies (e.g. *Vaughan* [1995]), there is a trade-off between s and μ_2 (and the other viscoelastic parameters). In our case this is because s enters the model multiplied by viscoelastic parameters (μ_1, μ_2, η_1, and η_2). Although it is likely that the margins are more crevassed relative to the rest of the glacier, and that the degree of crevassing also changes as one moves away from the calving front, in our simple rigid block model only the average value of s matters. So, for a length of glacier with s_1 over length L_1 and s_2 over length L_2, then $s = (s_1L_1 + s_2L_2)/(L_1 + L_2)$ (see

Figure 3.3).

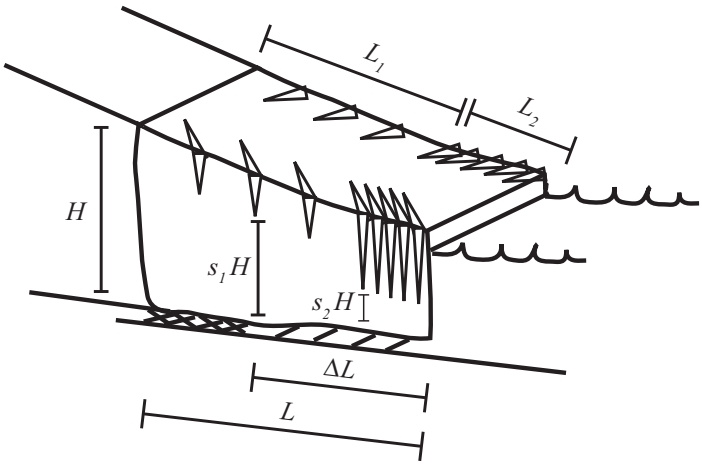

Figure 3.3: Schematic of crevassing and lost basal resistance. Extent of crevassing over length L_1 and L_2 is represented by s_1 and s_2 respectively. For this case, $s = (s_1 L_1 + s_2 L_2)/(L_1 + L_2)$. Basal resistance is lost over length ΔL.

Fracturing processes have two strong time dependencies that we address in our model of the relevant source mechanics for glacial earthquakes. The first effect is the seasonal variability of crevassing due to seasonal temperature variations. We expect more frequent and pervasive crevassing during summer months both due to the presence of liquid water, which aids in fracture propagation (e.g. *van der Veen* [1998], *Das et al.* [2008]), and decreased failure stress at higher temperatures (e.g. *Schulson* [2001]), which may be enhanced by existing crevasses and/or liquid water. The second effect is the increase in fractures caused by changes to the large-scale stress state in the terminus region potentially expected during a glacial earthquake event. Although both processes are easily understood qualitatively, and both imply more crevassing during times of glacial earthquakes, a quantitative physical description is not possible at this time. For this reason, we will discuss the possible implications of these

processes as they fit into the broader model framework but leave a detailed physical model of these processes for future work. These processes also provide additional grounds for using viscoelastic parameters reduced from nominal values.

3.3.3 Basal Processes

Modeling of surface velocity profiles (e.g. *Howat et al.* [2005]) with Glen's law suggests that, in the outlet glaciers of interest, a substantial fraction of their very high velocities are likely to be accommodated through both ice deformation and basal motion of some sort (e.g. *Truffer and Echelmeyer* [2003]) so an understanding of basal processes is required in a complete model of terminus dynamics. Unfortunately, it is currently not possible to resolve the detailed mechanics of basal motion. It is sometimes argued (e.g. *Truffer and Echelmeyer* [2003]) that it is unlikely for till to be responsible because till is presumed not to be able to withstand high shear stresses (often in excess of 100 kPa) inferred to exist at the base of these glaciers. However, that argument requires pore pressure conditions close to flotation whereas till with pore pressures less than lithostatic can sustain much higher shear stresses (e.g. *Tulaczyk et al.* [2000]). It is unclear exactly how high pore pressures are in the locations we attempt to model. It is known that these glaciers are nearly thin enough to be at flotation at their termini but, at the base of a 1 km-thick glacier, the pore pressure could be up to 98% of the ice pressure and potentially still sustain shear stresses of 100 kPa. It is also not clear exactly how high the shear stresses are very near the calving front. It has further been argued that most till would have been rapidly washed away by the active water system inferred to exist under these glaciers

[*Iken et al.*, 1993], but this argument relies on properties of the basal water system which have not been well constrained. Thus, we shall assume both basal sliding and till deformation as well as any deformations associated with either to be plausible contributors to basal motion.

Both basal sliding and till deformation have properties that can lead to a dramatic loss in shear strength over the tens of seconds during which glacial earthquakes occur [*Iken*, 1981; *Kamb*, 1991; *Schoof*, 2005]. (We will show that many model classes require such basal motion at the event timescale.) For example, the shear stress accommodated by both basal sliding and till deformation are proportional to some positive power of the effective pressure $p_{eff} = p_{ice} - p_w$ [*Paterson*, 2002] where p_{ice} = ice pressure and p_w = water pressure in a basal cavity system or within till, respectively. Thus, an increase of p_w to a large fraction of p_{ice} can cause dramatic weakening. This is essentially the argument of *Iken* [1981] for instability in sliding with a basal cavity system but the timescale must be set by hydraulic processes. The theory of *Kamb* [1991], on the other hand, yields an independent result for the timescale of instability (given by his Equation 32) though the model requires fairly extreme till properties as well as instantaneous adjustment of velocity perturbations to water pressure variations. In addition, further effects, such as rate-weakening till (e.g. *Kamb* [1991]), other transient rate-and-state effects [*Ruina*, 1983; *Tse and Rice*, 1986; *Dieterich*, 1994; *Lapusta et al.*, 2000; *Liu and Rice*, 2007], or fracture of basal ice resulting in lower basal roughness can result in unstable slip. As a result of these many possibilities, we simply assume that basal instability occurs over a length of glacier ΔL (see Figure 3.3) and determine a posteriori what form the basal instability

must satisfy in order to satisfy observational constraints; we do not attempt to distinguish between basal sliding and bed deformation. In other words, we parameterize shear strength as $\tau = f(t) \cdot p_{ice}$ and allow the form of $f(t)$ to be fit by observations. It should be noted here that in Section 3.4.1, $f(t)$ will be called upon to vary on timescales much faster than the fastest hydraulic changes currently documented in the literature (e.g. *Iken* [1981] and *Kamb and Engelhardt* [1987]).

3.3.4 Calving

We incorporate calving into our model as it can potentially produce a force resulting in a glacial earthquake. Direct observations (e.g. *Truffer et al.* [2006], *MacAyeal et al.* [2008]) show that massive calving events exist and may produce large forces, and our model attempts to include a quantitative description of such events. If one defines calving as losing basal resistance to a portion of the glacier with no marginal shear forces then it can be modeled as above, with $L_2 = L$ and $s_2 = 0$, so we do not consider this option here. If, on the other hand, one defines calving as the fracture process that results in a crack separating the calved portion from the rest of the glacier, then calving can occur with the to-be-calved portion in one of three configurations: (1) (partially) grounded with basal traction, (2) partially grounded without basal traction but not neutrally buoyant, or (3) ungrounded and buoyant in water. If calving occurs under "equilibrium" conditions (i.e. without acceleration of either the calved portion or the remainder of the glacier) then the calved portion remains in the one of three configurations it started in. In case (1), the shear resistance previously taken up by the pre-calved portion must now be accommodated on the glacier side,

thus transferring stress upstream (see Figure 3.4a). There is no net change in force on the glacier system as a whole but the transfer in stress is exactly equivalent to a complete loss of basal resistance over length L being accommodated by increasing basal and marginal stressing over a length of glacier L (see Figure 3.4a). We therefore treat this case in the glacier motion framework outlined in Sections 3.3.1-3.3.3.

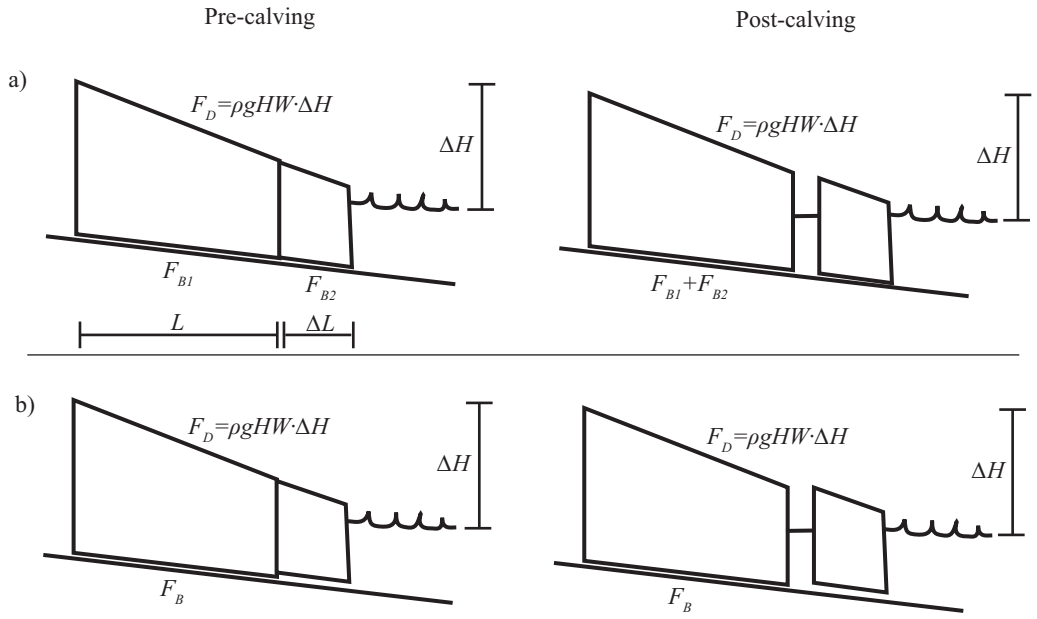

Figure 3.4: Schematic of the forces acting on the glacier pre-calving and post-calving, (a) with shear resistance on the pre-calved portion of glacier, and (b) without shear resistance. Case (a) can be modeled with lost basal resistance; case (b) has no net changes in forces.

In cases (2) and (3), there is no net change in force on the glacier since the pre-calving and post-calving water height is the same, yielding the same driving force, and the resistive shear forces are also identical (see Figure 3.4b). On the calved portion, the picture is different. For cases (1) and (2), there may be gravitational energy available allowing the calved portion to slide along its base, post-calving. However,

only if the bed slope is sufficiently positive (in the same direction as the surface slope) can the calved portion accelerate away from the calving front (see Figure 3.5). The timescale for this process is given approximately by

$$T \approx \pi \sqrt{\frac{\rho H_C \cos\beta}{\rho_w g \sin^2\beta}} \tag{3.9}$$

where we assume a rectangular cross section (Figure 3.5b) with side lengths H_C and L_C, with the latter in freely slipping contact with the bed, and where ρ = ice density, ρ_w = water density, g = gravitational acceleration, β = bed slope (see Appendix A). For $H_C > 500$ m and $\beta < 4°$, $T > 200$ s. Furthermore, observations [*Joughin et al.*, 2008b] imply that glacial earthquake events can occur on negative bed slopes. We therefore do not consider this possibility further. Finally, in case (3), there is no gravitational energy available so the iceberg has no net force on it.

Since we have now considered all possibilities of equilibrium calving and rejected them as ways of producing a calving force, F_C, capable of generating a glacial earthquake, we require iceberg acceleration during the calving process to determine F_C. This acceleration must be approximately horizontal (with a dip angle of less than about 30 degrees) to match seismic observations [*Tsai and Ekström*, 2007]. A simple way in which this acceleration can occur is if the calved iceberg of dimensions H_C, W_C, L_C, is taller than it is long ($H_C > L_C$); it can tip over and possibly provide a force to the glacier front as in the model of *MacAyeal et al.* [2003]. Calving events of this type have been observed at a number of outlet glaciers [*Truffer et al.*, 2006; *O'Neel et al.*, 2007] but analysis of related seismicity has so far focused on short-period seismicity [*O'Neel et al.*, 2007] possibly associated with small slip events. To model the long-period character of this iceberg tipping process, we follow *MacAyeal*

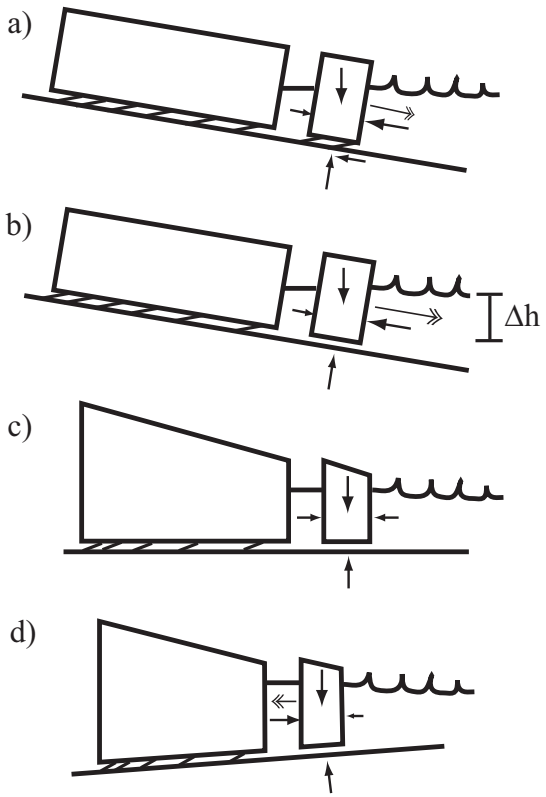

Figure 3.5: Schematic of the forces acting on the calved portion of glacier, (a) on a positive bed slope and with shear resistance, (b) on a positive bed slope without shear resistance, (c) on a horizontal bed, and (d) on a negative bed slope. Solid arrows denote forces, double-headed arrows denote possible acceleration. Acceleration away from the calving front is only possible in cases (a) and (b). In panel (b), Δh denotes the height of water to the middle of the base of the iceberg.

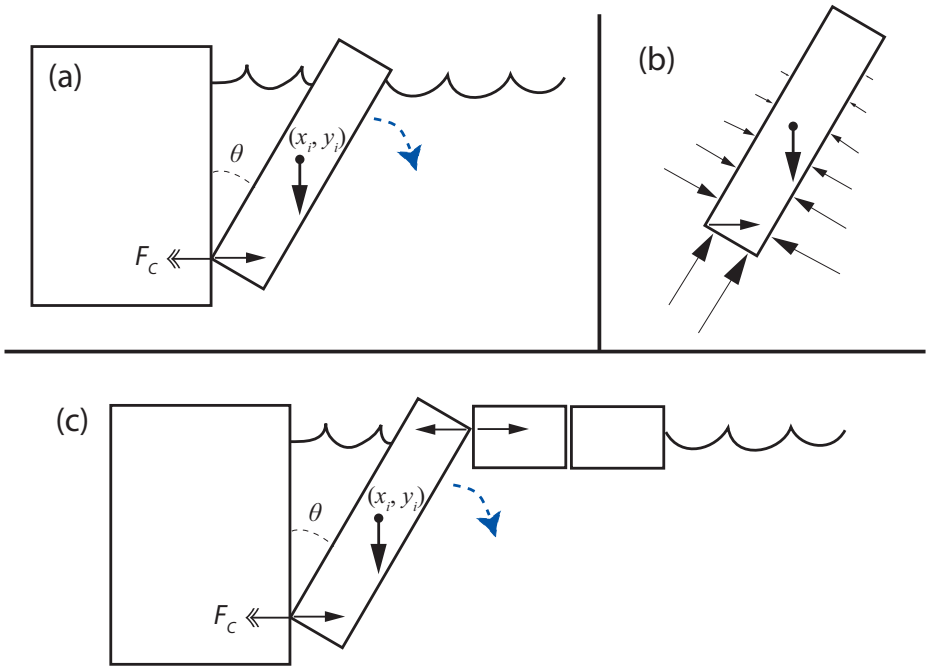

Figure 3.6: (a) Schematic of the tipping iceberg calving process modeled; the dotted arrow schematically denotes the rotation of the iceberg; the double arrow denotes the calving-contact force contributing to the seismic signal; the solid arrows denote forces. (b) Force vectors acting on the calved iceberg . (c) Schematic of the tipping iceberg with a mechanically competent ice melange.

et al. [2003] except we allow for horizontal, vertical and rotational acceleration (see Appendix A for details). The system of equations we satisfy is

$$F_x = M_{xa}\ddot{x}_i \tag{3.10}$$

$$F_y = M_{ya}\ddot{y}_i \tag{3.11}$$

$$\tau_{rot} = I_a\ddot{\theta} \tag{3.12}$$

where x_i and y_i are mass center coordinates of the iceberg, forces are from gravity, hydrostatic water pressure and the calving-contact force at the glacier front (see Figure 3.6), τ_{rot} is torque, $\ddot{\theta}$ is angular acceleration, M_{xa} and M_{ya} are mass, and I_a is moment of inertia where M_{xa}, M_{ya} and I_a include 'added mass' effects [*Lamb*, 1953; *Milne-Thomson*, 1955; *Brennen*, 1982]. In this first modeling effort, we approximate the flow as if it were remote from boundaries, and neglect surface wave dissipation and other edge effects due to the free surface and calving front. Preliminary modeling of these other effects shows that these effects cause significant but less than order of magnitude changes to the amplitude and timescale. However, since the iceberg is near the free surface we ignore added mass effects in the vertical direction such that $M_{ya} = M_C = \rho W_C H_C L_C$. Horizontally, we use the rectangular block added mass formula of *Brennen* [1982] with height equal to the vertical cross-sectional height so that

$$M_{xa} \approx M_{xa0} = \rho W_C H_C L_C + \frac{1.5\pi}{4}\rho_w W_C (H_C^2 \cos^2\theta + L_C^2 \sin^2\theta). \tag{3.13}$$

Rotationally, we calculate the added moment of inertia from the elliptical formula of *Brennen* [1982], setting the major and minor axis lengths to the height and length of

the rectangular block, respectively, so that

$$I_a \approx \frac{W_C}{24}[2\rho H_C L_C(H_C^2 + L_C^2) + \rho_w(H_C^2 - L_C^2)^2]. \tag{3.14}$$

In the model, the calving-contact force is frictionless and thus exactly horizontal (so that iceberg weight is only supported by buoyant forces), $F_C = -F_x$, and only achieves positive (directed upstream) values; corresponding opposite momentum is delivered to the iceberg and ocean, and is transmitted to the solid Earth at much longer timescales by sea water viscosity. By default, the CSF model includes both an acceleration and deceleration phase of equal time, so the associated CSF timescale must be twice as long as the acceleration phase. Note that x_i, y_i and θ are not independent since contact is assumed (see Figure 3.6). The assumption of point-like contact is an obvious idealization but in this first modeling effort we assume a contact area that is small relative to iceberg size. The assumption of frictionless contact is also an obvious idealization; including the vertical shear forces associated with friction at the contact point may explain the small deviations from horizontal (up to 30 degrees) observed in reality [*Tsai and Ekström*, 2007]. Finally, one can derive a simple analytic expression for the CSF amplitude A (mass times distance moved) and timescale T of this process by approximating the system as an inverted pendulum driven by its own buoyant weight over the horizontal distance traveled. The CSF amplitude is given by

$$A \approx 0.5 M_C(H_C - L_C) = 0.5\rho W_C L_C H_C(H_C - L_C). \tag{3.15}$$

Writing the pendulum equation as $(T/2\pi)^2\ddot{\theta} - \sin\theta = 0$ ($\theta = 0$ being an unstable equilibrium) then the characteristic timescale is given by

$$T \approx 2\pi\sqrt{\frac{\rho H_C}{(\rho_w - \rho)g}} \tag{3.16}$$

(although the actual time is dependent on initial conditions).

The calving model discussed above is just one possible way in which iceberg acceleration can occur. There are potentially many other scenarios including, for example, one in which the iceberg impacts the fjord bed [Amundson et al., submitted, 2008]; but we shall discuss just one variation on the above theme that involves the melange of icebergs that often floats in front of the glacier. Although this iceberg melange is typically composed of many individual bergs, it has been observed to act somewhat mechanically competent (e.g. *Truffer et al.* [2006]), with forces capable of being transmitted across km of icebergs with little time delay. If a calving event, such as the tipping event previously described, pushes into this melange, it can potentially resist motion much more than the added mass effects of just the water. We therefore allow for this melange added mass (which affects only the horizontal acceleration if the melange is confined to move horizontally) by including a second contact force $F_{C2} = M_M(2\ddot{x}_i$. Here, $2x_i$ is the distance between contact points and M_M is the effective mass from the iceberg melange (see Figure 3.6c), which is used as a parameter in subsequent simulations. This is equivalent to modifying M_{xa} in Equation (3.10) to be

$$M_{xa} \approx M_{xa0} + 2M_M, \tag{3.17}$$

where M_{xa0} is the original effective mass in the x-direction as in Equation (3.13). In contrast to the simple tipping calving model which yields identical forces whether the iceberg tips bottom out or top out, the model with an iceberg melange only has a simple interpretation when the iceberg tips top out (see Figure 3.6c). The interpretation is not obvious when the iceberg tips bottom out but net melange motion

must eventually be comparable since similar volume must still be vacated for the tipped iceberg.

3.3.5 A Unifying Model of Outlet Glacier Termini Forces

We have thus far described how ice deformation, fracture of ice, basal processes and calving dynamics can affect the generation of glacial earthquakes. We now incorporate these effects into a single model that results in a prediction of the seismic force history. In addition to the calving-contact force at the glacier tongue, the resistive forces arising from ice deformation and basal "friction", we also have a driving force from gravity given by $F_D \approx \rho g \alpha \cdot HWL$ (which we take as constant through a seismic event since the total height differential $\alpha \cdot L$ responsible for the driving force is minimally affected by the event). Combining these processes, we obtain an expression for the glacier block acceleration $\ddot{x}_b$:

$$M\ddot{x}_b = F_D - F_M - F_B - F_L - F_C, \tag{3.18}$$

where M = mass of glacier block, F_M = marginal shear force, F_B = basal shear force, F_L = longitudinal force (positive if tensile) at upstream end of block, and F_C = calving-contact force. The change in force on the (non-glacial) solid Earth, which generates a seismic response, is given by

$$F_S(t) = F_M(t) + F_B(t) + F_L(t) - F_M(0) - F_B(0) - F_L(0). \tag{3.19}$$

Since we treat F_D as constant, and initially $\ddot{x}_b$ and $F_C(0) = 0$, then equivalently

$$-F_S(t) = M\ddot{x}_b + F_C(t). \tag{3.20}$$

In general, then, the seismic force can be thought of as having contributions from acceleration of the glacier and from acceleration of the calved iceberg. Since F_C is expected to always be non-negative (directed upstream), the two contributions reinforce only when $\ddot{x}_b$ is positive (downstream acceleration). However, positive F_C only contributes to F_S when $\ddot{x}_b = 0$ and simply decreases $\ddot{x}_b$ when $\ddot{x}_b > 0$. Thus, in the following analysis we consider the two cases separately in 2 distinct model classes. That is, in class I models glacial earthquakes result from perturbations in glacier motion, and we set $F_C = 0$. In class II models glacial earthquakes result from iceberg calving, and we set $\ddot{x}_b = 0$.

In class I models, the forces F_M and F_L can be calculated in terms of the motion history $x_b(t)$ using the viscoelastic framework and simplified deformation of Section 3.3.1. That is, we use the rheology described in Equations (3.7) and (3.8) for $F_M(t)$ with $\epsilon_{xy} = x_b/(2W_S)$ and Equations (3.7) and (3.8) with all stresses multiplied by 3 to approximately account for tensile rather than shear stressing for $F_L(t)$ with $\epsilon_{xx} = x_b/L_S$. (For downslope horizontal stress change with no vertical change and plane-strain constraint in the transverse horizontal direction, the elastic stiffness is $2\mu_2/(1-\nu) \approx 3\mu_2$.) We additionally prescribe $F_B(t)$ (representing a drop in strength) and set $F_C = 0$. With expressions for these forces substituted, we solve Equation (3.18) for $x_b(t)$ with initial conditions $x_b(0) = x_{b0}$, $\dot{x}_b(0) = u_{ss}$ = steady state speed, and substitute into Equation (3.20) to solve for $F_S(t)$.

In class II models, we solve Equations (3.10), (3.11) and (3.12) for x_i and y_i with initial conditions $x_i(0) = x_{i0}$, $y_i(0) = y_{i0}$, $\dot{x}_i(0) = 0$, $\dot{y}_i(0) = 0$ corresponding to a rotationally unstable iceberg. Equation (3.10) then gives $F_x = -F_C$ which can be

substituted into Equation (3.20) to solve for $F_S(t)$. Once $F_S(t)$ is known, the CSF amplitude is easily obtained by double integration in time:

$$A = \int_0^T \dot{A}(t)dt = \int_0^T \int_0^t F_S(t')dt'dt \tag{3.21}$$

3.3.6 Physical Constraints

The size of outlet glaciers and the background surface velocity profiles are relatively well-constrained by observations (e.g. *Joughin et al.* [2004] and *Howat et al.* [2005]). Model parameter values are unique for individual glaciers, but typical values are on the order of $\alpha \leq 4°$ (usually $\alpha \leq 2°$), $W_S \leq 2$ km, $u_{ss} \approx 8$ km/yr, $H \approx 1$ km, $W \approx 4$ km, $\Delta L \leq L \leq 30$ km, and $A_{Gl} = 68 \cdot 10^{-25}$ s^{-1}(Pa)$^{-3}$ [*Bamber et al.*, 2001; *Paterson*, 2002; *Joughin et al.*, 2004; *Howat et al.*, 2005]. We shall use these representative values with $\alpha \approx 0.02 \approx 1°$, $W_S \approx 1$ km and $\Delta L = L$ for the rest of this paper. (Note that choosing $\Delta L < L$ would result in a lower-amplitude response.) In steady state, these parameter choices result in $F_L \approx 0$, $F_D \approx 180\,\text{kPa}\cdot LW$, $F_M \approx 270\,\text{kPa}\cdot LH_{eff}$ and $40\,\text{kPa} \cdot LW \leq F_B \leq 180\,\text{kPa} \cdot LW$. This estimate for F_B leads to an estimate of the initial dimensionless basal shear strength $f(0) = f0$ as $0.005 \leq f_0 \leq 0.02$. However, the estimates for F_B and f_0 are both quite sensitive to the choice of W_S, which is not well constrained.

3.4 A Unifying Model of Outlet Glacier Termini Forces

If we attempt to model a glacial earthquake without the inclusion of calving, relying on only block-like glacier motion (like in Figure 3.3), and assume nominal material property values, then the correct amplitude and timescale cannot be achieved. That is, choosing $\mu_1 = \mu_2 = 2 \cdot 10^9$ Pa, $\eta_1 = 1 \cdot 10^{12}$ Pa s, $n = 3$, $A_{Gl} = 68 \cdot 10^{-25}$ s^{-1}(Pa)$^{-3}$, $L = \Delta L = 5$ km, $L_S = L/2$, $s = H_{eff}/H = 1$, $F_C(t) = 0$ and with an instantaneous drop of $f(t)$ from f_0 to zero then, at timescales less than 10^3 s, only the elastic term (μ_2) is important and we achieve CSF amplitudes of $A = 1.1 \cdot 10^{12}$ kg m over a timescale of $T = 2.5$ s. An analytic approximation for this elastic response can also be obtained from a simple elastic force balance (see Appendix A) which yields:

$$A \approx \frac{\rho^2 g H W^2 W_S \cdot \Delta L}{s\mu_2[1 + 3WW_S/(2LL_S)]} \cdot \left[\alpha - \frac{2s}{\rho g W}\left(\frac{u_{ss}}{2W_S A_{Gl}}\right)^{1/3}\right] \tag{3.22}$$

and

$$T \approx \pi\sqrt{\frac{2\rho W W_S L L_S}{s\mu_2(3WW_S + 2LL_S)}}. \tag{3.23}$$

The amplitude is 10 to 200 times smaller than observations and the time scale is eight to 40 times too short. If we have successfully included all the physics pertinent to the generation of glacial earthquakes, then the only way in which observations can be matched is to modify at least one of the model parameters from its nominal value. We take ρ, g, and W to be well-constrained by observations, leaving α, H, L, ΔL, μ_1, μ_2, η_1, A_{Gl}, W_S, H_S, L_S, s, $f(t)$, and $F_C(t)$ as at least partially adjustable parameters.

3.4.1 Class I Models - Seismogenesis by Glacier Block Acceleration

In this class of models, we keep $F_C(t) = 0$ (seismogenesis in the absence of calving) for reasons discussed in Section 3.3.5. We also choose to include longitudinal deformation only on the upstream side of the sliding glacier block (and terminating in open waters on the other) since it requires less change from nominal values and is strongly suggested by observation (8). In order to achieve CSF amplitudes of $0.4 \cdot 10^{14}$ kg m (median value for glacial earthquakes) we require a combination of decreasing μ_1, μ_2, η_1, and s or increasing ΔL, L_S, W_S, A_{Gl} and α. Setting $\mu_2 = 5 \cdot 10^7$ Pa (vs. lab value of $2 \cdot 10^9$ Pa) or $s = 0.2$ can individually account for the observed CSF amplitudes whereas changes in μ_1, η_1, ΔL, L_S, W_S, A_{Gl} or α alone cannot. Large decreases in μ_1 and η_1 (e.g. $\mu_1 = 2.5 \cdot 10^7$ Pa and $\eta_1 = 5 \cdot 10^8$ Pa s vs. lab values of $2 \cdot 10^9$ Pa and $1 \cdot 10^{12}$ Pa s, respectively) must be coupled in order to have a significant effect; increases in L_S and W_S also must be coupled but W_S is constrained to less than 2 km; increases in A_{Gl} only increase the proportion of resistance taken up by the bed initially in steady state and is also constrained to less than $200 \cdot 10^{-25}$ $\mathrm{s}^{-1}(\mathrm{Pa})^{-3}$; ΔL and α are constrained in Section 3.3.6. In order to achieve timescales of 50 s, we require choosing timescales of variation in $f(t)$ close to 50 s; choosing very low values of μ_2 with possibly low values of s ($\mu_2 = 5 \cdot 10^6$ Pa or $\mu_2 = 2 \cdot 10^7$ Pa and $s = 0.2$); or choosing 10 s$\leq \eta_1/\mu_1 \leq$20 s. While some of these choices are perhaps on the extreme side of plausible, all of the suggested changes in parameter values are made to variables with sufficiently uncertain field values to warrant at least an examination of the possibility of a value different from nominal of the extent chosen.

In principle, there are infinite combinations of choices that will result in an amplitude and timescale consistent with seismic observation. For example, one could choose (as values different than nominal) $\Delta L = 9$ km, $\mu_2 = 5 \cdot 10^8$ Pa, $W_S = 1.5$ km, $s = 0.5$ and $f(t)$ varying on a 50-s timescale to satisfy observations. However, certain parameter sets require fewer changes from nominal values, or contain pairs of changes that are physically paired (coupled). Thus, we focus our attention on three subclasses of models that satisfy the amplitude and timescale constraints. All three subclasses require changes in $f(t)$. In two of the three subclasses, we assume the form of $f(t)$ can be chosen arbitrarily to fit timescales set by a variety of glaciological processes (such as subglacial hydraulic flow) whose short time behavior are rather unconstrained. This philosophy is different than the one typically taken in earthquake modeling where the frictional time-dependence is an outcome of the analysis, on the basis of a specified constitutive law. Before turning to these three subclasses, we note that although the dependence of amplitude and timescale on the parameters is nonlinear, we can linearize the model and find the first order response away from the nominal values. This linear response provides guidance for our parameter choices, and is given in Table 3.1.

Model IA - Highly Fractured, Timescale set by Basal Strength $f(t)$

In this subclass of models, we choose nominal viscoelastic parameters. In order to achieve correct amplitudes we can, for example, set $\Delta L = L = 5.5$ km and $s = 0.2$. In order to achieve correct time scales (20-100 s), we must utilize the timescale controlling

Table 3.1: Linear response of amplitude and timescale to block acceleration parameters

Parameter	Amplitude Response	Timescale Response
α	$38 \cdot 10^{11}$ kg m/°	0
H	$11 \cdot 10^{11}$ kg m/km	0
ΔL	$2.9 \cdot 10^{11}$ kg m/km	0
μ_1	0	0
μ_2	$-29 \cdot 10^{11}$ kg m/$\Delta \log_{10}$Pa	-3.1 s/$\Delta \log_{10}$Pa
η_1	$-0.12 \cdot 10^{11}$ kg m/$\Delta \log_{10}$(Pa s)	0
A_{Gl}	$24 \cdot 10^{11}$ kg m/$\Delta \log_{10}(\mathrm{s}^{-1}\mathrm{Pa}^{-3})$	0
W_S	$18 \cdot 10^{11}$ kg m/km	3.4 s/km
H_S	0	0
L_S	$1.1 \cdot 10^{11}$ kg m/km	0.1 s/km
s	$-46 \cdot 10^{11}$ kg m/1	-1.6 s/1
$f(t)$	0	1s/1s

basal motion $f(t)$ so that for example

$$f(t) = \begin{cases} f_0 & t < 0,\, t > 2t_0 \\ f_0/2 \cdot [1 + \cos(\pi t/t_0)] & 0 < t < 2t_0 \end{cases} \tag{3.24}$$

where $t_0 \approx 50$ s. In this case, the time dependence of the glacial earthquake is completely governed by a process (loss of basal resistance) that (in our model) has a completely unconstrained time history, and we therefore set it to match timescale observations.

Model IB - Very Low Maxwell Shear Modulus μ_2, $f(t)$ Regains Strength

Choosing $\Delta L = 2.2$ km, $W_S = 500$ m and $\mu_2 = 1.6 \cdot 10^6$ Pa (and nominal other values) generates correct amplitudes and time scales but the spring is underdamped so in order to have only one oscillation, $f(t)$ must jump back to f_0 after 50 seconds, e.g.

$$f(t) = \begin{cases} f_0 & t < 0,\, t > 50 \text{ s} \\ 0 & 0 \text{ s} < t < 50 \text{ s} \end{cases} . \tag{3.25}$$

Many seismic waveforms are in fact consistent with a multiple oscillation signal, so there is a certain leeway in exactly how long $f(t)$ drops to zero. In this case, the ice would be allowed to slide back uphill, which seems peculiar but could not be precluded if there were sliding on a fully fluid layer. For example, using

$$f(t) = \begin{cases} f_0 & t < 0 \\ f_0 \cdot [1 - \exp(-t/150 \text{ s})] & t > 0 \end{cases} \tag{3.26}$$

would also satisfy observations. As in Model IA, the timescale is partially set by the timescale of a process that has an unconstrained timescale in our model. It is perhaps worth noting, though, that with rate-and-state dependent friction as in earthquake studies (e.g. *Ruina* [1983]), this general strengthening behavior may be expected when sliding velocity diminishes significantly.

Model IC - Low Kelvin Shear Modulus μ_1 and Low Associated Viscosity η_1

The final end member of parameter choices is to modify both η_1 and μ_1 to values substantially lower than nominal, i.e. $\mu_1 = 2.5 \cdot 10^7$ Pa and $\eta_1 = 5 \cdot 10^8$ Pa s and drop $f(t)$ to zero. Here, η_1/μ_1 is chosen to match the timescale desired and we no longer require $f(t)$ to accommodate this timing. Note that these drastic changes from nominal values are perhaps warranted if the ice is effectively weakened by fracture or other mechanisms.

3.4.2 Class II Model - Seismogenesis by Calving of Large Icebergs

Model IIA: Calving of Rotationally Unstable Icebergs

As an alternative to the class I set of models, where glacier acceleration is responsible for the seismic force, here the calving-contact force is directly responsible and assumed to couple directly to the solid Earth without acceleration of the glacier ($\ddot{x}_b = 0$). We use the calving model described in Section 3.3.4. Without modification, neutrally buoyant initial conditions and with iceberg dimensions $H_C = 500$ m, $W_C = 5$ km, $L_C = 265$ m, this model (IIA) produces approximately the correct amplitude and a slightly long timescale. These choices for H_C, W_C, L_C and were taken to best fit the amplitude and timescale constraints; for example, the rather exact value of L_C chosen is due to the sensitivity of both amplitude and timescale to both H_C and L_C as in accord with Equations (3.15) and (3.16). The model of iceberg tipping also matches observations of calving style [*Truffer et al.*, 2006] (J. Amundson, private communication, 2008) of some large calving events, which have been observed to tip both bottom out and top out. In Figure 3.7, amplitude and timescale results are shown for a range of different iceberg dimensions (100 m$\leq H_C \leq$1 km, $0.2H_C \leq L_C \leq 0.7H_C$, $W_C \leq 5$ km). The model has difficulty matching timescales especially for the larger events (see Figure 3.7) since maximum amplitude scales approximately as $A \propto T^6$ as expected from Equations (3.15) and (3.16) with $L \propto H$ (maintaining approximately constant aspect ratio). Unlike the too-short timescale problem for class I models, however, the too-long timescale problem cannot be solved

Table 3.2: Linear response of amplitude and timescale to tipping iceberg parameters

Parameter	Amplitude Response (kg m/km)	Timescale Response (s/km)
H_C	$18 \cdot 10^{13}$	34
W_C	$0.6 \cdot 10^{13}$	0
L_C	$3.8 \cdot 10^{13}$	-174

by calling upon a rate-limiting process working in parallel; but the timescale may be reduced if, for example, the iceberg loses contact with the glacier face earlier than expected from this simple calculation. As in class I models, the dependence of amplitude and timescale on the parameters is nonlinear but we can linearize and obtain the first order response away from the above chosen values. This linear response is given in Table 3.2.

Model IIB - Inclusion of Effective Mass from Ice Melange

As discussed in Section 3.3.4, there are potentially a number of variations on this calving model. Using, for example, the modification of Equation (3.17) instead of Equation (3.13), we find a parameter regime in which the timescale of the large amplitude calving-contact force is not set by the rotational timescale of Equation (3.16) but is instead set by the timescale of iceberg bobbing given approximately by

$$T \approx 2\pi\sqrt{\frac{H_C}{g}}. \tag{3.27}$$

In particular, when initial conditions are significantly different from neutrally buoyant, the calving-contact force still develops on the tipping timescale of Equation (3.16). However, the force is strongly modulated by the bobbing timescale of

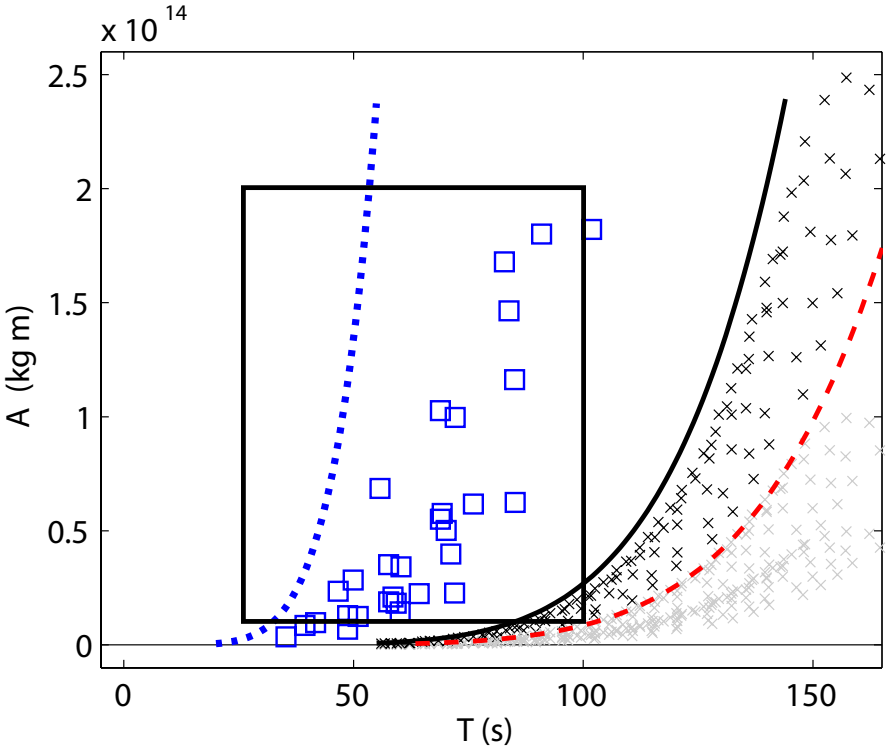

Figure 3.7: Timescale vs. amplitude for model class II (iceberg calving). Black crosses represent different model runs with $W_C = 5$ km and different values of H_C and L_C (see text) for model IIA (no melange). Gray crosses are versions of the same runs with W_C scaled down. The (blue) squares represent different model runs with $W_C = 2$ km and different values of H_C, L_C, and M_M for model IIB (with melange, $M_M = 1.5M_C$). The dashed (red) line is the scaling of Equations (3.15) and (3.16) for model IIA with $L_C = H_C/2$ and $W_C = 5$ km. The solid black line is the same scaling as the dashed (red) line, but scaled up to approximately denote the cutoff below which timescale/amplitude pairs are possible for model IIA. The dotted (blue) line is the scaling of Equations (3.15) and (3.27) for model IIB with $L_C = H_C/2$ and $W_C = 2$ km. The rectangular box denotes an estimate of the range of observed glacial earthquakes. Model IIB clearly fits observations better than model IIA.

Equation (3.27), sometimes resulting in a force with dominant period set by the bobbing timescale. With this much shorter timescale, a reasonable fit to observations can be produced with the less extreme parameter choice $H_C = 700$ m, $W_C = 2$ km, $L_C = 210$ m, and $M_M = 1.5M_C$. As shown in Figure 3.7 (squares), even with a smaller range of parameter choices than used in model IIA (200 m$\leq H_C \leq$1 km, $0.2H_C \leq L_C \leq 0.5H_C$, $W_C \leq 2$ km, $M_M \leq 4M_C$), amplitudes and timescales fit better in the observational range.

3.4.3 Model Comparison

The seismic forces predicted by Models IA, IB, IC, IIA and IIB, with parameter choices as described above, are shown in Figure 3.8 [cumulative CSF amplitude, $A(t)$] and Figure 3.9 [CSF rate, $\dot{A}(t)$]. Since the current seismic data can be equally well modeled with asymmetric forces of the same characteristic CSF amplitude and timescale (see Figure 3.10), this data cannot distinguish between the four model possibilities. In addition to satisfying observational constraints (2)-(4) (see Section 3.2), all models also correctly predict observations (6) and (7). Observation (6) is satisfied since the calving fronts of the glaciers in question have moved substantially over the past 15 years [*Joughin et al.*, 2004; *Howat et al.*, 2005; *Luckman et al.*, 2006] and all models are expected to generate their seismic signal near the calving front. Observation (7) is satisfied since the different glaciers have different model parameter values and therefore the models predict different characteristic amplitudes. The exact values, however, are not constrained well enough for us to decide whether the magnitude (or even the sign) of the variations are correctly modeled in detail. It is somewhat

more complicated to compare the models with the final observational constraint (5) since (5) (likely) involves a number of factors that are not completely understood. However, the fact that calving is well known to vary seasonally, while outlet glacier flow is more steady [*Echelmeyer and Harrison*, 1990; *Joughin et al.*, 2008a], and with respect to local glacier conditions strongly suggests that model class II can be expected to produce events in accord with (5) but perhaps not in a predictable sense. Furthermore, adding a simple time-dependent crevassing criterion (i.e. larger, more numerous crevasses during warm periods) to the class I models can produce variations in event size and number that also agrees with the observation that more events but slightly smaller ones occur during warmer times [*Tsai and Ekström*, 2007]. However, the details of such a criterion likely involve the understanding of the calving (and pre-calving) process in more depth than is currently known. Thus, we do not attempt to model this time-dependence in any (more) realistic manner. Model class I may also be able to satisfy (5) if basal processes vary seasonally, as some studies might suggest (e.g. *Kamb et al.* [1985], *Zwally et al.* [2002]) (although other studies suggest minimal seasonal variations of these processes [*Echelmeyer and Harrison*, 1990; *Truffer et al.*, 2006; *Joughin et al.*, 2008a]).

In summary, we have assembled a unified model of short-timescale outlet glacier dynamics that includes both changes in flow and calving in a physical way. Taking parameter values in the range of reasonable, with the important caveat that a number of important parameters have very loose constraints, we find only five classes (here called IA, IB, IC, IIA and IIB) of models (or a combination) that are able to satisfy the primary observations (1)-(4). After adding a simple parameterization of time-

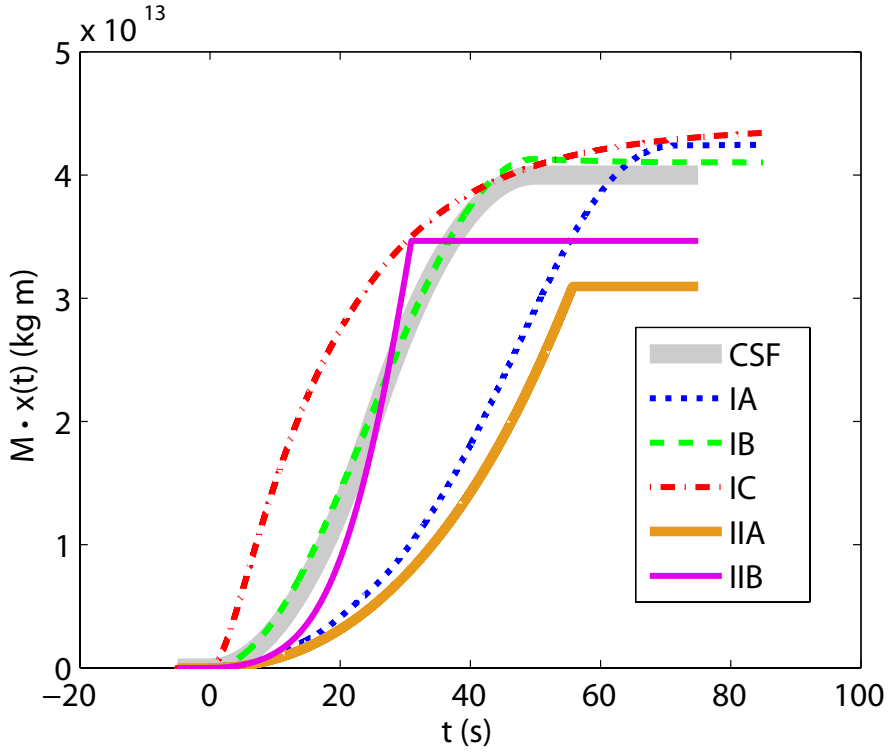

Figure 3.8: Cumulative CSF amplitude for: the seismic model fitting the observations (CSF), the three variations on the model class I (IA, IB, IC), and model class II (IIA, IIB). All five model results are consistent with the CSF model used to model seismic observations (see Figure 3.10).

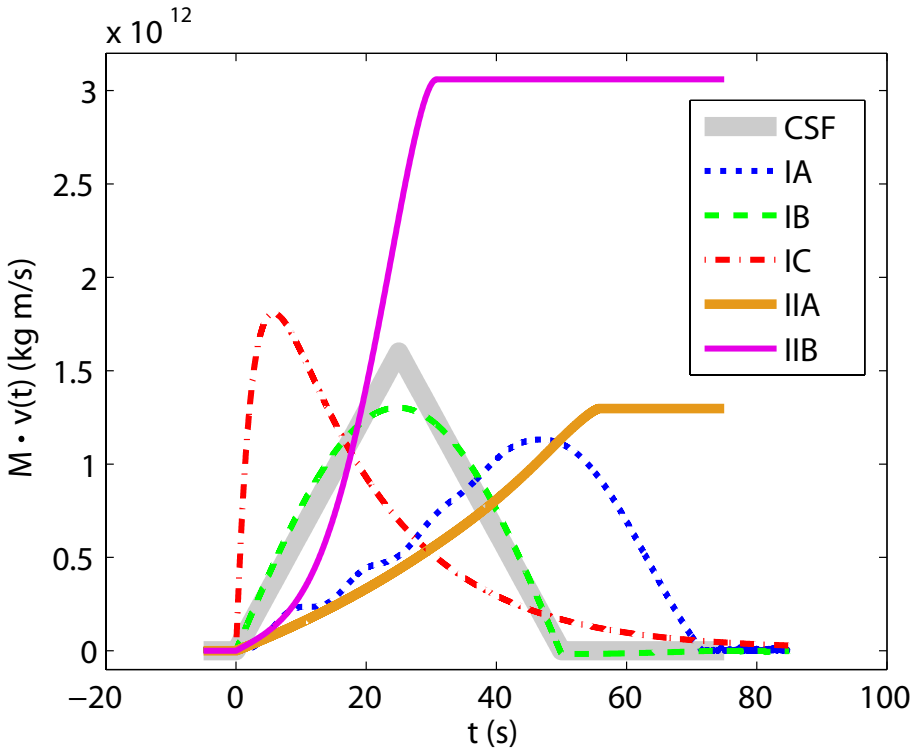

Figure 3.9: CSF rate for: the seismic model fitting the observations (CSF), the three variations on the model class I (IA, IB, IC), and model class II (IIA, IIB). Model class II does not have a deceleration phase so the CSF rate does not return to zero. However, the horizontal portion of the curve does not contribute to the CSF amplitude.

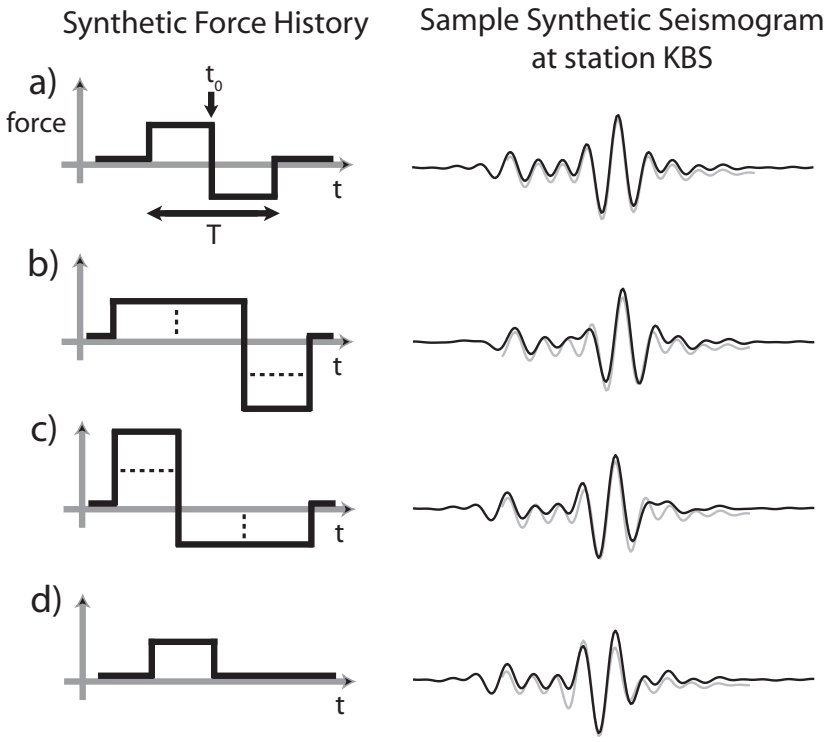

Figure 3.10: Synthetic force histories and associated synthetic seismograms for (a) the symmetric centroid single force (CSF) used to fit the seismic observations, (b) an asymmetric CSF with a longer but lower amplitude acceleration and shorter high amplitude deceleration, (c) an asymmetric CSF model with opposite character to (b), and (d) forcing with only an acceleration phase. Synthetic seismograms (black lines) are modeled and filtered as in *Tsai and Ekström* [2007]; gray lines are the best-fit CSF to the synthetic data, offset slightly vertically for clarity. Case (a) corresponds roughly with model IB, (b) with IA, (c) with IC, (d) with II. All four models fit observations with residual variance (normalized misfit) less than 0.10, compared with typical residual variance on real data of between 0.3 and 0.5. The amplitudes of (b) and (c) are approximately twice that of (a) and the amplitude of (d) is approximately half that of (a).

dependent crevassing (or of basal processes), we find that all five classes of models are able to successfully model all current observations (1)-(8). It is therefore difficult to decide which of the five possibilities is closer to reality. However, if viscoelastic parameters are thought to be within an order of magnitude of the nominal values, then models IA, IIA or IIB should be favored over models IB and IC. Although model IIA has trouble producing the entire range of observations, it does not have as many free parameters as model IA. Furthermore, a slight modification of model IIA resulting in model IIB has only one additional free parameter (the mass of the iceberg melange) but agrees well with the primary observations. For this reason, we favor model class II.

3.5 Predictions of the Models and Future Observational Constraints

So far, we have focused on constructing five classes of models that are consistent with observations but it is perhaps the consequences and predictions of the models that are more interesting and can (someday) potentially definitively distinguish the correct mechanism from the incorrect ones. The first obvious difference among models is that model class I requires motion of the glacier itself whereas model class II requires motion of a calved iceberg and glacier motion is secondary. Thus, observations of glacier and/or iceberg motion (of the magnitudes discussed in section 3) coincident with a glacial earthquake event (or lack of such motion) would be diagnostic of either model class I or II. Recent GPS observations from the Helheim and

Jakobshavn glaciers [*Nettles et al.*, 2007; *Fahnestock et al.*, 2007] suggest that little surface motion occurs during glacial earthquakes, thereby arguing against model class I. The other obvious difference between all five models is the exact form of the force history on the Earth (see Figure 3.8). However, these differences are not large enough to be distinguished from modeling of global seismic data and would therefore require modeling of high-quality, local seismic data.

Another set of differences that is more promising in terms of distinguishing between models is the difference in bulk viscoelastic parameters required by the different models. As discussed in Section 3.4.3, models IA and II do not require great differences from the nominal values whereas models IB and IC do (model IB with μ_2 1000 times smaller than nominal; model IC with μ_1 80 times smaller and η_1 2000 times smaller). In situ bulk viscoelastic parameters are difficult to measure but could possibly be done with a combination of tidal flexure [*Vaughan*, 1995] on outlet glaciers with a significant floating tongue, high precision GPS on highly variable-velocity outlet glaciers (e.g. *Bindschadler et al.* [2003]), and in situ measurements of temperature and the degree of internal small-scale fracturing. Fracturing and crevassing in general is predicted to be different among the models. As discussed in Section 3.3.2, s trades off directly with viscoelastic parameters so that bulk differences in (lower values of) viscoelastic parameters may be a result of differences in (lower values of) s. Thus, models requiring very low bulk viscoelastic parameters may be expected to have large amounts of crevassing and fracture. Additionally, it is possible that crevassing affects different viscoelastic parameters differently, so that crevassing could possibly be responsible for all differences in viscoelastic parameters. Furthermore, if time-

dependent crevassing is partially responsible for allowing (large) glacial earthquakes to occur then one might expect to observe many micro-earthquakes associated with the cracking (e.g. *Neave and Savage* [1970], *O'Neel et al.* [2007]), either seasonally or concurrently with the earthquake events. However, extensive crevassing of the sort considered would probably be meltwater-driven, and may not have a seismic signature if the process is too slow.

If model class II is correct, one would also expect related short-period seismicity related to cracking events that accompany calving as has been observed in analogous outlet glaciers in Alaska [*Qamar*, 1988; *O'Neel et al.*, 2007]. Furthermore, visual observations (like those of *Truffer et al.* [2006] and Amundson et al. [submitted, 2008]) of calving coincident with glacial earthquakes would be diagnostic of model class II. Model IIB would additionally predict glacial earthquakes only occurring when the glacier fjord has substantial iceberg mass, another potential visual or satellite observable. Model IIB could thus explain the lack of glacial earthquakes at Columbia Glacier, where large icebergs calve but there is little ice melange.

Finally, one should remember that the most incomplete part of model class I is the part regarding the basal processes leading to $f(t)$. The reason for this incompleteness is the vastly inadequate knowledge of the factors most important to determining $f(t)$. There are currently only suggestions [*Iken*, 1981; *Kamb*, 1991; *Schoof*, 2005] that the variations in $f(t)$ needed for these models to work can be produced by physical processes. Thus, basal observations would greatly improve our ability to form a predictive model class I. For example, determining whether till deformation or basal sliding contributes more to steady-state velocities would narrow the myriad of

possibilities for basal instabilities substantially, therefore making the modeling of $f(t)$ more tractable. Having a more physical model of $f(t)$ could in turn yield additional predictions for class I model behavior. While possibly irrelevant to the types of glacial earthquakes discussed here, the basal mechanisms of class I models are presumably important to other types of episodic glacial motion.

3.6 Conclusions and Implications

Using available observational constraints, we have constructed a general model framework to understand very short timescale (< 100 s) variability at the calving margin of fast-flowing outlet glaciers. Since key variables are unknown, we find it necessary to parameterize several processes within the model framework. Under this framework, we are able to construct five classes of models that result in instabilities that match known observations of glacial earthquakes. Although current observations cannot definitively rule out any of possibilities, model class II (iceberg calving) has fewer adjustable parameters, requires more realistic parameter choices, and is significantly more consistent with observations. The addition of iceberg melange (model IIB) further improves the consistency of model class II with observations (at the cost of an added free parameter). We therefore strongly favor model class II but reserve final judgment for the future, when observations should be able to conclusively distinguish amongst the model classes.

3.7 Acknowledgments

We thank I. Joughin, R. B. Alley, I. M. Howat, M. Nettles, and G. Ekström for helpful discussion and thank S. O'Neel, M. Truffer, and S. Tulaczyk for constructive reviews. This work was supported by a National Science Foundation Graduate Research Fellowship to VCT and, in its later stages, by NSF-OPP grant ANT-0739444.

3.8 Connection to Other Chapters

This chapter utilizes the seismological results of Chapter 2 as primary constraints on the mechanisms of glacial earthquakes discussed. The direct connections with other chapters are not as strong. However, my focus prior to embarking on this project on glacial earthquakes was primarily on traditional tectonic earthquakes, and the project initiated my personal interests in glaciology and ice physics. Thus, this project was directly responsible for my interest in the modeling done on drainage of water through cracks in glaciers (Chapter 4) and on melt features in lake ice (Chapter 5). Furthermore, the modeling done in this chapter and Chapter 4 fundamentally rely on the same foundation of solid and fluid mechanics, though applied in very different ways.

Chapter 4

A Model for Turbulent Hydraulic Fracture & Application to Glaciers

4.1 Abstract

The problem of hydraulic fracture has been studied extensively, with focus ranging from enhanced hydrocarbon flow to boreholes, to water-driven glacial cracking, to magma eruption through Earth's crust. Although some of this work has addressed fast-flowing fluids in the fracture, the work applied to glaciers has, so far, focused either on static or relatively long timescale conditions. However, glaciological observations (such as we review) suggest that the fluid-induced fracture process may occur quickly, possibly driven by turbulently flowing water during crack growth. Here, we take the approximation of a fully turbulent flow into an elastic ice medium with small fracture toughness to derive an approximate expression for the crack-tip speed. We accomplish this by first showing that a Manning-Strickler channel model for wall

resistance to turbulent flow leads to a mathematical structure similar to that for resistance to laminar flow of a power-law viscous fluid. We then adapt the asymptotic crack solution for that latter case by *Desroches et al.* [1994], and calculate a steady-state plane-strain crack-tip speed, displacement profile and pressure profile. We also compute a turbulent solution for a plane-strain self-similar crack by similarly adapting the power-law self-similar solution of *Adachi and Detournay* [2002]. To apply our model, we use parameter values thought appropriate for a basal crack driven by the rapid drainage of a surface meltwater lake near the margin of the Greenland Ice Sheet [*Das et al.*, 2008]. Thus, we first estimate a maximum excess crack-inlet pressure of 0.9 MPa, corresponding to neglect of any hydraulic head loss in flow from the glacier surface to crack entry at the bed, a horizontal basal crack length of 1 km, and a wall roughness scale for flow resistance of 10 cm, and hence estimate a maximum crack-tip speed of 2 m/s. Accounting for more realistic pressure head loss and 3D geometry reduces that speed to 1 m/s. Making various linear elastic fracture mechanics approximations perhaps relevant to this setting, we additionally model both vertical and horizontal surface displacements and find order-of-magnitude agreement with the meter-scale ice sheet displacements observed through GPS by *Das et al.* [2008] associated with meltwater lake drainage. Our model also predicts a final basal crack (subglacial lake) radius of 5-10 km, and a drop in surface-lake water level consistent with that observed.

4.2 Introduction

Hydraulic fracture has, since the 1940's, been a subject of great interest in the context of inducing production from oil and gas wells (see e.g. *Mendelsohn* [1984] for a review). More recently, the topic has been explored in depth theoretically [*Lister*, 1990; *Desroches et al.*, 1994; *Dyskin et al.*, 2000; *Adachi and Detournay*, 2002; *Savitski and Detournay*, 2002; *Detournay*, 2004; *Garagash and Detournay*, 2005; *Roper and Lister*, 2007], in the context of magma-driven cracking [*Rubin*, 1995], and in the context of water-aided vertical crevassing in glaciers [*Weertman*, 1971a, 1973; *Smith*, 1976; *van der Veen*, 1998; *Kenneally*, 2003; *Alley et al.*, 2005; *van der Veen*, 2007; *Krawczynski et al.*, 2009]. These works have successfully applied the results of linear elastic fracture mechanics (LEFM) with different assumptions of fluid-related boundary conditions on the crack face. The boundary conditions used have ranged from the simple quasi-static loading case common in the glaciological literature [*Weertman*, 1973; *Smith*, 1976; *van der Veen*, 1998, 2007; *Krawczynski et al.*, 2009] to the more complex but realistic case for which the pressure distribution within the crack is determined along with the crack separation as a coupled fluid-flow/elasticity problem [*Desroches et al.*, 1994; *Adachi and Detournay*, 2002].

As interest regarding the very short timescale behavior of glaciers intensifies [*Bindschadler et al.*, 2003; *Ekström et al.*, 2006; *Das et al.*, 2008; *Wiens et al.*, 2008], it will become of paramount importance to understand the fracture process in glaciers since it influences fundamental aspects of glacial dynamics, including flow speeds, calving behavior, and stability of the ice sheet (e.g. *Zwally et al.* [2002]; *Kenneally* [2003]; *Joughin et al.* [2008b]; *Tsai et al.* [2008]). The current literature on the processes

leading to crevasse extension to depth is fairly small (see previous paragraph) but there is agreement that the presence of liquid water greatly enhances the ability for crevasses to quickly grow, become macroscopic and affect large-scale features of ice sheets. Recent observations by *Das et al.* [2008] of drainage of a large supraglacial meltwater lake into, and presumably to the bed of, the Greenland Ice Sheet within a timespan of a few hours shows that water flow rates into crevasses can be very fast. A crude estimate of the Reynolds number, $\Re$, for this observed flow can be made by assuming the full volume of initial lake water ($V_0 \approx 4.4 \cdot 10^7$ m^3) drains into a crack system of lateral dimension close to the lake dimension ($L_c \approx 3$ km) over the $T \approx 2$-hour timescale of observed drainage. With water density of $\rho \approx 10^3$ kg/m^3 and viscosity of $\eta \approx 2 \cdot 10^{-3}$ Pa s, this crude estimate yields $\Re = \rho V_0/(L_c T \eta) \approx 10^6$, which is within the fully turbulent regime. These observations therefore motivate the present work, in which we consider the turbulent flow of draining surface water as causing the opening of a basal crack within a linear-elastic ice medium. Although these approximations of fully turbulent flow within a purely elastic medium are clearly short-timescale end-member cases of a more realistic scenario, they are reasonable and allow for considerable simplification of the mathematical analysis.

In Section 4.3, we present solutions for the crack-tip speeds, pressure profiles and displacement profiles for steady-state crack growth and self-similar crack growth. In Section 4.4, we then apply these results to glacial crack propagation, compare our results to the recent observations of *Das et al.* [2008], and find reasonable agreement between model and observation. Although we do not explicitly consider the case of jokulhlaup (subglacial outburst flood) initiation, our model applies to the initial

growth stages of these events to the extent that jokulhlaup initiation can be thought of as the crack-like growth of a subglacial lake under excess water pressure (see e.g. *Roberts* [2005]). The model may also have some relevance to satellite-inferred fluid interchanges between sub-glacial lakes documented by *Fricker et al.* [2007].

4.3 Model Setup: Turbulent Hydraulic Fracture

In this section, we consider a crack within an elastic medium driven open by the turbulent flow of water through the crack. To model this, we adapt various power-law viscous-flow crack solutions [*Desroches et al.*, 1994; *Adachi and Detournay*, 2002] for use with a Manning-Strickler channel model [*Manning*, 1891; *Strickler*, 1923, 1981] for wall shear resistance to turbulent flow (see e.g. *Rouse* [1955]). The geometry considered here is that of a plane strain horizontal crack of length $2L$ within an impermeable linearly-elastic medium, located at a depth H beneath the surface. The crack opening profile is given by $h(x)$ for $-L < x < L$ (see Figure 4.1).

4.3.1 Manning Turbulent Friction

For flow through a channel of height h, the average shear stress on the channel walls τ is given by

$$2\tau \equiv \frac{f}{4}\rho U^2 = -h\frac{\partial p}{\partial x}, \tag{4.1}$$

for $0 < x < L$, where h is the local channel height, $\partial p/\partial x$ is the pressure gradient (see Figure 4.1), f is the commonly-used "Darcy-Weisbach" friction factor, ρ is the fluid density, and U is the fluid velocity averaged across h, and the sign in Equation (4.1) is

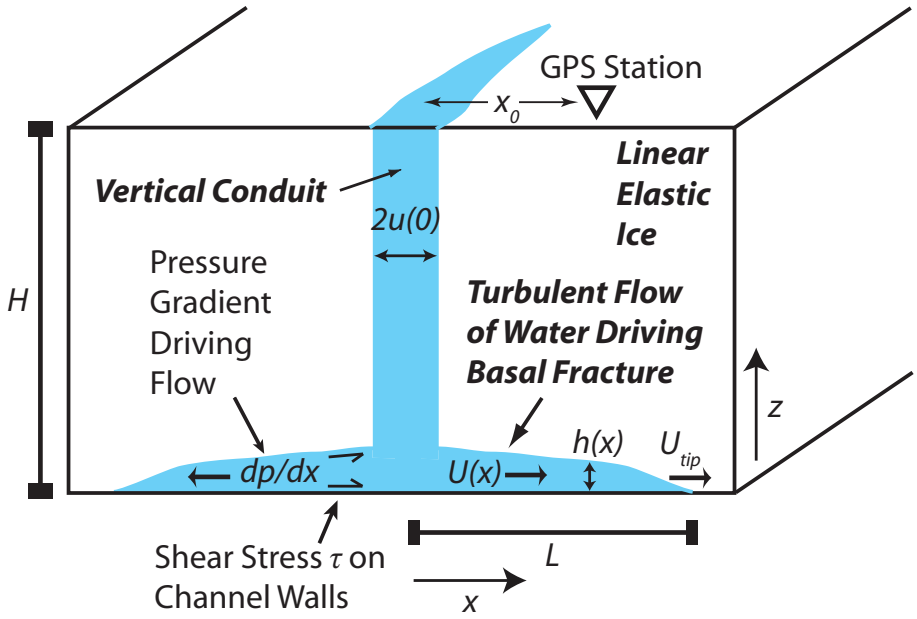

Figure 4.1: Schematic of the model. A vertical conduit (crack) of height H connects a surficial lake with a basal crack, which is driven open by turbulent flow of water through the crack system. In the model solutions, a 2D plane strain problem is solved for simplicity, effectively assuming the surficial crack is infinitely long. However, in applying the results, we assume the third dimension length scales with L, the half-length of the basal crack. The variables are described in the text.

reversed when $x < 0$. In order to use this relationship between the velocity and pressure gradient in the crack solution, we must estimate f. Here, we assume that the flow is fully turbulent so that f is given by the Gauckler-Manning-Strickler approximation [*Manning*, 1891; *Strickler*, 1923, 1981]

$$f = 0.113 \left(\frac{k}{R_h}\right)^{1/3} = f_0 \left(\frac{k}{h}\right)^{1/3} = 0.143 \left(\frac{k}{h}\right)^{1/3}, \tag{4.2}$$

where $R_h = h/2$ is the hydraulic radius and k is the Nikuradse channel wall roughness height [*Rubin and Atkinson*, 2001]. When the two walls have different roughness, it is appropriate to interpret $k^{1/3}$ as the average of $k^{1/3}$ for the upper and lower walls. This expression, Equation (4.2), is known to be approximately valid when the Reynolds number $\Re$ is sufficiently large, $\Re \gtrsim 10^5$ (see e.g. *Rubin and Atkinson* [2001]; *Gioia and Chakraborty* [2006]; *White* [2008]). This inequality is verified in Section 4.4 for the case of interest. This scaling is also equivalent to the commonly used Manning approximation

$$U_{Manning} = \frac{1}{n} R_h^{2/3} S^{1/2}. \tag{4.3}$$

Here, n is the Manning roughness parameter,

$$S = -\frac{1}{\rho g}\frac{\partial p}{\partial x}\Big(= \frac{2\tau}{\rho g h}\Big) \tag{4.4}$$

is the negative hydraulic head gradient (positive in the direction of flow) (e.g. *Rouse* [1955]), and g is gravitational acceleration. In Equations (4.1) and (4.4), we have assumed that the gravity forcing due to slope of the flow channel is negligible compared to the pressure gradient; otherwise, the slope is added to the definition of S. The value of f_0 used in Equation (4.2) is equivalent to setting

$$n = (0.0380 \text{ s m}^{-1/2}) \cdot k^{1/6} \tag{4.5}$$

(e.g. $n = 0.026$ s m$^{-1/3}$ when $k = 0.1$ m).

Substituting Equation (4.2) into Equation (4.1) gives

$$-\frac{\partial p}{\partial x} = \frac{f_0}{4}\rho U^2 \frac{k^{1/3}}{h^{4/3}} = 0.0357 \rho U^2 \frac{k^{1/3}}{h^{4/3}}. \tag{4.6}$$

The turbulent Manning-Strickler scaling therefore provides one relationship between the local pressure gradient $\partial p(x,t)/\partial x$, fluid velocity $U(x,t)$, and channel opening $h(x,t)$.

4.3.2 Basic Equations Governing Turbulent Hydraulic Fracture

The problem of a fracture driven through an impermeable linear elastic body by injection of a power-law viscous fluid has been studied by a number of authors. Key results include an analytical near-tip solution in plane strain [*Desroches et al.*, 1994], a (numerical) self-similar solution for a plane strain fracture of finite length [*Adachi and Detournay*, 2002], and a solution for a penny-shaped fracture [*Savitski and Detournay*, 2002]. Here, we use an approach analogous to these power-law solutions but modified to make use of the turbulent scaling of Section 4.3.1. In so doing, we find it convenient to consider the related problem of a plane strain crack in an imagined homogeneous medium (as shown in Figure 4.2). For this model crack, we assume there to be three fundamental considerations that relate the crack opening displacement profile $w(x,t)$, the crack pressure profile $p(x,t)$, and the crack fluid velocity profile $U(x,t)$. (The relation of w, the crack opening in an imagined homogeneous ice material, to h, the channel width at the glacier interface with its bed, is discussed

below; we will choose h proportional to w with a coefficient of proportionality that is rationalized in Appendix B.) Elasticity theory provides one equation, the turbulent scaling of Equation (4.6) provides another, and fluid mass conservation provides the third equation. As in *Desroches et al.* [1994] and *Adachi and Detournay* [2002], we solve the case for negligible fracture energy. As will be shown in Section 4.4, with estimates of ice fracture energy from *Rist et al.* [1999] and guidelines like those of *Savitski and Detournay* [2002] and *Bunger and Detournay* [2008], this approximation is reasonable for the glacial application considered.

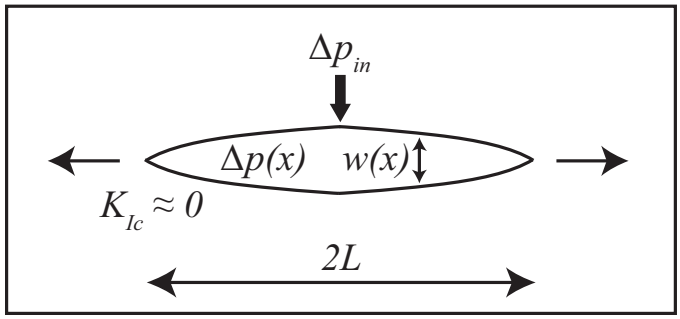

Figure 4.2: Schematic for stress calculation. The actual crack opening, h, is assumed to be ξw, where w is the modeled full width and ξ is given by Equation (4.8). The excess pressure at $x = 0$ is assumed to be given by Δp_{in} and the fracture toughness K_{Ic} is assumed negligible.

For a crack (of length $2L$) in an infinite, homogeneous elastic medium, it is well known that a singular integral equation [*Muskhelishvili*, 1953] relates $w(x,t)$ and $p(x,t)$. In the following, we assume that there exists a local hydrostatic ice overburden pressure given by σ_0 so that the pressure causing crack opening is given by the excess pressure $\Delta p(x,t) \equiv p(x,t) - \sigma_0$. The integral equation can then be represented as

$$\Delta p(x,t) = \frac{E'}{4\pi} \int_{-L}^{L} \frac{\partial w(s,t)}{\partial s} \frac{ds}{x-s}, \tag{4.7}$$

where $E' = E/(1-\nu^2)$, E is Young's modulus, and ν is Poisson's ratio. For the crack of interest at the glacial bed, the material on the upper side of the crack (ice) is significantly more compliant than the material on the lower side (rock) and therefore is responsible for most of the crack opening. For this bimaterial case, then, we make the approximation that the actual physical opening displacement $h(x,t)$ is a fraction of the imagined opening $w(x,t)$ in the homogeneous medium of the more compliant material (ice), so that $h(x,t) = \xi w(x,t)$ where $\xi < 1$ (e.g. compare Figure 4.1 and Figure 4.2). Thus, in all calculations done here, the physical crack opening h is interpreted to be exactly ξw where w is the opening calculated in a homogeneous ice medium by Equation (4.7). In Appendix B we provide justification of this approximation based on elastic analyses of cracks along bimaterial interfaces, and suggest that

$$\xi \approx \frac{1 + E'_{ice}/E'_{bed}}{2} \approx 0.55 \tag{4.8}$$

is an appropriate factor for ice in contact with (or separating from) granitic bedrock. In using Equation (4.6) for this case, then

$$-\frac{\partial \Delta p}{\partial x} = \frac{f_0}{4\xi^{4/3}} \rho U^2 \frac{k^{1/3}}{w^{4/3}} = 0.0793 \rho U^2 \frac{k^{1/3}}{w^{4/3}}, \tag{4.9}$$

and k is assumed to be equal on both sides of the bimaterial channel. Finally, if we assume an incompressible fluid (i.e. constant ρ) then the mass conservation equation (setting $h = \xi w$ and cancelling the ξ) can be written as

$$\frac{\partial (wU)}{\partial x} + \frac{\partial w}{\partial t} = 0. \tag{4.10}$$

Note that for a steady-state crack with crack-tip velocity U_{tip}, $w(x,t) = w(x - U_{tip}t)$, and Equation (4.10) simplifies to $U(x,t) = U_{tip}$ [*Desroches et al.*, 1994], i.e. the

fluid velocity is everywhere equal to the crack-tip velocity. This result will apply asymptotically, near the tip, for non-steady configurations and time-variable U_{tip}.

4.3.3 Adaptation of the Power-Law Viscous Fluid Crack Solution to the Turbulent Case, Simple Approximate Model

In this section, we follow *Desroches et al.* [1994] and begin with a steady-state solution for a semi-infinite crack, $U(x,t) = U_{tip}$ and so drop the explicit x and t dependence on U. Since there is no explicit time dependence in the other two governing equations, we also drop the explicit t dependence of $w(x,t)$ and $\Delta p(x,t)$ for that semi-infinite case, instead writing $w(x)$ and $\Delta p(x)$. In Section 4.3.5, we will revert to Equation (4.10).

At this point, we observe that Equation (4.9) has the same form as the power-law viscous flow lubrication equation [*Bird et al.*, 1987], which can be written as

$$-\frac{d\Delta p}{dx} = \frac{c_0}{w^{1+n}}, \tag{4.11}$$

where w is the crack opening width, n is the power-law index relating shear stress τ with shear rate $\dot{\gamma}$ ($\tau \propto \dot{\gamma}^n$), and c_0 is a factor that includes a dependence on U (which is proportional to U^2 for our turbulent case and to U^n for the *Desroches et al.* [1994] power-law case). Thus, by simply using the $n = 1/3$ case, we can utilize the same *Muskhelishvili* [1953] procedure as in *Desroches et al.* [1994], which yields a solution of the same form for both $w(x)$ and $\Delta p(x)$, and obtain (for the crack tip at $x = L$)

$$w(x) = \frac{14A}{3E'} R^{6/7} \sin\frac{\pi}{7}, \tag{4.12}$$

and

$$\Delta p(x) = P - AR^{-1/7}\cos\frac{\pi}{7}, \tag{4.13}$$

where $R \equiv L - x$ is the distance along the crack behind the crack tip, P is a constant which is undetermined in this analysis, and the constant A is directly relatable to $U_{tip} = \dot{L}$ through substitution into Equation (4.9) (with $U = U_{tip}$). Solving for A gives

$$A = E'\left[\frac{(7/4)^3(3/14)^4 \cdot f_0^3}{\cos^3(\pi/7)\sin^4(\pi/7)\cdot\xi^4}\left(\frac{\rho U_{tip}^2}{E'}\right)^3 \cdot k\right]^{1/7}. \tag{4.14}$$

Stresses within the elastic medium σ_{xx}, σ_{yx} and σ_{yy} can similarly be expressed in polar coordinates (r, θ) around the crack tip, for example, with

$$\sigma_{yy} = -P + r^{-1/7}F_{yy}(\theta). \tag{4.15}$$

Full expressions for $F_{yy}(\theta)$ and all other stresses are given in Appendix B. This solution, which is obtained by seeking an appropriate analytic function representation of the *Muskhelishvili* [1953] potentials or, equivalently, by assuming a *Williams* [1952] power-law stress field near the crack tip, is an exact steady-state solution of the governing equations of elasticity and fluid flow for a semi-infinite crack, and it represents the leading-order near crack-tip singularity part of the full solution in other cases. However, it meets no appropriate boundary conditions away from the crack tip at $x = L$ or at the glacier surface.

We can, nevertheless, follow *Desroches et al.* [1994] and use that solution as a basis of an approximate analysis for a finite crack of length $2L$ (see Figure 4.1). That involves assuming that Equation (4.13), with x replaced by $|x|$, holds over all of $0 \le |x| \le L$, and then by choosing P so that the stress intensity factor due to $\Delta p(x)$

is zero (otherwise, the asymptotically correct form of the crack opening profile as in Equation (4.12) would be violated). To accomplish that, we set

$$\int_0^L \frac{\Delta p(x)dx}{\sqrt{L^2-x^2}} = 0, \tag{4.16}$$

which gives $P = 1.23374AL^{-1/7}$. Writing this approximation in terms of the inlet excess pressure $\Delta p_{in} \equiv \Delta p(0)$ (instead of as a function of U_{tip}) then yields

$$\Delta p(x) = \Delta p_{in} + 2.7075\Delta p_{in}\left[1 - \left(\frac{L}{L-x}\right)^{1/7}\right]. \tag{4.17}$$

This approximation is consistent with the neglect of fracture energy (see Figure 4.2), but ignores the presence of the free surface at the top of the glacier (i.e. it assumes $L \ll H$). Although not completely appropriate, we will use the solution for the entire range of L, including when $L > H$.

With Equation (4.17) describing the pressure along the crack face, then Equation (4.12) gives

$$w(x) = \frac{2.7075}{\delta}L\frac{\Delta p_{in}}{E'}\left(\frac{L-x}{L}\right)^{6/7} = 6.0843L\frac{\Delta p_{in}}{E'}\left(\frac{L-x}{L}\right)^{6/7}, \tag{4.18}$$

for $0 < x < L$, where

$$\delta \equiv \frac{3\cos(\pi/7)}{14\sin(\pi/7)} = 0.4450. \tag{4.19}$$

Finally, inserting Equations (4.17) and (4.18) into Equation (4.9) and rearranging gives an expression for U_{tip} in terms of known (or potentially measurable) quantities

$$\begin{aligned} U_{tip} &= \frac{2\xi^{2/3}2.7075^{7/6}}{(7f_0)^{1/2}\delta^{2/3}}\sqrt{\frac{\Delta p_{in}}{\rho}}\left(\frac{\Delta p_{in}}{E'}\right)^{2/3}\left(\frac{L}{k}\right)^{1/6} \\ &= 7.36\sqrt{\frac{\Delta p_{in}}{\rho}}\left(\frac{\Delta p_{in}}{E'}\right)^{2/3}\left(\frac{L}{k}\right)^{1/6}. \end{aligned} \tag{4.20}$$

It is of interest to note that if we had used the homogeneous-medium version of Equation (4.9) ($h = w$), the numerical coefficient would change from 7.36 to 11.0 and the remainder of Equation (4.20) would remain unchanged. (One can also note that the crack-tip asymptotic solution is applicable in the near-tip region of a penny-shaped crack (e.g. *Savitski and Detournay* [2002]) so that Equation (4.20) may apply approximately in this case as well.)

4.3.4 Scaling Analysis

The result of Equation (4.20) can perhaps be more easily understood through a simple scaling analysis. In this scaling analysis, we let $L = L_0\hat{L}$, $w(x) = w_0\hat{w}$, $\Delta p(x) = \Delta p_0\hat{p}$, and $U = U_0\hat{U}$, where hatted variables are non-dimensional and variables with a subscript zero are characteristic scales for the respective original variables. Inserting these expressions into Equation (4.7) gives $w_0/L_0 = \Delta p_0/E'$. Similarly, Equation (4.9) gives $\Delta p_0/L_0 = \rho U_0^2 k^{1/3}/w_0^{4/3}$. Solving for the velocity scale U_0 then yields

$$U_0 = \sqrt{\frac{\Delta p_0}{\rho}} \left(\frac{\Delta p_0}{E'}\right)^{2/3} \left(\frac{L_0}{k}\right)^{1/6}. \tag{4.21}$$

If no physics other than that of Equations (4.7), (4.9) and (4.10) enters the problem, then the only reasonable pressure scale is the excess inlet pressure, i.e. $\Delta p_0 = \Delta p_{in}$, and if $L \ll H$ then the instantaneous crack half-length L must be the relevant scale for L_0. That is, given a pressure scale Δp_{in} and a single length scale L, the scaling of Equation (4.20) is completely determined by dimensional analysis, and only the numerical factor is dependent on the choices made in Section 4.3.3. One may note, however, that if the crack has an additional length scale (e.g. if $H \sim L$) then both

Equation (4.20) and Equation (4.21) can have an added dependence on a function of L/H.

4.3.5 Self-Similar Analysis

Finally, following an approach similar to those of *Spence and Sharp* [1985] and *Adachi and Detournay* [2002], we numerically find an exact self-similar solution, also for the case in which $L \ll H$. After scaling the equations as in Section 4.3.4, we look for a non-dimensionalized self-similar solution of the form

$$L(t) = L_0 \hat{t}^{\alpha}/\alpha, \tag{4.22a}$$

$$w(x,t) = w_0 \hat{t}^{\beta} \hat{w}(\hat{x})/\beta, \tag{4.22b}$$

$$\Delta p(x,t) = \Delta p_0 \hat{p}(\hat{x}), \tag{4.22c}$$

$$U(x,t) = \phi U_0 \hat{t}^{\gamma} \hat{U}(\hat{x}). \tag{4.22d}$$

It should be observed that here L_0 can be chosen arbitrarily (in that it will be seen to cancel from all final expressions). Once L_0 is chosen and the correspondence $\Delta p_0 = \Delta p_{in}$ is made, then w_0 and U_0 are determined by these choices, but $U(x,t)$ has an extra condition to satisfy, $U(L(t),t) = dL(t)/dt$, which is met by proper choice of ϕ. Here, $\hat{t} \equiv \phi U_0 t/L_0$ is a non-dimensional time, $\hat{x} \equiv x/L(t)$ is a non-dimensional position, and α, β, γ and ϕ are numerical constants. In this self-similar solution, it is assumed that $\Delta p_{in} \equiv \Delta p(0,t)$ is constant so that Equation (4.22c) does not have any time dependence. Substituting these expressions into Equations (4.7), (4.9) and (4.10), we find that the time dependence can only be satisfied with $\alpha = 6/5$, $\beta = 6/5$, $\gamma = 1/5$ (but ϕ is still to be determined). We therefore find that in this

self-similar solution $L(t)$ and $w(x,t)$ grow slightly faster than linearly with time. We are also left with 3 non-dimensional ordinary differential equations for the self-similar displacement profile $\hat{w}(\hat{x})$, pressure profile $\hat{p}(\hat{x})$ and velocity profile $\hat{U}(\hat{x})$. These 3 expressions are

$$\hat{p}(\hat{x}) = \frac{1}{4\pi}\int_{-1}^{1} \frac{d\hat{w}(\hat{s})}{d\hat{s}}\frac{d\hat{s}}{\hat{x}-\hat{s}}, \tag{4.23}$$

$$-\hat{w}^{10/3}\frac{d\hat{p}}{d\hat{x}} = \frac{(6/5)^{1/3}f_0}{4\xi^{4/3}}\phi^2(\hat{U}\hat{w})^2, \tag{4.24}$$

and

$$\frac{d(\hat{U}\hat{w})}{d\hat{x}} = \frac{d(\hat{x}\hat{w})}{d\hat{x}} - 2\hat{w}. \tag{4.25}$$

Similarly translating boundary conditions gives $\hat{w}(1) = 0$, $\hat{p}(0) = 1$, and $\hat{U}(1) = 1$. Integrating Equation (4.25) from $\hat{x}$ to 1 and substituting into Equation (4.24) yields

$$-\hat{w}^{10/3}\frac{d\hat{p}}{d\hat{x}} = \frac{(6/5)^{1/3}f_0}{4\xi^{4/3}}\phi^2\left(\hat{x}\hat{w} + 2\int_{\hat{x}}^{1}\hat{w}(\hat{s})d\hat{s}\right)^2. \tag{4.26}$$

It now only remains to numerically solve Equations (4.23) and (4.26) subject to $\hat{w}(1) = 0$ and $\hat{p}(0) = 1$. To accomplish this, we follow an approach like that of *Adachi and Detournay* [2002] and take the $\hat{w}$ and $\hat{p}$ profiles to be given as series, the first term of which solves the crack-tip asymptotic (e.g. consistent with Equations (4.12-4.13)) and the rest of the terms which do not contribute a stress intensity factor. That is, we take

$$\hat{w} = D\left[\frac{1}{\delta}\left(\frac{1-\hat{x}^2}{2}\right)^{6/7} + A_1 w_1(\hat{x}) + A_2 w_2(\hat{x}) + A_3 w_3(\hat{x}) + \dots\right] \tag{4.27}$$

and

$$\hat{p} = D\Big[F(\hat{x}) + A_1(c_1 - |\hat{x}|) + A_2(c_2 - \hat{x}^2) + A_3(c_3 - |\hat{x}|^3) + \dots\Big]. \tag{4.28}$$

Table 4.1: Values of $w_k(0)$ and average value of $w_k(\hat{x})$ up to $k = 4$. Average values are numerically calculated but agree with stated exact result to within numerical error.

	w_1	w_2	w_3	w_4
Value at $\hat{x} = 0$	$4/\pi$	$4/3$	$4/\pi$	$6/5$
Average value	$2/3$	$\pi/4$	$4/5$	$\pi/4$

Here, c_k are constants chosen to remove any contribution to the stress intensity factor (i.e. consistent with negligible fracture resistance) from each of the $c_k - |\hat{x}|^k$ terms and thus satisfy

$$\int_0^1 \frac{(c_k - |\hat{x}|^k)d\hat{x}}{\sqrt{1-\hat{x}^2}} = 0 \quad \text{or} \quad c_k = \frac{2}{\pi}\int_0^{\pi/2} \sin^k \varphi d\varphi, \tag{4.29}$$

where the substitution $\hat{x} = \sin\varphi$ was made. $F(\hat{x})$ and the w_k are chosen so that each term of the $\hat{w}$ and $\hat{p}$ expressions pairwise satisfy Equation (4.23), i.e.,

$$F(\hat{x}) = \frac{1}{4\pi}\int_{-1}^{1} \frac{1}{\delta}\frac{d}{d\hat{s}}\left(\frac{1-\hat{s}^2}{2}\right)^{6/7} \frac{d\hat{s}}{\hat{x}-\hat{s}} = -\frac{3}{7\cdot 2^{6/7}\pi\delta}\int_{-\pi/2}^{\pi/2} \frac{\sin\varphi\cos^{5/7}\varphi d\varphi}{\hat{x}-\sin\varphi} \tag{4.30}$$

and

$$c_k - |\hat{x}|^k = \frac{1}{4\pi}\int_{-1}^{1} \frac{dw_k(\hat{s})}{d\hat{s}}\frac{d\hat{s}}{\hat{x}-\hat{s}}, \tag{4.31}$$

where Equation (4.31) can be inverted to solve for w_k using the *Muskhelishvili* [1953] approach. This results in non-singular $dw_k/d\hat{x}$ at $|\hat{x}| = 1$, consistent with choosing $w_k(\pm 1) = 0$, provided that the c_k are chosen according to Equation (4.29). The result, as simplified by *Adachi and Detournay* [2002], is

$$w_k(\sin\varphi) = \frac{4}{\pi}\int_0^{\pi/2} (c_k - \sin^k\theta)\ln\left|\frac{\cos\varphi+\cos\theta}{\cos\varphi-\cos\theta}\right|\cos\theta d\theta. \tag{4.32}$$

$F(\hat{x})$ and the $w_k(\hat{x})$ are plotted in Figures 4.3 and 4.4, respectively. Values of $w_k(0)$ and averages of $w_k(\hat{x})$ over the crack are tabulated in Table 4.1.

D and the A_k are then constants to be determined so that the remaining Equation (4.26) is satisfied. Note that δ is inserted in Equation (4.27) so that $F(\hat{x})\cdot[(1-$

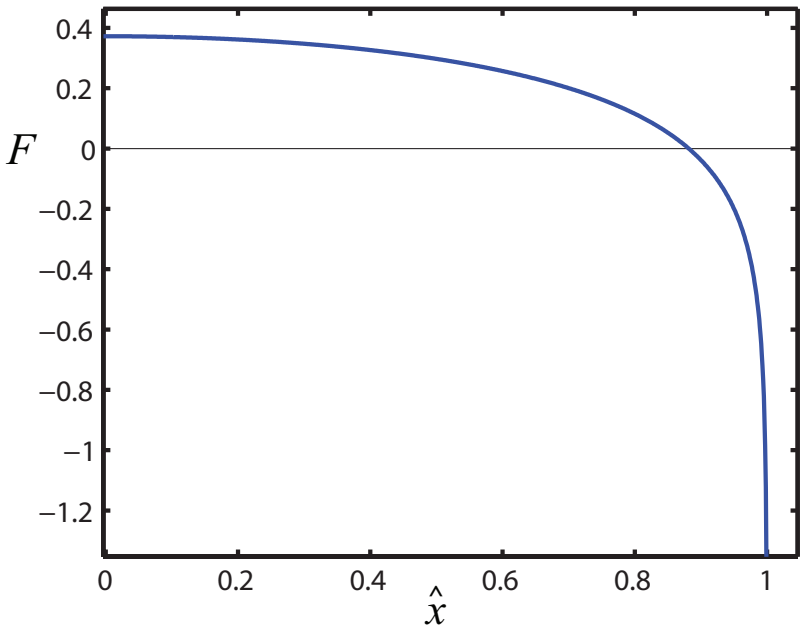

Figure 4.3: $F(\hat{x})$ as calculated numerically from Equation (4.30).

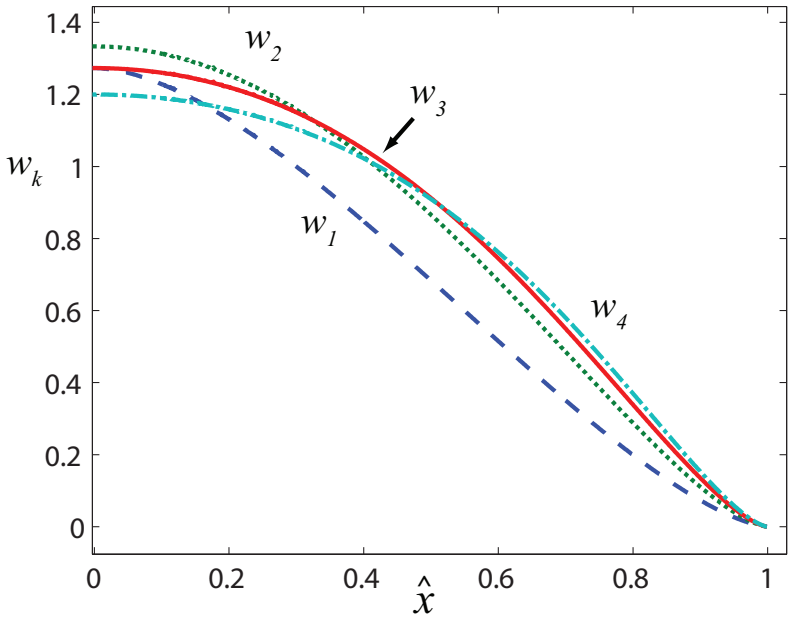

Figure 4.4: $w_k(\hat{x})$ as calculated numerically from Equation (4.32). The blue dashed line is w_1, the dotted green line is w_2, the solid red line is w_3 and the dashed-dotted cyan line is w_4.

$\hat{x}^2)/2]^{1/7} \rightarrow -1$ as $\hat{x} \rightarrow \pm 1$. Equation (4.26) can be satisfied by choosing ϕ and the A_k coefficients appropriately, and the boundary condition $\hat{p}(0) = 1$ can be satisfied by choosing D appropriately. To determine ϕ, we substitute Equations (4.27-4.28) into Equation (4.26) and take the limit as $\hat{x} \rightarrow 1$. The resulting limit is independent of the A_k and gives

$$\phi = \frac{2\xi^{2/3} D^{7/6}}{(6/5)^{1/6} \cdot (7f_0)^{1/2} \cdot \delta^{2/3}}. \tag{4.33}$$

Note that $(6/5)^{1/6}\phi$ is the numerical coefficient in Equation (4.22d) analogous to the 7.36 coefficient of Equation (4.20), and unsurprisingly has the same functional dependence on f_0 and δ. To determine the A_k, we minimize the normalized squared error between the left-hand-side (LHS) and right-hand-size (RHS) of Equation (4.26). That is, we minimize

$$\epsilon_m \equiv \frac{\sum_i \left[RHS(\hat{x}_i) - LHS(\hat{x}_i)\right]^2}{\left[\sum_i LHS(\hat{x}_i)\right]^2} \tag{4.34}$$

over equally spaced points $\hat{x}_i$ between 0 and 1. We find that using only 5 terms in the series (including up to the A_4 term) gives an adequate minimization of ϵ_m, as shown in Figure 4.5a. (See also Figure 4.5b for the analogous comparison for the steady-state solution.) As in *Spence and Sharp* [1985], the resulting values of A_k are relatively insensitive to the exact choice of misfit functional ϵ_m. The values obtained for D, A_k and c_k are given in Table 4.2, and the resulting profiles for $\hat{w}$ and $\hat{p}$ are shown in Figure 4.6 compared to the profiles for the approximate solution of Section 4.3.3. The $\hat{U}$ profile is shown in Figure 4.7. This value of D results in

$$\phi = 4.99, \tag{4.35}$$

which is different than the 7.36 coefficient of Equation (4.20) by less than a factor of

Table 4.2: Self-similar parameters D, A_k and c_k

D	A_1	A_2	A_3	A_4	c_1	c_2	c_3	c_4
1.991	0.450	-0.431	0.151	-0.014	$\frac{2}{\pi}$	$\frac{1}{2}$	$\frac{4}{3\pi}$	$\frac{3}{8}$

2.

One can explicitly find $L(t)$ by solving Equation (4.22a) in terms of all the now known quantities to obtain

$$L(t) = \frac{5\phi^{6/5}U_0^{6/5}}{6L_0^{1/5}}t^{6/5} = \frac{5}{6}\phi^{6/5}\left(\frac{\Delta p_{in}}{\rho}\right)^{3/5}\left(\frac{\Delta p_{in}}{E'}\right)^{4/5}\frac{t^{6/5}}{k^{1/5}}, \tag{4.36}$$

so that

$$\begin{aligned} U_{tip} \equiv \frac{dL}{dt} &= U(L(t),t) = (6/5)^{1/6}\phi U_0\left(\frac{L(t)}{L_0}\right)^{1/6} \\ &= (6/5)^{1/6}\phi\sqrt{\frac{\Delta p_{in}}{\rho}}\left(\frac{\Delta p_{in}}{E'}\right)^{2/3}\left(\frac{L(t)}{k}\right)^{1/6}, \end{aligned} \tag{4.37}$$

and

$$w(x,t) = L(t)\frac{\Delta p_{in}}{E'}\hat{w}(\hat{x}) = \frac{1.991}{\delta}L(t)\frac{\Delta p_{in}}{E'}\left[\left(\frac{L(t)^2-x^2}{2L(t)^2}\right)^{6/7} + \delta A_1 w_1(\hat{x}) + \delta A_2 w_2(\hat{x}) + \delta A_3 w_3(\hat{x}) + \cdots\right]. \tag{4.38}$$

For later reference, $\hat{w}(0) = 2.816$ and the average value of $\hat{w}$ is 1.859 so that the maximum actual crack opening is given by $h(0) = 2.816\xi L(t)\Delta p_{in}/E'$ and the average value of h is given by

$$h_{avg} = 1.859\xi L(t)\Delta p_{in}/E'. \tag{4.39}$$

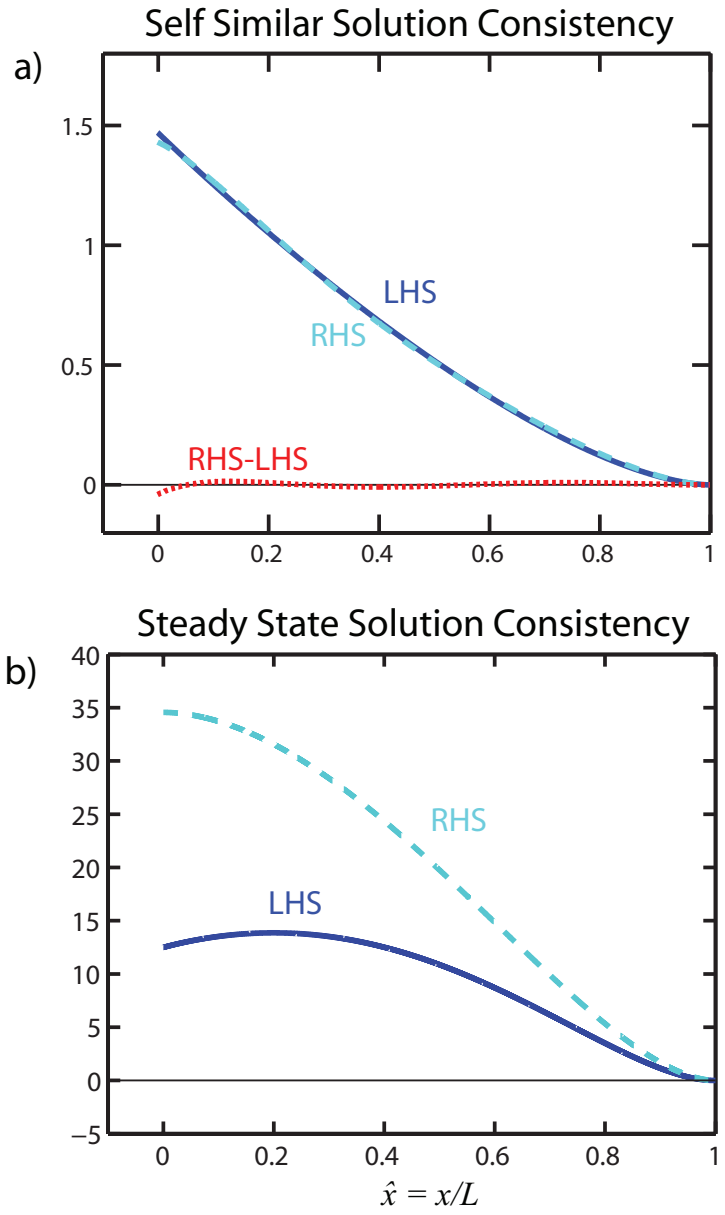

Figure 4.5: (a) Plotted are the LHS (solid blue) and RHS (dashed cyan) of Equation (4.26) and the difference $RHS - LHS$ (dotted red) for the self-similar solution. (b) For comparison with panel (a), plotted are the analogous LHS and RHS of a scaled version of Equation (4.9) multiplied by $w^{10/3}$ on both sides, using w as calculated to be consistent with the steady-state Δp in Equation (4.7). As expected, the steady-state solution is consistent asymptotically as $\hat{x} \to 1$ but, unlike the self-similar solution, has significant differences away from $\hat{x} = 1$.

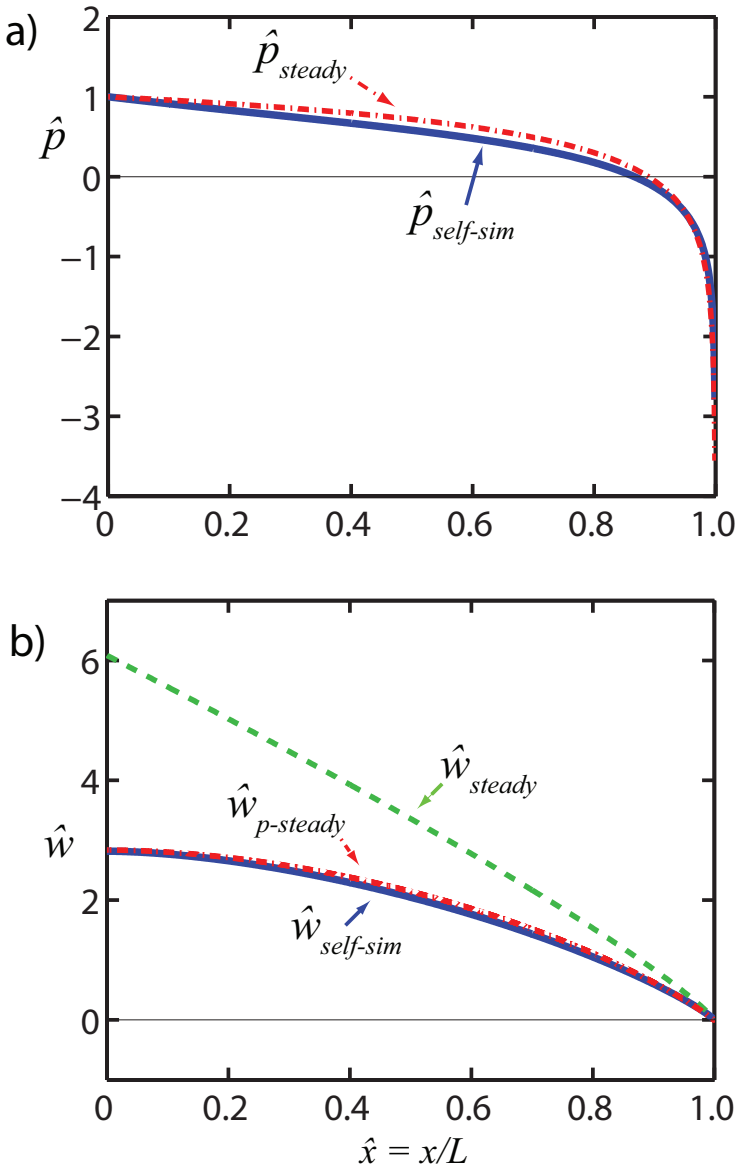

Figure 4.6: Comparison of steady-state and self-similar solutions. (a) Plotted are the $\hat{p}$ (scaled pressure) for the self-similar solution ($\hat{p}_{self-sim}$) and the steady-state solution ($\hat{p}_{steady}$). The actual pressure is given by $p(x) = \Delta p_{in}\hat{p}(\hat{x})$. (b) Plotted are the $\hat{w}$ (scaled model opening) for the self-similar solution ($\hat{w}_{self-sim}$), the $\hat{w}$ of Equation (4.18) for the steady-state solution ($\hat{w}_{steady}$), and the $\hat{w}$ consistent with the steady-state $\hat{p}_{steady}$ distribution in Equation (4.7) ($\hat{w}_{p-steady}$). The actual opening is given by $h(x) = \xi w(x) = \xi L(t)\Delta p_{in}/E' \cdot \hat{w}(\hat{x})$.

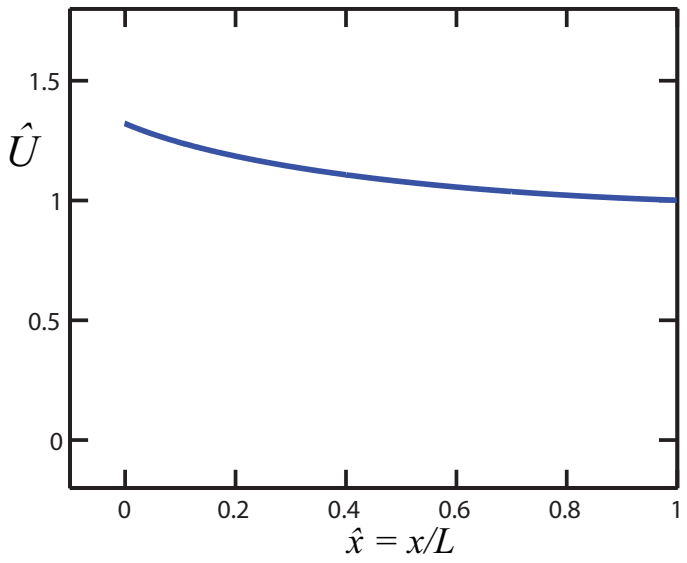

Figure 4.7: Plotted is the $\hat{U}$ (scaled fluid velocity) for the self-similar solution. $\hat{U}(0) \approx 1.321$, and $\hat{U}(1) = 1$ as required by the condition $U(L) = U_{tip}$. For comparison, the steady-state solution has $\hat{U}(\hat{x}) \equiv 1$. The actual fluid velocity is given by $U(x) = (6/5)^{1/6}\phi U_0 (L(t)/L_0)^{1/6}\hat{U}(\hat{x})$.

4.4 Understanding Glacial Crack Propagation

To apply the results of the previous section to crack propagation at the bed of a glacier, we must estimate the parameters that enter Equation (4.20) or (4.37). Here, to make direct contact with the observations of *Das et al.* [2008] of GPS displacements associated with the drainage of a Greenland meltwater lake, we take the margin of the Greenland Ice Sheet as the region of interest. Estimates of the Young's modulus of glacial ice varies substantially, with a range of $0.9 - 10$ GPa [*Vaughan*, 1995]. We choose, as representative, laboratory values of Young's modulus at $-5°$C of $E = 6.2$ GPa [*Jellinek and Brill*, 1956] and Poisson's ratio $\nu = 0.3$ [*Vaughan*, 1995], giving $E' = 6.8$ GPa. Fluid density is taken as $\rho = 1000$ kg/m^3 and ice density is taken as $\rho_{ice} = 910$ kg/m^3. The study area of *Das et al.* [2008] had 980 m-thick ice ($H = 0.98$ km), so the pressure at the base of the ice sheet in excess of the ice pressure due to a column of standing water there would be $\Delta p_{static} = (\rho - \rho_{ice})gH_w \approx 0.87$ MPa, where the height of water, H_w, is taken as equal to the ice thickness, H, and $g \approx 9.81$ m/s^2. The actual excess pressure at the inlet is reduced from this value due to frictional losses from the surface to the bed, but as a high-end first approximation we take $\Delta p_{in} = \Delta p_{static} = 0.87$ MPa. The channel roughness k is the least constrained of all parameters but is likely a healthy but small fraction of the channel opening (with range perhaps being 0.005 m $< k <$ 0.2 m). Luckily the dependence of U_{tip} on k is quite weak (power law with an exponent of one sixth) so we take a reasonable, high estimate of $k \approx 0.1$ m, which is consistent with a Manning roughness of $n \approx 0.026$ s m$^{-1/3}$. Taking $L = H \approx 1.0$ km and substituting these values into Equation (4.37) then yields a (maximum) estimate of

$U_{max} = 1.8$ m/s. The dependence on L is also weak so that with $L = 10$ km, we would have $U_{max} = 2.6$ m/s.

As discussed earlier, our analysis assumes high Reynolds number, ignores bed topography, neglects fracture energy and assumes a lubrication approximation to the neglect of the acceleration term of the full Navier-Stokes equation. We verify that these approximations are reasonable for the Greenland basal crack situation considered here. Taking $U \gtrsim 2$ m/s, $h \gtrsim 0.1$ m (which apply for crack lengths of interest $L \gtrsim 1$ km), $\rho \approx 10^3$ kg/m^3, and viscosity of $\mu \approx 2 \cdot 10^{-3}$ Pa s, then $\Re \gtrsim 10^5$, which puts it in the fully turbulent regime. The hydraulic head gradient is given by $S \approx \Delta p_{in}/(\rho g L) \approx 0.1$ so that bed slopes $\ll 5^\circ$ can be safely ignored. Taking ice fracture toughness of $K_{Ic} \approx 1.6 \cdot 10^5$ Pa m$^{1/2}$ [*Rist et al.*, 1999], we can compare the total energy lost in the pressure gradient (per unit surface area of the crack), $e_{loss} \equiv E_{loss}/Area \approx \Delta p_{in} h \gtrsim 0.9 \cdot 10^5$ J/m^2, with the fracture energy $K_{Ic}^2/E \approx 4.1$ J/m^2. Since the pressure gradient energy loss is much greater than the fracture energy (except at the very earliest stages of crack growth, when $h \lesssim 10^{-5}$ m or equivalently $L \lesssim 0.1$ m), it is reasonable to neglect the fracture energy. This inequality is analogous to the one suggested by *Savitski and Detournay* [2002] and *Bunger and Detournay* [2008] for Newtonian viscous flows; unlike in their analysis, which is for constant inflow rate, our constant Δp_{in} solution has negligible fracture energy during the later stages of crack growth (and is only toughness dominated at the very earliest stages). Finally, $\rho U^2 \lesssim 10^4$ Pa as compared with $\Delta p_{in} \approx 8 \cdot 10^5$ Pa so that the acceleration term of the Navier-Stokes equation ($\partial U/\partial t + U \partial U/\partial x$) can be neglected compared with the pressure gradient term ($\partial p/\partial x$), and thus the lubrication approximation is

reasonable as well.

4.4.1 Approximations for Comparison with Observations

To compare against observations, it is useful to calculate the total volume of water in the crack, the net flow rate into the basal crack and the expected surface displacements. Since the results of Section 4.3 are for a 2D plane-strain fracture in a body without a free surface, whereas the geometry of the observations of *Das et al.* [2008] clearly has three-dimensional structure and a free surface close to the crack, it is not obvious how the previous results can be utilized. In this section, we make use of some approximations that allow calculation of the desired quantities. In Section 4.4.2, we discuss possible improvements to these approximations.

We first discuss how to calculate volumes, flow rates, and surface displacements within our turbulent self-similar solution, which strictly applies only in the range $L \ll H$. In order to allow these results to be generalized from 2D plane strain to a 3D geometry, and later to arbitrary L/H in Section 4.4.2), we find it useful to compare our self-similar solution to the (static) solution for a crack opened by a uniform pressure, taken to be Δp_{in}, over the entire crack face. For this uniform pressure plane strain crack of (instantaneous) length $2L$ in a homogeneous medium, the crack opening profile is given by

$$w_U(x) = \frac{4\Delta p_{in} L}{E'}\sqrt{1-\hat{x}^2}, \tag{4.40}$$

where, as before, $\hat{x} \equiv x/L$ (see e.g. *Tada et al.* [2000]). Approximately accounting for the bimaterial case, as before, the average opening is then given (as a function of

L) by

$$\bar{h}_U = \xi \bar{w}_U = \frac{\xi}{2L} \int_{-L}^{L} w_U(x) dx = \frac{\xi \pi \Delta p_{in} L}{E'}. \tag{4.41}$$

Now, we show that both the volume and flow rate can be expressed in terms of $\bar{h}_U$ and $L(t)$ (which is known from the self-similar solution, Equation (4.36)). Comparing the self-similar openings of Equations (4.38) and (4.39) with the uniform pressure openings of Equation (4.40) and (4.41), we observe that we can write

$$h(x) = \frac{\bar{h}_U}{\pi} \hat{w}(\hat{x}), \tag{4.42}$$

and

$$h_{avg} = C_1 \bar{h}_U \tag{4.43}$$

where C_1 is given by $C_1 = 1.859/\pi = 0.592$. We can then express the 2D crack volume V_{2D} as

$$V_{2D}(t) = 2h_{avg}(t) \cdot L(t) = 2C_1 \bar{h}_U(t) L(t), \tag{4.44}$$

where $\bar{h}_U$ is given as a function of L in Equation (4.41). Similarly, the 2D flow rate Q_{2D} is given by

$$Q_{2D} = \frac{dV_{2D}}{dt} = 2C_1 \frac{d(\bar{h}_U L)}{dL} \cdot \frac{dL}{dt} = 2C_1 \frac{d(\bar{h}_U L)}{dL} \cdot U_{tip}. \tag{4.45}$$

Without modification, the $\bar{h}_U$ of Equation (4.41) substituted into Equation (4.45) gives $d(\bar{h}_U L)/dL = 2\bar{h}_U$ and thus $Q_{2D} = 4\bar{h}_U U_{tip}$. Furthermore, the self-similar solution for U_{tip} (Equation (4.37)) can be rewritten in terms of $\bar{h}_U$ by substituting $\Delta p_{in}/E' = \bar{h}_U/(\xi \pi L)$ such that

$$U_{tip} = C_2 \sqrt{\frac{\Delta p_{in}}{\rho}} \left(\frac{\bar{h}_U}{L}\right)^{2/3} \left(\frac{L}{k}\right)^{1/6}, \tag{4.46}$$

with

$$C_2 = \frac{(6/5)^{1/6}\phi}{(\xi\pi)^{2/3}} = \frac{2D^{7/6}}{(7f_0)^{1/2}(\pi\delta)^{2/3}} \approx 3.571. \tag{4.47}$$

Thus, for a given L, we can calculate $\bar{h}_U$ through Equation (4.41), and then calculate V_{2D} through Equation (4.44) and Q_{2D} through Equation (4.45).

Before calculating surface displacements, we note that the vertical crack (moulin) system connecting the surface to the basal crack likely contributes to both the volume of water stored as well as surface displacements. To estimate these quantities for the vertical connecting crack, we approximate this additional crack as being a plane stress center crack of length $2a$ in a homogeneous body, opened by a uniform pressure equal to the depth-averaged pressure in excess of hydrostatic ice pressure (see Figure 4.8). This approximation is only valid if stresses in the solid (ice) are close to hydrostatic and may not be accurate if the region has high extensional or compressional horizontal stresses. Furthermore, this plane stress crack will only be opened significantly if basal shear stresses are low, suggesting that $a < L$ (where we anticipate the 3D geometry of the basal crack as being close to circular, as will be suggested below). With these caveats, this elliptically shaped connecting crack then has volume given by

$$V_c = \pi a u_0 H_w = \frac{2\pi\Delta p_{avg} a^2 H_w}{E} \tag{4.48}$$

where $2u_0$ is the crack center opening, and $\Delta p_{avg} \approx \Delta p_{in}/2$ is taken as the depth-averaged pressure in excess of the local hydrostatic pressure. Contribution to flow rate is calculated, as above, to be

$$Q_c = \frac{dV_c}{dt} = \frac{dV_c}{da} \cdot \frac{da}{dt} = \frac{4\pi\Delta p_{avg} a H_w}{E} \cdot \frac{da}{dt}. \tag{4.49}$$

We now calculate model vertical and horizontal surface displacements based on

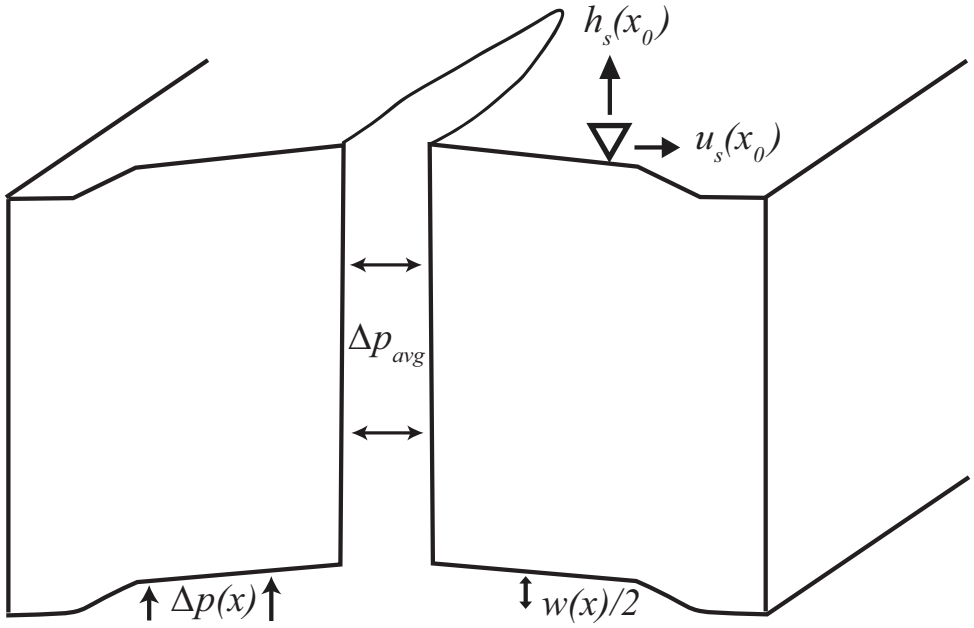

Figure 4.8: Schematic of surface displacements at a distance x_0 from the center of the connecting conduit. As discussed in the text, the vertical displacement is calculated using Equation (4.53), and the horizontal displacement is approximated with Equation (4.59) as being due to an average pressure Δp_{avg} along the connecting conduit face.

the basal plane strain self-similar crack solution and the approximate plane stress connecting crack. First, the vertical surface displacements (uplift) due to both cracks are easily calculated using the reciprocal theorem and the Boussinesq-Flamant line-source solution (see e.g. *Timoshenko and Goodier* [1987]). The result, e.g. as in the Appendix of *Walsh and Rice* [1979], is that the vertical surface uplift h_s in a homogeneous half-space due to a vertical displacement w^* of a horizontal surface is

$$h_s = \int_{surf} \sigma^*_{zz} w^* dx, \tag{4.50}$$

where σ^*_{zz} is given by

$$\sigma^*_{zz} = \frac{2}{\pi} \cdot \frac{(z - z_0)^3}{[(x - x_0)^2 + (z - z_0)^2]^2}, \tag{4.51}$$

and (x_0,z_0) is the uplift location. Applying this to the basal crack, and utilizing the bimaterial approximation for the displacement of the top side of the crack, $w^* \approx w(x)/2$ (see Appendix B), then

$$h_s(x_0) = \int_{-L}^{L} \frac{1}{\pi} \cdot \frac{H^3 w(x)}{[(x - x_0)^2 + H^2]^2} dx, \tag{4.52}$$

where variables are as before ($h(x) = \xi w(x)$ is the crack opening). Putting this into non-dimensional form and substituting Equation (4.42) for $\xi w(x)$, we obtain

$$h_s(x_0) = \frac{H^3 \bar{h}_U}{\xi \pi^2 L^3} \int_{-1}^{1} \frac{\hat{w}(\hat{x}) d\hat{x}}{[(\hat{x} - \hat{x}_0)^2 + \hat{H}^2]^2}, \tag{4.53}$$

where $\hat{H} \equiv H/L(t)$, $\hat{x}_0 = x_0/L(t)$, $\hat{w}(\hat{x})$ is the scaled self-similar opening given in Equation (4.27), and other variables are as before. Thus, given a surface location x_0 (relative to the crack inlet at $x = 0$ and in the plane of crack growth) and crack length $L(t)$, Equation (4.53) gives h_s in terms of our self-similar solution.

We can similarly account for the vertical displacement due to the horizontal opening of the vertical crack, and as shown below find that this contribution is negligible. Again as in *Walsh and Rice* [1979], the contribution due to the vertical crack's horizontal displacement u^* is

$$h_s^V = \int_{surf} \sigma_{xx}^* u^* dz, \tag{4.54}$$

where σ_{xx}^* is given by

$$\sigma_{xx}^* = \frac{2}{\pi} \cdot \frac{(x - x_0)^2 (z - z_0)}{[(x - x_0)^2 + (z - z_0)^2]^2}. \tag{4.55}$$

Applying this to the vertical crack then

$$h_s^V(x_0) = \int_0^H \frac{2x_0^2 z u^*(z) dz}{\pi (x_0^2 + z^2)^2}. \tag{4.56}$$

Noting that for the observations of *Das et al.* [2008], $x_0/H \approx 1.7$ then this contribution to h_s is bounded by

$$h_s^V(x_0) \leq \int_0^1 \frac{2 \cdot 1.7^2 \cdot \hat{z} d\hat{z}}{\pi (1.7^2 + \hat{z}^2)^2} \cdot \max[u^*] = 0.08 \max[u^*]. \tag{4.57}$$

Since $\max[u^*]$ is expected to be of similar (or smaller) magnitude to w^*, the contribution h_s^V is thus expected to be an order of magnitude less than that due to the basal crack opening, and we therefore neglect this contribution.

For horizontal surface displacements, we similarly expect an order of magnitude smaller contribution from vertical opening of the basal crack compared to horizontal opening of the (vertical) connecting crack, and hence ignore this former contribution. The horizontal displacement at a distance x_0 perpendicular to the center of the plane stress center crack (see Figure 4.8) can be obtained by integrating the results of *Tada et al.* [2000] as follows. *Tada et al.* [2000] provides the displacement at x_0 due to a

pair of point forces of amplitude P_1 to be

$$u_{P1}(x_0) = \frac{4P_1}{\pi E}\left[\tanh^{-1}\sqrt{\frac{a^2-b^2}{a^2+x_0^2}} + \frac{1+\nu}{2}\cdot\frac{x_0^2}{b^2+x_0^2}\sqrt{\frac{a^2-b^2}{a^2+x_0^2}}\right], \tag{4.58}$$

where b is the distance from the center of the crack of the pair of forces. Integrating this expression over the crack face ($0 \le b \le a$) gives the corresponding expression, due to a constant pressure Δp_{avg} along the crack, of

$$\begin{aligned} u_s(x_0) = \frac{2\Delta p_{avg} a}{E}\Bigg[&\sqrt{1+(x_0/a)^2} - (x_0/a) \\ &+\frac{1+\nu}{2}(x_0/a)\Big(1 - \frac{x_0/a}{\sqrt{1+(x_0/a)^2}}\Big)\Bigg], \end{aligned} \tag{4.59}$$

which we take as an approximation to the horizontal surface displacement.

Since the previous expressions are for an unrealistic 2D plane strain geometry (for example, true volume is not easily defined for the basal crack), it is useful to generalize this to a 3D geometry. We do this in the following, somewhat ad-hoc manner. First, we note that the 3D crack opening can be expected to be close to circular since a shorter crack length in a particular direction would be more unstable to growth under the same loading conditions. Thus, for this 3D extension, we first consider a (circular) penny-shaped crack of radius L in a homogeneous medium, loaded with uniform pressure Δp_{in} and clamped on the edges. For this uniform loading case, *Sneddon* [1946] gives

$$w_U^{3D}(r) = \frac{8\Delta p_{in} L}{\pi E'}\sqrt{1-\hat{r}^2}, \tag{4.60}$$

where $\hat{r} \equiv r/L$ and r is distance from the center of the crack. Approximately accounting for the bimaterial case, as before, the average opening is then

$$\bar{h}_U^{3D} = \xi \bar{w}_U^{3D} = \frac{\xi}{\pi L^2}\int_0^L 2\pi r w_U^{3D}(r)dr = \frac{16\xi\Delta p_{in} L}{3\pi E'}. \tag{4.61}$$

Comparing the penny-shaped openings of Equation (4.60) and Equation (4.61) with the 2D plane-strain openings of Equation (4.40) with Equation (4.41), we observe that the two constant pressure loading cases have opening displacements with identical functional forms and have average openings that differ by a factor of $16/(3\pi^2) \approx 0.540$. Thus, a plausible ad-hoc procedure that approximately accounts for the 3D penny-shaped geometry in the turbulent flow case is to utilize the same plane strain displacement profile $\hat{w}(\hat{x})$ on the penny-shaped crack $\hat{w}(\hat{r}) = \hat{w}(\hat{x})$ as well as utilize the same scaling factors C_1 and C_2, but replace all instances of $\bar{h}_U$ by $\bar{h}_U^{3D}$ (i.e. in Equations (4.42), (4.43), (4.46), and (4.53)). In this way, we can now calculate a true basal crack volume,

$$V_b = C_1 \pi L^2 \bar{h}_U^{3D}, \tag{4.62}$$

a corresponding flow rate,

$$Q_b = \frac{dV_b}{dt} = \frac{dV_b}{dL} U_{tip}, \tag{4.63}$$

and appropriately scale the vertical displacement (Equation (4.53)) to account for the added stiffness of the 3D geometry. The horizontal displacement of Equation (4.59) is unaffected by this procedure. We note that future work is necessary to check the validity of this scaling procedure since, for example, the constants C_1 and C_2 for a penny-shaped crack could easily be different than those chosen based on the 2D plane-strain solution. We also note that (3D) volumes can be estimated for the plane strain solution by replacing the $\bar{h}_U^{3D}$ of Equation (4.62) with $\bar{h}_U$.

4.4.2 Possible Improvements on the Approximations

As previously mentioned, the results presented are strictly only applicable when $L \ll H$ and when the loss of pressure due to flow from the surface to the base is a small fraction of the pressure in excess of the hydrostatic value. Here, we first find that both of these approximations are of concern. Following these two estimates, we discuss possible approaches to addressing the two problems.

First, we can make an estimate of how large L becomes by equating the volume of water taken up by the basal crack plus vertical crack ($V_b + V_c$) with the initial volume of water in the surface lake (V_0). The initial lake volume was observed to be $V_0 = 4.4 \cdot 10^7$ m^3 [*Das et al.*, 2008], and we calculate the sum of the crack volumes to be

$$V_b(L) + V_c(a) = \pi \frac{\Delta p_{in}}{E} L^3 \left(\frac{16 \xi C_1 (1-\nu^2)}{3\pi} + \frac{a^2 H_w}{L^3} \right). \tag{4.64}$$

Choosing $a = L$ as a plausible upper bound on V_c (as discussed in the next paragraph, which results in a lower bound on L) predicts that $L \gtrsim 5.25$ km is reached and thus suggests that the approximation $L \ll H$ should be revisited.

Second, we estimate the pressure loss from turbulent flow en route to the bed by applying the turbulent Manning-Strickler scaling of Equation (4.6) with each term estimated for flow through the vertical crack. As in our earlier plane stress calculation for this vertical crack, we assume a depth-averaged value of excess pressure $\Delta p_{in}/2$ opening the crack, giving a cross-sectionally averaged opening of $2u_{avg} \equiv \pi u_s(0)/2 \approx \pi \Delta p_{in} a / 2E$. We expect that a lies in the range $0.1 \lesssim a/L < 1$ since significant opening will only occur over the region with minimal basal shear stress to counteract the excess pressure (i.e. $a < L$) but for $a \ll L$ the excess pressure should encourage a to grow (i.e.

$a \gtrsim 0.1L$). Taking $L \approx 3$ km and $a/L \approx 0.8$ as plausibly representative, then $2u_{avg} \approx$ 0.48 m. The average fluid velocity through this vertical crack U_{vert} can be estimated by equating the volumetric flow rate in the vertical crack $\pi a u_s(0) U_{vert} = 4 a u_{avg} U_{vert}$ to the volumetric flow rate into the basal crack $dV_b/dt \equiv dV_b/dL \cdot U_{tip}$ (where V_b is given by Equation (4.62)). Using the procedures of Section 4.4.1, we estimate dV_b/dt using $\bar{h}_U^{3D}$, which gives $U_{tip} \approx 1.4$ m/s and therefore $dV_b/dt \approx 8.5 \cdot 10^3$ m^3/s. Using these values, then $U_{vert} \approx 3.7$ m/s and the loss of pressure in excess of hydrostatic through the connecting conduit would be

$$\Delta p_{loss} = \frac{0.0357 \rho U_{vert}^2 k^{1/3} H}{(2u_{avg})^{4/3}} \approx 0.58 \text{ MPa}, \tag{4.65}$$

which is a large fraction (67%) of the maximum excess pressure of 0.87 MPa, and is a higher fraction when L is smaller. Any sinuosity in the path from the surface to the base, or a smaller value of a/L, would also increase this pressure head loss. Thus, both the $L \ll H$ approximation and the approximation of no loss of excess pressure at the basal inlet are of concern.

In this first attempt to predict observed measurements, we take two parallel approaches to addressing the problem of not satisfying $L \ll H$. In the first, we simply apply our previous model results in all regimes of L/H, despite L growing significantly larger than H. This is done in the hope that the weak dependence of Equation (4.37) on L lends some credibility to using the $L \ll H$ solution beyond its known range of usability. In a second approach, we attempt to approximately account for the range beyond $L \ll H$ by matching our solution with a plate theory (beam theory) scaling applicable in the limit $L \gg H$. For this latter approach, we again find it convenient to compare with the constant loading case, this time of uniform pressure Δp_{in} over

a penny-shaped plate of radius L clamped on the edges. For this case, *Timoshenko and Woinowsky-Krieger* [1959] gives

$$h_U^P(r) = \frac{3\Delta p_{in} L^4}{16 E' H^3}(1-\hat{r}^2)^2, \tag{4.66}$$

where, as before, $\hat{r} = r/L$. The average opening is then

$$\bar{h}_U^P = \frac{1}{16} \cdot \frac{\Delta p_{in} L}{E'} \cdot \frac{L^3}{H^3}. \tag{4.67}$$

Comparing Equation (4.67) for $\bar{h}_U^P$, which applies when $L \gg H$, with Equation (4.61) for $\bar{h}_U^{3D}$, which applies when $L \ll H$, we suggest a summed version of $\bar{h}_U$ (the average opening under uniform pressure) defined by

$$\bar{h}_U^S \equiv \bar{h}_U^{3D} + \bar{h}_U^P = \frac{16\xi \Delta p_{in} L}{3\pi E'} \left[1 + \frac{3\pi}{256\xi} \cdot \frac{L^3}{H^3}\right]. \tag{4.68}$$

This summed approximation asymptotically satisfies both solutions in the appropriate limits and defines a smooth transition between them. The validity of this 'linear sum' transition is unknown and unfortunately untestable within the scope of the current work, but we hope to address the validity of this approximation in future work. If the transition is strongly non-linear, with transition occurring at much larger L/H than in Equation (4.68), the first approach to addressing this problem would be more appropriate. However, with this definition of $\bar{h}_U^S$, we can invoke a similar procedure as was suggested in Section 4.4.1 and simply replace $\bar{h}_U$ with $\bar{h}_U^S$ in all expressions (Equations (4.42), (4.43), (4.46), (4.53), and (4.62)), and otherwise use the same self-similar solution. We note that the form of the displacement profile is not expected to stay the same but, as we have no other plausible solution to rely on, we use the same displacement profile and assume that the primary effect of including plate theory

is the scaling accounted for by $\bar{h}_U^S$. It can also be noted that the eventual strong dependence of $\bar{h}_U^S$ on L (to the 4th power) implies very large vertical displacements for moderately large values of L in this model. See Figure 4.9 for a comparison of vertical displacements calculated for the 3 different choices $\bar{h}_U$, $\bar{h}_U^{3D}$ and $\bar{h}_U^S$ (with numerical values chosen as in Section 4.4).

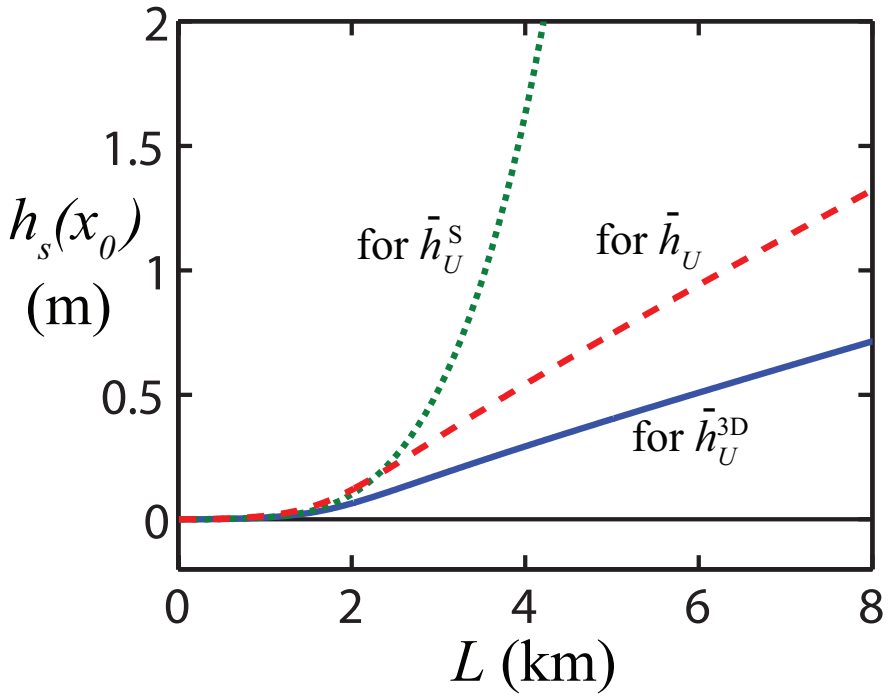

Figure 4.9: Crack displacements at $x_0 = 1.7$ km for the 3 different choices $\bar{h}_U$ (red dashed line, 2D plane strain), $\bar{h}_U^{3D}$ (blue solid line, 3D penny-shaped without plate corrections) and $\bar{h}_U^S$ (green dotted line, 3D with approximate plate corrections). For this plot, χ is assumed to be 1 so that $\Delta p_{in} \approx 0.87$ MPa.

To account for pressure loss in the connecting conduit, we no longer set $\Delta p_{in} = \Delta p_{static}$ but instead let $\Delta p_{in} \equiv \chi \Delta p_{static}$, where $0 \leq \chi \leq 1$. We then solve for the unknowns χ and U_{vert} (average fluid velocity in the vertical crack) by equating the

excess pressures at the juncture between the vertical crack and the basal crack inlet, and similarly equating the volumetric flow rates there. We use the same turbulent scaling as was used in Equation (4.65), noting again that this depth-averaged, lumped-parameter treatment of flow in the vertical crack is a crude approximation to the true situation. With this caveat, the first equality is satisfied by

$$(1-\chi)\Delta p_{static} = \frac{0.0357\rho U_{vert}^2 k^{1/3} H}{(\pi a \chi \Delta p_{static}/2E)^{4/3}}, \tag{4.69}$$

where $\chi\Delta p_{static}$ has replaced Δp_{in}. The second (flow rate) equality is satisfied (as also discussed prior to Equation (4.65)) by setting

$$4au_{avg}U_{vert} = \frac{\pi a^2 \Delta p_{static} U_{vert} \cdot \chi}{E} = \frac{dV_b}{dt} = \frac{dV_b}{dL}U_{tip}, \tag{4.70}$$

where U_{tip} is given by Equation (4.46) and dV_b/dL is calculated as

$$\frac{dV_b}{dL} = C_1 \pi \frac{d(L^2 \bar{h}_U)}{dL}. \tag{4.71}$$

$\bar{h}_U$ in both Equation (4.46) and (4.71) is one of the three choices $\bar{h}_U$, $\bar{h}_U^{3D}$ or $\bar{h}_U^S$ depending on whether one wants to calculate quantities based on the 2D plane strain displacements, the 3D penny-shaped displacements without plate corrections, or the 3D displacements with plate corrections. For example, using $\bar{h}_U^{3D}$ in Equation (4.46) gives

$$U_{tip} = C_2 \sqrt{\frac{\Delta p_{static}}{\rho}} \left(\frac{16\xi\Delta p_{static}}{3\pi E'}\right)^{2/3} \left(\frac{L}{k}\right)^{1/6} \chi^{7/6} \tag{4.72}$$

(where the exponent of 7/6 on χ comes from $1/2 + 2/3$). Similarly, using $\bar{h}_U^{3D}$ in Equation (4.71) gives

$$\frac{dV_b}{dL} = \frac{16 C_1 \xi \Delta p_{static}}{3E'} \frac{d(\chi L^3)}{dL} = \frac{16 C_1 \xi \Delta p_{static}}{E'} \cdot \chi L^2 (1 + \frac{L}{3\chi}\frac{d\chi}{dL}), \tag{4.73}$$

where it will be shown that the $d\chi/dL$ term can be safely ignored compared with the other term (this is also true for the $\bar{h}_U$ model, but not for the $\bar{h}_U^S$ model). Using these expressions in Equation (4.70), and solving for U_{vert} gives

$$U_{vert} = 4.83\sqrt{\frac{\Delta p_{static}}{\rho}}\left(\frac{\Delta p_{static}}{E}\right)^{2/3}\left(\frac{L}{k}\right)^{1/6}\left(\frac{L}{a}\right)^{2}\cdot\chi^{7/6} \tag{4.74}$$

Substituting U_{vert} into Equation (4.69), and ignoring the $d\chi/dL$ term, allows us to solve algebraically for χ in terms of known quantities (and given L and a). Using values from Section 4.4, then

$$\chi = \frac{(a/L)^{16/3}\cdot(L/H)}{0.456 + (a/L)^{16/3}\cdot(L/H)}. \tag{4.75}$$

Explicitly calculating $d\chi/dL$ with this solution, we find that $(L/3\chi)d\chi/dL \leq 1/3$ regardless of L, and thus small compared to 1, which validates ignoring that contribution in Equation (4.73). If we had used $\bar{h}_U$ (2D plane strain) instead of $\bar{h}_U^{3D}$, Equation (4.75) would have a numerical factor of 3.55 instead of 0.456, while not changing the rest of the expression. If we had instead used $\bar{h}_U^S$ (including approximate plate bending) instead of $\bar{h}_U^{3D}$ to calculate χ, then we can no longer ignore the $d\chi/dL$ term and instead must numerically solve the differential equation to find $\chi(L)$. The χ for these three cases are plotted in Figure 4.10abc for a few different plausible choices of a/L. For the $\bar{h}_U^S$ model (including approximate plate bending), the strong dependence of U_{tip} on L implies the fast asymptote of $\chi \to 0$ as L grows.

Finally, in the late stages of crack growth, when the surface lake is gone but there remains excess water pressure driving the basal crack open (with height of liquid water H_w now below the surface height of the glacier H), we assume that the crack system continues to grow while conserving the total water volume in the basal crack plus

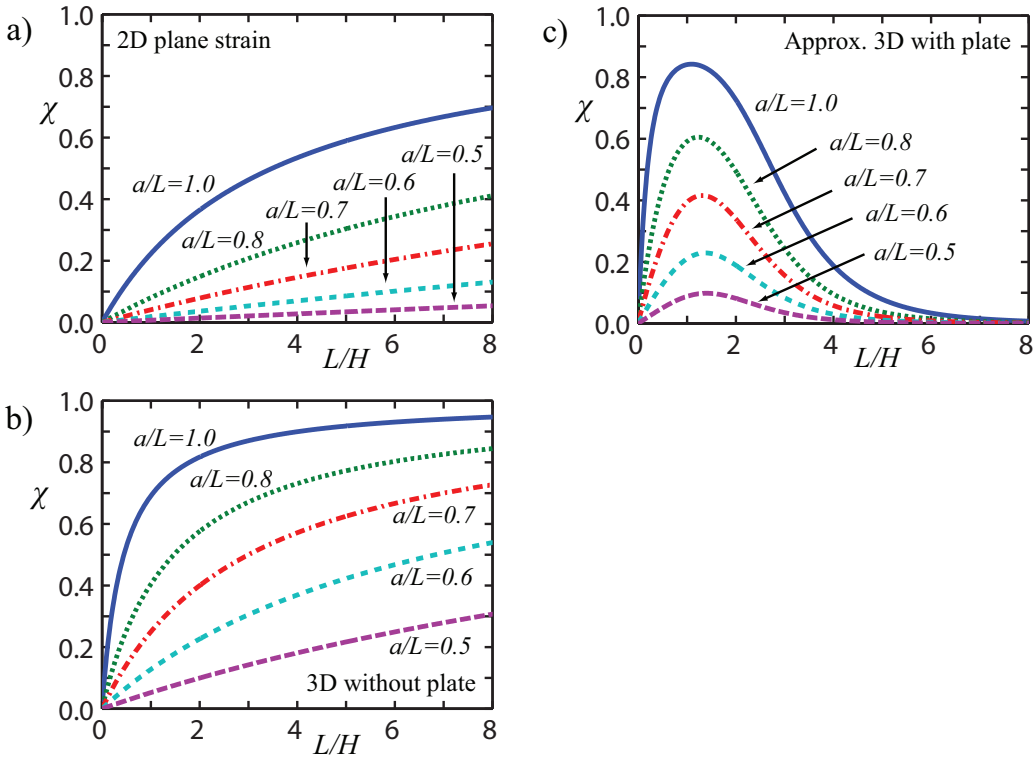

Figure 4.10: χ as a function of L (in km) for a range of plausible a/L. (a) For model with $\bar{h}_U$ (2D plane strain). As shown, $\chi \to 0$ as $L/H \to 0$ and $\chi \to 1$ as $L/H \to \infty$. (b) For model with $\bar{h}_U^{3D}$ (3D without plate). Again, $\chi \to 0$ as $L/H \to 0$ and $\chi \to 1$ as $L/H \to \infty$. (c) For model with $\bar{h}_U^{S}$ (approximate 3D with plate). These curves of case (c) asymptote to the corresponding curves shown in (b) when $L/H \to 0$. In all panels, solid blue is for $a/L = 1.0$, dotted green is for $a/L = 0.8$, dash-dotted red is for $a/L = 0.7$, short-dashed cyan is for $a/L = 0.6$ and long-dashed purple is for $a/L = 0.5$.

vertical crack. We now find it convenient to separate the contributions to pressure loss into a hydrostatic component due to $H_w < H$ such that $\Delta p_{hy} \equiv \chi_w \Delta p_{static}$ in hydrostatic equilibrium, and a fractional dynamic component on top of this such that $\Delta p_{in} \equiv \chi \Delta p_{hy} \equiv \chi \cdot \chi_w \Delta p_{static}$. H_w and χ_w can easily be related by expressing hydrostatic balance in terms of H_w, which yields

$$\frac{H_w}{H} = \frac{\rho_{ice}}{\rho} + \frac{\rho - \rho_{ice}}{\rho}\chi_w. \tag{4.76}$$

As expected, when $\chi_w \to 1$, $H_w \to H$ and when $\chi_w \to 0$, $H_w \to 0.91H$. Since the geometric changes in H_w/H are small compared to the effects of χ_w on Δp_{in}, we continue to approximate $H_w \approx H$ when it enters equations geometrically. With this approximation, we then find that χ is still determined by Equation (4.75). Maintaining $V_b + V_c = V_0$ (using Equation (4.64) implemented with $\bar{h}_U^{3D}$) then determines $\chi_0 \equiv \chi\chi_w$ to be

$$\chi_0 = \frac{EV_0}{\pi \Delta p_{static} L^3} \cdot \frac{L/H}{0.503L/H + (a/L)^2}. \tag{4.77}$$

Thus, $\Delta p_{in}/\Delta p_{static} \equiv \chi_0$ is again determined algebraically as a function of L (and a/L) during the late stages of basal crack growth.

4.4.3 Comparison of Model Results with Greenland Observations

We now compare our model results for crack growth, surface displacements, and corresponding surface-lake water-level time series with the recent observations of rapid surface-lake drainage in Greenland by *Das et al.* [2008]. All displacements plotted are for the observation site at the surface and roughly 1.7 km removed from the center

of the connecting conduit ($x_0 = 1.7$ km).

The surface displacements used are those calculated by the Boussinesq-Flamant solution of Equation (4.53) for the vertical uplift (as a function of L) and by the plane stress approximation of Equation (4.59) for horizontal displacement (as a function of a). In Equation (4.53), we use either $\bar{h}_U$, $\bar{h}_U^{3D}$ or $\bar{h}_U^S$ as discussed in Section 4.4.2, giving us solutions for a 2D plane strain model, a 3D penny-shaped model without plate corrections, and a 3D model with plate corrections (respectively). In Figures 4.11 and 4.12, we plot vertical and horizontal displacements at $x_0 = 1.7$ km as a function of L (including the effect of χ) for various choices of a/L. The strong (negative power) dependence of χ on L for the $\bar{h}_U^S$ model implies very small basal excess pressures ($\Delta p_{in} = \chi \Delta p_{static}$) and hence small horizontal displacements (as shown in Figure 4.12) for large values of L, and therefore cannot achieve the meter-scale displacements observed [*Das et al.*, 2008]. The very low values of χ attained also imply very low fluid velocities in the basal crack, which eventually leave the turbulent regime that this work is based upon. Thus, this model that includes plate corrections may not be realistic and this should be kept in mind when interpreting the results for this case. Another reason for this unrealistic behavior may be the assumption of a mathematical crack that closes completely under zero excess pressure Δp_{in}, whereas a realistic rough crack would not have complete closure to flow even with $\Delta p_{in} = 0$.

The observed horizontal displacements (with a maximum of about 0.8 m) are approximately 25% smaller than the observed vertical displacements (with a maximum of about 1.1 m) [*Das et al.*, 2008], and this general behavior is achieved for a range of plausible a/L in both the plane strain ($\bar{h}_U$) and 3D penny-shaped ($\bar{h}_U^{3D}$) models

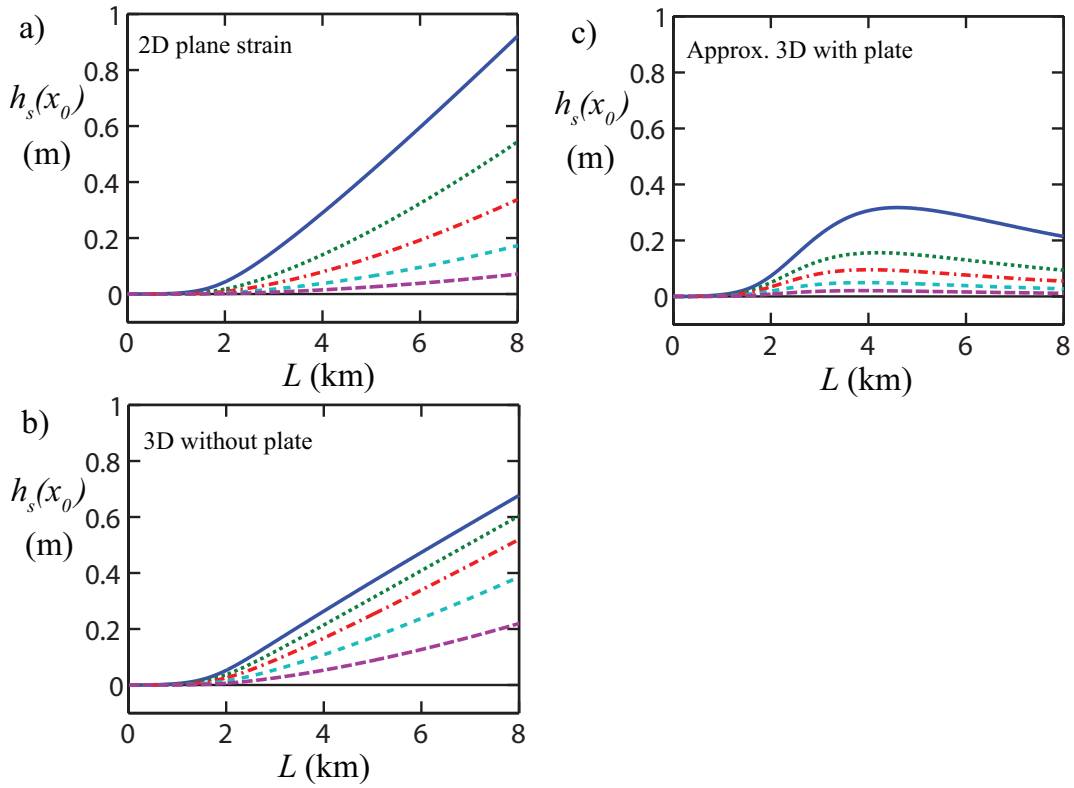

Figure 4.11: Vertical displacements at $x_0 = 1.7$ km as a function of L for a range of a/L. All line styles and colors are as in Figure 4.10. (a) For 2D model with $\bar{h}_U$. (b) For 3D model with $\bar{h}_U^{3D}$. (c) For approximate 3D-plate model with $\bar{h}_U^{S}$.

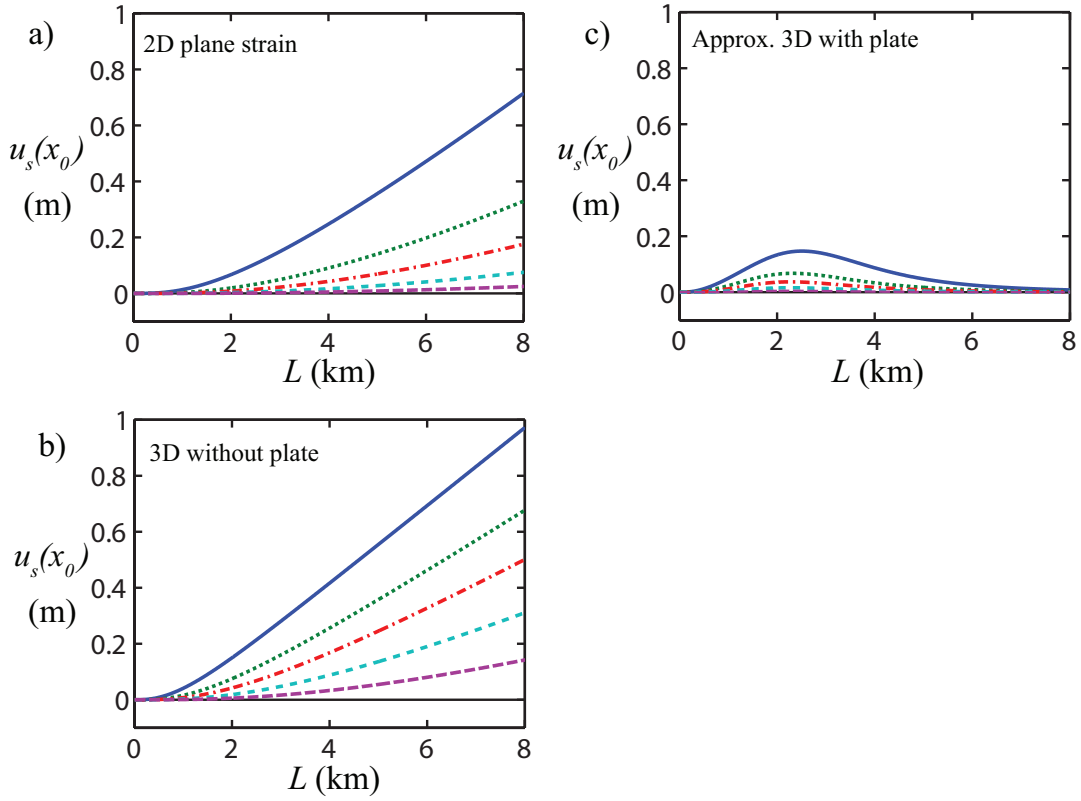

Figure 4.12: Horizontal displacements at $x_0 = 1.7$ km as a function of L for a range of a/L. All line styles and colors are as in Figure 4.10. (a) For 2D model with $\bar{h}_U$. (b) For 3D model with $\bar{h}_U^{3D}$. (c) For approximate 3D-plate model with $\bar{h}_U^S$. It should be noted that none of the horizontal displacements in the $\bar{h}_U^S$ model exceed 0.2 m whereas the observations do, suggesting that this model cannot accurately match observations.

(e.g. compare the displacements of Figure 4.11 with those of Figure 4.12). In the plane strain model, $0.8 \lesssim a/L \lesssim 1.0$ approximately satisfy this condition. In the 3D model (without the plate), $0.5 \lesssim a/L \lesssim 0.7$ approximately satisfy this condition. For the approximate 3D-plate model, no range of a/L yields comparable behavior, but higher values ($a/L \gtrsim 0.8$) agree better. For the results shown below, we choose $a/L = 1.0$ for the plane strain model, $a/L = 0.6$ for the 3D model, and $a/L = 1.0$ for the approximate 3D-plate model. We note that we expect a/L to remain roughly constant throughout crack growth since the size of the basal crack is the limiting factor on the growth of the vertical connecting conduit.

In our model, given the basal crack length L at a given time, we can calculate the basal crack growth rate $dL/dt \equiv U_{tip}$ from Equation (4.46), the basal crack input pressure $\Delta p_{in} = \chi \Delta p_{static}$ from Equations (4.75) and (4.77), the crack volumes from Equation (4.64), and the surface displacements from Equations (4.53) and (4.59). Using the instantaneous $dL/dt = U_{tip}$ to step forward in time (i.e. assuming quasistatic crack growth), we can therefore integrate in time to obtain $L(t)$ given only knowledge about the initial lake volume and an initial small crack length L_0. If we also assume a lake geometry, we can additionally calculate the drop in water level in the surface lake (and vertical crack) by equating lake water volume loss to the water volume stored in the crack system (Equation (4.64)). Thus, for model input, we take the initial lake volume of $V_0 = 4.4 \cdot 10^7$ m^3, initial lake area of $A_0 = 5.6 \cdot 10^6$ m^2 [*Das et al.*, 2008], and assume the lake to have a paraboloid shape. We do not model the very end of the drainage event, when we expect water in the basal crack to drain into the subglacial hydraulic system and eventually result in zero net displacement.

The decrease of $\chi_0 \to 0$ at these late times also implies much lower fluid velocities, which eventually no longer satisfy the fully turbulent ($\Re \gtrsim 10^5$) approximation used throughout this work.

The model results for the plane strain model (using $\bar{h}_U$), the 3D model (using $\bar{h}_U^{3D}$) and the approximate 3D-plate model (using $\bar{h}_U^S$) are shown in Figures 4.13 and 4.14 as a function of time. Figure 4.13a shows the crack length $L(t)$, the total volume in the basal crack plus vertical crack $V_b(L(t)) + V_c(a(t))$, and the water level in the lake $W_L(t)$. As discussed earlier, the volume is capped at V_0, after which crack growth changes from using the χ of Equation (4.75) to that of Equation (4.77) and is responsible for the inflection points in L and W_L as V_0 is reached. When the lake is empty, W_L refers to the remaining water level in the vertical crack ($H_w - H$). Note that the quantities are plotted in different units so as to fit on the same graph. In Figure 4.13b is a comparison of the modeled W_L of Figure 4.13a with the observed W_L of *Das et al.* [2008]. Since the model starting time is arbitrary, we have adjusted the observation times so that the water level begins to drop around $t = 0$. As shown, the 3D penny-shaped model (implemented with $\bar{h}_U^{3D}$) matches the observed W_L fairly well whereas the 2D model (implemented with $\bar{h}_U$) is about 30% too fast, and the approximate 3D-plate model (implemented with $\bar{h}_U^S$) initially matches the observed W_L but then becomes worse as the plate terms have larger contributions ($L \gtrsim H$). Figure 4.14a shows the vertical and horizontal displacements of the same models. The cusps occur when the volume $V_b + V_c$ reaches V_0. In Figure 4.14b, we compare the modeled displacements with the observed displacements of *Das et al.* [2008]. As shown, the 3D model again captures the timescale relatively well while predicting

amplitudes a factor of 3 too small, whereas the 2D model is again about 30% too fast and predicts amplitudes slightly better, and the approximate 3D-plate model does not predict timescales or amplitudes well. We reiterate that this approximate 3D-plate model may not capture the transition from $L \ll H$ to $L \gg H$ in a realistic way, and further work should be done to test the validity of the approximation.

Displacements in the along-flow direction are not modeled explicitly, but our model predicts complete loss of basal resistance over the basal crack area while the basal crack is in existence and is thus consistent with the observed increase in steady flow towards the Greenland coast during the transient basal crack lifetime. If we take $L \approx 10$ km as the maximum basal crack length, which is achieved long after the peak displacements occur (see Figures 4.13 and 4.14), and take the initial average basal shear stress to be $\tau_{b0} \approx 10^5$ Pa [*Bamber et al.*, 2001] then the loss of basal shear force would be approximately $3 \cdot 10^{13}$ N. This loss of basal shear force could plausibly account for the observed factor of 3 increase in background flow velocities for the day following the observed drainage [*Das et al.*, 2008]. Although also not explicitly modeled, we expect seismicity when strain rates are high and therefore over the full timescale of basal crack growth, not just the timescale of initial lake drainage, which is consistent with the observed seismicity [*Das et al.*, 2008].

4.4.4 Complications in Comparison with Greenland Observations

In the preceding sections, a very simplified approach was taken in which we considered the approximate elastic response of ice coupled to the turbulent flow of water

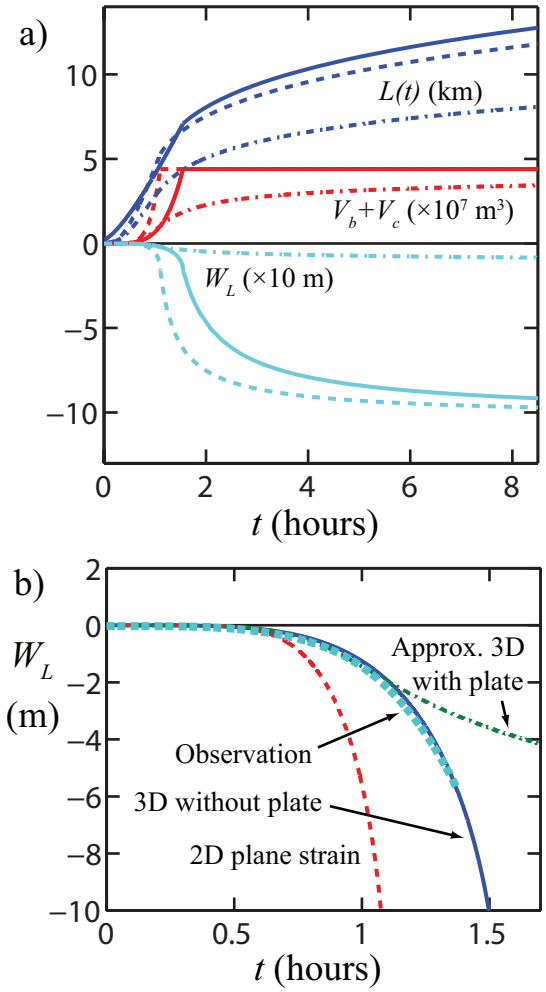

Figure 4.13: (a) Modeled basal crack length $L(t)$, total crack system volume $V_b + V_c$ and water level W_L for the 2D, 3D, and approximate 3D-plate models. Solid lines denote the 3D model (without plate) results, the dashed lines denote the 2D plane strain results, and the dashed-dotted lines denote the approximate 3D-plate model. The colors, as labeled, are for $L(t)$ (blue), V_b+V_c (red), and W_L (cyan, below the zero line). (b) Modeled W_L compared against the observed W_L. The red dashed line is the 2D prediction, the blue solid line is the 3D prediction, the green dashed-dotted line is the approximate 3D-plate prediction, and the thick cyan dotted line is the observed W_L. The observation times have been shifted so that the water level begins to drop around $t = 0$.

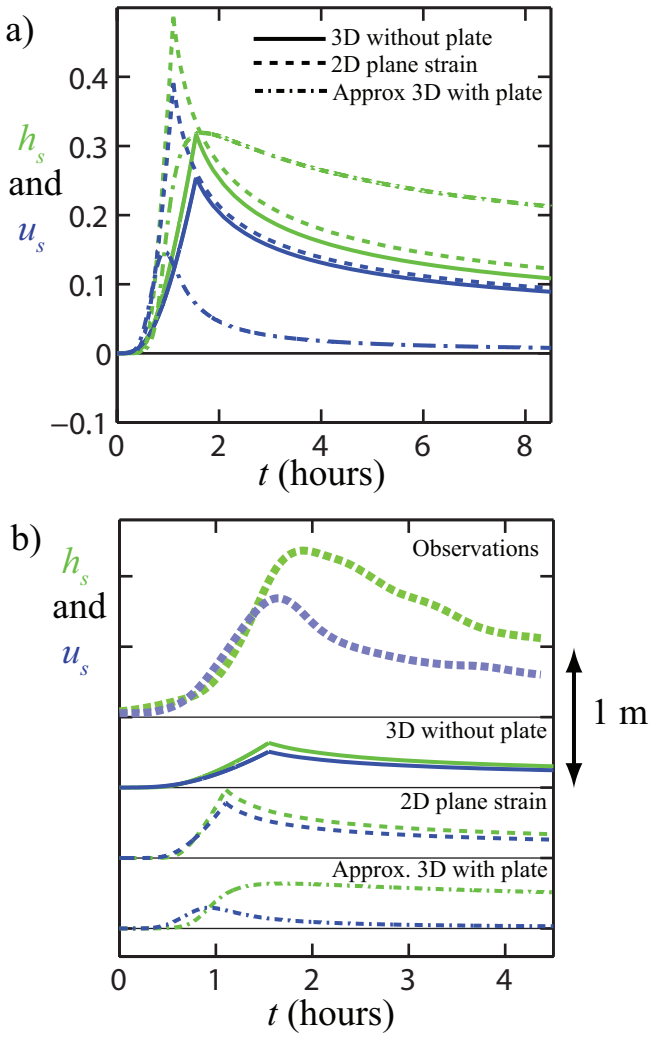

Figure 4.14: (a) Modeled vertical displacements h_s and horizontal displacements u_s for the 2D, 3D, and approximate 3D-plate models. Solid lines denote the 3D model (without plate) results, the dashed lines denote the 2D plane strain results, and the dashed-dotted lines denote the approximate 3D-plate results. The colors, as labeled, refer to vertical (green) and horizontal (blue) displacements. (b) Modeled h_s and u_s compared against the observed quantities (thick dotted curves). Here, the curves are offset (by 0.5 m) for clarity. The colors are the same as in panel (a).

through a connecting and basal crack. In this analysis, a large number of complicating factors were ignored and here we comment on some of the perhaps more important of these issues.

As discussed above, although we use them outside the known range of applicability, the self-similar results strictly apply only when $L \ll H$. Our attempt at modifying the solution to approximately account for plate theory corrections when $L \gtrsim H$ did not successfully predict observations better than the models without a plate term added. However, since the true mechanics is more complex than the approximate corrections suggested, it would be useful to account for this more properly and hence obtain a solution that is accurate in all regimes of L/H. It may be possible to construct such a solution using the bimaterial crack approach of *Hutchinson and Suo* [1992] or the matched asymptotic approach of *Bunger and Detournay* [2002]. We leave this important problem for future work.

Perhaps the next most significant simplification is that of an elastic ice medium. It is well known that glacier ice displays viscous properties (e.g. *Paterson* [2002]; *Hooke* [2005]) and should be modeled as a viscoelastic material on timescales close to the Maxwell time (ratio of effective viscosity to elastic stiffness) for glacier ice, which is plausibly in the hour to few hours range (e.g. *Tsai et al.* [2008]). The fact that the full timescale of interest (a few hours) may be longer than the Maxwell time suggests that the analysis described here is not completely realistic, and may explain why our predicted displacements are smaller than observed (as there would be added viscous strains on top of the elastic strains calculated). This shortcoming of the model is a serious one that we hope to deal with in future work. Nevertheless, the fact that the

Maxwell time is not vastly shorter than the process timescale and that there is rough agreement between model and observation suggests that there is merit to the fully elastic approximation. The elastic approximation should, in any event, be valid near the moving rupture front where the time scale of substantial stress changes is much shorter.

In addition to not accounting for viscous effects, the only fractures accounted for are those of the vertical connecting crack and the basal crack. In reality, numerous small fractures might be expected to open and close as the ice deforms, both due to brittle straining (e.g. *Schulson* [2001]) and due to small-scale hydrofracturing (during crack growth). For example, the positive excess pressures over most of the basal crack favor small scale hydrofracturing upwards into the ice, whereas the strongly negative pressure near the crack tips should encourage the opening of nearby horizontal fractures. The small upwards hydrofractures would be more likely where the largest extensional stresses are. Both small-scale hydrofracturing and brittle straining would contribute to effectively large-scale viscous deformation and would have associated seismicity. This would be consistent with the observed seismicity [*Das et al.*, 2008] and therefore would be useful to have explicitly accounted for in future work. Moreover, this work assumes all of the lake water drains into the two large cracks, without leaking off into any conduits or other hydraulic network. As commented on previously, this is not expected to be a good approximation at the end of drainage. It also may not be a good approximation if there exist large conduits surrounding the crack system prior to the rapid drainage, or if there are layers of weak englacial ice which water could infiltrate.

We also do not account for entrainment of any significant amounts of till or ice fragments in the basal flow channel, which may have an effect on the form of the fluid resistance, Equation (4.1) (see e.g. *Roberts* [2005]). Using the Shields criterion (see e.g. *Buffington* [1999]) to estimate the size of the largest entrained grain fragments D^*, then

$$D^* = \frac{\tau}{\tau_c^*(\rho_s - \rho)g}, \tag{4.78}$$

where τ_c^* is the dimensionless critical Shields stress, ρ_s is the grain density, and other variables are as before. For fully turbulent flow, τ_c^* is approximately given by $\tau_c^* \approx 0.045$ [*Lamb et al.*, 2004]. Using the steady-state estimate of pressure gradient (Equation (4.17)), we can then estimate τ using Equation (4.1) and find

$$D^* = \frac{h \cdot \partial \Delta p / \partial x}{2\tau_c^*(\rho_s - \rho)g} \approx 4.3 \cdot \frac{(\rho - \rho_{ice})H}{(\rho_s - \rho)L} \cdot (1 - x/L)^{-6/7} \cdot h. \tag{4.79}$$

For $L \approx 3$ km and $\rho_s/\rho \approx 3$, then $D^*/h \approx 0.06(1 - x/L)^{-6/7}$. Thus, even at $x = 0$ where the pressure gradient is smallest, any grains larger than 6% of the opening ($0.06 \cdot 1$ m $= 6$ cm) would be entrained, leading to a larger τ than used throughout this paper. This underestimate of τ (and therefore of f) may also help to explain the disagreement between our model results and the *Das et al.* [2008] observations.

In our analysis, we also determine pressures and displacements based on 2D plane strain and plane stress approximations, but then modify these solutions for use in a 3D penny-shaped crack. However, future work should be done to verify the validity of this modification procedure. The basal crack is also assumed to be perfectly horizontal, neglecting any bed slope relative to the pressure head gradient. If bed slopes are significant, we would expect the crack to favor propagation in the down-slope direction.

Another important simplification is that we assume no melting or freezing of the ice and liquid water flowing through the cracks. The heating rate (per unit area) due to the turbulent flow τU can be estimated as $f_0 \rho U^3 \approx 10^2$ J m^{-2} s^{-1}, which would only melt warm ice by ≈ 1 mm/hr (since the latent heat of water is $3 \cdot 10^5$ J/kg). Thus, no melting or freezing is a reasonable approximation as long as the thermal diffusion timescale is longer than the process time of a few hours. This diffusion timescale is given by $\tau_d = l^2/\kappa$ where l is the conductive length scale and κ is thermal diffusivity. With $\kappa \approx 10^{-6}$ m^2/s [*Hooke*, 2005] then for $l \gtrsim 10$ cm, $\tau_d \gtrsim 2$ hrs. While it is not clear what range of conductive length scales exist through the crack system, it may be a reasonable guess that $l > 10$ cm, in which case melting and freezing is not important over the timescale of interest. We additionally ignore any instabilities in melting and freezing that might lead to fingering features at the crack front (e.g. as in *Walder* [1982] or *Tsai and Wettlaufer* [2007]). Such short wavelength features are not expected of 3D crack growth without any melting [*Rice*, 1985].

4.5 Discussion

The results of this work fall naturally into two main parts. In the first part (Section 4.3), we present a general model for turbulent hydraulic fracture, and present solutions under the assumption of either steady-state or self-similar crack growth. To our knowledge, this is the first analysis of hydraulic fracture in which the fluid flow is assumed to be turbulent and the solution obtained is consistent with this turbulent flow. Our self-similar solution for crack growth (e.g. Equations (4.36)-(4.38)) therefore scales with physical parameters in a distinctly different manner as

compared with self-similar solutions with Newtonian viscous flow [*Spence and Sharp*, 1985] or power-law fluid flow [*Adachi and Detournay*, 2002]. Since all three of these cases assume a linear elastic medium around the crack, the scalings for crack opening with pressure and crack length are the same, e.g. with Equation (4.38) depending linearly on crack length (L) multiplied by the ratio of pressure (Δp_{in}) to elastic modulus (E'). However, due to differences in the flow regime assumed, the scalings for crack tip velocity (U_{tip}) are very different. For example, *Spence and Sharp* [1985] show that, in the Newtonian viscous case, a self-similar solution in which Δp_{in} is constant can be achieved for an exponential increase in flow rate ($Q_{2D} \propto e^{ct}$) but not for a situation in which flow rate has a power-law dependence ($Q_{2D} \propto t^c$), whereas our turbulent solution has prescribed constant inlet pressure Δp_{in} and has $Q_{2D} \propto t^{7/5}$. This prediction of flow rate, or equivalently of crack growth rate, cannot be made from quasistatic solutions like those of *Weertman* [1973] or *van der Veen* [2007] in which flow rate is treated as a given rather than as a quantity to be solved for in a self-consistent manner. It may also be noted that the turbulent hydraulic fracture results of Section 4.3 may be useful regardless of the validity or merit of the following sections in which we attempt to apply the model a lake drainage event in Greenland.

The second main part of this work (Section 4.4) focuses on applying the turbulent hydraulic fracture model of Section 4.3 to model the rapid drainage of a meltwater lake in Greenland, as recently observed by *Das et al.* [2008]. In utilizing the idealized model of Section 4.3, a number of approximations are necessarily taken and the limitations of these approximations have been discussed in Section 4.4.4. This model of meltwater lake drainage makes quantitative predictions of the dynamic growth of

the basal crack as well as approximate surface displacements and water drainage rate associated with this growth. In comparison, *Krawczynski et al.* [2009] also model the turbulent flow of water through a vertical crack but use the observed drainage rate to constrain the vertical crack geometry and do not consider the effects of basal crack growth. Moreover, *Krawczynski et al.* [2009] do not attempt to model the growth of the crack system, but instead focus on determining the volume of water necessary for the crack to grow to the base of the ice sheet. The modeling of *van der Veen* [2007] also does not attempt to determine the growth rate of either the vertical or basal crack under the realistic conditions of approximately constant excess pressure Δp_{in}. The work of *Weertman* [1971b] also considers a case of turbulent flow driving crack opening but does not use a crack opening and pressure distribution that are consistent with the fluid flow equations, and therefore does not arrive at a realistic prediction of crack growth [*Stevenson*, 1982]. To our knowledge, *Weertman* [1971b], *van der Veen* [2007], *Krawczynski et al.* [2009] and the present work encompass all of the work done so far in attempting to model rapid meltwater lake drainage events. As such, our model results are the only ones capable of quantitative predictions of crack growth rates, drainage rates, and surface displacements associated with the drainage.

4.6 Conclusions

We have presented a general model in which turbulent flow of water drives open a fracture within a purely elastic medium. We find that given certain assumptions about physical parameters, we can calculate the crack-tip speed as well as the pressure and displacement profiles along the crack. We present a steady-state solution and a

self-similar solution (both with $L \ll H$). We then apply the self-similar results to the case of a surface lake draining to the base of the Greenland Ice Sheet. Despite needing to use the models beyond their known range of validity, we nonetheless find that our models can be constructed to have order of magnitude agreement with the observations of *Das et al.* [2008]. Our prediction is of basal crack growth eventually up to a radius of 5-10 km, with lake water-level predictions matching observations well, but with predicted surface displacements a factor of 3 smaller than observed. The inclusion of additional complexity, such as viscous creep and a more realistic treatment of the whole range of L/H, may help yield model results in better agreement between the observations, and we suggest possible directions for future work.

4.7 Connection to Other Chapters

The models presented here of turbulent hydraulic fracture share some features with the models presented in both Chapter 3 and Chapter 5. Similarities with the models of glacial earthquakes in Chapter 3 include use of elasticity, fracture properties, and general principles of solid mechanics. The models are similar to the model of 'lake star' formation in Chapter 5 in that both models study the flow of liquid water within an ice medium (though in very different flow regimes).

Chapter 5

The Formation of Lake Stars

5.1 Abstract

Star patterns, reminiscent of a wide range of diffusively controlled growth forms from snowflakes to Saffman-Taylor fingers, are ubiquitous features of ice covered lakes. Despite the commonality and beauty of these "lake stars" the underlying physical processes that produce them have not been explained in a coherent theoretical framework. Here we describe a simple mathematical model that captures the principal features of lake-star formation; radial fingers of (relatively warm) water-rich regions grow from a central source and evolve through a competition between thermal and porous media flow effects in a saturated snow layer covering the lake. The number of star arms emerges from a stability analysis of this competition and the qualitative features of this meter-scale natural phenomena are captured in laboratory experiments.

5.2 Introduction

The scientific study of the problems of growth and form occupies an anomalously broad set of disciplines. Whether the emergent patterns are physical or biological in origin, their quantitative description presents many challenging and compelling issues in, for example, applied mathematics [*Hou et al.*, 2001], biophysics [*Brenner et al.*, 1998; *Levine and Ben-Jacob*, 2004], condensed matter [*Cross and Hohenberg*, 1993; *Aranson and Tsimring*, 2006] and geophysics [*Goldenfeld et al.*, 2006; *Short et al.*, 2006] wherein the motion of free boundaries is of central interest. In all such settings a principal goal is to predict the evolution of a boundary that is often under the influence of an instability. Here we study a novel variant of such a situation that occurs naturally on the frozen surfaces of lakes.

Lakes commonly freeze during a snowfall. When a hole forms in the ice cover, relatively warm lake water will flow through it and hence through the snow layer. In the process of flowing through and melting the snow this warm water creates dark regions. The pattern so produced looks star-like (see Figure 5.1) and we refer to it as a "lake star". These compelling features have been described qualitatively a number of times (e.g. *Knight* [1987]; *Katsaros* [1983]; *Woodcock* [1965]) but work on the formation process itself has been solely heuristic. *Knight* [1987] outlines a number of the physical ideas relevant to the process, but does not translate them into a predictive framework to model field observations. Knight's main idea is that locations with faster flow rates melt preferentially, leading to even faster flow rates and therefore to an instability that results in fingers. This idea has features that resemble those of many other instabilities such as, for example, those observed during the

growth of binary alloys [*Worster*, 1997], in flow of water through a rigid hot porous media [*Fitzgerald and Woods*, 1994], or in more complex geomorphological settings [*Schörghofer et al.*, 2004], and we structure our model accordingly.

Figure 5.1: Typical lake star patterns. The branched arms are approximately 1 m in length. Quonnipaug Lake, Guilford, Connecticut, 8 March, 2006.

Katsaros [1983] and *Woodcock* [1965] attribute the holes from which the stars emanate and the patterns themselves to thermal convection patterns within the lake, but do not measure or calculate their nature. However, often the holes do not exhibit a characteristic distance between them but rather form from protrusions (e.g. sticks that poke through the ice surface) *Knight* [1987] and stars follow thereby ruling out a convective mechanism as being necessary to explain the phenomena. The paucity of literature on this topic provides little more than speculation regarding the puncturing mechanism but lake stars are observed in all of these circumstances. Therefore, while hole formation is necessary for lake star formation, its origin does not control the mechanism of pattern formation, which is the focus of the present work.

5.3 Theory

The water level in the hole is higher than that in the wet snow–slush–layer [*Knight*, 1987] and hence we treat this warm water[1] region as having a constant height above the ice or equivalently a constant pressure head, which drives flow of water through the slush layer, which we treat as a Darcy flow of water at 0°C. We model the temperature field within the liquid region with an advection-diffusion equation and impose an appropriate (*Stefan*) condition for energy conservation at the water-slush interface. The water is everywhere incompressible. Finally, the model is closed with an outer boundary condition at which the pressure head is assumed known.

Although we lack *in-situ* pressure measurements, circular water-saturated regions (a few meters in radius) are observed around the lake stars. Hence, we assume that the differential pressure head falls to zero somewhere in the vicinity of this circular boundary. The actual boundary at which the differential pressure head is zero is not likely to be completely uniform (as in Figure 4 of *Knight* [1987]) but treating it as uniform is a good approximation in the linear regime of our analysis. Finally, we treat the flow as two-dimensional. Thus, although the water in direct contact with ice must be at 0°C, we consider the depth-averaged temperature, which is above freezing. Additionally, the decreasing pressure head in the radial direction must be accompanied by a corresponding drop in water level. Therefore, although the driving force is more accurately described as deriving from an axisymmetric gravity current, the front whose stability we assess is controlled by the same essential physical

[1] A finite body of fresh water cooled from above will have a maximum below-ice temperature of 4 °C.

processes that we model herein. Our analysis could be extended to account for these three-dimensional effects.

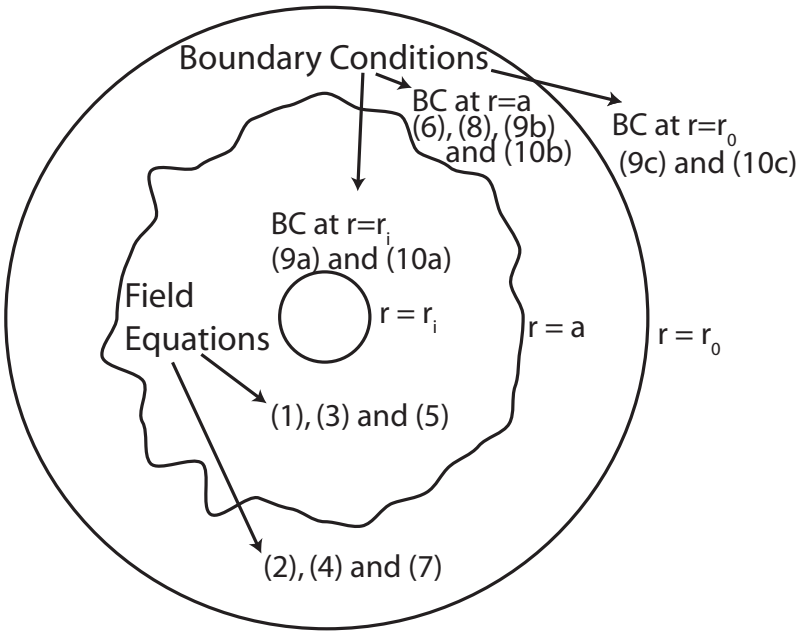

Figure 5.2: Schematic of the geometry of the model. The perspective is looking down on a nascent star. The equations (refer to text for numbering) are shown in the domains of the system where they are applicable.

The system is characterized by the temperature T, a Darcy fluid velocity $\mathbf{u}$, pressure p, and an evolving liquid-slush interface a. The liquid properties are κ (thermal diffusivity), C_P (specific heat at constant pressure) and μ (dynamic viscosity) and the slush properties are Π (permeability), ξ (solid fraction) and L (latent heat). We non-dimensionalized the equations of motion by scaling the length, temperature, pressure and velocity with r_0, T_0, p_0, and $\frac{\Pi p_0}{\mu r_0}$, respectively. Thus, our model consists of the following system of dimensionless equations:

$$\frac{\partial \theta}{\partial t} + \mathbf{u} \cdot \nabla \theta = \epsilon \nabla^2 \theta, \quad r_i < r < a(\phi, t), \tag{5.1}$$

$$\theta = 0, \quad a(\phi, t) < r < 1, \tag{5.2}$$

$$p = 1, \quad r_i < r < a(\phi, t), \tag{5.3}$$

$$\nabla^2 p = 0, \quad a(\phi, t) < r < 1, \tag{5.4}$$

$$\nabla \cdot \mathbf{u} = 0, \quad r_i < r < a(\phi, t), \tag{5.5}$$

$$\mathbf{u} \mid_{a_-} = \mathbf{u} \mid_{a_+}, \qquad r = a(\phi, t), \tag{5.6}$$

$$\mathbf{u} = -\nabla p, \quad a(\phi, t) < r < 1, \tag{5.7}$$

with boundary conditions

$$\dot{a} = -\frac{\epsilon}{S} \nabla \theta, \quad r = a(\phi, t), \tag{5.8}$$

$$\theta = \begin{cases} 1, & r = r_i \\ 0, & r = a(\phi, t) \\ 0, & r = 1 \end{cases}, \tag{5.9}$$

and

$$p = \begin{cases} 1, & r = r_i \\ 1, & r = a(\phi, t) \\ 0, & r = 1 \end{cases}, \tag{5.10}$$

where (5.1) describes the temperature evolution in the liquid, (5.4) and (5.5) describe mass conservation with a Darcy flow (5.7) in the slush, (5.8) is the Stefan condition, and (5.9) and (5.10) are the temperature and pressure boundary conditions, respectively (see Figure 5.2). Note that (5.3) and (5.5) can both be satisfied since the liquid region has an effectively infinite permeability.

The dimensionless parameters ϵ and S of the system are given by

$$\epsilon \equiv \frac{\kappa}{u_0 r_0}, \qquad \text{and} \qquad S \equiv \frac{\xi L}{C_P T_0}, \tag{5.11}$$

which describe an inverse Peclet number and a Stefan number respectively. Because the liquid must be less than or equal to 4°C, we make the conservative estimates that $T_0 < 4°\text{C}$, $\xi > 0.3$, and use the fact that $L/C_P \approx 80°\text{C}$ from which we see $S > 6 \gg 1$. Using $\kappa \approx 10^{-7}\text{m}^2\text{s}^{-1}$, and the field observations of *Knight* [1987] to constrain u_0 (1 cm/hr $< u_0 <$ 10 cm/hr) and r_0 (0.3 m $< r_0 <$ 3 m), we find that $\epsilon < 0.1 \ll 1$. We therefore employ the quasi-stationary ($S \gg 1$) and large Peclet number ($\epsilon \ll 1$) approximations, and hence equations (5.1) - (5.10) are easily solved for a purely radial flow with cylindrical symmetry (no ϕ dependence) and circular liquid-slush interface. This (boundary layer) solution is

$$\mathbf{u} = u\hat{r} = -\frac{1}{\ln(a_0)}\frac{1}{r}\hat{r}, \quad r_i < r < 1, \tag{5.12}$$

$$p_b = \frac{\ln(r)}{\ln(a_0)}, \quad r > a_0, \tag{5.13}$$

$$\theta_0 = 1 - \left(\frac{r}{a_0}\right)^{\frac{1}{\epsilon}(-1/\ln(a_0)+2\epsilon)}, \quad r < a_0, \tag{5.14}$$

$$\frac{Sa_0\dot{a}_0}{-1/\ln(a_0)+2\epsilon}=1, \tag{5.15}$$

where equation (5.15) has an approximate implicit solution for a_0 given by

$$\frac{a_0^2}{4}-\frac{1}{2}a_0^2\ln(a_0)=\frac{t}{S}. \tag{5.16}$$

We perform a linear stability analysis around this quasi-steady cylindrically symmetrical flow. Proceeding in the usual way, we allow for scaled perturbations in θ and a with scaled wavenumber $k'=\epsilon k$, non-dimensional growth rate σ, and amplitudes $f(r)$ and g respectively. Keeping only terms linear in ϵ, $1/S$ and g, we solve (5.4) subject to (5.10), substitute into (5.6) and satisfy (5.5) and (5.1). This gives the non-dimensional growth rate (σ) as a function of scaled wave number (k'):

$$\sigma=\frac{1}{2a_0\ln^2(a_0)S}\left(\sqrt{1+4k'^2\ln^2(a_0)}-1\right)\left(\frac{a_0}{-k'\ln(a_0)}-1\right). \tag{5.17}$$

Equation (5.17) can be approximated in $0\leq x\lesssim 1$ as

$$\sigma\approx\frac{a_0}{\ln^2(a_0)S}x(1-x), \tag{5.18}$$

where $x\equiv -k'\ln(a_0)/a_0$.

The stability curve (5.17) and the approximation (5.18) are plotted in Figure 5.3. The essential features of (5.17) are a maximum in the range $0<k'<a_0/\ln(a_0)$, zero growth rate at $k'=a_0/\ln(a_0)$ and a linear increase in stability with k' for large k'. The long-wavelength cut-off is typical of systems with a Peclet number, here with the added effect of latent heat embodied in the Stefan number. This demonstrates the competition between the advection and diffusion of heat and momentum (in a

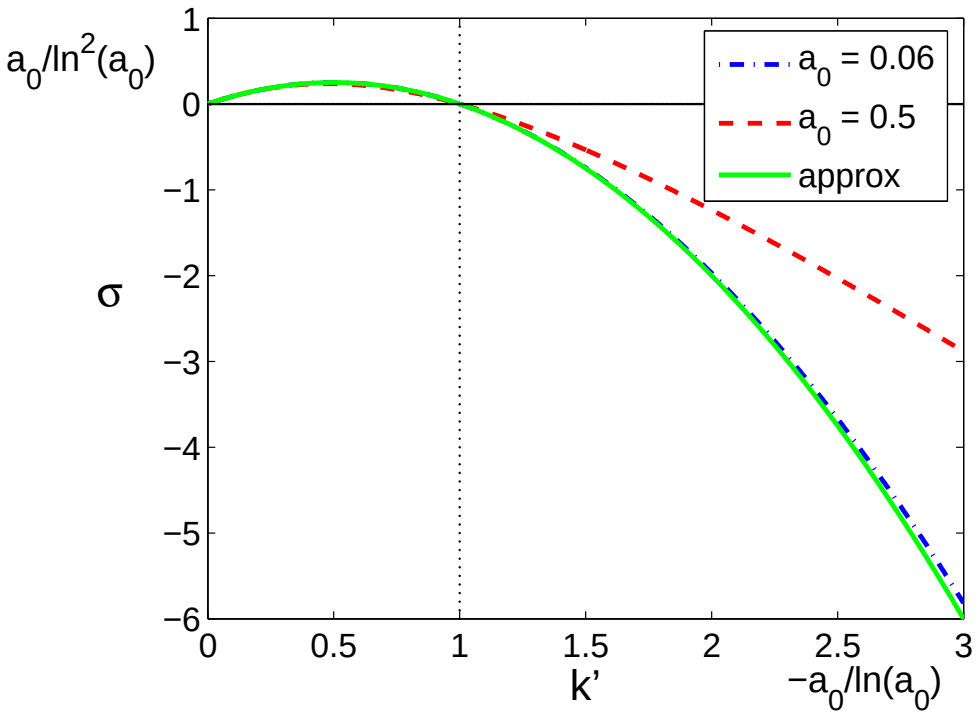

Figure 5.3: Stability curve: Non-dimensional growth rate σ versus non-dimensional wavenumber k'. Scales for the axes are given at the upper left (σ axis) and the lower right corners (k' axis). σ is plotted for the range of plausible a_0 (dot-dashed blue and dashed red curves) and for the approximation (5.18) (solid green curve).

harmonic pressure field); the former driving the instability and the latter limiting its extent. The maximum growth rate occurs at approximately

$$k'_{max} \approx \frac{a_0}{-2\ln(a_0)}, \tag{5.19}$$

with (non-dimensional) growth rate

$$\sigma_{max} \approx \frac{a_0}{4S\ln^2(a_0)}. \tag{5.20}$$

Translating (5.19) and (5.20) back into dimensional quantities, we find that the most unstable mode has angular size given by

$$\phi_{degrees} = \frac{720^\circ\kappa}{u_0 r_0}\left(\frac{r_0}{a_0}\right)\ln\left(\frac{r_0}{a_0}\right), \tag{5.21}$$

and has growth rate given by

$$\sigma_{dim} = \frac{u_0}{4Sr_0\ln^2(r_0/a_0)}\left(\frac{a_0}{r_0}\right). \tag{5.22}$$

5.4 Extracting Information from Field Observations

Field observations of lake stars cannot be *controlled*. A reasonable estimate for r_0 is the radius of the wetted (snow) region around the lake stars, and observations [*Knight*, 1987; *Woodcock*, 1965; *Katsaros*, 1983] bound the value as $1.5\text{m} \lesssim r_0 \lesssim 4\text{m}$. This is simply because if there were significant excess pressure at this point then the wetting front would have advanced further. However, it is also possible that the effective value of r_0, say r_0^{eff}, is less than this either because the wetted radius is smaller earlier in the star formation process or because the ambient pressure level is reached at smaller

radii. Here, we take a_0 to be the radius of the roughly circular liquid-filled region at the center of the lake star (r_ℓ) as the best approximation during the initial stages of star formation (see Figure 5.4). Field observations show that $0.1\text{m} \lesssim r_\ell \lesssim 0.5\text{m}$, [*Knight*, 1987; *Woodcock*, 1965; *Katsaros*, 1983] and hence $0.07 \lesssim r_\ell/r_0 \lesssim 0.15$. We note that equations (5.21) and (5.22) are more sensitive to a_0/r_0 than a_0 or r_0 independently[2]. With this interpretation of r_0 we find a reasonable estimate of u_0 as $1.4 \cdot 10^{-5}\text{m/s} \lesssim u_0 \lesssim 2.8 \cdot 10^{-5}\text{m/s}$. Using these parameter values, the most unstable mode should have wavelength between 8° and 130°. Letting the number of branches be $N = 360°/\phi_{deg}$, then $3 < N < 45$ and we clearly encompass the observed values for lake stars ($4 < N < 15$), but note that values ($N > 15$) are never seen in the field.

Despite the dearth of field observations, many qualitative features embolden our interpretation. For example, the stars with larger values of a_0/r_0 have a larger number of branches. Moreover, for any value of a_0/r_0, our analysis predicts an increase in N with r_0 and u_0. Indeed, u_0 increases with p_0 (higher water height within the slush layer) and Π (less well-packed snow). Therefore, we ascribe some of the variability among field observations to variations in these quantities (which have not been measured in the field) and the remainder to nonlinear effects. Because the dendritic arms are observed long after onset and are far from small perturbations to a radially symmetric pattern, as one might see in the initial stages of the Saffman-Taylor instability, the process involves non-linear cooperative phenomena. Hence, our model should only approximately agree with observations. Although a rigorous non-linear analysis of the

[2]For the later stages of growth, clearly in the nonlinear regime not treated presently, a_0 may also be interpreted as the radius of the lake star (r_{LS}). Field observations show $1\text{m} \lesssim r_{LS} \lesssim 2\text{m}$ [*Knight*, 1987; *Woodcock*, 1965; *Katsaros*, 1983] and hence $0.3 \lesssim r_{LS}/r_0 \lesssim 0.6$.

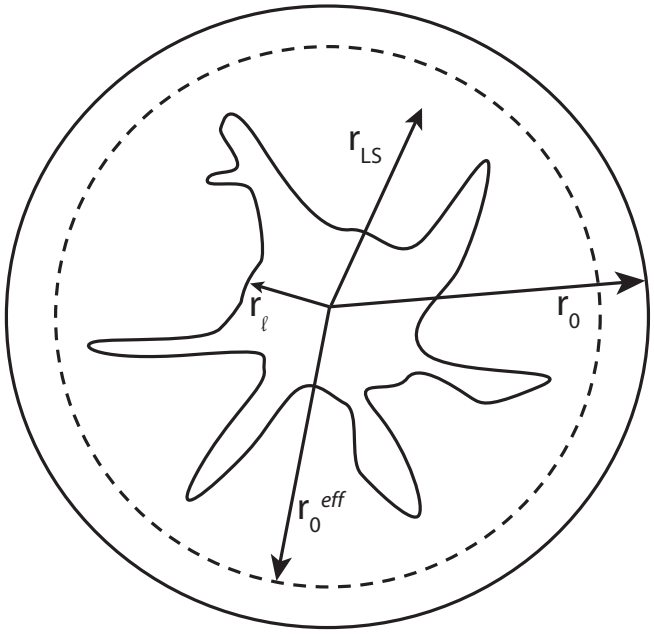

Figure 5.4: Schematic showing r_0, r_0^{eff}, r_{LS} and r_ℓ.

long term star evolution process (e.g. *Cross and Hohenberg* [1993]; *Aranson and Tsimring* [2006]) may more closely mirror field observations, the present state of the latter does not warrant that level of detail. Instead, we examine the model physics through simple proof of concept experimentation described presently.

5.5 Demonstrating Lake Stars in the Laboratory

A 30 cm diameter circular plate is maintained below freezing (≈ -0.5°C), and on top of this we place a 0.5 to 1 cm deep layer of slush through which we flow 1°C water. Given the technical difficulties associated with its production, the grain size, and hence the permeability, of the slush layer, is not a controlled variable. This fact influences our results quantitatively. In fourteen runs we varied the initial size of the

water-filled central hole (a_0), that of the circular slush layer (r_0), and the flow rate (Q), which determines u_0. The flow rate is adjusted manually so that the water level (h_0) in the central hole remains constant[3]. Fingering is observed in every experimental run and hence we conclude that fingers are a robust feature of the system. Two distinct types of fingering are observed: small-scale fingering (see Figure 5.5) that forms early in an experimental run, and larger channel-like fingers (see Figure 5.6) that are ubiquitous at later times and often extend from the central hole to the outer edge of the slush. Since the channel-like fingers provide a direct path for water to flow, effectively *shorting* Darcy flow within the slush, their subsequent dynamics are not directly analogous to those in natural lake stars. However, in *all* runs, the initial small-scale fingers have the characteristics of lake stars and hence we focus upon them. We note that because the larger channel-like fingers emerge out of small-scale fingers, they likely represent the non-linear growth of the linear modes of instability, a topic left for future study. Finally, we measure the distance between fingers (d_f), so that for each experiment we can calculate $u_0 = Q/(2\pi r_0 h_0)$, $\phi_{calc} \equiv \phi_{degrees}$, from equation (5.21), and $\phi_{obs} = 180^\circ d_f/(\pi a_0)$, and we can thereby compare experiment, theory and field observations.

In Figure 5.7 we plot ϕ_{obs} versus ϕ_{calc} for the various field observations for which we have estimates of parameters, the laboratory experiments described above, and the model [equation (5.21)]. There is a large amount of scatter in both the exper-

[3]In many of the runs, we begin the experiment without the central hole. In practice, however, the first few drops of warm water create a circular hole with radius one to three times the radius of the water nozzle (0.5cm $< a_0 <$ 1.0cm). It is significantly more difficult to prepare a uniform permeability sample with a circular hole initially present; these runs are therefore more difficult to interpret.

Figure 5.5: Typical experimental run where small- scale fingers are present. For scale, the nozzle head has diameter of 5 mm.

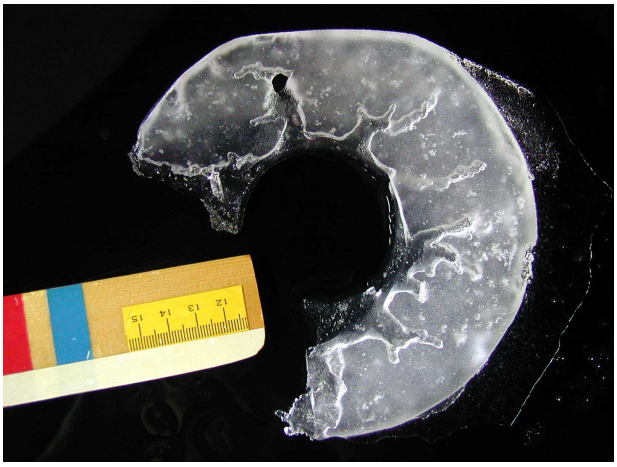

Figure 5.6: Typical run where channels form. This picture is taken from the underside. Note: part of the slush broke off when it was flipped to image it. The ruler scale is in cm.

imental and observational data and the data does not lie on the one-to-one curve predicted by the model. However, the experiments are meant to demonstrate the features of the model predictions, and the results have the correct qualitative trend (having a best-fit slope of 0.34). We also attempt to find trends in the experimental data not represented by the model by comparing $y \equiv \phi_{obs}/\phi_{calc}$ vs. various combinations of control parameters ($\equiv x$) including r_0, a_0, r_0/a_0, $r_0 u_0$, $r_0/a_0 \ln(r_0/a_0)$ and $\ln(r_0/a_0)/(a_0 u_0)$. For all plots of y vs. x, our model predicts a zero slope (and y-intercept of 1). A non-random dependence of y on x would point to failure of some part of our model. Thus, to test the validity of our model, we perform significance tests on all non-flagged data with the null hypothesis being a non-zero slope. In all cases, the null hypothesis is accepted (not rejected) at the 95% confidence level. Thus, although the agreement is far from perfect, the simple model captures all of the significant trends in the experimental data.

5.6 Conclusions

By generalizing and quantifying the heuristic ideas of *Knight* [1987], we have constructed a theory that is able to explain the radiating finger-like patterns on lake ice that we call lake stars. The model yields a prediction for the wavelength of the most unstable mode as a function of various physical parameters that agrees with field observations. Proof of concept experiments revealed the robustness of the fingering pattern, and to leading order the results also agree with the model. There is substantial scatter in the data, and the overall comparison between field observations, model and experiment demonstrates the need for a comprehensive measurement pro-

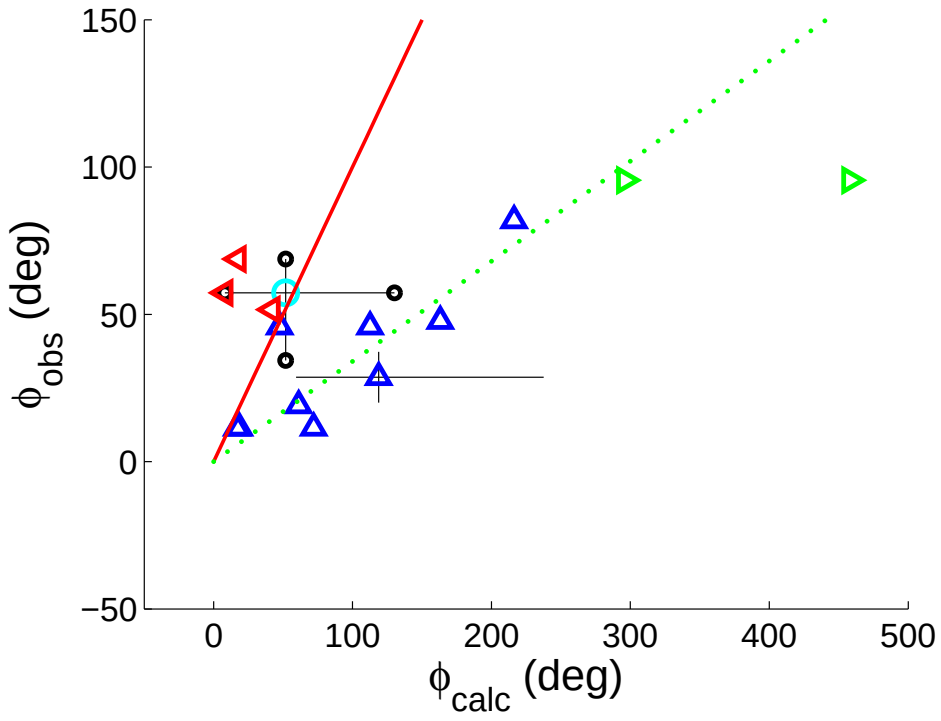

Figure 5.7: Comparison of theory, experiment and field observations. Circles are field observations (cyan, best constrained field observation; black, range of plausible field observations), triangles are experimental results (blue upward-pointing triangles were unambiguous; red left-pointing triangles have channels but show no clear small-scale fingers, so channel spacing is taken for d_f; green right-pointing triangles were compromised by the quality of the images). Errors are approximately 0.3 cm, 0.5 cm, 2 mm, 5 ml/min and 0.2 cm (respectively) for the five measured quantities. All experimental results thus have error bars of at least a factor of two in the x-coordinate and 30% in the y-coordinate. Typical error bars are shown on one measurement. The solid red line is the theoretical prediction; the dotted green line is the best fit line to the blue triangles.

gram and a fully nonlinear theory which will yield better quantitative comparisons. However, the general predictions of our theory capture the leading order features of the system.

5.7 Acknowledgments

We thank K. Bradley and J. A. Whitehead for laboratory and facilities support and D. H. Rothman for helpful comments. This research, which began at the Geophysical Fluid Dynamics summer program at the Woods Hole Oceanographic Institution, was partially funded by National Science Foundation (NSF) Grant No. OCE0325296, NSF Grant No. OPP0440841 (J.S.W.), and Department of Energy Grant No. DE-FG02-05ER15741 (J.S.W.). V. C. T. acknowledges financial support from NSF.

5.8 Connection to Other Chapters

This chapter is perhaps the least related to other chapters of this thesis. The primary reason for this is that I attended a summer workshop on 'ice' due to my (then) new-found interest in glaciers only to find that people were primarily interested in melt phenomena rather than ice dynamics. I thereby became fascinated with this problem of melt features on lake ice, and proceeded to the do the research presented in this chapter. As previously mentioned, the model superficially shares features with the model of Chapter 4, in that both examine flow of water through ice, but the flow regimes are quite different, leading to major differences in the governing physics. To an even lesser extent, since large earthquakes are thought to be affected by the

Darcy-like flow of fluids through fault zones (a topic of interest to me that is not represented in this thesis), there is also a weak connection to Chapter 6.

Chapter 6

Multiple CMT Source Analysis of the 2004 Sumatra Earthquake

6.1 Abstract

While it is agreed that the great Sumatra earthquake of December 26, 2004 was among the largest earthquakes of the past century, there has been disagreement on how large it was, which part of the fault ruptured, and how the rupture took place. We present a centroid-moment-tensor (CMT) analysis of the earthquake in which multiple point sources are used in the inversion to mimic a propagating slip pulse. The final model consists of five point sources, with the southernmost sources accounting for the majority of the moment release. The presumed fault planes of the southern sources strike northwest, while those in the north strike northeast, consistent with the geometry of the subduction trench. Slip on the fault is found to be more oblique in the north than in the south. The inversion with five sources leads to a moment

magnitude for the Sumatra earthquake of $M_W = 9.3$, consistent with estimates from long-period normal-mode amplitudes.

6.2 Introduction

The great Sumatra earthquake of December 26, 2004 was one of the largest earthquakes of the past century. Standard Harvard centroid-moment-tensor (CMT) analysis [*Dziewonski et al.*, 1981; *Ekström et al.*, 2005] of this event provided a point-source mechanism and moment magnitude (M_W) of 9.0. *Ammon et al.* [2005] have produced 3 different model slip distributions, each of which has $9.0 < M_W < 9.2$. *Park et al.* [2005] find that a model with $M_0 = 6.5 \cdot 10^{29}$ dyne-cm ($M_W = 9.1$) explains normal-mode spectral data. Work by *Stein and Okal* [2005] analyzing long-period normal modes (${}_0S_2$, ${}_0S_3$ and ${}_0S_4$) suggests a larger seismic scalar moment of $M_0 = 1.0 \cdot 10^{30}$ dyne-cm, equivalent to $M_W = 9.3$. These authors argue that the most likely source of the additional moment release they detect is slow slip in the northern aftershock zone of the Sumatra earthquake. *Banerjee et al.* [2005] estimate a moment magnitude of 9.1-9.2 based on geodetic data and argue for even slower moment release. Other geodetic analyses [*Vigny et al.*, 2005] suggest that no slow slip is required.

The original CMT analysis was limited by its simple parameterization of the earthquake as a point source in space with a prescribed, triangular moment-rate function. The large centroid time shift of 139 s found in the standard CMT analysis and the results of later studies (e.g. *Ammon et al.* [2005]) suggest that the earthquake had a total duration of 300-600 s. Because the original CMT analysis was conducted

in the 300-500 s pass band, it is likely that the result of that analysis does not provide an accurate representation of the overall rupture characteristics. To allow for the representation of greater complexity during the rupture process, and to account for moment release occurring over the full duration of the earthquake, we model the Sumatra earthquake with a series of point sources distributed in space and time.

6.3 Analysis

We present a modified CMT analysis in which we fit a model with five sources to mantle-wave data filtered in the 200-500-s period range. The data we use were recorded by the IRIS Global Seismographic Network (GSN) and represent a similar dataset to that used in the original Harvard CMT. We edit seismograms recorded during approximately the first nine hours after the earthquake to select only high quality, on-scale segments of the records. A total of 81 stations and 217 components are included in the final analysis.

In the multiple-source CMT analysis, we determine moment-tensor elements and centroid parameters for a set of several sources simultaneously. As in the standard, single-source CMT analysis, allowing for perturbations to the centroid location and time introduces a nonlinearity in the problem, and the best-fit solution is therefore obtained by iterative inversion. A starting centroid location and time must be provided for each source. Here, we also use an iterative approach to the inclusion of successive sources. We first invert for the centroid parameters for a single source. A second source is then introduced with an initial location approximately 1° N of the single-source location, with a time delay of approximately 30 s. This time delay is

chosen with a rupture speed of ≈ 3 km/s in mind [*Ammon et al.*, 2005; *Ishii et al.*, 2005]. The locations and times of both sources are then allowed to move to fit the data. The times and locations of the two sources are unaffected by the initial choice of the location and time for the second source. All starting locations between 1° to 3° N, −2° to 2° E and with a time delay of 20-80 s relative to the first source lead to the same final locations and times for these sources. The inversion with three sources builds upon the previous inversion in the same way the two-source inversion builds upon the one-source result. The same best-fit result is attained for a wide range of initial values.

Inversions with four and five sources are conducted in a similar fashion. The results in these cases depend more strongly on the initial values for the locations and times. The variance reduction can always be improved by including more sources, and we therefore test the statistical significance of the improvement in variance reduction achieved by including these sources. We compare models in which sources four and five lie along the fault with models in which those sources are placed in random locations. We perform a hypothesis test with the null hypothesis being no difference in residual variance between the random and non-random cases. Using the distribution of residual variance at various depths along the fault as the sample distribution, we reject the null hypothesis at the 99.9% confidence level. The reduction in residual variance that results from including additional sources is thus not due only to an increase in the number of free parameters. An inversion with six sources results in only a marginal improvement in fit over the five-source model and we therefore choose to limit our analysis to five sources.

The long-period waveforms provide limited constraints on centroid depth, and we therefore fix all centroid depths at 25 km. The main effect of changing the source depths is to produce a change in the dip angles of the sources, which leads to a change in the scalar moment. In general, larger estimates of dip lead to smaller estimates of scalar moment. Fixing the source depths at 20 km or 30 km results in slightly steeper dip angles and total scalar moments that are smaller than that of our preferred solution by 11% and 19%, respectively; the misfit to the data also increases. Other source depths lead to shallower or steeper dips, with larger or smaller scalar moments, but no inversion fixed at depths between 14 km and 30 km leads to dips as steep as those estimated from slab contours ($12^\circ - 18^\circ$) [*Ammon et al.*, 2005]. The timing, focal geometries, and relative sizes of the sources do not change significantly as a result of changes to the source depth.

6.4 Results

As detailed in Table 6.1, the inversion for a single source results in a moment of $4.22 \cdot 10^{29}$ dyne-cm, similar to that from the standard CMT. The addition of the second source lowers the residual variance by a substantial amount (19%) and increases the total moment by 31%. The moment of the first source increases slightly (2%) with the inclusion of the second source. The inclusion of the third source reduces the residual variance by 34% relative to the two-source model, though the moment of this source is only 36% of that of the original, single-point-source moment. In this step, the total moment becomes more evenly distributed between the individual sources, with the moment of the second source more than doubling in size. We interpret these results

Table 6.1: Inversion results for source models with varying numbers of sources. Times are relative to 00:58:53.5 UT December 26, 2004. The depths of all sources are constrained at 25 km as discussed in the text. Moment is in units of 10^{30} dyne-cm.

# of Sources	Residual Variance	Lat N (°)	Long E (°)	Time (s)	Moment	Total Moment	Total M_W
1	0.25002	3.22	94.33	127.1	0.422	0.422	9.02
2	0.20190	3.07	94.45	110.2	0.432	0.554	9.10
		4.20	93.13	196.2	0.122		
3	0.13376	3.10	94.62	94.4	0.320	0.769	9.19
		5.02	93.14	170.3	0.298		
		7.78	91.73	299.7	0.151		
4	0.12325	3.15	94.64	93.0	0.298	0.875	9.23
		5.22	93.04	162.5	0.329		
		8.30	91.45	285.9	0.206		
		11.09	90.21	392.5	0.042		
5	0.11110	3.27	94.60	93.0	0.318	1.166	9.31
		5.39	93.16	162.6	0.387		
		8.39	91.91	281.2	0.275		
		11.19	91.30	378.5	0.105		
		13.29	92.14	490.4	0.081		

as implying a distribution of three areas of large moment release.

The inclusion of sources four and five has a less dramatic effect on the residual variance, but including each source leads to a statistically significant improvement in fit. We note that the addition of each source increases the total moment of the earthquake by an amount greater than its individual contribution to the moment. For example, although source five has a moment of only $0.08 \cdot 10^{30}$ dyne-cm, including this source increases the total moment by $0.29 \cdot 10^{30}$ dyne-cm relative to the four-source inversion.

The final five-source model is depicted in Figure 6.1 and source parameters are listed in Table 6.2. The total moment obtained is $1.17 \cdot 10^{30}$ dyne-cm, equivalent to moment magnitude $M_W = 9.3$. We find two large slip patches (27% and 33% of the total moment) in the southern portion of the fault, the locations of which roughly

Table 6.2: Source parameters for the final, five-source model. Strike, dip and rake are given in degrees. Moment is given in units of 10^{30} dyne-cm. ϵ describes the relative size of the non-double-couple component of the moment tensor and is calculated as $-e_2/\max(|e_1|, |e_3|)$ where e_i are the ordered eigenvectors of the moment tensor. Values for a composite ("Comp") solution obtained by summing the moment-tensor components of the individual sources are also listed. The centroid location and time for the composite source are 6.6° N, 93.0° E and 214 s.

Source	Strike	Dip	Rake	Moment	M_W	ϵ
I	318	6.4	94	0.318	8.94	0.00
II	345	6.3	109	0.387	9.00	0.00
III	343	5.8	95	0.275	8.90	0.02
IV	15	8.4	132	0.105	8.62	0.04
V	35	8.1	155	0.081	8.54	0.01
Comp	343	6.1	107	1.15	9.31	0.02

agree with the locations of regions of high slip in the *Ammon et al.* [2005] models. However, the moment release in these two areas is substantially larger than suggested by the results of *Ammon et al.* [2005]. This is particularly true for the northern of the two sources. Another large slip patch (24% of the total moment) is located farther north (8.4° N). The moment release at 11° N represents about 9% of the total, with the final 7% at 13° N.

A composite moment-rate function is shown in Figure 6.2. A large fraction of the total moment is released in the first 200 seconds of the rupture, but substantial moment is released later as well, peaking with source three just prior to 300 seconds and continuing until more than 500 seconds after the initiation of rupture. Of the three *Ammon et al.* [2005] models, our results have the best agreement with model III in both the slip distribution and moment-rate function, though our results imply a larger moment release at all points along the fault than any of their models. The locations of our southern three sources also agree well with the locations of highest radiated energy in the model of *Ishii et al.* [2005] and the locations of the northern

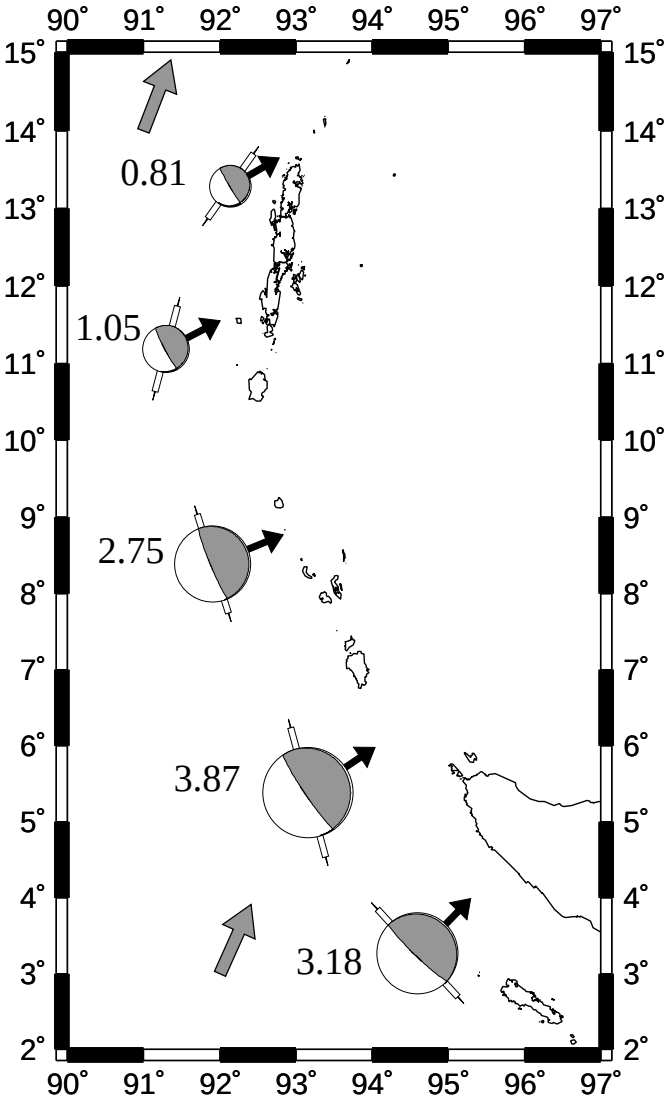

Figure 6.1: Locations and focal mechanisms of the five CMTs of our final model. The areas of the focal mechanisms are proportional to their scalar moments, which are given next to each mechanism in units of 10^{29} dyne-cm. The needles denote the strike directions of the shallowly dipping nodal planes; the black arrows denote the slip directions projected onto the horizontal plane. The gray arrows show the long-term plate motions of the Indian plate relative to the Eurasian plate [*DeMets et al.*, 1994].

two sources agree with the northern extent of that model.

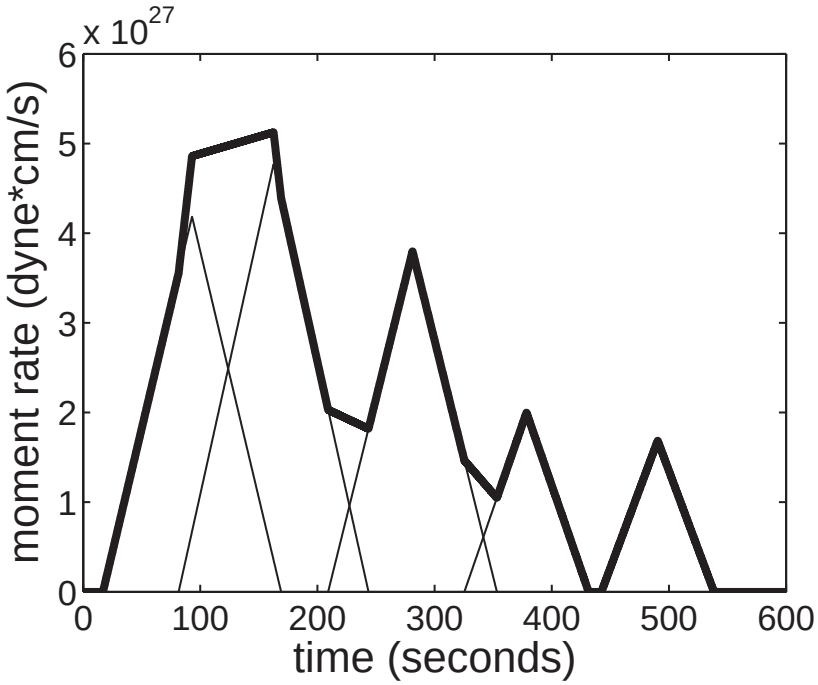

Figure 6.2: Source time function. The thin black lines denote the individual sources. The heavy black line denotes the sum. Source durations were chosen to satisfy $t = 2.2 \cdot 10^{-8} \cdot (M_0)^{1/3}$ [*Ekström and Engdahl*, 1989; *Ekström et al.*, 2005], where t = time (s) and M_0 = moment (dyne-cm). The source durations are fixed parameters in the inversion. The zero time corresponds to the hypocentral time of 00:58:53.5.

The effects of directivity are clear in the data we analyze. As shown in Figure 6.3, the amplitudes of the minor-arc arrivals are enhanced in the azimuth of rupture propagation while the amplitudes of the major-arc arrivals are enhanced in the opposite azimuth. The use of multiple sources allows us to model these directivity effects well. From the centroid locations and times of the sources, we calculate a 'propagation velocity,' by which we mean the distance between successive centroid locations divided by the time between them. Some care must be taken in interpreting this velocity, as it represents the propagation of moment release only in some averaged sense. The

velocities between adjacent sources (I-II, etc.) are respectively 4.1, 3.0, 3.3, and 2.2 km/s. The rupture thus appears to have begun fast and slowed after passing source II, slowing again after passing source IV, in agreement with the geodetic estimates of *Vigny et al.* [2005].

The total moment ($1.17 \cdot 10^{30}$ dyne-cm) we obtain agrees well with the estimate ($1.0 \cdot 10^{30}$ dyne-cm) of *Stein and Okal* [2005], but our result does not require a component of moment release that is sufficiently slow to excite only the longest-period normal modes. We interpret our results as indicating that most of the moment was released in the early, southern portion of the faulting, and that the earthquake rupture progressed northward at typical rates. The final 16% of the moment corresponding to the northern portion of the fault also appears to have been released at a normal rate.

The focal mechanisms of the five sources change systematically from south to north. The strike of the mechanisms rotates clockwise (see Table 6.2), in good agreement with the geologically observed change in strike of the subduction interface. The slip vectors rotate from nearly pure thrust to oblique slip with a large strike-slip component, again consistent with the geometry of the subduction interface and, in general, with plate motions. However, slip directions differ markedly from the direction of long-term plate motion between India and Eurasia [*DeMets et al.*, 1994], a result consistent with significant extensional and strike-slip deformation in the overriding plate. Many upper-plate aftershocks have strike-slip focal mechanisms, especially in the region near 8° N, where the discrepancy between slip direction and long-term plate motions is largest and where we find high moment release in our model. The

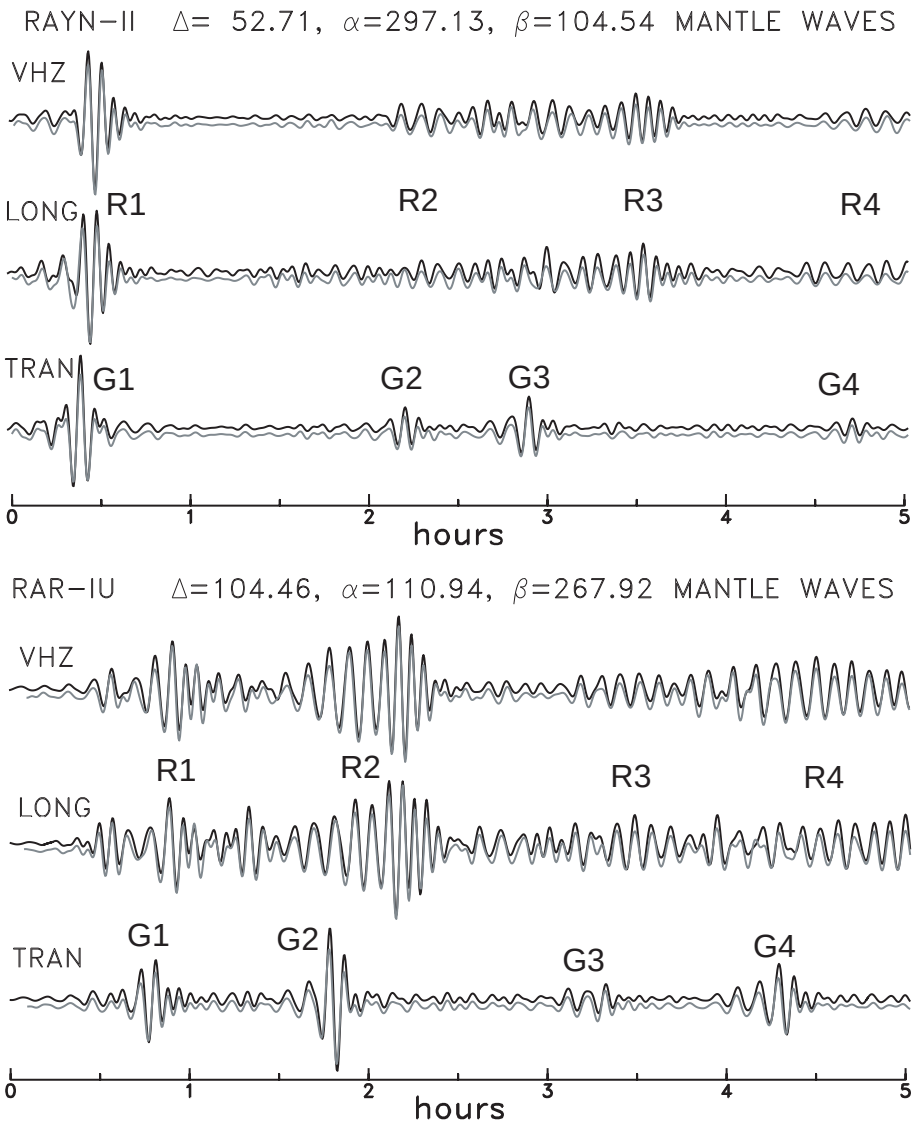

Figure 6.3: Examples of fit to seismograms achieved using the source model determined in this study. Black lines show data seismograms; gray lines show synthetic seismograms for the five-source model, offset slightly for clarity. Station RAYN lies roughly in the direction of rupture propagation. The odd arrivals (minor arc and subsequent orbits) are enhanced in amplitude. Station RAR lies roughly in the direction opposite to rupture propagation. The even arrivals (major arc and subsequent orbits) are enhanced in amplitude. Δ is the distance (in $^\circ$) of the station from the earthquake. α is the azimuth of the station relative to the earthquake. β is the azimuth of the earthquake relative to the station. VHZ=vertical; LONG=longitudinal; TRAN=transverse. The zero time is as in Table 6.1.

aftershocks in this region include the Nicobar swarm of late January 2005 [*Nettles et al.*, 2005], which were primarily strike-slip and normal events in the upper plate. Our model suggests that near 8° N the Sumatra earthquake may have released a substantial portion of the stress normal to the interface but left a significant amount of stress in the fault-parallel direction, which is in the process of being accommodated as strike-slip earthquakes in the adjacent region.

Finally, it should be noted that our analysis cannot distinguish between a model with a few, discrete locations of large slip and a model with more uniform slip. However, our results are indicative of at least three, and possibly five, regions of concentrated moment release. This view is consistent with the non-uniform slip distributions obtained by *Ammon et al.* [2005] and *Ishii et al.* [2005].

6.5 Acknowledgments

We thank H. Kanamori, C. Ammon, M. Antolik, R. Bürgmann, M. Ishii, T. Lay and two anonymous reviewers for helpful comments. The GSN data analyzed were collected and distributed by the Incorporated Research Institutions for Seismology (IRIS) and the USGS. This research was supported by a Harvard University James Mills Peirce Fellowship and a National Science Foundation (NSF) Graduate Research Fellowship (VCT) and by NSF grant EAR-0207608.

6.6 Connection to Other Chapters

This chapter uses similar seismic waveform modeling as in Chapter 2 to constrain glacial earthquakes. While not directly related to work in other chapters, there is hope that using the results of Chapter 7 will help improve our knowledge of seismic velocity structure that will in turn help to better constrain the properties of large devastating earthquakes like the Sumatra earthquake.

Chapter 7

On Establishing the Accuracy of Noise Tomography Measurements

7.1 Abstract

It has previously been shown that the Green's function between two receivers can be retrieved by cross-correlating time series of noise recorded at the two receivers. This property has been derived assuming that the energy in normal modes is uncorrelated and perfectly equipartitioned, or that the distribution of noise sources is uniform in space and the waves measured satisfy a high frequency approximation. While a number of authors have successfully extracted travel time information from seismic surface-wave noise, the reason for this success of noise tomography remains unclear since the assumptions inherent in previous derivations do not hold for dispersive surface waves on the Earth. Here, we present a simple ray-theory derivation that facilitates an understanding of how cross correlations of seismic noise can be used to

make direct travel-time measurements, even if the conditions assumed by previous derivations do not hold. Our new framework allows us to verify that cross-correlation measurements of isotropic surface-wave noise give results in accord with ray-theory expectations, but that if noise sources have an anisotropic distribution or if the velocity structure is non-uniform then significant differences can sometimes exist. We quantify the degree to which the sensitivity kernel is different from the geometric ray and find, for example, that the kernel width is period-dependent and that the kernel generally has non-zero sensitivity away from the geometric ray, even within our ray theoretical framework. These differences lead to usually small (but sometimes large) biases in models of seismic-wave speed, and we show how our theoretical framework can be used to calculate the appropriate corrections. Even when these corrections are small, calculating the errors within a theoretical framework would alleviate fears traditional seismologists may have regarding the robustness of seismic noise tomography.

7.2 Introduction

In 2001, *Lobkis and Weaver* [2001] showed that the cross-correlation of signals from two receivers in a diffuse acoustic field yields the Green's function between the two receivers. They provided two plausibility arguments and a complete derivation of this property, all relying at least partially on the definition of a diffuse field as having uncorrelated and random modal amplitudes with equal variances, or alternatively that the energy in normal modes is uncorrelated and perfectly equipartitioned. Since this initial derivation, other derivations of the "noise-correlation" property have been

made under different assumptions. Using a reciprocity theorem, *Wapenaar* [2004] and *Wapenaar et al.* [2006] have shown that the same property holds for a general elastodynamic, inhomogeneous medium if the noise sources are numerous, well distributed and uncorrelated. Using a stationary-phase approximation, *Snieder* [2004] and *Snieder et al.* [2006] have also demonstrated that the property holds for a uniform-velocity medium with locally isotropic noise, and that equipartitioning of modal energy is not required. It has also recently been pointed out by a number of authors [*Roux et al.*, 2005; *Chavez-Garcia et al.*, 2005; *Chavez-Garcia and Luzon*, 2005; *Sanchez-Sesma and Campillo*, 2006; *Sanchez-Sesma et al.*, 2006; *Nakahara*, 2006] that the essential points of the noise correlation property have been known since the seminal work of *Eckart* [1953], *Aki* [1957], *Claerbout* [1968] and *Cox* [1973], and that the property has simply been rediscovered in a new context. All derivations of the 'noise correlation' property find that under certain favorable conditions, the Green's function between two stations can be obtained from the cross correlation of noise.

The existence of this noise-correlation property has led a number of authors to apply the idea to a variety of physical systems, including the Earth. By cross-correlating time series of seismic coda [*Campillo and Paul*, 2003] or ambient seismic noise [*Shapiro and Campillo*, 2004], these initial applications demonstrated that a time series resembling the Green's function can be obtained from real seismic noise, and moreover that path-average seismic velocities measured using noise-correlation techniques agree well with those measured using traditional earthquake-based approaches. More recently, numerous studies have utilized multiple station-station pairs to create regional models of Rayleigh-wave group and phase velocity [e.g., *Shapiro et al.*, 2005; *Sabra et al.*,

2005; *Yao et al.*, 2006; *Yang et al.*, 2007; *Benson et al.*, 2007; *Cho et al.*, 2007]. While noise-correlation tomography offers several advantages over traditional surface-wave techniques, most notably independence from earthquake occurrence and the ability to use shorter period waves, the Earth does not fully comply with the assumptions inherent in the derivations described above and the implications of this fact should be understood. Specifically, in the Earth, velocity is not uniform, sources are not isotropically distributed, and modal energy is not equipartitioned. In fact, strong directional dependence (and hence anisotropic distribution) of ambient noise sources has been partially characterized by *Stehly et al.* [2006] and *Yang and Ritzwoller* [2008]. *Yang and Ritzwoller* [2008] show (using numerical simulations) that the error due to this dependence is often small. A number of authors [e.g., *Derode et al.*, 2003; *Larose et al.*, 2006; *Yang and Ritzwoller*, 2008] have also shown with numerical or experimental simulations that a time series resembling the Green's function is often obtained through cross-correlation. However, much of the literature does not clearly distinguish between the ability to obtain a Green's function-like time series and the ability to make a meaningful travel-time measurement on it; moreover, the literature lacks a simple analytical approach to the problem of quantifying the effects of non-uniformity of velocities and noise sources in tomographic travel-time measurements. This gap in the current literature motivates the present work.

In this work, we focus on understanding why it is possible to make travel-time measurements on direct arrivals of correlated noise even with a non-uniform distribution of noise sources, a non-uniform velocity structure and potentially dispersive waves. To achieve this goal, in Section 7.3.1, we first present a simple ray-theoretical

derivation that explains the relationship between a standard cross-correlation measurement of noise and the ray-theoretical travel time between the pair of stations. Using this new approach, we can then evaluate the success of a travel-time measurement without resorting to numerical simulations. We are thus able to easily explore a variety of situations in which the success of these measurements is not clear a priori and furthermore give a quantitative assessment of the errors accrued. In Section 7.3.3, we then show that when noise sources are uniformly (isotropically) distributed and the medium has uniform velocities, our approach becomes approximately equivalent to a stationary-phase approach like that of *Snieder* [2004] and we therefore recover similar conclusions regarding the success of noise tomography applications. Under an infinite-frequency approximation, our results simplify considerably, allowing one to assess the validity of a travel-time measurement with virtually no computation. Finally, in Section 7.4, taking advantage of the new approach, we present a few examples that exemplify the types of issues that commonly arise and suggest a method of correcting for these (typically small but occasionally large) errors between the actual station-station travel time and the time measured by standard correlation measurements.

7.3 Theoretical Development for Noise Correlation Measurements

7.3.1 An Analytic Description of the Travel-Time Measurement of Distributed Noise

In this section, we provide a simple analysis of how the cross-correlation of noise recorded at two seismic stations can be used to make a meaningful travel-time measurement. In this analysis, we do not make the common assumptions of a uniform noise distribution, a uniform velocity medium, or equipartition of energy, but instead make assumptions that are perhaps more reasonable for the Earth. Specifically, we assume that there exist potentially frequency-dependent noise sources distributed in space with density $\rho_S(\boldsymbol{x}, \omega)$ (as a function of position $\boldsymbol{x}$ and at each frequency ω) that send waves along straight ray paths through a potentially dispersive medium, and these sources are observed at each station x with travel time given by $\Delta t_x = \Delta x_{sx}/v_{avg-sx}$ where Δx_{sx} is the source-station distance and v_{avg-sx} is the average velocity along that path (at the given frequency). While this ray-theoretical description is quite simplified, it follows similar assumptions of many traditional tomographic studies [e.g., *Ritsema et al.*, 2004; *Kustowski et al.*, 2008] that obtain very realistic velocity structures. All shortcomings of these studies, such as the lack of finite-frequency kernels [*Montelli et al.*, 2004], lack of mode coupling [*Li and Romanowicz*, 1995], and lack of ray curvature around velocity anomalies are also shortcomings of the present work. The intention of this work is to highlight differences between noise tomography and traditional tomography, not to address issues common

to both approaches. Since all comparisons are also done with respect to ray theory (e.g. in Section 7.4), errors due to known deficiencies of ray theory should be added to the errors discussed here (possibly resulting in a smaller net error).

We make the further assumption that, as in all other derivations of a noise-correlation property [e.g., *Lobkis and Weaver*, 2001; *Snieder*, 2004; *Wapenaar*, 2004], the cross-correlation is performed over a sufficiently long time series that the cross-correlation is simply the sum of individual sinusoidal source terms, with all cross-terms canceling out. A simple example of this is as follows. Let $C_{xy}(\Delta t)$ be the normalized cross-correlation between displacement seismograms $D(t)$ at points x and y as a function of travel-time delay Δt. (This analysis applies to any component of the seismogram as long as the same component is used at both stations.) First, we consider the simple case of a deterministic wave source observed at point x with response given by $D(x,t) = \cos(\omega t + \phi)$ where ϕ is a constant phase delay, and the same source observed with relative time delay Δt_d at y such that $D(y,t) = \cos[\omega(t - \Delta t_d) + \phi]$. For this single-source situation, then

$$\begin{aligned} C_{xy}(\Delta t, \omega) &= \frac{1}{T}\int_{-T}^{T} D(x,t)D(y,t+\Delta t)dt \\ &= \cos[\omega(\Delta t - \Delta t_d)] - \frac{\sin[2\omega T]}{2\omega T}\cos[\omega(\Delta t - \Delta t_d) + 2\phi] \\ &\approx \cos[\omega(\Delta t - \Delta t_d)], \end{aligned} \tag{7.1}$$

where the last approximation is valid as long as $T \gg 1/\omega$, i.e. the correlation time T is sufficiently long, and holds for arbitrary phase shift ϕ. If ϕ is allowed to vary only over timescales longer than Δt, we observe that the same result holds by breaking the integral into shorter pieces. Thus, we find that a 'noise source' (with ϕ varying stochastically over long timescales) observed through cross correlation is identical to a

deterministic source of the same ω and Δt_d. We further observe that adding stochastic terms $N_1(t)$ and $N_2(t)$ to $D(x,t)$ and $D(y,t)$ respectively, so that the displacement responses are given by $D(x,t) = \cos(\omega t) + N_1(t)$ and $D(y,t) = \cos[\omega(t - \Delta t_d)] + N_2(t)$, does not affect the cross-correlation response as long as N_1 and N_2 are uncorrelated with each other and uncorrelated with $\cos(\omega t)$. As stated above, these facts have been shown by many previous authors and we refer the reader to those works for further discussion of the assumptions. It should be noted that Δt_d should be interpreted as the travel-time delay between when the noise source is observed at point x and point y, and can be expressed as

$$\Delta t_d = \Delta t_y - \Delta t_x = \frac{\Delta x_{sy}}{v_{avg-sy}} - \frac{\Delta x_{sx}}{v_{avg-sx}}. \tag{7.2}$$

When $D(x,t)$ and $D(y,t)$ are given by a sum of sinusoids at varying Δt_d, then Equation (7.1) immediately generalizes to a sum. For example, if there are two equal cosine source terms, with travel-time delay of Δt_{d1} and Δt_{d2} respectively, then the assumption of canceling cross-terms leads to

$$C_{xy}(\Delta t, \omega) = \cos[\omega(\Delta t - \Delta t_{d1})] + \cos[\omega(\Delta t - \Delta t_{d2})]. \tag{7.3}$$

If sources are distributed with a distribution of travel-time delays, and have unequal amplitude or prevalence, then cross-terms still cancel and this generalizes further to give

$$C_{xy}(\Delta t, \omega) = \int \rho(\Delta t_d, \omega) \cos[\omega(\Delta t - \Delta t_d)] d\Delta t_d, \tag{7.4}$$

where $\rho(\Delta t_d, \omega)$ is the 'density' of noise sources with travel-time delay Δt_d and frequency ω. Considering the effects of a source having a given amplitude and non-infinite duration in Equation (7.1) shows that this density function should weight

source amplitude variations by a factor of amplitude squared while weighting source prevalence linearly with total source duration. For example, if one noise source had an amplitude three times that of a second source, the second source would need to contribute over a duration nine times longer in order to have an equal contribution to $\rho(t,\omega) \equiv \rho(\Delta t_d, \omega)$. Equation (7.4) has a very simple interpretation. The cross-correlation response (at a given frequency) is simply the weighted sum of individual noise source terms that accounts for the prevalence of each source. In this analysis, attenuation is not explicitly considered but could be accounted for by a suitable re-definition of $\rho(t,\omega)$.

Before turning to the issue of how to determine $\rho(t,\omega)$, we discuss one final point regarding a time-windowed response. One is often interested only in a small segment of the cross-correlation (e.g. around a packet of waves near the group velocity) rather than the whole cross-correlation function. In these cases, it is standard practice to zero the data outside of the time window expected to contribute. This windowing procedure is exactly equivalent to down-weighting the sources contributing at these travel-time delays and we therefore express a windowed cross-correlation measurement as

$$\begin{aligned} C_{xy}(\Delta t, \omega, W) &= \int W(\Delta t_d)\rho(\Delta t_d, \omega)\cos[\omega(\Delta t - \Delta t_d)]d\Delta t_d \\ &= Re\left[e^{i\omega\Delta t}\int W(t)\rho(t,\omega)e^{-i\omega t}dt\right], \end{aligned} \tag{7.5}$$

where $W(t)$ is the chosen time window function.

If one knows $\rho(t,\omega)$ then one can calculate the windowed cross-correlation response using Equation (7.5), so it only remains to determine the relationship between the density of noise sources as a function of travel-time delay, $\rho(t,\omega)$, and the density of

noise sources in physical space, $\rho_S(\boldsymbol{x}, \omega)$. One can abstractly define this relationship as

$$\int_{\Delta t_1}^{\Delta t_2} \rho(\Delta t, \omega) d\Delta t = \int_{\boldsymbol{x}, \Delta t_1 \leq \Delta t \leq \Delta t_2} \rho_S(\boldsymbol{x}, \omega) |d\boldsymbol{x}|. \tag{7.6}$$

That is, the density of sources in a certain travel-time delay interval is simply the density of sources in space integrated over all spatial points with a travel-time delay within the given range. In certain important cases that will be discussed in Sections 7.3.2 and 7.3.5, the spatial density can be parameterized simply with a single scalar variable, ξ, such that one can explicitly write $\xi(\boldsymbol{x})$ as a scalar field and a constant value of ξ implies constant Δt. In this case, we similarly define

$$\int_{\xi_1}^{\xi_2} \rho_S(\xi, \omega) d\xi = \int_{\boldsymbol{x}, \xi_1 \leq \xi \leq \xi_2} \rho_S(\boldsymbol{x}, \omega) |d\boldsymbol{x}| \tag{7.7}$$

and one can then explicitly solve for $\rho(t, \omega)$ by noting

$$\begin{aligned} \int_{\Delta t_1}^{\Delta t_2} \rho(\Delta t, \omega) d\Delta t &= \int_{\xi(\Delta t_1)}^{\xi(\Delta t_2)} \rho_S(\xi, \omega) |d\xi| \\ &= \int_{\Delta t_1}^{\Delta t_2} \rho_S(\xi(\Delta t), \omega) \cdot \left| \frac{d\xi(\Delta t)}{d\Delta t} \right| d\Delta t \end{aligned} \tag{7.8}$$

so that

$$\rho(t, \omega) = \rho_S(\xi(t), \omega) \cdot \left| \frac{d\xi(t)}{dt} \right| = \rho_S(\xi, \omega) \cdot \left| \frac{dt(\xi)}{d\xi} \right|^{-1} \tag{7.9}$$

In Equation (7.9), $t(\xi)$ is the travel-time delay and is thus given by Equation (7.2) for each source point. In some instances, Equation (7.9) can be multi-valued, in which case one should sum the multi-valued contributions to ρ at each value of t.

We have now described an analytic procedure (Equation (7.5)) for measuring a windowed cross-correlation response for a given source distribution $\rho_S(\xi, \omega)$ and a given velocity distribution, through the dependence of Equation (7.2). A standard

travel-time measurement [e.g. *Ekström et al.*, 1997] of this cross-correlation is the phase lag of the cross-correlation peak and is therefore given by

$$\tau(\omega) = \frac{1}{\omega}\Big\{\phi\Big[\int W(t)\rho(t,\omega)e^{i\omega t}dt\Big] + 2\pi N\Big\}, \tag{7.10}$$

where ϕ is the phase (defined from 0 to 2π) of the complex signal and $2\pi N$ is the well-known phase ambiguity. This phase delay $\tau(\omega)$ (which has units of time) is the one measured by seismic noise tomography applications (irrespective of whether phase velocity or group velocity measurements are initially made). Differences between this quantity and the desired phase travel time are addressed below.

7.3.2 Application to Far-Field Surface Waves

When this new framework is applied to far-field surface waves, the description is especially simple. For surface waves, depth structure is integrated out so that the noise sources are effectively distributed in two dimensions (e.g. parameterized as a function of distance and azimuth). With the additional far-field assumption, sources are assumed to be along a circle infinitely far away, and an obvious natural scalar-variable parameterization is to set $\xi = \theta$ where θ is the azimuth of the source relative to the station-station line (see Figure 7.1). The density of sources is therefore described as $\rho_S(\theta,\omega)$ and its variation represents the variation in the strength of surface-wave noise sources at different azimuths. The travel-time delay, $\Delta t \equiv \Delta t_d$, for a source at a given azimuth is given by Equation (7.2), which can be rewritten as

$$\Delta t(\theta) \equiv t(\xi) = \frac{\Delta x \cos\theta}{v} + \frac{\Delta x_{sx}}{v_{avg-sy-sx}} - \frac{\Delta x_{sx}}{v_{avg-sx}}, \tag{7.11}$$

where Δx is the station-station distance, v is the average velocity on the path to station y in excess of the distance to station x (see Figure 7.1), $v_{avg-sy-sx}$ is the average velocity along the path shown in Figure 7.1, and Δx_{sx} and v_{avg-sx} are as defined in Section 7.3.1. All velocities are potentially dispersive, with implicit dependence on ω. If velocity perturbations are relatively small and well distributed, or if Δx is relatively small compared to the length-scale over which large velocity changes occur, then the second and third terms of Equation (7.11) will tend to cancel out, leaving the first term as the dominant contribution. These assumptions can fail to be achieved in many realistic situations. (They would fail if the path Δx_{sx} samples a medium with a very different average velocity compared with that sampled by the path Δx_{sy}.) However, based on typical station-station spacing used in noise tomography studies and typical velocity variations in the frequency range of interest [e.g. *Lin et al.*, 2008], both of these assumption are somewhat reasonable, and will be assumed for the remainder of Section 7.3. Thus, here, we take

$$\Delta t(\theta) \approx \frac{\Delta x \cos\theta}{v}. \tag{7.12}$$

Note that if velocity structure is non-uniform, v will have a dependence on θ and could more appropriately be written $v \equiv v(\theta)$ (but will be assumed to be spatially uniform for the rest of this section). Rearranging Equation (7.12) yields

$$\xi(\Delta t) \equiv \theta(\Delta t) = \arccos\left(\frac{v\Delta t}{\Delta x}\right). \tag{7.13}$$

Substituting Equation (7.13) into Equation (7.9) for $\rho(\Delta t)$ yields

$$\begin{aligned} \rho(\Delta t) &= \rho_S(\theta(\Delta t)) \cdot \frac{v/\Delta x}{\sqrt{1-(v\Delta t/\Delta x)^2}} \\ &= \rho_S(\theta) \cdot \frac{v/\Delta x}{|\sin\theta|}. \end{aligned} \tag{7.14}$$

$\rho(\Delta t)$ is the quantity that determines how different noise sources are weighted in their contribution to the travel-time measurement of Equation (7.10). It therefore represents the sensitivity to a given physical distribution of sources ρ_S. Substituting Equation (7.14) into Equation (7.10) thus yields the desired result

$$\tau(\omega) = \frac{1}{\omega}\Big\{\phi\Big[\int \frac{W(t)\rho_S(\theta(t))v/\Delta x}{\sqrt{1-(vt/\Delta x)^2}} e^{i\omega t} dt\Big] + 2\pi N\Big\}, \tag{7.15}$$

i.e. the travel-time measured from a cross-correlation measurement of an arbitrary distribution of far-field surface-wave noise sources in a medium with a given velocity structure. (Note the dependence of ρ_S, ρ and v on ω is left implicit in Equation (7.14) and henceforth. The meaning of infinite density points will be discussed in Section 7.3.4.) See Figure 7.2 for examples of various $\rho(\Delta t)$.

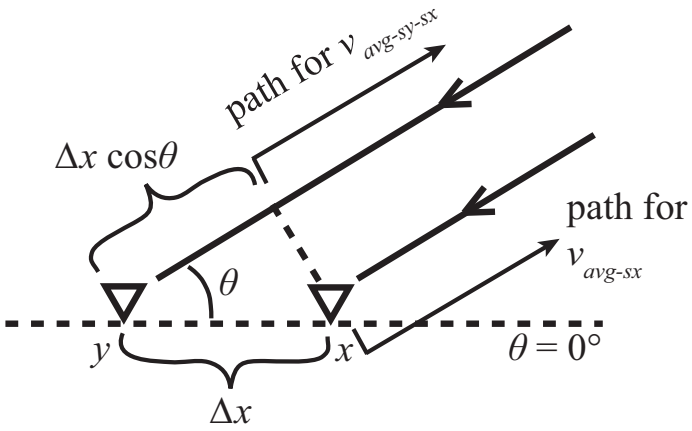

Figure 7.1: Schematic of the geometry considered. Stations x and y are separated by distance Δx, the long dotted line represents the great-circle path connecting the stations, θ is the azimuth of the noise source relative to the station-station path, and the difference in distance from the source to the two stations is given by $\Delta x \cos\theta$ for a source located infinitely far away. The average velocity along the $\Delta x \cos\theta$ path is given by v, and the remaining paths have average velocities $v_{avg-sy-sx}$ and v_{avg-sx} as shown.

When sources are not located infinitely far away from the stations but are instead

at distance r, we can modify our results as follows. Treating $\Delta x/r$ as a small parameter and v as constant, we expand Equation (7.2) to include one higher-order term, yielding

$$\Delta t(\theta, r) \approx \frac{\Delta x}{v} \cos(\theta) \cdot \left[1 - \frac{1}{8} \left(\frac{\Delta x}{r} \right)^2 \sin^2 \theta \right]. \tag{7.16}$$

It is clear from Equation (7.16) that as long as $r \gtrsim 5\Delta x$, the error introduced by using Equation (7.12) will be relatively minor, with an error to Δt of less than $1/(8 \cdot 5^2) \approx 0.5\%$. Since velocity perturbations of interest are also small, this approximation error may be important for sources very close to the stations (e.g. at $r/\Delta x = 2$ the error is as large as 3.1%), and the effect can be accounted for indirectly by modifying the true density $\rho_S(\theta, r)$ so that it represents an effective 'infinite distance' density $\rho_S(\theta) = M(\theta, r) \cdot \rho_S(\theta, r)$. For this transformation,

$$\begin{aligned} M(\theta, r) &= \left| \frac{\partial \theta(\Delta t, r)}{\partial \Delta t} \Big/ \frac{d\theta(\Delta t, \infty)}{d\Delta t} \right| \\ &= \left| \frac{d\Delta t(\theta, \infty)}{d\theta} \Big/ \frac{\partial \Delta t(\theta, r)}{\partial \theta} \right| \\ &\approx \left[1 - \frac{1}{8} \left(\frac{\Delta x}{r} \right)^2 (2 - \sin^2 \theta) \right]^{-1}, \end{aligned} \tag{7.17}$$

with $\Delta t(\theta, r)$ being the travel-time delay at azimuth θ and distance r. Equation (7.17) further shows that the effect of the multiplicative correction $M(\theta, r)$ is to enhance density in the vicinity of the station-station path ($\theta \sim 0$), which slightly helps to localize the cross-correlation peak (compare the solid blue and dashed red curves in Figure 7.2a). If multiple distances r are represented, as is likely the case in the Earth, then the correction factor can be averaged over the distance range of interest,

$$\rho_S(\theta) = \int M(\theta, r) \rho_S(\theta, r) dr. \tag{7.18}$$

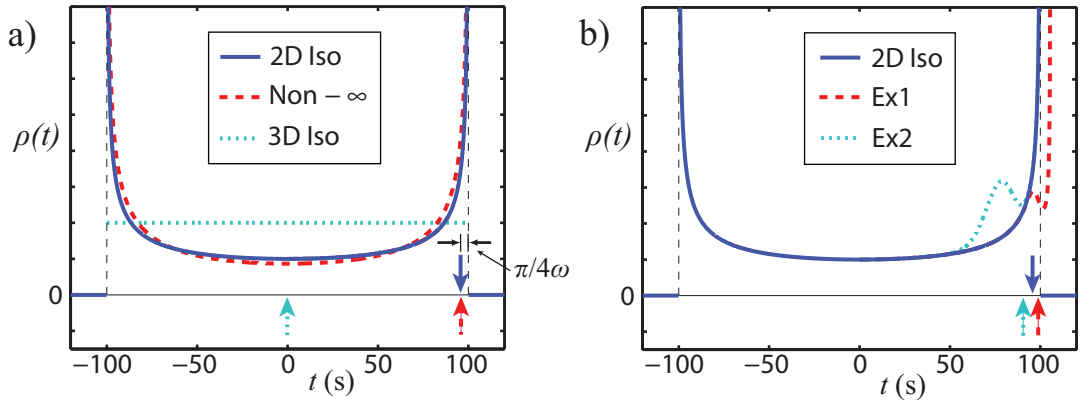

Figure 7.2: Density function vs. travel-time delay, $\rho(t) \equiv \rho(\Delta t_d, \omega)$, plotted for different situations, all with a station spacing of 400 km and a uniform background velocity of 4 km/s. Since only phases are measured, absolute amplitudes shown are arbitrary. The colored arrows along the zero-line denote the travel-time measurement (Equation (7.10)) of the respective $\rho(t)$ at a period of 40 s and with a broad windowing function around the expected (positive) travel time. (a) The blue solid line is for the 2D isotropic case ("2D Iso"); the red dashed line is for 2D isotropic but sources a finite distance away ("Non-∞"); and the cyan dotted line is for the 3D isotropic case ("3D Iso"). The "Non-∞" case is plotted using the approximation of Equation (7.17) with $r/\Delta x \approx 0.7$, and is re-normalized to make comparison easier. For $r/\Delta x \gtrsim 3$, the "Non-∞" line would be indistinguishable from the blue line. The actual measured travel times are 94.8 s for "2D Iso", 95.0 s for "Non-∞, and 0.0 s for "3D Iso". As expected from Equation (7.21), both "2D Iso" and "Non-∞" are shifted by close to $\pi/4\omega = 5$ s from the station-station travel time of 100 s. (b) The blue solid line, again, is the 2D isotropic case for comparison; the red dashed line is for the -1 km/s perturbation case of the first example of Section 7.4 ("Ex1"); and the cyan dotted line is for the second example of Section 7.4 ("Ex2"). When the red and cyan lines cannot be seen, it is because they are indistinguishable from the blue line. The actual measured travel times are 96.8 s for "Ex1", and 92.3 s for "Ex2".

7.3.3 Derivation of the Noise Correlation Property for Isotropic Surface-wave Noise

Previous three-dimensional (3D) results like those of *Lobkis and Weaver* [2001] and *Roux et al.* [2005] imply that the cross correlation $C_{xy}(t)$ is related to the (displacement) Green's function $G_{xy}(t)$ by

$$\frac{C_{xy}(t)}{dt} \equiv C'_{xy}(t) \approx -G_{xy}(t) + G_{xy}(-t) \tag{7.19}$$

and take a time derivative of the cross-correlation to arrive at an acausal Green's function. Since a time derivative is equal to multiplication by $i\omega$ in the frequency domain, this effectively results in a phase shift of $-\pi/2$ at each period. To obtain $G_{xy}(t)$ from the acausal Green's function, the result is then either averaged or (more commonly) the larger of the positive and negative signals is taken as representative. In order to go from the (e.g. vertical-vertical) Green's function $G_{xy}(t)$ to a surface-wave phase travel time, one performs a phase shift $\pi/4$ towards zero (a negative shift at positive t and vice versa) to account for the asymptotic far-field representation of the (2D) surface-wave Green's function [*Dahlen and Tromp*, 1998]. The phase travel time is then given by the time delay at the peak of the narrow-band filtered signal at a given period (up to a phase shift of 2π). The multiple phase shifts (including a shift of π for the negative sign) result in a net $-\pi/4$ shift for negative t and $+\pi/4$ for positive t in going from the original cross-correlation to the phase travel time.

We now show that this net phase shift is approximately correct but that the theoretical motivations for this result within the literature [*Sabra et al.*, 2005; *Yao et al.*, 2006; *Benson et al.*, 2007; *Lin et al.*, 2008], whether based on Equation (7.19)

or otherwise, are misleading. The essential reason that many previous derivations do not strictly apply to the travel-time measurement of surface waves is that they assume an isotropic incidence of the measured waves in 3D, whereas surface waves are waves that inherently travel in 2D since the third dimension (depth) is integrated out (and are waves due to sources primarily near the free surface). Since isotropic incidence of waves in 3D does not imply the same noise correlation properties as isotropic incidence of waves in 2D (see Section 7.3.5), derivations assuming 3D isotropic noise do not apply to measurements of isotropic surface-wave noise. The surface-wave results of *Snieder* [2004] do not share this same problem but instead only apply in the infinite frequency limit and therefore cannot easily be interpreted when measuring waves with a given finite frequency, ω.

In order to properly understand why previous surface-wave studies have been able to obtain reasonable travel-time measurements, we apply the results of Section 7.3.2. Assuming v is spatially uniform, Equation (7.14) allows the distribution of noise sources in space to be mapped into a distribution of sources in travel-time delay. If the sources are randomly (isotropically) distributed in azimuth, then $\rho_S(\theta)$ is constant. Choosing for convenience a normalization of 1 over the interval $0 \leq \theta \leq \pi$, i.e., $\int_0^\pi \rho_S(\theta) d\theta = 1$, then $\rho_S = 1/\pi$ and Equation (7.14) yields

$$\rho(\Delta t) = \frac{v/\Delta x}{\pi |\sin\theta|} = \frac{v/\Delta x}{\pi\sqrt{1-(v\Delta t/\Delta x)^2}}. \tag{7.20}$$

As shown in Appendix C, substituting Equation (7.20) into Equation (7.10) for $\tau(\omega)$ gives

$$\tau(\omega) \approx \frac{\Delta x}{v} - \frac{\pi}{4\omega} + \frac{2\pi N}{\omega} \tag{7.21}$$

for positive time delay and similarly

$$\tau(\omega) \approx -\left[\frac{\Delta x}{v} - \frac{\pi}{4\omega}\right] + \frac{2\pi N}{\omega}, \tag{7.22}$$

for negative time delay (also see Figure 7.2). Thus, we obtain approximately the same $\pi/4\omega$ phase shift as previously found, but without the problems inherent in applying those results to travel-time measurements of surface waves. Equations (7.21) and (7.22) apply strictly only in the same infinite frequency limit as in *Snieder* [2004], but Equation (A4) of Appendix C applies at all ω and one can easily compute the error accrued from the infinite frequency approximation, as plotted in Figure 7.3a for a positive windowing function (see Appendix C). This error, which is due to the errors in using the asymptotic approximations to the Bessel and Struve functions, is similar but not identical to the error in using a far-field approximation for traditional source-station tomography. As shown in Figure 7.3a, this error is significant for relatively long period (low frequency) waves and small station-station spacing (but depends on the windowing function used). For example, choosing $\Delta x = 100$ km, $v = 4$ km/s and $T \equiv 2\pi/\omega = 10$ s, would yield $\omega/(v/\Delta x) = 15.71$ and therefore a 0.9% error in the travel-time measurement if the infinite frequency approximation were used. To our knowledge, no papers in the existing noise tomography literature account for this error, which can be comparable to the few percent variations in velocities that typically occur in the Earth. Most authors [e.g. *Yao et al.*, 2006] simply throw away data for which station-station spacing is small rather than account for the correction suggested here. Including this data may improve tomographic resolution.

One may note that it has been pointed out by *Nakahara* [2006] that a Hilbert transform should be applied to the cross-correlation in order to obtain the (displace-

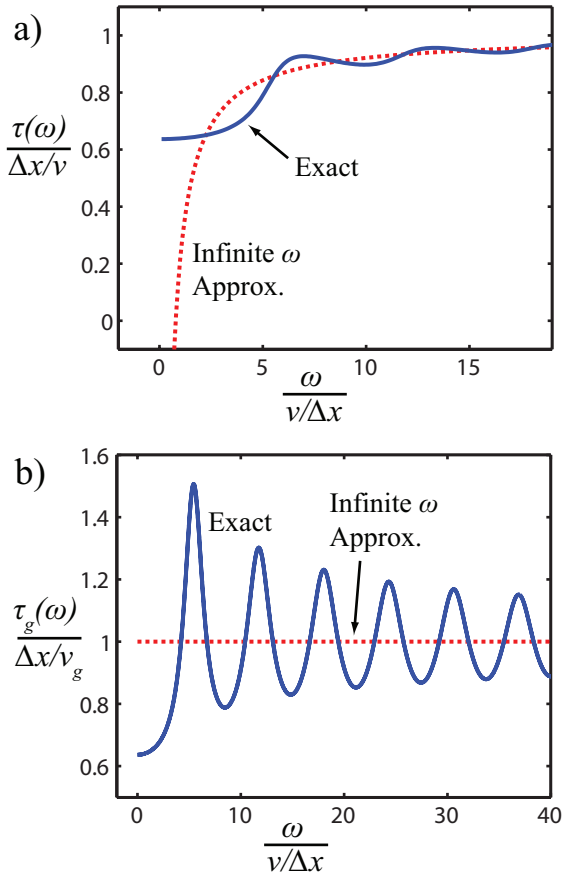

Figure 7.3: (a) Travel-time measurement $\tau(\omega)$ normalized by $\Delta x/v$ as a function of frequency ω normalized by $v/\Delta x$. The blue solid line is the exact result as given by Equation (C.4) for a strictly positive (boxcar) windowing function. The red dotted line is the high frequency approximation given by Equation (7.21) that is equivalent to a phase shift of $-\pi/4\omega$ (for positive time delay). For both curves, it has been assumed that the $2\pi N/\omega$ phase ambiguity has been properly accounted for. (b) Group travel time measurement $\tau_g(\omega)$ normalized by $\Delta x/v_g$ (where v_g is group velocity) as a function of frequency ω normalized by $v/\Delta x$. The blue solid line is the exact result calculated by substituting Equation (C.4) (with the same positive windowing function) into Equation (7.23). The red dotted line is the high frequency approximation calculated by substituting Equation (7.21) into Equation (7.23).

ment) Green's function, but that step is unnecessary since the phase information has already been obtained without needing to calculate the Green's function as an intermediate step. One should also note that although group velocity studies [*Shapiro et al.*, 2005; *Yang et al.*, 2007; *Benson et al.*, 2007; *Cho et al.*, 2007] do not initially arrive at the phase travel time, they make group velocity measurements based on this same phase travel time and are therefore affected in the same way. In general, the group travel time can be expressed in terms of the phase travel time as

$$\tau_g(\omega) = \tau(\omega) + \omega \cdot (d\tau/d\omega). \tag{7.23}$$

Interestingly, in the high frequency approximation (substituting Equation (7.21)), the group travel time is then given by

$$\tau_g(\omega) \approx \Delta x/v \cdot (1 - \omega/v \cdot (dv/d\omega)) = \Delta x/v_g \tag{7.24}$$

(for positive time delay), where v_g is group velocity, and therefore does not have an apparent time shift due to the cross-correlation measurement. However, this lack of apparent time shift is not a feature of the general expression (using Equation (C.4) rather than Equation (7.21) to calculate τ_g), which has large deviations from $\Delta x/v_g$ as shown in Figure 7.3b even when $\omega/(v/\Delta x)$ is relatively large. For example, choosing $\Delta x = 100$ km, $v = 4$ km/s and $T = 5$ s then $\omega/(v/\Delta x) \approx 31.4$ but there is still a $\approx 10\%$ error in assuming $\tau_g = \Delta x/v_g$. As for phase travel-time measurements, this error depends on the windowing function used.

7.3.4 An Infinite Frequency Description

So far, we have discussed how noise correlation measurements can be made on waves of a given frequency. It is often useful from both a practical and pedagogical standpoint to consider the infinite frequency limit since the description is considerably simpler in this limit. Taking the limit as $\omega \to \infty$ of Equation (7.10) for $\tau(\omega)$, one immediately recognizes that if there exist infinite-density points of $\rho(\Delta t)$ in Equation (7.14) then these points completely determine the cross-correlation response of Equation (7.10) as these points effectively act as delta functions in picking out travel times. These infinite-density points correspond to stationary travel-time delay points, making this description analogous to a stationary-phase approximation description like that utilized by *Snieder* [2004]. However, the relative simplicity of our approach allows quantitative examination of the conditions under which noise-correlation measurements give reasonable travel-time measurements. A few simple examples of this are now given.

When noise is isotropically distributed in 2D, then ρ_S is constant and Equation (7.14) has infinite density points at $\theta = 0$, π or equivalently $\Delta t = \pm \Delta x / v$, consistent with the limit as $\omega \to \infty$ of Equations (7.21) and (7.22). Thus, we immediately recover the result that the cross-correlation has a response at the (positive and negative) travel-time delay between the two stations.

In the framework of our formulation, the infinite-frequency cross-correlation measurement can fail to retrieve the expected station-station travel-time delay either because $\rho(\Delta t)$ achieves an infinite response at time delays other than $\Delta t = \pm \Delta x / v$ or because $\rho(\Delta t)$ achieves a less-than-infinite response at $\Delta t = \pm \Delta x / v$. These fail-

ures can occur due to a non-uniform source distribution $\rho_S(\theta)$ or due to a non-uniform velocity distribution $v(\theta, r)$. For example, if $\rho_S(\theta)$ drops to zero at $\theta = 0$ and $\theta = \pi$ then $\Delta t = \pm \Delta x / v$ may not have infinite $\rho(\Delta t)$ and the travel-time measurement will instead yield a value near the average Δt of $\rho(\Delta t)$ (or of $W(\Delta t)\rho(\Delta t)$ if a windowing function is used as well). On the other hand, the velocity distribution $v(\theta, r)$ can easily be such that $\Delta t(\theta)$ has multiple stationary points, thus giving additional Δt for which $\rho(\Delta t)$ is infinite. In these cases, one must take a limit of Equation (7.10) to determine which infinite values are most important.

7.3.5 Noise Correlation for 3D-Isotropic Noise

Many previous authors have discussed the relationship between the cross correlation and the Green's function when noise is distributed isotropically in 3D [*Lobkis and Weaver*, 2001; *Snieder*, 2004; *Roux et al.*, 2005; *Nakahara*, 2006]. However, none of these descriptions addresses the case when this 3D-distributed noise is dispersive in nature (with different frequency waves traveling at different velocities), and more importantly they do not discuss whether meaningful travel times can be measured in this case. While the dispersion of (3D) body waves is less important than for (2D) surface waves, at least a small amount of physical dispersion exists through the dispersive effects of attenuation and this fact makes it of interest to consider the case of dispersive 3D-distributed sources. Due to the different dimensionality, it will be shown that a very different conclusion must be made about the possibility of measuring travel times from standard noise correlation measurements when sources are distributed isotropically in 3D. (Unlike previous work, we only discuss implications for

travel-time measurements and do not discuss implications for the related but different problem of Green's function reconstruction.)

Before continuing, the applicability of this 3D-isotropic description should perhaps be commented upon. Most sources of seismic energy occur near the surface [e.g. *Snieder*, 2004; *Kedar et al.*, 2008]; scattering of seismic energy is thought to be more efficient in the near-surface heterogeneous lithosphere [e.g. *Campillo and Paul*, 2003; *Larose et al.*, 2006]; and the increase of seismic velocities with depth effectively confines most seismic energy to (2D) surface waves. Thus, it is evident that most applications of seismic noise tomography are not well described by sources being evenly distributed in 3D and these sources also do not excite the Earth's normal modes equally. The bulk of current noise tomography applications, including all applications that explicitly measure travel times of surface waves, are therefore much better approximated with the 2D surface-wave description of Sections 7.3.2-7.3.4. However, there may be important applications in which noise sources are uniformly distributed in 3D, especially in smaller-scale industrial applications where noise sources could potentially be placed in such a configuration.

For 3D-distributed far-field sources in a uniform velocity 3D medium, the spatial density function $\rho_S(\boldsymbol{x}, \omega)$ can be written as $\rho_S(\theta, \phi, \omega)$ where θ is the polar angle and ϕ is the azimuth with respect to the station-station line. If, as in Section 7.3.2, we assume that Equation (7.12) applies, then the parameterization $\xi = \theta$ still works and we can again consider ρ_S parameterized as $\rho_S(\theta, \omega)$. For isotropic noise in this 3D case, $\rho_S(\theta, \phi, \omega)$ is constant so that performing an integration over ϕ yields $\rho_S(\theta, \omega) = |\sin\theta|$. Substituting this into Equation (7.14) then shows that

$\rho(t) \equiv \rho(t,\omega)$ is constant between $\pm\Delta x/v$ (see Figure 7.2). Putting this $\rho(t)$ into Equation (7.10) shows that $\tau(\omega) = 0 + 2\pi N/\omega$, i.e. the standard noise-correlation travel-time measurement yields a travel time of zero, and is therefore independent of any useful travel-time information. (No window is used since all delay times between $\pm\Delta x/v$ contribute equally.) A group velocity measurement would similarly give a group time-lag of zero. If sources were not exactly isotropically distributed, then the region with slightly higher $\rho(t)$ would contribute more to the phasing and would result in a phase shift centered at this travel-time delay $t_{\rho+}$ (up to a $2\pi N$ phase shift). The travel time resulting from a phase velocity measurement would be $t_{\rho+}$; a group velocity measurement would yield the associated time delay $t_{\rho+} + \omega \cdot (dt_{\rho+}/d\omega)$. Thus, the travel-time curve resulting from both phase and group velocity measurements would have no relation to the velocity structure between the stations but would instead give information about the anisotropy of the source distribution. This analysis should caution the potential user of 3D isotropic noise that if one wants to extract useful travel-time information, non-standard techniques for measuring phase or group travel times will be necessary. Again, it should be kept in mind that this section's analysis is for a uniform velocity 3D medium in which surface waves are not important, a situation that does not obviously apply to the Earth.

7.4 Examples of Applying the New Approach

Perhaps the most important conclusion of Section 7.3 is that most of the sensitivity to phase travel time occurs close to the station-station line in the 2D-isotropic case, unlike the 3D-isotropic case where the sensitivity is strong away from the station-

station line. Yet simply using the ray theory approximation, as done here, it is already the case that sensitivity to velocity structure is non-zero away from the station-station line (see Figure 7.2), and this sensitivity accounts for the approximate $\pi/4$ phase shift towards zero in the 2D-isotropic case. While some of this has been demonstrated in some recent numerical experiments [e.g., *Yang and Ritzwoller*, 2008; *Lin et al.*, 2008], no existing work demonstrates how to calculate this sensitivity without performing numerical experiments. It would be useful, for example, to calculate a phase sensitivity kernel as in traditional surface wave tomography [e.g., *Dahlen and Tromp*, 1998; *Zhou et al.*, 2004]. Unfortunately, since $\rho(t)$ is a function of the derivative of travel-time delay with azimuth and not the travel-time delay itself (see Equation (7.9)), our approach shows that one cannot describe a phase travel-time perturbation as an integral over a kernel multiplied by velocity perturbations. However, since $\rho(t)$ gives the travel-time delay through Equation 7.10), $\rho(t)$ itself can be thought of as a sensitivity kernel. So, given a velocity distribution, one can express the travel-time delay t as a function of azimuth as in Equation (7.11), take the derivative, and arrive at $\rho(t)$ directly which then yields the phase travel time as described by Equation (7.10). For a noise source distribution far from 2D isotropic, one must also perform analysis like that of *Stehly et al.* [2006] or *Yao and van der Hilst* [2008] to determine the distribution of sources to arrive at $\rho(t)$ as described by Equation (7.9). Using this forward modeling of the phase travel time iteratively with noise tomography results has the potential to enhance the accuracy and reproducibility of tomographic images derived from noise tomography. Even if the calculated corrections are small, quantifying the errors arising from a noise tomography approach would assuage concerns over the

robustness of the derived images. Furthermore, the shapes of noise-tomography sensitivity kernels are different than standard finite-frequency kernels [e.g. *Zhou et al.*, 2004] regardless of whether corrections are needed.

A simple example of this sensitivity slightly away from the station-station line is shown in Figure 7.4. In this example, the stations are 400 km apart and the source distribution $\rho_S(\theta)$ is taken as constant. The velocity is uniformly 4 km/s except for a roughly Gaussian velocity perturbation, centered three quarters of the way from station 1 to station 2, with a maximum of $\Delta v_{max} = -1$, 0 and +1 km/s (respectively) and length scale of 50 km (see Figure 7.4a). Equation (7.9) for $\rho(t)$ can be evaluated for this given velocity distribution by explicitly calculating $t(\xi) \equiv \Delta t(\theta)$ with Equation (7.2). Doing this numerically and substituting the result into Equation (7.10) with a broad (130 s) windowing function centered at positive delay time gives the phase travel time. Accounting for the approximate $\pi/4$ phase shift of Equation (7.21) expected of the isotropic case and then dividing the station-station distance by this phase-corrected travel time gives the average phase velocity between the stations (see Figure 7.2b). If only the ray between the stations contributed to determining the phase velocity, the three cases would have average velocities of 3.79, 4.00 and 4.23 km/s respectively and would be independent of period. Instead, as shown in Figure 7.4b, while the uniform velocity case ($\Delta v_{max} = 0$) yields approximately the correct result (with small errors due to choice of windowing function, finite discretization of the time series, and the $\pi/4$ approximation), both non-uniform velocity cases yield phase velocities closer to 4 km/s than is predicted for sensitivity strictly on the station-station line and both cases have a significant period dependence even though

the velocity structure in the example is non-dispersive. One should note that the discrepancy is worse for lower frequencies (longer periods) since these frequencies are more sensitive to a wider range of delay times, and thus more sensitive to structure away from the station-station line.

Another simple example is given that illustrates the sensitivity to an anisotropic noise source distribution. In this example, we again take the stations to be 400 km apart and the velocity is assumed to be uniformly 4 km/s. The source distribution is taken as $\rho_S(\theta) = 1 + 2\cos^{300}[(\theta - 40^\circ)/2]$ to represent a narrow, roughly Gaussian peak of sources around $\theta = 40^\circ$ superimposed on an isotropic distribution with half the strength (see Figure 7.5a). As expected, the (phase-corrected) velocity measured is close to the expected result (4 km/s) for periods much shorter than the time delay $\Delta t_{40} \approx \Delta x(1 - \cos 40^\circ)/v \approx 23$ s, but is sensitive to the anisotropy at longer periods (see Figure 7.5b). The increase in measured phase velocity at the long-period end is also expected since Δt_{40} is still comparable to the periods considered $(2\pi/\omega)$. (At even longer periods than shown, when $2\pi/\omega \gg \Delta t_{40}$, there is a small decrease in measured phase velocity due to the excess of sources within $|\Delta t| > \Delta x/v - \pi/\omega$ but this sensitivity drops as more unaffected regions are averaged over.) The decrease in measured phase velocity for intermediate period waves is perhaps a little counterintuitive, but is due to the excess of sources being at a time delay slightly less than $9\pi/4\omega$ (or $[1 + 2\pi N]/4\omega$ for any integer N) from $\Delta x/v$ and therefore shifting the measured phase travel time towards higher values.

It should be noted that the two examples were chosen to illustrate differences between ray-theoretical expectations and actual ray-theoretical measurement for cases

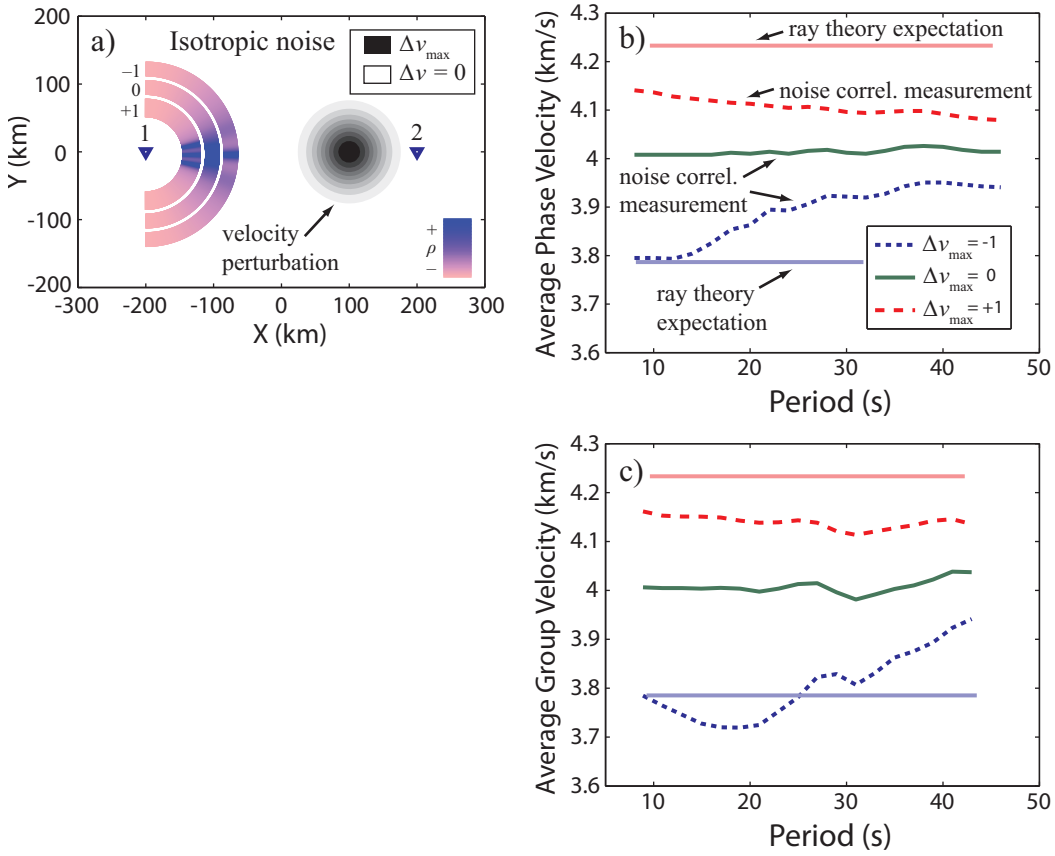

Figure 7.4: Example of phase and group velocities recovered in a non-uniform velocity medium. Panel (a) describes the geometry: the stations are triangles and the shading denotes the velocity perturbation away from 4 km/s. The colored rings surrounding station 1 denotes the azimuthal sensitivity $\rho(t(\theta))$ for the positive time delay window for the 3 cases considered, with colors ranging from light red (not sensitive, low ρ) to dark blue (sensitive, high ρ). Panel (b) describes the average phase velocity measured from station 2 to station 1, for $\Delta v_{max} = -1$, 0, and +1 (dotted blue, solid green and dashed red respectively). The average phase velocity along the station-station path is 3.79, 4.00 and 4.23 km/s respectively (as shown in matching faded lines). Whereas the average phase velocity for the uniform velocity closely approximates the expected value of 4.00 km/s, for both non-uniform velocity cases the velocities are different than the station-station path average. Panel (c) describes the average group velocity for the same configuration. Line colors and styles are as in panel (b). Since the example medium given is non-dispersive, the average group velocity along the station-station path is also 3.79, 4.00 and 4.23 km/s respectively.

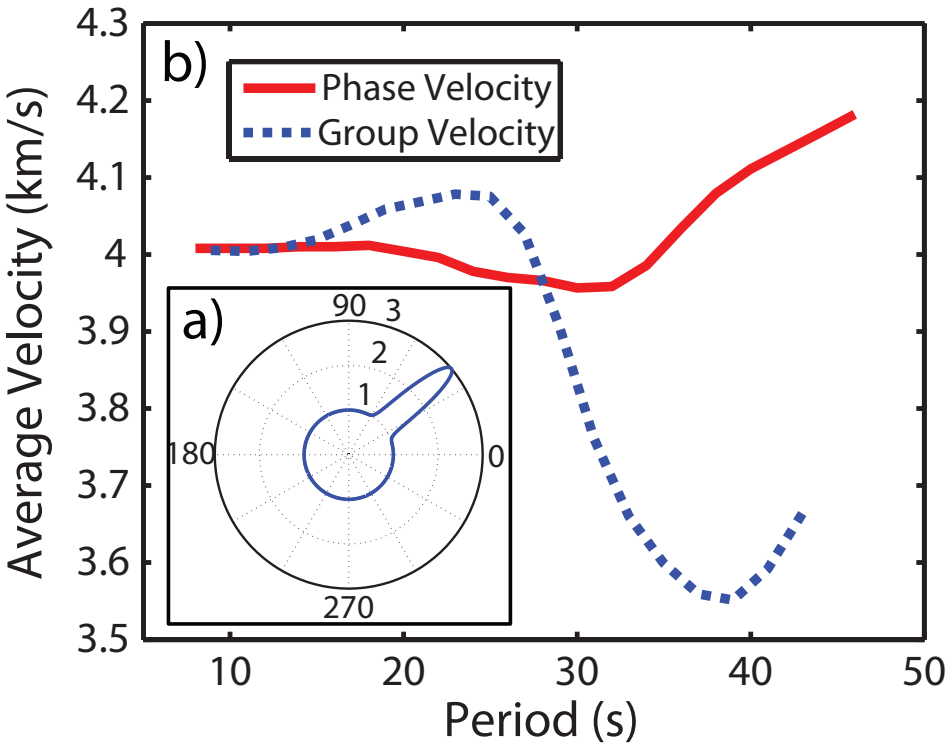

Figure 7.5: Example of phase and group velocities recovered when the source distribution is anisotropic. Inset (a) describes the noise source anisotropy, with $\rho_S(\theta)$ plotted in polar coordinates (with θ in degrees). Main panel (b) describes the average phase and group velocity measured around the expected (positive) travel time. Since the example medium is non-dispersive, the ray theory expectation is 4.0 km/s, independent of period.

that have significant differences. For many arbitrary distributions of noise sources and/or velocity structures, the differences are much smaller and therefore unimportant compared to other uncertainties in the measurements. For example, plotted in Figure 7.6 are 20-s and 40-s phase and group velocity measurements for the same anisotropic source distribution of the previous paragraph, except with anisotropy centered at different azimuths θ. Comparison of these curves shows that measurements for $\theta = 80^\circ$ are much closer to the expected 4 km/s compared to measurements for $\theta = 30^\circ$ or $\theta = 40^\circ$, and so would be unlikely to cause significant problems. However, the fact that the azimuth of the source anisotropy changes the measured travel times (at a given period) means that if source anisotropy is not correctly accounted for then it will be improperly mapped into anisotropic velocity structure.

The above conclusions apply equally well to group velocity studies as to phase velocity studies. The primary difference is that group velocity studies do not need to apply the $\approx \pi/4$ phase shift (see Equation (7.24)). In spite of this, it is important to recognize that group velocities are just as much affected by the energy arriving (slightly) away from the station-station line (see Figure 7.4c and Figure 7.5b) that accounts for the $\approx \pi/4$ phase shift in phase travel time. When the calculated travel times are significantly different than expected, group velocity tomographic images should also be corrected for this sensitivity to velocity structure away from the station-station line.

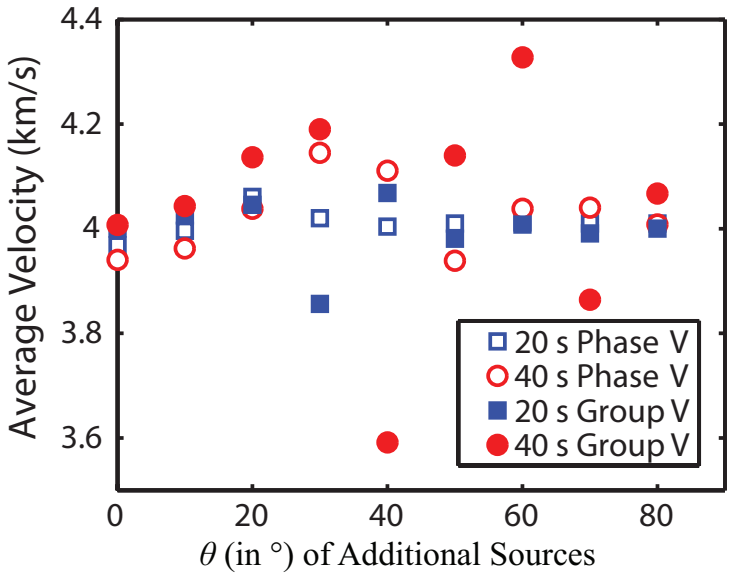

Figure 7.6: Example of 20-s and 40-s phase and group velocities recovered when the source distribution is anisotropic like in Figure 7.5 but with the additional sources at different azimuths, ranging from $\theta = 0°$ to $\theta = 80°$. As in Figure 7.5, the example medium is non-dispersive and the ray-theory expectation is 4.0 km/s, independent of period and source distribution.

7.5 Conclusions

We have presented a new, simple ray-theoretical derivation that describes the relationship between cross-correlations of seismic noise and the direct travel time measured between two stations. This new framework allows us to understand the travel-time measurement even when noise sources are potentially frequency-dependent, non-uniformly distributed, and within a dispersive, non-uniform velocity medium. Applying this new framework is relatively straightforward and shows why noise tomography has been generally successful but also allows for quantification of the errors that arise in assuming isotropic noise sources, a uniform-velocity medium, and infinite frequency waves. Using our approach, it is possible to correct for these factors. Since these corrections are not particularly computationally intensive, we suggest that future researchers should compute the corrections and implement them in areas where the corrections are significant. Doing this may, for example, allow a larger percentage of data to be useful than is currently used in most applications. Additionally, calculating these corrections, even if mostly negligible, would give seismic noise tomography results a more theoretically-sound basis and alleviate fears traditional seismologists may have regarding the robustness of noise tomography-derived images.

7.6 Acknowledgments

The author would like to thank C. A. Dalton, A. M. Dziewonski, M. G. Sterenborg, H. Kanamori, G. Ekström, H. Yao, M. Betancourt, and J. R. Rice for helpful discussion, and M. Ritzwoller and various anonymous reviewers for constructive criti-

cism. The author also thanks editors J. Trampert and M. Diament for their patience. This research was supported by a National Science Foundation Graduate Fellowship.

7.7 Connection to Other Chapters

It is hoped that the results of this chapter will help improve our knowledge of seismic velocity structure on a variety of length scales and at many different locations, including potentially subduction zones and within glaciers. Thus, application of this chapter's results could eventually yield additional constraints on glacial earthquakes (the interest of Chapters 2 and 3), subglacial cracks (the interest of Chapter 4), and large tectonic earthquakes (like the Sumatra earthquake of Chapter 6).

Chapter 8

Conclusions

The research presented in this thesis explores a number of topics that span the fields of seismology, glaciology, solid mechanics and fluid mechanics, as well as the intersection between them. The work can be summarized as having addressed the following main questions:

- What are glacial earthquakes and what physical mechanism is responsible for them?
- Can we understand meltwater lake drainage in Greenland as resulting from turbulent hydraulic fracture?
- Can we quantitatively understand the formation of 'lake stars' as being due to the flow of lake water through slushy ice?
- Can we determine the large-scale features of the 2004 Sumatra earthquake using only well-resolved seismic data?

- How can we better understand the accuracy of noise tomography under realistic Earth conditions?

The answers to these questions have been answered in the previous chapters of this thesis, and we briefly summarize the main points here:

- Glacial earthquakes are the seismic response to large calving icebergs that release their gravitational energy partly as seismic waves in the solid Earth as they calve.

- Yes, we can successfully construct models of turbulent hydraulic fracture that make predictions that resemble observations of meltwater lake drainage in Greenland.

- Yes, modeling 'lake stars' as arising from flow through slushy ice yields predictions that agree well with field observations as well as analog laboratory experiments.

- Yes, long-period seismic data resolves the 2004 Sumatra earthquake well when up to 5 sub-sources of energy release are used, and inversion of this data gives useful constraints on the earthquake that are otherwise difficult to obtain.

- Making realistic assumptions about the distribution of noise sources and velocity structure, we retrieve a noise-correlation property similar to that derived by other authors but which has deviations from previous expectations that are often fairly small but are occasionally large and can be calculated using our approach.

Bibliography

Adachi, J. I., and E. Detournay (2002), Self-similar solution of a plane-strain fracture driven by a power-law fluid, *Int. J. Numer. Anal. Meth. Geomech.*, **26**, 579–604, doi:10.1002/nag.213.

Aki, K. (1957), Space and time spectra of stationary stochastic waves, with special reference to microtremors, *Bull. Earthq. Res. Inst.*, **35**, 415–457.

Alley, R. B., and I. M. Whillans (1991), Changes in the West Antarctic Ice Sheet, *Science*, **254**, 959–963.

Alley, R. B., T. K. Dupont, B. R. Parizek, and S. Anandakrishnan (2005), Access of surface meltwater to beds of sub-freezng glaciers: preliminary insights, *Ann. Glaciol.*, **40**, 8–14.

Ammon, C. J., et al. (2005), Rupture process of the 2004 Sumatra-Andaman earthquake, *Science*, **308**, 1133–1139.

Amundson, J. M., M. Truffer, M. P. Luthi, M. Fahnestock, M. West, and R. J. Motyka (2008), Glacier, fjord, and seismic response to recent large calving events, Jakobshavn Isbrae, Greenland, *Geophys. Res. Lett.*, **35**, L22501, doi: 10.1029/2008GL035281.

Anandakrishnan, S., and R. B. Alley (1997), Tidal forcing of basal seismicity of ice stream C, West Antarctica, observed far inland, *J. Geophys. Res.*, **102**, 15,183–15,196.

Anandakrishnan, S., and C. R. Bentley (1993), Micro-earthquakes beneath ice stream-B and ice stream-C, West Antarctica - observations and implications, *J. Glaciol.*, **39**, 455–462.

Aranson, I. S., and L. S. Tsimring (2006), Patterns and collective behavior in granular media: Theoretical concepts, *Rev. Mod. Phys.*, **78**, doi: 10.1103/RevModPhys.78.641.

Bamber, J. L., R. L. Layberry, and S. P. Gogineni (2001), A new ice thickness and bed data set for the Greenland Ice Sheet, *J. Geophys. Res.*, **106**, 33,773–33,780.

Banerjee, P., F. F. Pollitz, and R. Bürgmann (2005), The size and duration of the Sumatra-Andaman earthquake from far-field static offsets, *Science*, **308**, 1769–1772.

Bauer, A. (1961), Influence de la dynamique des fleuves de glace sur celle de l'Islandsis du Groenland, *IASH*, **54**, 578–584.

Benson, G. D., M. H. Ritzwoller, M. P. Barmin, A. L. Levshin, F. Lin, M. P. Moschetti, N. M. Shapiro, and Y. Yang (2007), Processing seismic ambient noise data to obtain reliable broad-band surface wave dispersion measurements, *Geophys. J. Int.*, **169**, 1239–1260.

Bindschadler, R. A., M. A. King, R. B. Alley, S. Anandakrishnan, and L. Padman (2003), Tidally controlled stick-slip discharge of a West Antarctic ice stream, *Science*, **301**, 1087–1089.

Bird, R. B., R. C. Armstrong, and O. Hassager (1987), *Dynamics of Polymeric Liquids*, vol. 1, 2nd ed., 649 pp., John Wiley and Sons, Inc., New York.

Brennen, C. E. (1982), A review of added mass and fluid inertial forces, *Technical report cr82.010*, Naval Civil Eng. Lab., Department of the Navy, Port Nueneme.

Brenner, M. P., L. Levitov, and E. Budrene (1998), Physical mechanisms for chemotactic pattern formation by bacteria, *Biophys. J.*, **74**, 1677–1693.

Brodsky, E. E., E. Gordeev, and H. Kanamori (2003), Landslide basal friction as measured by seismic waves, *Geophys. Res. Lett.*, **30**, doi:10.1029/2003GL018485.

Budd, W. F., and T. H. Jacka (1989), A review of ice rheology for ice sheet modeling, *Cold Reg. Sci. Tech.*, **16**, 107–144.

Buffington, J. M. (1999), The legend of A. F. Shields, *J. Hydraul. Eng.*, **125**, 376–387.

Bunger, A. P., and E. Detournay (2002), Propagation of a penny-shaped fluid-driven fracture in an impermeable rock: asymptotic solutions, *Int. J. Solids Struc.*, **39**, 6311–6337.

Bunger, A. P., and E. Detournay (2008), Experimental validation of the tip asymptotics for a fluid-driven crack, *J. Mech. Phys. Sol.*, **56**, 3101–3115.

Campillo, M., and A. Paul (2003), Long-range correlations in the diffuse seismic coda, *Science*, **299**, 547–549.

Cappelen, J., B. V. Jorgensen, E. V. Laursen, L. S. Stannius, and R. S. Thomsen (2000), The observed climate of Greenland, 1958-99 - with climatological standard normals, *Technical report 00-18*, Danish Meteorological Institute.

Chavez-Garcia, F. J., and F. Luzon (2005), On the correlation of seismic microtremors, *J. Geophys. Res.*, **110**, B11313, doi:10.1029/2005JB003671.

Chavez-Garcia, F. J., M. Rodriguez, and W. R. Stephenson (2005), An alternative approach to the SPAC analysis of microtremors: exploiting stationarity of noise, *Bull. Seismol. Soc. Am.*, **95**, 277–293.

Cho, K. H., R. B. Herrmann, C. J. Ammon, and K. Lee (2007), Imaging the upper crust of the Korean peninsula by surface-wave tomography, *Bull. Seismol. Soc. Am.*, **97**, 198–207.

Claerbout, J. F. (1968), Synthesis of a layered medium from its acoustic transmission response, *Geophys.*, **33**, 264–269.

Cox, H. (1973), Spatial correlation in arbitrary noise fields with application to ambient sea noise, *J. Acoust. Soc. Am.*, **54**, 1289–1301.

Cross, M. C., and P. C. Hohenberg (1993), Pattern-formation outside of equilibrium, *Rev. Modern Phys.*, **65**, 851–1112.

Dahlen, F. A. (1993), Single-force representation of shallow landslide sources, *Bull. Seismol. Soc. Am.*, **83**, 130–143.

Dahlen, F. A., and J. Tromp (1998), *Theoretical Global Seismology*, Princeton University Press, Princeton.

Das, S., I. Joughin, M. D. Behn, I. M. Howat, M. A. King, D. Lizarralde, and M. P. Bhatia (2008), Fracture propagation to the base of the Greenland Ice Sheet during supraglacial lake drainage, *Science*, **320**, doi:10.1126/science.1153360.

Deichmann, N., J. Ansorge, F. Scherbaum, A. Aschwanden, F. Bernardi, and G. H. Gudmundsson (2000), Evidence for deep icequakes in an Alpine glacier, *Ann. Glaciol.*, **31**, 85–90.

DeMets, C., R. G. Gordon, D. F. Argus, and S. Stein (1994), Effect of recent revisions to the geomagnetic reversal time-scale on estimates of current plate motions, *Geophys. Res. Lett.*, **21**, 2191–2194.

Derode, A., E. Larose, M. Campillo, and M. Fink (2003), How to estimate the Green's function of a heterogeneous medium between two passive sensors? Application to acoustic waves, *App. Phys. Lett.*, **83**, 3054–3056.

Desroches, J., E. Detournay, B. Lenoach, P. Papanastasiou, J. R. A. Pearson, M. Thiercelin, and A. Cheng (1994), The crack tip region in hydraulic fracturing, *Proc. R. Soc. Lond. A*, **447**, 39–48.

Detournay, E. (2004), Propagation regimes of fluid-driven fractures in impermeable rocks, *Int. J. Geomech.*, **4**, 35–45.

Dieterich, J. H. (1994), A constitutive law for rate of earthquake production and its application to earthquake clustering, *J. Geophys. Res.*, **99**, 2601–2618.

Dyskin, A. V., L. N. Germanovich, and K. B. Ustinov (2000), Asymptotic analysis of crack interaction with free boundary, *Int. J. Solids Struc.*, **37**, 857–886.

Dziewonski, A. M., and D. L. Anderson (1981), Preliminary reference Earth model, *Phys. Earth Planet. Inter.*, **25**, 297–356.

Dziewonski, A. M., T. A. Chou, and J. H. Woodhouse (1981), Determination of earthquake source parameters from waveform data for studies of global and regional seismicity, *J. Geophys. Res.*, **86**, 2825–2852.

Echelmeyer, K. A., and W. D. Harrison (1990), Jakobshavn Isbrae, West Greenland: seasonal variations in velocity - or lack thereof, *J. Glaciol.*, **36**, 82–88.

Eckart, C. (1953), The theory of noise in continuous media, *J. Acoust. Soc. Am.*, **25**, 195–199.

Ekström, G. (2006), Global detection and location of seismic sources by using surface waves, *Bull. Seismol. Soc. Am.*, **96**, 1201–1212.

Ekström, G., and E. R. Engdahl (1989), Earthquake source parameters and stress distribution in the Adak Island region of the central Aleutian Islands, Alaska, *J. Geophys. Res.*, **94**, 15,499–15,519.

Ekström, G., J. Tromp, and E. W. F. Larson (1997), Measurements and global models of surface wave propagation, *J. Geophys. Res.*, **102**, 8137–8157.

Ekström, G., M. Nettles, and G. A. Abers (2003), Glacial earthquakes, *Science*, **302**, 622–624.

Ekström, G., A. M. Dziewonski, N. N. Maternovskaya, and M. Nettles (2005), Global seismicity of 2003: centroid-moment-tensor solutions for 1087 earthquakes, *Phys. Earth Planet. Inter.*, **148**, 327–351.

Ekström, G., M. Nettles, and V. C. Tsai (2006), Seasonality and increasing frequency of Greenland glacial earthquakes, *Science*, **311**, 1756–1758, doi: 10.1126/science.1122112.

England, A. H. (1965), A crack between dissimilar media, *J. App. Mech.*, **32**, 400–402.

Erdogan, F. (1965), Stress distribution in bonded dissimilar materials with cracks, *J. App. Mech.*, **32**, 403–410.

Fahnestock, M., M. Truffer, M. Luthi, R. Motyka, J. Amundson, and J. Brown (2007), GPS and conventional surveying measurement of glacier and iceberg motion in the Jakobshavns Isbrae system, *Eos. Trans. AGU*, **88**(52), Fall Meet. Suppl., Abstract G33C-03.

Fitzgerald, S., and A. W. Woods (1994), The instability of a vaporization front in hot porous rock, *Nature*, **367**, 450–453.

Fountain, A. G., R. W. Jacobel, R. Schlichting, and P. Jansson (2005), Fractures as the main pathways of water flow in temperate glaciers, *Nature*, **433**, 618–621.

Fricker, H. A., T. Scambos, R. Bindschadler, and L. Padman (2007), An active subglacial water system in West Antarctica mapped from space, *Science*, **315**, doi: 10.1126/science.1136897.

Garagash, D. I., and E. Detournay (2005), Plane-strain propagation of a fluid-driven fracture: Small toughness solution, *J. Appl. Mech.*, **72**, 916–928.

Gioia, G., and P. Chakraborty (2006), Turbulent friction in rough pipes and the energy spectrum of the phenomenological theory, *Phys. Rev. Lett.*, **96**, doi: 10.1103/PhysRevLett.96.044502.

Glen, J. W. (1955), The creep of polycrystalline ice, *Proc. R. Soc. A*, **228**, 519–538.

Goldenfeld, N., P. Y. Chan, and J. Veysey (2006), Dynamics of precipitation pattern formation at geothermal hot springs, *Phys. Rev. Lett.*, **96**, doi: 10.1103/PhysRevLett.96.254501.

Harper, J. T., N. F. Humphrey, W. T. Pfeffer, T. Fudge, and S. O'Neel (2005), Evolution of subglacial water pressure along a glacier's length, *Ann. Glaciol.*, **40**, 31–36.

Harrison, W. D., K. A. Echelmeyer, and C. F. Larson (1998), Measurement of temperature in a margin of Ice Stream B, Antarctica: implications for margin migration and lateral drag, *J. Glaciol.*, **44**, 615–624.

Hooke, R. L. (2005), *Principles of Glacier Mechanics*, 2nd ed., Cambridge University Press, Cambridge.

Hou, T. Y., J. Lowengrub, and M. Shelley (2001), Boundary integral methods for multi-phase problems in fluid dynamics and materials science, *J. Comput. Phys.*, **169**, 302–362.

Howat, I. M., I. Joughin, S. Tulaczyk, and S. Gogineni (2005), Rapid retreat and acceleration of Helheim glacier, East Greenland, *Geophys. Res. Lett.*, **32**, doi: 10.1029/2005GL024737.

Hutchinson, J. W., and Z. Suo (1992), Mixed mode cracking in layered materials, in *Advances in Applied Mechanics*, vol. **29**, edited by J. W. Hutchinson and T. Y. Wu, pp. 63–191, Academic Press, San Diego.

Iken, A. (1981), The effect of the subglacial water pressure on the sliding velocity of a glacier in an idealized numerical model, *J. Glaciol.*, **27**, 407–421.

Iken, A., K. Echelmeyer, W. Harrison, and M. Funk (1993), Mechanisms of fast flow in Jakobshavns Isbrae, West Greenland: part I. measurements of temperature and water level in deep boreholes, *J. Glaciol.*, **39**, 15–25.

Ishii, M., P. M. Shearer, H. Houston, and J. E. Vidale (2005), Rupture extent, duration, and speed of the 2004 Sumatra-Andaman earthquake imaged by the Hi-Net array, *Nature*, **435**, 933–936.

Jellinek, H. H. G., and R. Brill (1956), Viscoelastic properties of ice, *J. App. Phys.*, **27**, 1198–1209.

Joughin, I., W. Abdalati, and M. Fahnestock (2004), Large fluctuations in speed on Greenland's Jakobshavn Isbrae glacier, *Nature*, **432**, 608–610.

Joughin, I., S. Das, M. A. King, B. E. Smith, I. M. Howat, and T. Moon (2008a), Seasonal speedup along the western flank of the Greenland Ice Sheet, *Science*, **320**, doi:10.1126/science.1153288.

Joughin, I., I. Howat, R. B. Alley, G. Ekstrom, M. Fahnestock, T. Moon, M. Nettles, M. Truffer, and V. C. Tsai (2008b), Ice-front variation and tidewater behavior on Helheim and Kangerdlugssuaq glaciers, Greenland, *J. Geophys. Res.*, **113**, F01004, doi:10.1029/2007JF000837.

Kalifa, P., G. Ouillon, and P. Duval (1992), Microcracking and the failure of polycrystalline ice under triaxial compression, *J. Glaciol.*, **38**, 65–76.

Kamb, B. (1991), Rheological nonlinearity and flow instability in the deforming bed mechanism of ice stream motion, *J. Geophys. Res.*, **96**, 16,585–16,595.

Kamb, B., and H. Engelhardt (1987), Waves of accelerated motion in a glacier approaching surge: the mini-surges of Variegated Glacier, Alaska, USA, *J. Glaciol.*, **33**, 27–46.

Kamb, B., C. F. Raymond, W. D. Harrison, H. Engelhardt, K. A. Echelmeyer, N. Humphrey, M. M. Brugman, and T. Pfeffer (1985), Glacier surge mechanism: 1982-1983 surge of Variegated Glacier, Alaska, *Science*, **227**, 469–479.

Kamb, B., H. Engelhardt, M. A. Fahnestock, N. Humphrey, M. Meier, and D. Stone (1994), Mechanical and hydrologic basis for the rapid motion of a large tidewater glacier 2. interpretation, *J. Geophys. Res.*, **99**, 15,231–15,244.

Kanamori, H., and J. W. Given (1982), Analysis of long-period seismic waves excited by the May 18, 1980, eruption of Mount St. Helens - a terrestrial monopole, *J. Geophys. Res.*, **87**, 5422–5432.

Katsaros, K. B. (1983), Convection patterns in a pond, *Bull. Amer. Meteor. Soc.*, **64**, 277–279.

Kawakatsu, H. (1989), Centroid single force inversion of seismic waves generated by landslides, *J. Geophys. Res.*, **94**, 12,363–12,374.

Kedar, S., M. Longuet-Higgins, F. Webb, N. Graham, R. Clayton, and C. Jones (2008), The origin of deep ocean microseisms in the North Atlantic Ocean, *Proc. R. Soc. A*, **464**, 777–793.

Kenneally, J. P. (2003), Crevassing and calving of glacial ice, Ph.D. thesis, University of Maine, Orono, Maine.

Knight, C. A. (1987), Slush on lakes, in *Structure and dynamics of partially solidified systems*, edited by D. E. Loper, pp. 453–465, Martinus Nijhoff, Dordrecht.

Krawczynski, M. J., M. D. Behn, S. B. Das, and I. Joughin (2009), Constraints on lake volume required for hydrofracture through ice sheets, *Geophys. Res. Lett.*, *in press*, doi:xxx.

Kustowski, B., G. Ekström, and A. M. Dziewonski (2008), Anisotropic shear-wave velocity structure of the Earth's mantle: a global model, *J. Geophys. Res.*, **113**, doi:10.1029/2007JB005169.

Lamb, H. (1953), *Hydrodynamics*, 6th ed., University Press, Cambridge.

Lamb, M. P., W. E. Dietrich, and J. G. Venditti (2004), Is the critical Shields stress for incipient sediment motion dependent on channel-bed slope?, *J. Geophys. Res.*, **113**, doi:10.1029/2007JF000831.

Lapusta, N., J. R. Rice, Y. Ben-Zion, and G. Zheng (2000), Elastodynamic analysis for slow tectonic loading with spontaneous rupture episodes on faults with rate- and state-dependent friction, *J. Geophys. Res.*, **105**, 23,765–23,789.

Larose, E., L. Margerin, A. Derode, B. van Tiggelen, M. Campillo, N. Shapiro, A. Paul, L. Stehly, and M. Tanter (2006), Correlation of random wavefields: an interdisciplinary review, *Geophys.*, **71**, SI11–SI21.

Lay, T., and T. C. Wallace (1995), *Modern Global Seismology*, 521 pp., Academic Press, San Diego.

Levine, H., and E. Ben-Jacob (2004), Physical schemata underlying biological pattern formation - examples, issues and strategies, *Phys. Biol.*, **1**, P14–P22.

Li, X. D., and B. Romanowicz (1995), Comparison of global waveform inversions with and without considering cross-branch modal coupling, *Geophys. J. Int.*, **121**, 695–709.

Lin, F. C., M. P. Moschetti, and M. H. Ritzwoller (2008), Surface wave tomography of the western United States from ambient seismic noise: Rayleigh and Love wave phase velocity maps, *Geophys. J. Int.*, **XXX**, doi:10.1111/j1365-246X.2008.03720.x.

Lister, J. R. (1990), Buoyancy-driven fluid fracture: the effects of material toughness and of low-viscosity precursors, *J. Fluid Mech.*, **210**, 263–280.

Liu, Y., and J. R. Rice (2007), Spontaneous and triggered aseismic transient deformation in a subduction fault model, *J. Geophys. Res.*, **112**, doi: 10.1029/2007JB004930.

Lobkis, O. I., and R. L. Weaver (2001), On the emergence of the Green's function in the correlations of a diffuse field, *J. Acoust. Soc. Am.*, **110**, 3011–3017.

Luckman, A., and T. Murray (2005), Seasonal variation in velocity before retreat of Jakobshavn Isbrae, Greenland, *Geophys. Res. Lett.*, **32**, doi: 10.1029/2005GL022519.

Luckman, A., T. Murray, R. de Lange, and E. Hanna (2006), Rapid and synchronous ice-dynamic changes in East Greenland, *Geophys. Res. Lett.*, **33**, doi: 10.1029/2005GL025428.

MacAyeal, D. R., T. A. Scambos, C. L. Hulbe, and M. A. Fahnestock (2003), Catastrophic ice-shelf break-up by an ice-shelf-fragment-capsize mechanism, *J. Glaciol.*, **49**, 22–36.

MacAyeal, D. R., M. H. Okal, J. E. Thom, K. M. Brunt, Y. J. Kim, and A. K. Bliss (2008), Tabular iceberg collisions within the coastal regime, *J. Glaciol.*, **54**, 371–386.

Manning, R. (1891), On the flow of water in open channels and pipes, *Trans. Inst. Civil Eng.*, **20**, 161–207.

Mendelsohn, D. A. (1984), A review of hydraulic fracture modeling - part I: general concepts, 2D models, motivation for 3D modeling, *J. Energy Res. Tech.*, **106**, 369–376.

Milne-Thomson, L. M. (1955), *Theoretical Hydrodynamics*, 3rd ed., Macmillan, New York.

Montelli, R., G. Nolet, F. A. Dahlen, G. Masters, E. R. Engdahl, and S. H. Hung (2004), Finite-frequency tomography reveals a variety of plumes in the mantle, *Science*, **303**, 338–343.

Morgan, V. I., T. H. Jacka, G. J. Akerman, and A. L. Clarke (1982), Outlet glacier and mass-budget studies in Enderby, Kemp, and MacRobertson Lands, Antarctica, *Ann. Glaciol.*, **3**, 204–210.

Muskhelishvili, N. I. (1953), *Some Basic Problems of the Mathematical Theory of Elasticity*, 3rd ed., 704 pp., Noordhoff Ltd, Groningen, Holland.

Nakahara, H. (2006), A systematic study of theoretical relations between spatial correlation and Green's function in one-, two- and three-dimensional random scalar wavefields, *Geophys. J. Int.*, **167**, 1097–1105.

Neave, K. G., and J. C. Savage (1970), Icequakes on Athabasca glacier, *J. Geophys. Res.*, **75**, 1351–1362.

Nettles, M., G. Ekström, A. M. Dziewonski, N. N. Maternovskaya, and V. C. Tsai (2005), Source characteristics of the great Sumatra earthquake and its aftershocks, *Eos. Trans. AGU*, **86**, Jt. Assem. Suppl., Abstract U43A-01.

Nettles, M., et al. (2007), Short-time-scale variations in flow speed and behavior, Helheim Glacier, East Greenland, *Eos. Trans. AGU*, **88**(52), Fall Meet. Suppl., Abstract C13A-08.

Nettles, M., et al. (2008), Step-wise changes in glacier flow speed coincide with calving and glacial earthquakes at Helheim Glacier, Greenland, *Geophys. Res. Lett.*, **35**, L24503, doi:10.1029/2008GL036127.

Nye, J. F. (1965), The flow of a glacier in a channel of rectangular, elliptic or parabolic cross-section, *J. Glaciol.*, **5**, 661–690.

O'Neel, S., H. P. Marshall, D. E. McNamara, and W. T. Pfeffer (2007), Seismic detection and analysis of icequakes at Columbia Glacier, Alaska, *J. Geophys. Res.*, **112**, doi:10.1029/2006JF000595.

Park, J., et al. (2005), Earth's free oscillations excited by the 26 December 2004 Sumatra-Andaman earthquake, *Science*, **308**, 1139–1144.

Paterson, W. S. B. (2002), *The Physics of Glaciers*, 3rd ed., Butterworth-Heinemann, Oxford.

Qamar, A. (1988), Calving icebergs: a source of low-frequency seismic signals from Columbia Glacier, Alaska, *J. Geophys. Res.*, **93**, 6615–6623.

Rice, J. R. (1985), First-order variations in elastic fields due to variation in location of a planar crack front, *J. App. Mech.*, **52**, 571–579.

Rice, J. R., and G. C. Sih (1965), Plane problems of cracks in dissimilar media, *J. App. Mech.*, **32**, 418–423.

Rignot, E., D. Braaten, S. P. Gogineni, W. B. Krabill, and J. R. McConnell (2004), Rapid ice discharge from southeast Greenland glaciers, *Geophys. Res. Lett.*, **31**, doi:10.1029/2004GL019474.

Rist, M. A., P. R. Sammonds, S. A. F. Murrell, P. G. Meredith, C. S. M. Doake, H. Oerter, and K. Matsuki (1999), Experimental and theoretical fracture mechanics applied to Antarctic ice fracture and surface crevassing, *J. Geophys. Res.*, **104**, 2973–2987.

Ritsema, J., H. J. van Heijst, and J. H. Woodhouse (2004), Global transition zone tomography, *J. Geophys. Res.*, **109**, doi:10.1029/2003JB002610.

Roberts, M. J. (2005), Jokulhlaups: A reassessment of floodwater flow through glaciers, *Rev. Geophys.*, **43**, RG1002, doi:10.1029/2003RG000147.

Roper, S. M., and J. R. Lister (2007), Buoyancy-driven crack propagation: the limit of large fracture toughness, *J. Fluid Mech.*, **580**, 359–380, doi: 10.1017/S0022112007005472.

Rouse, H. (1955), *Elementary Mechanics of Fluids*, 9th ed., 376 pp., John Wiley and Sons, Inc., New York.

Roux, P., K. G. Sabra, W. A. Kuperman, and A. Roux (2005), Ambient noise cross correlation in free space: Theoretical approach, *J. Acoust. Soc. Am.*, **117**, 79–84.

Rubin, A. M. (1995), Propagation of magma-filled cracks, *Annu. Rev. Earth Planet. Sci.*, **23**, 287–336.

Rubin, H., and J. Atkinson (2001), *Environmental Fluid Mechanics*, 728 pp., Marcel Dekker, Inc., New York.

Ruina, A. (1983), Slip instability and state variable friction laws, *J. Geophys. Res.*, **88**, 10,359–10,370.

Sabra, K. G., P. Gerstoft, P. Roux, W. A. Kuperman, and M. C. Fehler (2005), Surface wave tomography from microseismcs in Southern California, *Geophys. Res. Lett.*, **32**, L14311, doi:10.1029/2005GL023155.

Sanchez-Sesma, F. J., and M. Campillo (2006), Retrieval of the Green's function from cross correlation: The canonical elastic problem, *Bull. Seismol. Soc. Am.*, **96**, 1182–1191.

Sanchez-Sesma, F. J., J. A. Perez-Ruiz, M. Campillo, and F. Luzon (2006), Elastodynamic 2D Green function retrieval from cross-correlation: canonical inclusion problem, *Geophys. Res. Lett.*, **33**, L13305, doi:10.1029/2006GL026454.

Savitski, A. A., and E. Detournay (2002), Propagation of a penny-shaped fluid-driven fracture in an impermeable rock: asymptotic solutions, *Int. J. Solids Struc.*, **39**, 6311–6337.

Schoof, C. (2005), The effect of cavitation on glacier sliding, *Proc. R. Soc. A*, **461**, 609–627.

Schörghofer, N., B. Jensen, A. Kudrolli, and D. H. Rothman (2004), Spontaneous channelization in permeable ground: theory, experiment, and observation, *J. Fluid Mech.*, **503**, 357–374.

Schulson, E. M. (2001), Brittle failure of ice, *Eng. Frac. Mech*, **68**, 1839–1887.

Shapiro, N. M., and M. Campillo (2004), Emergence of broadband Rayleigh waves from correlations of the ambient seismic noise, *Geophys. Res. Lett.*, **31**.

Shapiro, N. M., M. Campillo, L. Stehly, and M. H. Ritzwoller (2005), High-resolution surface-wave tomography from ambient seismic noise, *Science*, **307**, 1615–1618.

Short, M. B., J. C. Baygents, and R. E. Goldstein (2006), A free-boundary theory for the shape of the ideal dripping icicle, *Phys. Fluids*, **18**, doi:10.1063/1.2335152.

Smith, A. M. (2006), Microearthquakes and subglacial conditions, *Geophys. Res. Lett.*, **33**, doi:10.1029/2006GL028207.

Smith, G. P., and G. Ekström (1997), Interpretation of earthquake epicenter and CMT centroid locations in terms of rupture length and direction, *Phys. Earth Planet. Inter.*, **102**, 123–132.

Smith, R. A. (1976), The application of fracture mechanics to the problem of crevasse propagation, *J. Glaciol.*, **76**, 223–228.

Sneddon, I. N. (1946), The distribution of stress in the neighbourhood of a crack in an elastic solid, *Proc. Royal Soc. Lond. A*, **187**, 229–260.

Snieder, R. (2004), Extracting the Green's function from the correlation of coda waves: A derivation based on stationary phase, *Phys. Rev. E*, **69**, 1–8.

Snieder, R., K. Wapenaar, and K. Larner (2006), Spurious multiples in seismic interferometry of primaries, *Geophys.*, **71**, SI111–SI124.

Spence, D. A., and P. Sharp (1985), Self-similar solutions for elastohydrodynamic cavity flow, *Proc. Royal Soc. Lond. A*, **400**, 289–313.

Stehly, L., M. Campillo, and N. M. Shapiro (2006), A study of the seismic noise from its long-range correlation properties, *J. Geophys. Res.*, **111**, 1–12.

Stein, S., and E. A. Okal (2005), Speed and size of the Sumatra earthquake, *Nature*, **434**, 581–582.

Stevenson, D. J. (1982), Migration of fluid-filled cracks: Applications to terrestrial and icy bodies, *Proc. Lunar Planet. Sci. Conf.*, **r***13*, Abstract 1394.

Strickler, A. (1923), Beitrage zur frage der geschwindigkeitsformel und der rauhigkeitszahlen fur strome, kanale und geschlossene leitungen, *Tech. rep.*, Mitteilungen des Eidgenossischen Amtes fur Wasserwirtschaft 16, Bern, Switzerland.

Strickler, A. (1981), Contributions to the question of a velocity formula and roughness data for streams, channels and closed pipelines, *translation T-10 by T. Roesgen and W. R. Brownlie, W. M. Keck Lab of Hydraulics and Water Resourses*, California Institute of Technology, Pasadena.

Stroeve, J. C., M. C. Serreze, F. Fetterer, T. Arbetter, W. Meier, J. Maslanik, and K. Knowles (2004), Tracking the Arctic's shrinking ice cover: another extreme September minimum in 2004, *Geophys. Res. Lett.*, **32**, doi:10.1029/2004GL021810.

Stuart, G., T. Murray, A. Brisbourne, P. Styles, and S. Toon (2005), Seismic emissions from a surging glacier: Bakaninbreen, Svalbard, *Ann. Glaciol.*, **42**, 151–157.

Tada, H., P. C. Paris, and G. R. Irwin (2000), *The Stress Analysis of Cracks Handbook*, 3rd ed., 677 pp., ASME Press, New York.

Timoshenko, S., and S. Woinowsky-Krieger (1959), *Theory of Plates and Shells*, 2nd ed., 580 pp., McGraw-Hill, New York.

Timoshenko, S. P., and J. N. Goodier (1987), *Theory of Elasticity*, 3rd ed., 567 pp., McGraw-Hill, New York.

Truffer, M., and K. A. Echelmeyer (2003), Of isbrae and ice streams, *Ann. Glaciol.*, **36**, 66–72.

Truffer, M., K. A. Echelmeyer, and W. D. Harrison (2001), Implications of till deformation on glacier dynamics, *J. Glaciol.*, **47**, 123–134.

Truffer, M., J. Amundson, M. Fahnestock, and R. J. Motyka (2006), High time resolution velocity measurements on Jakobshavn Isbrae, *Eos. Trans. AGU*, **87**(52), Fall Meet. Suppl., Abstract C11A-1132.

Tsai, V. C., and G. Ekström (2007), Analysis of glacial earthquakes, *J. Geophys. Res.*, **112**, F03S22, doi:10.1029/2006JF000596.

Tsai, V. C., and J. R. Rice (2006), Possible mechanisms for glacial earthquakes, *Eos. Trans. AGU*, **87**(52), Fall Meet. Suppl., Abstract C41A-0290.

Tsai, V. C., and J. S. Wettlaufer (2007), Star patterns on lake ice, *Phys. Rev. E*, **75**, doi:10.1103/PhysRevE.75.066105.

Tsai, V. C., M. Nettles, G. Ekström, and A. M. Dziewonski (2005), Multiple CMT source analysis of the 2004 Sumatra earthquake, *Geophys. Res. Lett.*, **32**, L17304, doi:10.1029/2005GL023398.

Tsai, V. C., J. R. Rice, and M. Fahnestock (2008), Possible mechanisms for glacial earthquakes, *J. Geophys. Res.*, **113**, F03014, doi:10.1029/2007JF000944.

Tse, S. T., and J. R. Rice (1986), Crustal earthquake instability in relation to the depth variation of frictional slip properties, *J. Geophys. Res.*, **91**, 9452–9472.

Tulaczyk, S., W. B. Kamb, and H. F. Engelhardt (2000), Basal mechanics of Ice Stream B, West Antarctica 1. till mechanics, *J. Geophys. Res.*, **105**, 463–481.

van der Veen, C. J. (1998), Fracture mechanics approach to penetration of surface crevasses on glaciers, *Cold Reg. Sci. Tech.*, **27**, 31–47.

van der Veen, C. J. (2007), Fracture propagation as means of rapidly transferring surface meltwater to the base of glaciers, *Geophys. Res. Lett.*, **34**, L01501, doi: 10.1029/2006GL028385.

VanWormer, D., and E. Berg (1973), Seismic evidence for glacier motion, *J. Glaciol.*, **12**, 259–265.

Vaughan, D. G. (1995), Tidal flexure at ice shelf margins, *J. Geophys. Res.*, **100**, 6213–6224.

Venteris, E. R. (1999), Rapid tidewater glacier retreat: a comparison between Columbia Glacier, Alaska and Patagonian calving glaciers, *Global Planet. Change*, **22**, 131–138.

Vigny, C., et al. (2005), Insight into the 2004 Sumatra-Andaman earthquake from GPS measurements in southeast Asia, *Nature*, **436**, 201–206.

Walder, J. S. (1982), Stability of sheet flow of water beneath temperate glaciers and implications for glacier surging, *J. Glaciol.*, **28**, 273–293.

Walsh, J. B., and J. R. Rice (1979), Local changes in gravity resulting from deformation, *J. Geophys. Res.*, *bf 84*, 165–170.

Walsh, J. E., and W. L. Chapman (2001), 20th-century sea-ice variations from observational data, *Ann. Glaciol.*, **33**, 444–448.

Wapenaar, K. (2004), Retrieving the elastodynamic Green's function of an arbitrary inhomogeneous medium by cross correlation, *Phys. Rev. Lett.*, **93**, 1–4.

Wapenaar, K., E. Slob, and R. Snieder (2006), Unified Green's function retrieval by cross correlation, *Phys. Rev. Lett.*, **97**, doi:10.1103/PhysRevLett.97.234301.

Weaver, C. S., and S. D. Malone (1979), Seismic evidence for discrete glacier motion at the rock-ice interface, *J. Glaciol.*, **23**, 171–184.

Weertman, J. (1971a), Theory of water-filled crevasses in glaciers applied to vertical magma transport beneath oceanic ridges, *J. Geophys. Res.*, **76**, 1171–1183.

Weertman, J. (1971b), Velocity at which liquid-filled cracks move in the earth's crust or in glaciers, *J. Geophys. Res.*, **r***76*, 8544–8553.

Weertman, J. (1973), Can a water-filled crevasses reach the bottom surface of a glacier?, *Inter. Assoc. Sci. Hydro. Publ.*, **95**, 139–145.

White, F. M. (2008), *Fluid Mechanics*, 6th ed., 864 pp., McGraw-Hill, New York.

Wiens, D. A., S. Anandakrishnan, J. P. Winberry, and M. A. King (2008), Seasonal speedup along the western flank of the Greenland Ice Sheet, *Nature*, **453**, doi: 10.1038/nature06990.

Williams, M. L. (1952), Stress singularities resulting from various boundary conditions in angular corners of plates in extension, *J. Appl. Mech.*, **19**, 526–528.

Wolf, L. W., and J. N. Davies (1986), Glacier-generated earthquakes from Prince William Sound, Alaska, *Bull. Seismol. Soc. Am.*, **76**, 367–379.

Woodcock, A. H. (1965), Melt patterns in ice over shallow waters, *Limnol. Oceanogr.*, **10**, R290–R297.

Worster, M. G. (1997), Convection in mushy layers, *Annu. Rev. Fl. Mech.*, **29**, 91–122.

Yang, Y., and M. H. Ritzwoller (2008), Characteristics of ambient seismic noise as a source for surface wave tomography, *Geochem. Geophys. Geosyst.*, **9**, doi: 10.1029/2007GC001814.

Yang, Y., M. H. Ritzwoller, A. L. Levshin, and N. M. Shapiro (2007), Ambient noise Rayleigh wave tomography across Europe, *Geophys. J. Int.*, **168**, 259–274.

Yao, H., and R. D. van der Hilst (2008), Analysis of bias in surface wave phase velocities from ambient noise interferometry and an iterative approach for azimuthal anisotropy, *Eos. Trans. AGU*, **89**(53), Fall Meet. Suppl., Abstract S31A-1897.

Yao, H., R. D. van der Hilst, and M. V. de Hoop (2006), Surface-wave array tomography in SE Tibet from ambient seismic noise and two-station analysis - I. phase velocity maps, *Geophys. J. Int.*, **166**, 732–744.

Zhou, Y., F. A. Dahlen, and G. Nolet (2004), Three-dimensional sensitivity kernels for surface wave observables, *Geophys. J. Int.*, **158**, 142–168.

Zwally, H. J., W. Abdalati, T. Herring, K. Larson, J. Saba, and K. Steffen (2002), Surface melt-induced acceleration of Greenland ice-sheet flow, *Science*, **297**, 218–222.

Appendix A

Additional Materials for Chapter 3

A.1 Approximate Timescale for Calved Iceberg to Slide Down to Equilibrium

To arrive at the timescale of a calved iceberg sliding freely on a bed with positive slope β, we note that under hydrostatic water pressure (including along the bed) the net force in the down-slope direction is

$$F = \rho g H_C W_C L_C \sin\beta - \rho_w g W_C L_C \tan\beta \cdot \Delta h, \tag{A.1}$$

where Δh is the height to the water surface level as measured from the middle of the base of the iceberg (see Figure 3.5b), and the iceberg is assumed to be a rectangular block of height H_C, length L_C, and width W_C parallel to the bed. Defining x along the bed to be positive in the downstream direction and $x = 0$ where $\Delta h = 0$ then $\Delta h = x \sin\beta$ so that

$$F(x) = g W_C L_C \sin\beta \cdot (\rho H_C - \rho_w \tan\beta \cdot x). \tag{A.2}$$

Defining x_0 to be the point at which the driving force vanishes, then $\rho H_C = \rho_w \tan\beta \cdot x_0$ and

$$F(x) = \rho_w g W_C L_C \sin\beta \tan\beta \cdot (x_0 - x). \tag{A.3}$$

Substituting (A.3) into Newton's second law gives

$$\rho_w g W_C L_C \sin\beta \tan\beta \cdot (x_0 - x) = \rho W_C L_C H_C \cdot \ddot{x} \tag{A.4}$$

which, with initial conditions $x_0 - x(0) = x_1$ and $\dot{x}(0) = 0$, has solution

$$x(t) = x_0 - x_1 \cos(\pi \cdot t/T) \tag{A.5}$$

with timescale given by

$$T = \pi \sqrt{\frac{\rho H_C \cos\beta}{\rho_w g \sin^2\beta}}. \tag{A.6}$$

The above analysis is only true as long as the top-forward corner of the iceberg is not submerged, or equivalently

$$x \sin\beta < H_C \cos\beta - \frac{L_C}{2} \sin\beta. \tag{A.7}$$

Taking $x_1 \ll x_0$ then the solution (A.5) is valid as long as $x = x_0$ satisfies (A.7) or

$$\tan\beta < \left(1 - \frac{\rho}{\rho_w}\right) \frac{2H_C}{L_C} \approx \frac{H_C}{5L_C}, \tag{A.8}$$

which is true since $\beta \ll 1$. This analysis yields a lower bound estimate of the timescale since it assumes water freely moves to maintain hydrostatic balance.

A.2 Rotational Iceberg Calving Model

As in *MacAyeal et al.* [2003], we assume the forces on the iceberg are (1) hydrostatic water pressure applied at all submerged surfaces, (2) gravitational weight

of the iceberg , and (3) calving-contact force from the glacier face F_C (and from the iceberg melange F_{C2} in model IIB) (see Figure 3.6). Instead of solving for equilibrium conditions, these forces are then used in Equations (3.10)-(3.12). Forces from water pressure in the x-direction cancel out, leaving F_x as a sum of contact forces. (With no iceberg melange $F_C = -F_x$.) Accounting for weight and vertical pressure forces, where y_i is the water depth of the center of mass of the iceberg, F_y is given by either

$$F_y = gM_C \left(1 - \frac{\rho_w}{2\rho} - \frac{\rho_w y_i}{\rho H_C \cos\theta}\right) \tag{A.9}$$

when the top two corners of the iceberg are un-submerged or

$$F_y = gM_C \left(1 - \frac{\rho_w}{\rho} + \frac{\rho_w (H_C \cos\theta + L_C \sin\theta - 2y_i)^2}{8\rho H_C L_C \sin\theta \cos\theta}\right) \tag{A.10}$$

when only one corner is un-submerged. Similarly, τ_{rot} is given by

$$\tau_{rot} = -(F_C r_\perp + F_{C2} r_\perp) + \int\limits_{submerged} p_w r_\perp dA = -\tau_{rot1} + \tau_{rot2}, \tag{A.11}$$

where $r_\perp$ is closest distance to the center of mass of the line of action of the force,

$$\tau_{rot1} = \frac{H_C}{2} F_C \frac{2M_{xa} - M_{xa0}}{M_{xa}} \left(\cos\theta - \frac{L_C}{H_C}\sin\theta\right), \tag{A.12}$$

and τ_{rot2} is given by either

$$\tau_{rot2} = M_C g H_C \frac{\rho_w \sin\theta}{\rho \cos^2\theta} \left[\frac{1}{8}\cos^2\theta - \frac{y_i^2}{2H_C^2} - \frac{L_C^2}{24H_C^2}(1 + \cos^2\theta)\right] \tag{A.13}$$

when the top two corners of the iceberg are un-submerged or

$$\begin{aligned} \tau_{rot2} = {} & \tfrac{\rho_w g W_C}{6} \left(y_i - \tfrac{H_C}{2}\cos\theta - \tfrac{L_C}{2}\sin\theta\right)^2 \\ & \cdot \left[\tfrac{\sin^2\theta - \cos^2\theta}{\cos^2\theta \sin^2\theta} y_i + \tfrac{H_c}{\cos\theta} - \tfrac{L_C}{\sin\theta} + \tfrac{H_C \cos\theta}{2\sin^2\theta} - \tfrac{L_C \sin\theta}{2\cos^2\theta}\right] \end{aligned} \tag{A.14}$$

when only one corner is un-submerged. Note that τ_{rot1} accounts for the torque from the contact forces, τ_{rot2} accounts for the torque from the water pressure. Finally, to close the system of equations, we have the contact constraint

$$x_i = \frac{1}{2}(H_C \sin\theta + L_C \cos\theta). \tag{A.15}$$

Combining Equations (3.10), (3.12), (A.11), and (A.15) results in an equation of the form

$$A(\theta)\ddot{\theta} = B(\theta)\dot{\theta}^2 + C(\theta, y_i) \tag{A.16}$$

which, along with Equations (3.11), (A.9) and (A.10), are a 2D system of equations in the variables θ and y_i that are then solved numerically. Initial conditions are chosen with small but non-zero θ ($0.1 \leq \theta \leq 0.15$ radians) to ensure eventual tipping of the iceberg, and a range of initial y_i including that for a neutrally buoyant iceberg. Since the seismic response is only sensitive to large values of CSF rate, $\dot{A}$, the A and T reported are for the time range when $\dot{A}$ is a significant fraction of the maximum value of $\dot{A}$ attained (e.g. $\dot{A} \geq 0.2\max[\dot{A}]$).

A.3 Analytic Approximation for Purely Elastic Response

To arrive at an analytic approximation for the purely elastic response, we perform a force balance on the glacier block of mass $M = \rho HWL$ that is initially held by friction f_0, which drops to zero along the base over a length ΔL, and is then allowed to move as constrained by elastic elements at its side margins and upstream end. As

in Section 3.3.6, balancing gravitational driving force against basal friction plus the force accommodated by Glen's law at the margins (over length scale W_S) yields an expression for the steady-state basal friction

$$f_0 = \alpha - \frac{2s}{\rho g W}\left(\frac{u_{ss}}{2W_S A_{Gl}}\right)^{1/3}. \tag{A.17}$$

Allowing this friction to drop to zero over length ΔL gives a force perturbation

$$\Delta F = f_0 \Delta M g = f_0 \rho g H W \Delta L. \tag{A.18}$$

The elastic force from displacing Δx with marginal shear (over two sides of width W_S) and longitudinal stretching (over one side of length L_S, with elastic modulus approximately three times that of the shear modulus) is

$$F_E(\Delta x) = E\Delta x = sWH(3\mu_2 \Delta x/L_S) + 2sLH(\mu_2 \Delta x/W_S). \tag{A.19}$$

The glacier block then satisfies the simple differential equation

$$M\Delta\ddot{x} + E\Delta x = \Delta F, \tag{A.20}$$

which has a simple sinusoidal solution with amplitude and timescale given by

$$\Delta x_{max} = 2\Delta F/E \tag{A.21}$$

and

$$T = Period/2 = \pi\sqrt{\frac{M}{E}} \tag{A.22}$$

so that the CSF amplitude $A = M\Delta x_{max}$ and timescale are given by

$$A = \frac{\rho^2 g H W^2 W_S \cdot \Delta L}{s\mu_2[1 + 3WW_S/(2LL_S)]} \cdot \left[\alpha - \frac{2s}{\rho g W}\left(\frac{u_{ss}}{2W_S A_{Gl}}\right)^{1/3}\right] \tag{A.23}$$

and

$$T = \pi\sqrt{\frac{2\rho W W_S L L_S}{s\mu_2(3WW_S + 2LL_S)}}. \tag{A.24}$$

Appendix B

Additional Materials for Chapter 4

B.1 Validity of the Bimaterial Approximation

In Section 4.3.2, we approximate the bimaterial crack as having an opening given by ξ times the opening for a crack in a homogeneous sample of the more compliant material. Here, we verify the validity of this approximation for an ice-rock interface. Following the analysis of *Rice and Sih* [1965] (see also *England* [1965] and *Erdogan* [1965]), we consider a crack of length $2L$ along the bimaterial interface within an infinite medium with upper medium characterized by shear modulus G_1 and Poisson's ratio ν_1 and lower medium characterized by G_2 and ν_2. For our ice-rock case, we take ice elastic parameters as in Section 4.4 ($E_1 = 6.2$ GPa, $\nu_1 = 0.3$ so that $G_1 = 2.4$ GPa) and rock elastic parameters from near-surface granite seismic velocities of *Lay and Wallace* [1995] (and $\rho_2 = 2750$ kg/m^3) which give $G_2 = 23$ GPa $\approx 9.6 G_1$ and $\nu_2 = 0.3 \approx \nu_1$. With these choices, the bimaterial 'mismatch' constant

$$\epsilon \equiv \frac{1}{2\pi} \log \left[\left(\frac{\eta_1}{G_1} + \frac{1}{G_2} \right) / \left(\frac{\eta_2}{G_2} + \frac{1}{G_1} \right) \right], \tag{B.1}$$

with $\eta \equiv 3 - 4\nu$, has a value of $\epsilon = 0.075124$. Given an arbitrary crack pressure loading $P(x)$ along $-L < x < L$, the complex displacements $u_k + iv_k$ (u_k in the horizontal direction and v_k in the vertical direction, throughout this appendix) on either side of the crack ($k = 1$ or 2) are given by Equations (14) and (15) of *Rice and Sih* [1965] (evaluated along $z = \bar{z}$ where $z = z_1 + iz_2$ is a complex variable, with z_1 horizontal and z_2 vertical coordinates) to be

$$2G_1(u_1 + iv_1) = \eta_1 \int^{z} g(s)F(s)ds - e^{2\pi\epsilon} \int^{\bar{z}} g(\bar{s})F(\bar{s})d\bar{s} \tag{B.2}$$

on the upper side and

$$2G_2(u_2 + iv_2) = e^{2\pi\epsilon}\eta_2 \int^{z} g(s)F(s)ds - \int^{\bar{z}} g(\bar{s})F(\bar{s})d\bar{s} \tag{B.3}$$

on the lower side. As also given in *Rice and Sih* [1965],

$$F(z) = (z^2 - L^2)^{-1/2} \left(\frac{z+L}{z-L}\right)^{i\epsilon}, \tag{B.4}$$

with branch cut along the crack such that $zF(z) \to 1$ as $|z| \to \infty$, and

$$g(s) = \int_{-L}^{L} g(s,b)db, \tag{B.5}$$

where

$$g(s,b) = \frac{P(b)}{2\pi} \frac{e^{-\pi\epsilon}}{s-b} (L^2 - b^2)^{1/2} \left(\frac{L-b}{L+b}\right)^{i\epsilon}. \tag{B.6}$$

Along the crack face $-L < s < L$, $F(s)$ simplifies to

$$F(s_\pm) = -1 \cdot \pm ie^{\pm\pi\epsilon}(L^2 - s^2)^{-1/2} \cdot [\cos(\epsilon \log \frac{L+s}{L-s}) + i \sin(\epsilon \log \frac{L+s}{L-s})], \tag{B.7}$$

where $+$ is used for s above the crack, $-$ is used for s below the crack.

Substituting Equations (B.5) and (B.7) into Equations (B.2) and (B.3) gives expressions for the complex displacements along the crack face. Expanding each of these expressions as a power series in the parameter ϵ and approximating the expressions to first order in ϵ (ignoring all higher-order terms), we find that we can express the complex displacements along the crack face as

$$u_1 + iv_1 = \frac{1}{E_1'}(\epsilon I_1 + iI_2) + O(\epsilon^2) \tag{B.8}$$

and

$$u_2 + iv_2 = -\frac{1}{E_2'}(\epsilon I_1 + iI_2) + O(\epsilon^2). \tag{B.9}$$

I_1 and I_2 are (complicated) expressions that involve only real integrals, and the full crack opening displacement in a homogeneous medium characterized by G_1 and ν_1 is given by

$$2(u_1 + iv_1) = 0 + \frac{1}{E_1'}iI_2. \tag{B.10}$$

We then observe that to order ϵ, the displacement v_1 is unchanged from its value in the homogeneous case and that the displacement on the lower side, v_2 is given by

$$v_2 \approx -\frac{E_1'}{E_2'}v_1 \approx -\frac{v_1}{9.6}. \tag{B.11}$$

Thus, the full opening in the bimaterial case $v_1 - v_2$ is approximately ξ of the full opening in the homogeneous case where ξ is given by

$$\xi \approx \frac{1 + E_1'/E_2'}{2} \approx 0.55. \tag{B.12}$$

We therefore use the approximation $h = 0.55w$.

B.2 Stresses in the Bulk

Here, we describe the stresses in the elastic medium associated with the crack-tip solution of *Desroches et al.* [1994] that are used to obtain Equations (4.12) and (4.13). Following *Desroches et al.* [1994], we write the *Muskhelishvili* [1953] potential as

$$\phi(z) = \frac{A}{2\alpha} z^{\alpha}, \tag{B.13}$$

where $z = z_1 + iz_2$ is again a complex variable, and α is a constant (different than the α used in the main text). We follow *Desroches et al.* [1994] and take the other *Muskhelishvili* [1953] potential as $\psi(z) = \phi(z) - z\phi'(z)$ in order to maintain zero shear along the crack axis $y = 0$. We can then calculate the stresses in polar coordinates to be given by

$$\frac{\sigma_{\theta\theta} + \sigma_{rr}}{2} = \frac{\sigma_{xx} + \sigma_{yy}}{2} = Ar^{\alpha-1}\cos[(\alpha - 1)\theta] \tag{B.14}$$

and

$$\begin{aligned} \frac{\sigma_{\theta\theta} - \sigma_{rr}}{2} + i\sigma_{r\theta} &= e^{2i\theta}\left(\frac{\sigma_{yy} - \sigma_{xx}}{2} + i\sigma_{yx}\right) \\ &= (1-\alpha)Ar^{\alpha-1}\sin(\theta)[-\sin(\alpha\theta) + i\cos(\alpha\theta)]. \end{aligned} \tag{B.15}$$

Solving for the stresses gives

$$\sigma_{rr}(r,\theta) = Ar^{\alpha-1} \cdot \left[\frac{3-\alpha}{2}\cos[(1-\alpha)\theta] - \frac{1-\alpha}{2}\cos[(1+\alpha)\theta\right], \tag{B.16}$$

$$\sigma_{r\theta}(r,\theta) = Ar^{\alpha-1} \cdot \left[\frac{1-\alpha}{2}\sin[(1-\alpha)\theta] - \frac{1-\alpha}{2}\sin[(1+\alpha)\theta\right], \tag{B.17}$$

and

$$\sigma_{\theta\theta}(r,\theta) = Ar^{\alpha-1} \cdot \left[\frac{1+\alpha}{2}\cos[(1-\alpha)\theta] + \frac{1-\alpha}{2}\cos[(1+\alpha)\theta\right]. \tag{B.18}$$

These expressions give the stress components of the *Desroches et al.* [1994] solution except for a possible added uniform pressure, $\sigma_{\theta\theta} = -P$ and $\sigma_{rr} = -P$, and an additional added crack-parallel stress $\sigma_{xx} = constant$ (which will not enter our analysis). Equation (4.13) is then obtained by demanding that $p(x)$ and the crack opening gap satisfy the fluid equations (Equations (4.7), (4.9) and (4.10)) in the case of steady state growth, leading to $\alpha = 2/(2+n) = 6/7$ and evaluating Equation (B.18) along the crack opening to yield

$$\Delta p(x) - P = -\sigma_{\theta\theta}(R, \pi) = -AR^{-1/7} \cos\left(\frac{\pi}{7}\right). \tag{B.19}$$

Appendix C

Additional Material for Chapter 7

C.1 Proof of the $\pi/4$ Phase Shift Applicable to Surface-Wave Noise Tomography

We take v to be spatially uniform but potentially dispersive, $t(\theta) = \Delta x \cos\theta / v$ and rewrite Equation (7.20) as

$$\rho(t(\theta)) \propto \frac{v/\Delta x}{\sqrt{1-(v\Delta t/\Delta x)^2}} = \frac{v/\Delta x}{|\sin\theta|}. \tag{C.1}$$

For a positive windowing function

$$W(t) = \begin{cases} 1, & t > 0 \\ \\ 0, & t < 0 \end{cases}. \tag{C.2}$$

Equation (7.10) thus simplifies to

$$\begin{aligned} \omega\tau(\omega) + 2\pi N &= \phi\left[\int_0^{\Delta x/v} \frac{v/\Delta x}{\sin\theta(t)} e^{i\omega t} dt\right] \\ &= \phi\left[\int_0^{\pi/2} e^{i\cos\theta\omega\Delta x/v} d\theta\right]. \end{aligned} \tag{C.3}$$

The integral in Equation (C.3) is identified as a Bessel integral, giving

$$\omega\tau(\omega) + 2\pi N = \phi\big[\alpha_1[J_0(\omega\Delta x/v) + iH_0(\omega\Delta x/v)]\big] \tag{C.4}$$

where J_0 is a Bessel function of the first kind of order zero, H_0 is a Struve function of order zero, and α_1 is a constant. Taking $\omega\Delta x/v \gg 1$, Equation (C.4) can be approximated as

$$\begin{aligned} \omega\tau(\omega) + 2\pi N &\approx \phi\big[\alpha_1[J_0(\omega\Delta x/v) + iY_0(\omega\Delta x/v)]\big] \\ &\approx \phi\left[\frac{\alpha_2}{\sqrt{\omega\Delta x/v}} \cdot \exp\left[i\left(\frac{\omega\Delta x}{v} - \frac{\pi}{4}\right)\right]\right] \\ &\approx \frac{\omega\Delta x}{v} - \frac{\pi}{4}, \end{aligned} \tag{C.5}$$

where Y_0 is a Bessel function of the second kind of order zero and α_2 is a constant. Thus, for positive time delay

$$\tau(\omega) \approx \frac{\Delta x}{v} - \frac{\pi}{4\omega} + \frac{2\pi N}{\omega} \tag{C.6}$$

and similarly, for negative time delay

$$\tau(\omega) \approx -\left[\frac{\Delta x}{v} - \frac{\pi}{4\omega}\right] + \frac{2\pi N}{\omega}. \tag{C.7}$$

We therefore derive the approximate $\pi/4\omega$ phase shift between $\tau(\omega)$ (the phase delay as measured by noise-correlation techniques) and $\Delta x/v$ (the phase travel time in a homogeneous velocity medium) without calculation of the surface-wave Green's function. It may be noted that the 2D surface-wave Green's function can be expressed in terms of J_0 and Y_0 so that comparison with Equation (C.4) would result in an explicit relationship between noise-correlation measurements and the Green's function response, as in other works.